



The
University
Of
Sheffield.

A Novel Heat Recovery Device for Passive Ventilation Systems

By:

Dominic Bernard O'Connor

A thesis submitted in partial fulfilment of the requirements for the degree of
Doctor of Philosophy

The University of Sheffield
Faculty of Engineering
Department of Mechanical Engineering

September 2016

The candidate confirms that the work submitted is his/her own, except where work which has formed part of jointly-authored publications has been included. The contribution of the candidate and the other authors to this work has been explicitly indicated below (**page iii**). The candidate confirms that appropriate credit has been given within the thesis where reference has been made to the work of others.

This copy has been supplied on the understanding that it is copyright material and that no quotation from the thesis may be published without proper acknowledgement

Acknowledgements

The completion of this project would not have been possible without the support and help from a number of people, to whom I owe a great deal of thanks. First and foremost, I would like to acknowledge the guidance and input from my project supervisors, Dr Ben Hughes and Dr John Calautit. Without their encouragement and support over both my undergraduate and postgraduate studies, this project would not have been conceivable. I truly appreciate everything each of them has done and how far they have helped me come.

I would like to thank my Mum, Brother, Sister and Brother-in-law for their unwavering support in having a student in the family for seven years. Their encouragement to keep going was required and provided me with something to work towards; I hope I have made them proud.

I would like to thank all my friends for their time, energy and encouragement, including when I needed to be away from the project. I would like to pay special thanks to Omar Matar, Katy Butler, Katie Allen, Shane Collins, Matt Rees, Adam Imrie, Jonathan Griffith, and Heather Owston along with many more for their support and continual jokes about opening windows. I would also like to thank my colleague, Polytimi Sofotasiou, for her boundless energy, enthusiasm, knowledge and company on the long nights of thesis writing.

I would like to acknowledge the academic, technical and support staff at the University of Leeds and the University of Sheffield for all their help and support.

Finally, I would like to dedicate this PhD to my Dad.

Abstract

The purpose of this study was to assess the performance of a novel heat recovery device for integration with a passive ventilation system. Current heat recovery devices are not suitable for integration with passive ventilation systems due to the high pressure drop experienced by airstreams across the devices. This would result in low ventilation supply rates required for good indoor air quality. The device could be also reconfigured to dehumidify an incoming airstream, lowering the relative humidity of the air. These modifications would improve the air quality and reduce energy demand on mechanical ventilation systems.

The novel heat recovery device was designed and constructed using 3D printing techniques and tested experimentally using different inlet conditions for two counter-current airstreams. Numerical analysis using Computational Fluid Dynamics (CFD) calculated solutions for air velocity, gauge air pressure, air temperature and relative humidity before and after the heat recovery device using the same geometry as the printed prototype. The experimental testing of prototypes of the heat recovery device validated these characteristics.

The results from the experiments and CFD analysis showed that the novel design of the heat recovery device achieved the three primary objectives of the project. The pressure drop measured across the heat recovery device was between 10.02-10.31Pa, significantly lower 150Pa experienced in standard devices. The resultant air velocity suggested that an air supply rate of 140.86 litres per second was possible, high enough to provide ventilation to a room with 17 occupants. The device was capable of increasing the temperature of the incoming airstream by up to 0.68°C when the temperature of the outgoing airstream was 40°C. Finally, the relative humidity of an incoming airstream with 100% relative humidity was reduced by up to 67.01%, at regeneration temperatures between 25-40°C, significantly lower than current temperatures of 120°C.

Contents

Acknowledgements.....	ii
Abstract.....	iii
Contents.....	iv
List of Tables	viii
List of Figures	xi
Preface	xix
Nomenclature	xxi
List of Abbreviations:	xxiii
Chapter 1.....	1
1 Introduction	1
1.1 Aims and Objectives.....	8
1.2 Project Methodology	9
1.3 Thesis Structure	10
Chapter 2.....	12
2 Literature Review.....	12
2.1 Introduction	12
2.2 Indoor Air Quality.....	12
2.3 Passive Ventilation Principles	15
2.4 Passive Ventilation Applications	24
2.5 Commercial Wind Towers.....	34
2.5.1 Wind Tower Development.....	35
2.5.2 Wind Tower Testing	41
2.6 Energy Recovery Ventilation Devices.....	46
2.6.1 Rotary Thermal Wheels.....	49
2.6.2 Fixed Plate Exchangers.....	54
2.6.3 Membrane Fixed Plate Exchanger	57
2.6.4 Heat Pipes	59

2.6.5	Run-Around Systems.....	62
2.6.6	Phase Change Materials.....	64
2.7	Applications of HRV in Passive Ventilation	68
2.7.1	Application of rotary thermal wheel.....	68
2.7.2	Application of Fixed Plate Heat Exchangers.....	69
2.7.3	Application of Heat Pipes.....	71
2.7.4	Application of Run-Around Systems	73
2.7.5	Application of Phase Change Materials	74
2.7.6	Heat Recovery Integration	75
2.8	Summary	78
2.9	Research Gap	79
	Chapter 3.....	81
3	CFD Methodology: Theory and Modelling.....	81
3.1	Introduction	81
3.2	CFD Principles and Theory	81
3.2.1	Governing Equations.....	81
3.2.2	Flow Solvers: Solution Algorithm.....	87
3.2.3	Solution Convergence	88
3.2.4	Physical Domain	89
3.2.5	Mesh Generation	89
3.2.6	Mesh Quality.....	90
3.2.7	Mesh Adaption.....	92
3.2.8	Quantification of CFD error and Uncertainties	93
3.3	Computational Fluid Dynamics (CFD) Modelling	94
3.3.1	Problem Identification	94
3.3.2	Design Geometry	97
3.3.3	CFD Design Geometry	98
3.3.4	Mesh Generation	103

3.3.5	Mesh Verification.....	106
3.3.6	Boundary Conditions.....	109
3.4	CFD Model Limitations.....	112
3.5	Summary	113
Chapter 4.....		114
4	Experimental Methods.....	114
4.1	Introduction	114
4.2	Experiment Design	114
4.3	Ductwork Design and Testing	118
4.3.1	Ductwork Flow Profile.....	119
4.3.2	Ductwork Flow Calibration.....	126
4.4	Experimental Model.....	128
4.4.1	Radial Blades	130
4.4.2	Inner Rotary Wheel Shell	132
4.4.3	Outer Rotary Wheel Shell	134
4.4.4	Rotary Wheel Casing	135
4.4.5	Rotary Wheel Assembly	137
4.5	Experimental Setup and Measurement Procedures.....	139
4.5.1	Air Velocity Measurement	140
4.5.2	Relative Humidity and Air Temperature Measurement	141
4.6	Experimental Test Equipment.....	143
4.6.1	Hot-wire Anemometer	143
4.6.2	Humidity and Temperature Sensor Probe.....	145
4.6.3	Data Acquisition System	146
4.7	Experimental Limitations	147
4.8	Summary	148
Chapter 5.....		149
5	Validation of Computational Fluid Dynamics (CFD) Model	149

5.1	Introduction	149
5.2	Heat Recovery Configuration Validation.....	149
5.2.1	Air Velocity	149
5.2.2	Air Temperature.....	153
5.3	Dehumidification Configuration Validation	157
5.3.1	Air Velocity	158
5.3.2	Air Temperature.....	161
5.3.3	Relative Humidity.....	166
5.4	Quantification of CFD Uncertainties	170
5.5	Summary	171
	Chapter 6.....	172
6	Results and Discussions	172
6.1	Introduction	172
6.2	Heat Recovery Rotary Wheel.....	173
6.2.1	Flow Visualisation	173
6.2.2	Air Velocity	176
6.2.3	Air Pressure	182
6.2.4	Air Temperature.....	187
6.3	Dehumidification Rotary Wheel.....	195
6.3.1	Flow Visualisation	196
6.3.2	Air Velocity	199
6.3.3	Air Pressure	205
6.3.4	Air Temperature.....	209
6.3.5	Relative Humidity.....	216
6.4	Summary	225
	Chapter 7.....	226
7	Conclusions and Future Work.....	226
7.1	Heat Recovery Rotary Wheel Analysis.....	226

7.2	Dehumidification Rotary Wheel Analysis.....	228
7.3	Key Findings	230
7.4	Recommendations for Future Work	234
	List of References.....	236

List of Tables

Table 2-1	– Suspected risk factors of HVAC types and building features [45].....	14
Table 2-2	– Brief comparison summary of Reynolds-Averaged Navier Stokes (RANS), Large Eddy Simulation (LES) and Direct Numerical Simulation (DNS) CFD Models.....	23
Table 2-3	– Comparison of Passive Ventilation Design Principles	33
Table 2-4	– Experimental Setup for each of the Designs and Comparison of Flow Rates at Different Wind Angles [19]	38
Table 2-5	– Summary and details of heat recovery devices	76
Table 3-1	– Range of skewness values and corresponding cell quality [173].....	91
Table 3-2	– CFD model boundary conditions for 32 and 20 radial blade heat recovery rotary wheel configurations	111
Table 3-3	– CFD model boundary conditions for 32 and 20 radial blade dehumidification rotary wheel configurations.....	112
Table 4-1	– Material property comparison.....	131
Table 4-2	– Co-ordinates for air velocity measurement locations (x, y, z)	141
Table 4-3	– Co-ordinates for relative humidity and air temperature measurement locations (x, y, z)	143
Table 4-4	– Testo 425 hot-wire anemometer specifications	144
Table 4-5	– Testo humidity/temperature probe specifications.....	146
Table 5-1	– Comparison of experiment and CFD air temperatures before and after the 32 radial blade rotary wheel configuration	155
Table 5-2	– Comparison of experiment and CFD air temperatures before and after the 20 radial blade rotary wheel configuration	157
Table 5-3	– Comparison of experiment and CFD air temperatures before and after the 32 radial blade rotary wheel configuration	163
Table 5-4	– Comparison of experiment and CFD air temperatures before and after the 20 radial blade rotary wheel configuration	165

Table 5-5 – Comparison of experiment and CFD relative humidity before and after the 32 radial blade rotary wheel configuration	168
Table 5-6 – Comparison of experiment and CFD relative humidity before and after the 20 radial blade rotary wheel configuration	170
Table 6-1 – Gauge pressure measurements before and after the rotary wheel in the incoming and outgoing airstreams for the 32 radial blade configuration.....	184
Table 6-2 – Gauge pressure measurements before and after the rotary wheel in the incoming and outgoing airstreams for the 20 radial blade configuration.....	185
Table 6-3 – Air temperature measurements for the incoming and outgoing airstreams for 32-blade arrangement	190
Table 6-4 – Percentage error for CFD model compared to experiment results for air temperature after the wheel. Heat source and heat sink values for incoming and outgoing airstreams and adjusted values for error	191
Table 6-5 – Air temperature measurements for the incoming and outgoing airstreams for 20-blade arrangement	193
Table 6-6 – Percentage error for CFD model compared to experiment results for air temperature after the wheel. Heat source and heat sink values for incoming and outgoing airstreams and adjusted values for error	194
Table 6-7 – Gauge pressure measurements before and after the rotary wheel in the incoming and outgoing airstreams for the 32 radial blade configuration.....	206
Table 6-8 – Gauge pressure measurements before and after the rotary wheel in the incoming and outgoing airstreams for the 20 radial blade configuration.....	207
Table 6-9 – Air temperature measurements for the incoming and outgoing airstreams for the 32-blade dehumidification rotary wheel	212
Table 6-10 – Percentage error for CFD model compared to experiment results for air temperature after the wheel. Heat source and heat sink values for incoming and outgoing airstreams and adjusted values for error	213
Table 6-11 – Air temperature measurements for the incoming and outgoing airstreams for the 20-blade dehumidification rotary wheel.....	215
Table 6-12 – Percentage error for CFD model compared to experiment results for air temperature after the wheel. Heat source and heat sink values for incoming and outgoing airstreams and adjusted values for error	216
Table 6-13 – Relative humidity measurements for the incoming and outgoing airstreams for the 32-blade dehumidification rotary wheel.....	219

Table 6-14 – Percentage error for CFD model compared to experiment results for relative humidity after the wheel. Mass source and mass sink values for incoming and outgoing airstreams and adjusted values for error	220
Table 6-15 – Relative humidity measurements for the incoming and outgoing airstreams for the 20-blade dehumidification rotary wheel	222
Table 6-16 – Percentage error for CFD model compared to experiment results for relative humidity after the wheel. Mass source and mass sink values for incoming and outgoing airstreams and adjusted values for error	224

List of Figures

Figure 1-1 – The approximate service and residential sector shares of primary energy use for 13 countries [4].....	1
Figure 1-2 – Wind creates a positive pressure on the windward side of a structure and a negative pressure on the leeward side [14]	3
Figure 1-3 – Schematic of a commercial multi-directional wind tower system [21].....	4
Figure 1-4 – Matrix structure of a rotary wheel recovery device used for mechanical HVAC	8
Figure 1-5 – PhD Methodology Flowchart	10
Figure 2-1 – Schematic view of different natural ventilation principles [48].	17
Figure 2-2 – Schematic diagram of the full-scale building with a vertical plate inside [49] ..	18
Figure 2-3 – (a) Mixing ventilation and (b) displacement ventilation [52]	19
Figure 2-4 – The general notation for a two-opening building with solar radiation [53].....	20
Figure 2-5 – Basic design configurations of an atrium space considered [70]	26
Figure 2-6 – An enclosure with (a) an unventilated atrium, and (b) a ventilated atrium. The arrows indicate the flowpaths through the enclosure. The shading represents the warm air in the upper regions of the room and atrium. The lighter shading in the upper atrium in (b) is representative of the cooler layer which forms due to the direct ventilation [71].....	27
Figure 2-7 – Schematic of solar chimney with vertical absorber geometry [74].....	29
Figure 2-8 – Airflow pattern in a conventional wind tower [79]	32
Figure 2-9 – Experimental testing set-up of the Windvent at Sheffield Hallam University [83]	34
Figure 2-10 – Airflow pattern and pathlines in and around the windcatcher (3-layer louvers and 12-layer louvers) (a) Airflow pattern, (b) Pathline [84]	37
Figure 2-11 – Experimental test set-up in the wind tunnel [88].....	40
Figure 2-12 – Required flow fields in wind tunnel test sections: (a) entirely uniform flow for aeronautical applications and (b) laterally uniform flow for Wind Engineering studies [90]	42
Figure 2-13 – Picture of the scaled air model in the test chamber [91]	42
Figure 2-14 – Isometric view of two-sided wind catcher model and its connected house model along with their dimensions and locations of pressure taps. All dimensions are in millimeter [94].....	43
Figure 2-15 – Schematic drawing of the wind tunnel at BSRIA [88].....	44
Figure 2-16 – Working principle of wheel heat recovery unit [107].....	49
Figure 2-17 – Relationship between pressure drop and air superficial velocity [38]	50

Figure 2-18 – Effect of outdoor air temperature (a) on input energy required, and (b) on fresh air temperature [115]	51
Figure 2-19 – Simple schematic showing the concurrent operation of a fixed plate heat exchanger.....	54
Figure 2-20 – Heat exchanger plastic frame flow channels [128].....	55
Figure 2-21 – The flow channel geometry for corrugated fixed plate heat exchangers [130]	56
Figure 2-22 – Schematic of a membrane-based energy recovery ventilator: (a) core in counter flow arrangement; (b) schematic of the physical model in a co-current and counter flow arrangements [133].	58
Figure 2-23 – Schematic representation of heat-pipe heat recovery unit in operation [139]	59
Figure 2-24 - Types of oscillating heat pipes [141]	61
Figure 2-25 – Schematic diagram of a run-around heat recovery system [144]	63
Figure 2-26 – Schematic diagram of heat transfer process of PCMs [154].....	66
Figure 2-27 – The melting enthalpy and melting temperature for the different groups of phase change materials. [151].....	67
Figure 2-28 – Comparison of air supply rate for a wind tower and a wind tower with a rotary thermal wheel against the guideline supply rate of 8l/s/p. [157]	69
Figure 2-29 – The schematic diagram of experimental chamber and total dimension [159]	70
Figure 2-30 – Temperature contour lines of a cross sectional plane in the test channel; (a) evaporative cooling (b) heat pipe device [160]	72
Figure 2-31 – The schematic view of the ventilation system in the passive house [163].....	73
Figure 2-32 – Schematic diagram of operation of Cool-Phase system [167].....	75
Figure 3-1 – Pressure-based segregated algorithm flowchart [168]	88
Figure 3-2 – Extraction of fluid domain from a solid CAD model representing a room [170]	89
Figure 3-3 – Ideal and Skewed Triangles and Quadrilaterals [173]	91
Figure 3-4 – Sinusoidal wave matrix structure of a rotary thermal wheel	94
Figure 3-5 – Concept of concentric circles model.....	96
Figure 3-6 – Concept of radial blade model.....	96
Figure 3-7 – A) 32 radial blade configuration, B) 20 radial blade configuration.....	97
Figure 3-8 – A) Experiment ductwork, B) Experiment wheel casing.....	98
Figure 3-9 – Ductwork and radial blade rotary wheel model used in CFD model	99

Figure 3-10 – Standard dimensions for radial blade rotary wheel	100
Figure 3-11 – The four configurations of radial blade rotary wheel tested A) 32x copper blades, B) 20x copper blades, C) 32x silica blades, D)20x silica blades.....	100
Figure 3-12 – The configurations of radial blade rotary wheel with fluid volumes A) 32x copper blades, B) 20x copper blades, C) 32x silica blades, D)20x silica blades	101
Figure 3-13 – Fluid volume extraction from solid volume geometry	102
Figure 3-14 – Position of additional fluid volumes representing copper/silica gel volumes (shown in green)	103
Figure 3-15 – Meshes used for A) 32x copper blades, B) 20x copper blades, C) 32x silica blades, D)20x silica blades	104
Figure 3-16 – Structured hexagonal mesh for additional silica gel volumes in 32x silica gel radial blade geometry.....	105
Figure 3-17 – Surface contours of cell equiangle skew for A) 32x copper blades, B) 20x copper blades, C) 32x silica blades, D)20x silica blades	105
Figure 3-18 – Surface contours for y^+ values for A) 32x copper blades, B) 20x copper blades, C) 32x silica blades, D)20x silica blades.....	106
Figure 3-19 – Air velocity flow profile for 32x silica gel configuration for increasing mesh size	107
Figure 3-20 – Air velocity flow profile for 20x silica gel configuration for increasing mesh size	108
Figure 3-21 – Error percentage of velocity at mid-height in the duct for 32x and 20x configurations of rotary wheel for increasing mesh size using tetrahedral shaped cells ...	108
Figure 3-22 – Error percentage of velocity at mid-height in the duct for 32x and 20x configurations of rotary wheel for increasing mesh size using hexagonal shaped cells	109
Figure 3-23 – Boundary conditions for flow domain through the ductwork.....	110
Figure 4-1 – Design of radial blade rotary wheel A) 32 blade configuration B) 20 blade configuration.....	115
Figure 4-2 – CAD schematic of the ductwork used for experimental testing.....	116
Figure 4-3 – The final experiment setup.....	118
Figure 4-4 – Acrylic ductwork used in experimental testing.....	119
Figure 4-5 – Location of measurement points for ductwork flow profile	120
Figure 4-6 – Flow profile of forward driven flow through channel at measurement location with axial fan arrangement.....	121

Figure 4-7 – Flow profile of forward driven flow through channel at measurement location with axial fans and mesh cloth arrangement.....	122
Figure 4-8 – Flow profile of forward driven flow through channel at measurement location with axial fans and honeycomb arrangement	123
Figure 4-9 – Experimental setup of suction driven flow by outlet mounted fans (rotary wheel was not mounted for calibration tests)	124
Figure 4-10 – Flow profile of suction driven flow through the incoming airstream channel at measurement location.....	125
Figure 4-11 – Flow profile of suction driven flow through the outgoing airstream channel at measurement location.....	125
Figure 4-12 – Mesh of ductwork channel used for CFD calibration	126
Figure 4-13 – Comparison of incoming and outgoing airstream velocity with CFD simulation	127
Figure 4-14 – Streamline contours of flow through ductwork channel using experiment boundary conditions.....	128
Figure 4-15 – HP Designjet 3D Printer	129
Figure 4-16 – Printing bay of HP Designjet 3D Printer [170]	129
Figure 4-17 – Schematic of A) model material spool B) support material spool.....	130
Figure 4-18 – Heat recovery radial blade made of copper metal.....	130
Figure 4-19 – Dehumidification radial blade made of acrylic and silica gel.....	132
Figure 4-20 – Inner rotary wheel configuration.....	133
Figure 4-21 – Angles of inner wheel configuration.....	133
Figure 4-22 – Outer rotary wheel configuration including close up of toothed outer shape for rotation by gear	134
Figure 4-23 – Toothed gear used for rotation	135
Figure 4-24 – Front and inside view of rotary wheel casing	135
Figure 4-25 – Motor located in mount with toothed gear in position	136
Figure 4-26 – Assembly of rotary wheel casing	136
Figure 4-27 – Assembly of inner and outer rotary wheel shells with copper plate radial blade	137
Figure 4-28 – A) 20 radial blade heat recovery rotary wheel, B) 20 radial blade dehumidification rotary wheel	138
Figure 4-29 – Assembly of radial blade rotary wheel and wheel casing.....	138
Figure 4-30 – Assembly of rotary wheel and casing into experimental ductwork	139

Figure 4-31 – Final experiment setup	140
Figure 4-32 – Air velocity measurement locations	140
Figure 4-33 – Relative humidity and air temperature measurement locations	142
Figure 4-34 – Testo 425 hot-wire anemometer.....	144
Figure 4-35 – Testo humidity/temperature probe with and without cover.....	145
Figure 4-36 – Testo 176P1 absolute pressure data logger	146
Figure 5-1 – Side elevation of incoming airstream velocity contours for 32 radial blade configuration.....	150
Figure 5-2 – Comparison between experiment and CFD air velocity in the incoming airstream before the 32 blade rotary wheel.....	150
Figure 5-3 – Comparison between experiment and CFD air velocity in the incoming airstream after the 32 blade rotary wheel.....	151
Figure 5-4 – Side elevation of incoming airstream velocity contours for 20 radial blade configuration.....	151
Figure 5-5 – Comparison between experiment and CFD air velocity in the incoming airstream before the 20 blade rotary wheel.....	152
Figure 5-6 – Comparison between experiment and CFD air velocity in the incoming airstream after the 20 blade rotary wheel.....	152
Figure 5-7 – Side elevation of incoming airstream temperature contours for 32 radial blade configuration.....	153
Figure 5-8 – Comparison between experiment and CFD air temperature after 32 radial blade rotary wheel configuration in the incoming airstream.....	154
Figure 5-9 – Comparison between experiment and CFD air temperature after 32 radial blade rotary wheel configuration in the outgoing airstream	154
Figure 5-10 – Side elevation of incoming air temperature contours for 20 radial blade configuration.....	156
Figure 5-11 – Comparison between experiment and CFD air temperature after 20 radial blade rotary wheel configuration in the incoming airstream.....	156
Figure 5-12 – Comparison between experiment and CFD air temperature after 20 radial blade rotary wheel arrangement in the outgoing airstream.....	157
Figure 5-13 – Side elevation of incoming airstream velocity contours for 32 radial blade configuration.....	158
Figure 5-14 – Comparison between experiment and CFD air velocity in the incoming airstream before the 32 blade rotary wheel	159

Figure 5-15 – Comparison between experiment and CFD air velocity in the incoming airstream after the 32 blade rotary wheel	159
Figure 5-16 – Side elevation of incoming airstream velocity contours for 20 radial blade configuration.....	160
Figure 5-17 – Comparison between experiment and CFD air velocity in the incoming airstream before the 20 blade rotary wheel	160
Figure 5-18 – Comparison between experiment and CFD air velocity in the incoming airstream after the 20 blade rotary wheel	161
Figure 5-19 – Contours of air temperature in the incoming airstream for the 32 radial blade dehumidification rotary wheel configuration.....	162
Figure 5-20 – Comparison between experiment and CFD air temperature after 32 radial blade rotary wheel configuration in the incoming airstream.....	162
Figure 5-21 – Comparison between experiment and CFD air temperature after 32 radial blade rotary wheel configuration in the outgoing airstream	163
Figure 5-22 – Contours of air temperature in the incoming airstream for the 20 radial blade dehumidification rotary wheel configuration.....	164
Figure 5-23 – Comparison between experiment and CFD air temperature after 20 radial blade rotary wheel configuration in the incoming airstream.....	164
Figure 5-24 – Comparison between experiment and CFD air temperature after 20 radial blade rotary wheel configuration in the outgoing airstream	165
Figure 5-25 – Contours of relative humidity in the incoming airstream for the 32 radial blade dehumidification rotary wheel configuration.....	166
Figure 5-26 – Comparison between experiment and CFD relative humidity after 32 radial blade rotary wheel configuration in the incoming airstream.....	167
Figure 5-27 – Comparison between experiment and CFD relative humidity after 32 radial blade rotary wheel configuration in the outgoing airstream	167
Figure 5-28 – Contours of relative humidity in the incoming airstream for the 20 radial blade dehumidification rotary wheel configuration.....	168
Figure 5-29 – Comparison between experiment and CFD relative humidity after 20 radial blade rotary wheel configuration in the incoming airstream.....	169
Figure 5-30 – Comparison between experiment and CFD relative humidity after 20 radial blade rotary wheel configuration in the outgoing airstream	169
Figure 6-1– Contours of air velocity for the 32 radial blade configuration A) Test HR-32-1 incoming air, B) Test HR-32-1 outgoing air	174

Figure 6-2 – Contours of air velocity for the 20 radial blade configuration A) Test HR-20-1 incoming air, B) Test HR-20-1 outgoing air	175
Figure 6-3 – Average air velocity for tests HR-32-1 to HR-32-4 measured before and after the rotary wheel in the incoming airstream	177
Figure 6-4 – Average air velocity for tests HR-32-1 to HR-32-4 measured before and after the rotary wheel in the outgoing airstream.....	178
Figure 6-5 – Average air velocity for tests HR-20-1 to HR-20-4 measured before and after the rotary wheel in the incoming airstream	180
Figure 6-6 – Average air velocity for tests HR-20-1 to HR-20-4 measured before and after the rotary wheel in the outgoing airstream.....	181
Figure 6-7 – Contours of gauge pressure for the 32 radial blade configuration A) Test HR-32-1 incoming air, B) Test HR-32-1 outgoing air	183
Figure 6-8 – Contours of gauge pressure for the 20 radial blade configuration A) Test HR-20-1 incoming air, B) Test HR-20-1 outgoing air	185
Figure 6-9 – Contours of air temperature for the 32 radial blade configuration A) Test HR-32-4 incoming air, B) Test HR-32-4 outgoing air	188
Figure 6-10 – Temperature change before and after rotary wheel for incoming and outgoing airstreams for 32-blade arrangement	189
Figure 6-11 – Contours of air temperature for the 20 radial blade configuration A) Test HR-20-4 incoming air, B) Test HR-20-4 outgoing air.....	191
Figure 6-12 – Temperature change before and after rotary wheel for incoming and outgoing airstreams for 32-blade arrangement	192
Figure 6-13 – Contours of air velocity for the 32 radial blade configuration A) Test DH-32-4 incoming air, B) Test DH-32-4 outgoing air.....	197
Figure 6-14 – Contours of air velocity for the 20 radial blade configuration A) Test DH-20-4 incoming air, B) Test DH-20-4 outgoing air.....	199
Figure 6-15 – Average air velocity for tests DH-32-1 to DH-32-4 measured before and after the rotary wheel in the incoming airstream	199
Figure 6-16 – Average air velocity for tests DH-32-1 to DH-32-4 measured before and after the rotary wheel in the outgoing airstream	201
Figure 6-17 – Average air velocity for tests DH-20-1 to DH-20-4 measured before and after the rotary wheel in the incoming airstream	202
Figure 6-18 – Average air velocity for tests DH-20-1 to DH-20-4 measured before and after the rotary wheel in the outgoing airstream	203

Figure 6-19 – Contours of gauge pressure for the 32 radial blade configuration A) Test DH-32-4 incoming air, B) Test DH-32-4 outgoing air.....	205
Figure 6-20 – Contours of static pressure for the 20 radial blade configuration A) Test DH-20-4 incoming air, B) Test DH-20-4 outgoing air.....	207
Figure 6-21 – Contours of air temperature for the 32 radial blade configuration A) Test DH-32-4 incoming air, B) Test DH-32-4 outgoing air.....	210
Figure 6-22 – Air temperature change measurements for the 32-blade dehumidification rotary wheel in the incoming and outgoing airstreams	211
Figure 6-23 – Contours of air temperature for the 20 radial blade configuration A) Test DH-20-3 incoming air, B) Test DH-20-3 outgoing air.....	213
Figure 6-24 – Air temperature change measurements for the 20-blade dehumidification rotary wheel in the incoming and outgoing airstreams	214
Figure 6-25 – Contours of relative humidity for the 32 radial blade configuration A) Test DH-32-4 incoming air, B) Test DH-32-4 outgoing air.....	217
Figure 6-26 – Relative humidity change measurements for the 32-blade dehumidification rotary wheel in the incoming and outgoing airstreams	218
Figure 6-27 – Contours of relative humidity for the 20 radial blade configuration A) Test DH-20-3 incoming air, B) Test DH-20-3 outgoing air.....	221
Figure 6-28 – Relative humidity change measurements for the 20-blade dehumidification rotary wheel in the incoming and outgoing airstreams	221

Preface

The work presented in this thesis was carried out between October 2013 and January 2015 at the School of Civil Engineering, University of Leeds and January 2015 and September 2016 at the Department of Mechanical Engineering, University of Sheffield. As an outcome of the work, the following research output has been published and awarded:

Peer-reviewed journals:

1. **D. O'Connor, J.K. Calautit, and B.R. Hughes.** A Study of Passive Ventilation Integrated with Heat Recovery. *Energy and Buildings*, 2014, 82, 799-811, DOI:10.1016/j.enbuild.2014.05.050
2. **D. O'Connor, J.K. Calautit, and B.R. Hughes.** Effect of Rotation Speed of a Rotary Thermal Wheel on Ventilation Supply Rates of Wind Tower System, *Energy Procedia*, 2015, 75, 1705-1710, DOI:10.1016/j.egypro.2015.07.432
3. **D. O'Connor, J.K. Calautit, and B.R. Hughes.** A Review of Heat Recovery Technology for Passive Ventilation Applications, *Renewable and Sustainable Energy Reviews*, 2015, 54, 1481-1493, DOI:10.1016/j.rser.2015.10.039
4. **D. O'Connor, J.K. Calautit, and B.R. Hughes.** A Novel Design of a Desiccant Rotary Wheel for Passive Ventilation Applications, *Applied Energy*, 2016, 179, 99-109, DOI:10.1016/j.apenergy.2016.06.029

Conference papers:

1. **D. O'Connor, J.K. Calautit, and B.R. Hughes.** Effect of Rotation Speed of a Rotary Thermal Wheel on Ventilation Supply Rates of Wind Tower System, The 7th International Conference on Applied Energy, Abu Dhabi (ICAE 2015), United Arab Emirates, 28-31 March, 2015

Book chapters:

1. **D. O'Connor, J.K. Calautit, and B.R. Hughes,** Commercial Wind Towers for Heating and Cooling Based on Climatic Conditions, In: O.T. Haynes ed. *Natural Ventilation: Strategies, Health Implications and Impacts on the Environment*. New York: Nova Science Publishers, 65-117

Intellectual Property:

1. **B.R. Hughes, D. O'Connor, and J.K. Calautit**, Wind Tower, PCT/GB2014/052513
2. **B.R. Hughes, D. O'Connor, and J.K. Calautit**, Rotary Desiccant Wheel, GB1506768.9

Awards:

1. **Best Student Paper**, Performance Investigation of a Commercial Wind Catcher with Horizontally-Arranged Heat Transfer Devices (HHTD), 3rd Annual International Conference on Architecture and Civil Engineering (ACE 2015), Singapore, 13-14 April, 2015

Nomenclature

Diffusion flux of species j , (mol/m ² s)	\vec{J}_j
Effective conductivity, (W/m.K)	k_{eff}
External body force, (N)	\vec{F}
Fluctuating dilation in compressible turbulence to the overall dissipation rate	Y_M
Fluctuating velocity, (m/s)	u'_i
Fluid density, (kg/m ³)	ρ
Fluid velocity, (m/s)	\vec{u}
Generation of turbulence kinetic energy due to buoyancy	G_b
Generation of turbulence kinetic energy due to the mean velocity gradients	G_k
Gravitational body force, (N)	\vec{g}
Heat of chemical reaction and other volumetric source defined by user, (W)	S_h
Heat Capacity	C_p
Height, (m)	H
Inverse effective Prandtl number for energy dissipation rate	α_ε
Inverse effective Prandtl number for turbulence kinetic energy	α_k
Length, (m)	L
Mass added to the continuous phase from the dispersed second phase, (kg)	S_m
Mass flow rate	\dot{m}
Mass fraction of species j , (g/g)	Y_j
Mean velocity, (m/s)	\bar{u}_i
Molecular viscosity, (Pa s)	μ
Net rate of production of species i by chemical reaction	R_i
Rate of creation by additional from the dispersed phase	S_i
Reference temperature (K)	T_{ref}
Relative humidity, (%)	rH
Sensible enthalpy for an ideal gas, (kJ/kg)	h
Gauge pressure, (Pa)	p
Stress tensor, (N/m ²)	$\bar{\tau}$
Temperature	T
Time, (s)	t
Turbulence dissipation rate, (m ² /s ³)	ε
Turbulence kinetic energy, (m ² /s ²)	k

Turbulent Prandtl number for energy dissipation rate	σ_ϵ
Turbulent Prandtl number for turbulence kinetic energy	σ_k
Turbulent thermal conductivity, (W/m.K)	k_t
Unit tensor, (N/m ²)	I
User defined source term for energy dissipation rate (m ² /s ³)	S_ϵ
User defined source term for turbulence kinetic energy, (m ² /s ²)	S_k

List of Abbreviations:

Acrylonitrile Butadiene Styrene	ABS
Computational Fluid Dynamics	CFD
Cool Thermal Energy Storage	CTES
Direction Numerical Simulation	DNS
Fractional Step Method	FSM
Fused Deposition Modelling	FDM
Heating, Ventilation and Air-Conditioning	HVAC
Indoor Air Quality	IAQ
Latent Heat Energy Storage	LHES
Large Eddy Simulation	LES
Oscillating Heat Pipes	OHP
Phase Change Materials	PCM
Pressure-Implicit with Splitting Operators	PISO
Reynolds-Average Navier Stokes	RANS
Sick Building Syndrome	SBS
Semi-Implicit Method for Pressure-Linked Equations	SIMPLE
Semi-Implicit Method for Pressure-Linked Equations Consistent	SIMPLEC
Supported Liquid Membranes	SLM
Two-phase Closed Thermosiphon	TPCT

Chapter 1

1 Introduction

Increased industrialisation and urbanisation have led to increased global energy consumption [1]. The generation of power to meet this demand has increased the emission of greenhouse gases. Countries around the world, including the United Kingdom, have agreed to cut these gases from pre-1990 levels by 80% by the year 2050 [2]. Increased public awareness of the need to reduce the emission of greenhouse gases adds to the pressure of governments to act quickly and sufficiently. In respect to this, it is important for engineers to be capable of understanding the challenges faced and the needs of the public to develop appropriate systems and technologies to counter this global challenge.

As economic development continues, it is important to identify the sectors in which energy is most significantly used. In this way, key operators and governing bodies of these areas can take the necessary steps to reduce the energy use through energy reduction measures or improved energy efficiency. At present, the construction, operation and management of buildings is the single highest consumer of energy use. Buildings account for up to 40% of the total global energy use. The industrial and transport sectors are the remaining dominant end users, the breakdown of energy use can be seen in Figure 1-1 [3,4].

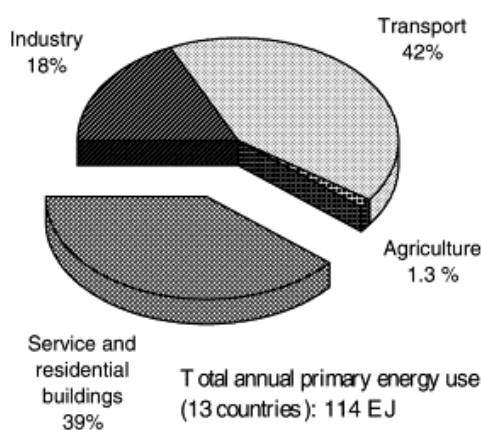


Figure 1-1 – The approximate service and residential sector shares of primary energy use for 13 countries [4]

Furthermore, the total contribution of buildings to the emission of greenhouse gases range from 37% to 45% [5,6]. It is clear that the construction, operation and maintenance of buildings provides a significant opportunity for engineers and designers to limit the total energy use of new buildings. Furthermore, improving the efficiency of existing structures

through retrofit and integration of new technologies without impairing the ability of a building to provide a safe, clean and suitable space for its occupants is necessary.

The supply rate and quality of the air within a building has a large impact on the health of occupants. The effects of poor air quality range from the less serious, such as losses in productivity, to serious impacts on occupant health from Sick Building Syndrome (SBS) [7]. One means of ensuring occupant health against poor concentration levels and SBS is to provide a continuous supply of fresh, clean air [8]. Providing fresh, clean air and removing polluted indoor air, high in concentration of carbon dioxide (CO₂), from occupied spaces improves conditions for occupants. Air-handling units, primarily mechanical Heating, Ventilation and Air-Conditioning (HVAC) systems most commonly perform this. A number of recommendations and guidelines for the supply rate of fresh air into occupied spaces have been made. These ensure that occupants are not exposed to high concentrations of CO₂ and other harmful pollutants that can contribute to SBS. The recommendations of supply air range from a minimum of 3 litres per second per person to a recommended value of 8 litres per second per person but with a design capability of 10 litres per second per person [9].

HVAC units are amongst the most highly energy intensive processes operating in a building. This is due to the high volume of air required to be distributed around a building by HVAC systems to meet ventilation supply rate guidelines. In addition, the changes to the condition of the air necessary for occupant comfort require high energy demands. Depending on the local climate, mechanical HVAC is responsible for up to 50% of the total energy use [10]. The continued use of HVAC in buildings represents an on-going mechanical, energy intensive process that could be replaced by alternative technologies. A number of innovations have led to an increase in efficiency of HVAC systems and reductions to the total energy consumption [11,12]. Research into improving the efficiency of HVAC systems will aid the reduction of total energy consumed in building operation and maintenance. Limiting or removing the need for mechanical HVAC systems would provide more significant energy savings, thereby reducing financial costs to building operators and lowering greenhouse gas emissions. However, this is not possible as ventilation is necessary for occupant well-being, therefore alternative methods and technologies need to be explored.

Mechanical HVAC systems can be classified as active systems, which drive air around a building using mechanical means that require energy input. Passive ventilation systems manipulate pressure differences in and around a building to circulate air [13]. Passive ventilation systems are capable of ventilating an occupied space with very low energy demands, particularly when compared with mechanical HVAC systems [14]. Engineers have

designed ventilation systems that require very little energy by developing an understanding of pressure differences around a building. These pressure differences are created by wind speed and direction, and the stack effect as warmed, less dense air rises out of openings at height. By manipulating these pressure differences, air is able to circulate through a building [15].

A number of different types of passive ventilation system exist which take advantage of different operating conditions dependent on the building such as solar chimneys, air vents wind towers, scoops and suction cowls [16]. The stack effect, cross-ventilation and combinations of the two can be used by systems to provide ventilation supply air to fulfil the levels required by guideline values [17]. Cross-ventilation forces air through a building due to pressure differences created by the wind speed and direction and the forces generated on the surfaces of the building, this can be seen in Figure 1-2. The stack effect takes advantage of the varying density of air due to temperature. Warm air is less dense and so rises to the top of a building and escapes due to buoyancy. Cooler air is denser and so enters the building at a lower level to replace the rising warm air. The most common example of passive ventilation is the use of windows to allow fresh air into a building.

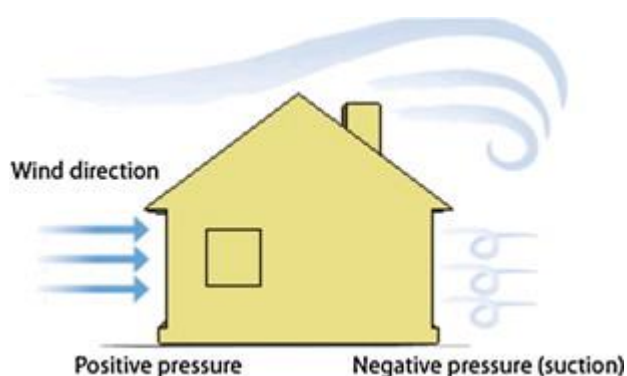


Figure 1-2 – Wind creates a positive pressure on the windward side of a structure and a negative pressure on the leeward side [14]

Commercial wind towers are an example of a passive ventilation system that are becoming more common. Uptake has been particularly high for education and commercial buildings in the UK due to the high occupancy [18]. Mounted to the top of a building and connected to the space below by a vertical shaft, wind towers are able to ventilate buildings due to the ability to take advantage of both the cross-ventilation and the stack effect, as can be seen in Figure 1-3. High pressure is created on the windward face of an object and low pressure is generated on the side and leeward faces of an object due to the flow separation at the corners of an object [19]. The differences in pressure on the faces of the object cause the flow of air from high-pressure zones to low pressure zones. Wind towers take advantage of

this effect by using louvres and internal dividers to split a vertical shaft into zones that act as inlets and exhausts depending on the direction of the wind. The stack effect works through the wind tower by exhausting warm air as it rises in the space, drawn out by the zones of low pressure by the side and leeward faces [20].

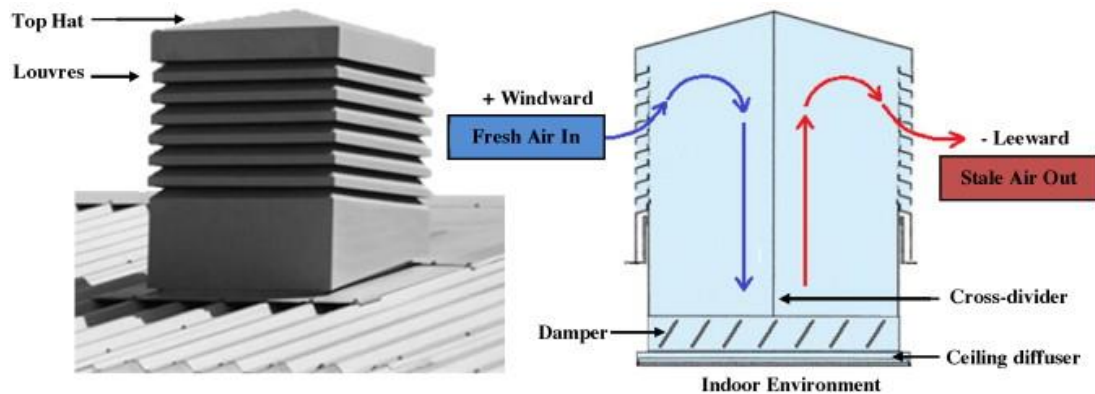


Figure 1-3 – Schematic of a commercial multi-directional wind tower system [21]

Above a wind speed of 1m/s, wind towers are able to adequately supply ventilation air to an occupied space using cross-ventilation and the stack effect [17]. Ventilation rates are further increased when windows are opened in the ventilated space. The average wind speed in the UK, as measured by weather stations around the country, is above 4m/s [22]. This is suitably higher than the required speed for supply ventilation rates. The use of wind towers in the UK has the additional benefit of cooling occupants during summer months [23]. The fresh, outdoor air that is introduced into the building is generally at a lower temperature than the internal air temperature. In summer months, this provides cooling to occupants and reduces the need for mechanical ventilation systems and cooling systems.

The benefit of free cooling during the summer months further improves the attractiveness of the system to building operators in addition to the introduction of fresh air for low energy costs due to passive ventilation. However, this benefit has a trade-off that cannot be overlooked. Wind towers do not currently incorporate systems that can alter the incoming air temperature or humidity. The air that is introduced is completely dependent on the local climate conditions. When a wind tower is in operation and the temperature of the fresh air is too low and causes the thermal comfort of occupants to be compromised, complaints about draughts become an issue. Though some research shows that the effect of the draughts is negligible beyond 1m from the ceiling duct of the wind tower, considerations of the outdoor air conditions should be taken into account [24].

Though the operation of the wind towers during the summer months is generally acceptable, use of the wind tower during winter is less suitable in northern European and UK climates that have colder months compared to southern Europe and the Middle East. Introducing this air directly into occupied spaces would benefit occupants in terms of ventilating pollutants but the air temperature would not provide thermal comfort. Additional energy input would be necessary to raise the internal air temperature to adequate levels for thermal comfort. This would negate the energy saved through use of the wind tower for ventilation.

Similar circumstances have been observed with mechanical HVAC systems where additional energy is required to increase the incoming air temperature. To counter this, heat recovery devices provide a solution. Heat recovery devices have been integrated into HVAC systems with the purpose of extracting heat from exhaust air to be returned to the inlet air. Though the integration of the heat recovery device enabled energy reduction for heating demands by raising the temperature of the inlet air, the total energy costs have been seen to increase [10]. This was due to the increased pressure drop experienced by the incoming ventilation air. Pressure loss occurs as a fluid moves through a closed system such as ductwork. The pressure of the moving fluid is directly linked to the velocity of the fluid, this is most often seen through the continuity of pressure and velocity experienced in the Bernoulli equation [25]. The Bernoulli equation details the conservation of energy in fluid flow. System losses are not be accounted for in the Bernoulli equation, therefore additional terms must be added. High-pressure losses across the heat recovery device results in low air velocity that is not able to provide the minimum required air supply rates of 3 litres per second per person [9]. In order to overcome the increased pressure loss, additional fans are required to maintain the air supply rates at the same levels prior to the integration of the heat recovery device. The energy demand required to operate the additional fans increases the total energy requirements of mechanical HVAC systems, offsetting any saving from the heat recovery device.

Despite this outcome, integrating a device into a wind tower to alter the condition of the incoming air is an attainable objective. Wind towers have an initial advantage over mechanical HVAC by requiring little energy to operate in comparison. Integrating a heat recovery device, which requires fans to drive the air to meet the supply ventilation rates, would likely require less energy than the total energy demand of a mechanical HVAC system with a heat recovery device. However, this negates the attractive low energy credentials of a wind tower system to building operators. Another factor to consider for the integration of a heat recovery device into a wind tower system is the proximity of the inlet and exhaust air

streams. As the air streams run in a counter-current direction directly next to each other, the distance between them is minimal and reduces inefficiency of lost heat during transfer between the two. For some HVAC systems where the inlet and exhaust air streams are not located close to each other, complex heat recovery systems are required.

Though wind towers are able to ventilate a building, a consequence of low air velocity of incoming air in wind towers is that the maximum pressure drop that can be experienced by the airstream and maintain an acceptable supply ventilation rate is 2Pa [26,27]. Therefore, to ensure the year round low energy credentials of wind towers as a viable ventilation system, the design of a novel heat recovery system is required. The new system should be capable of transferring the maximum possible heat from the exhaust airstream to the incoming airstream with as low a pressure loss as possible to remove the need for additional fans.

The integration of heat recovery into passive ventilation systems would be beneficial during the winter months in the UK and northern European climates. As previously discussed, the local climate during winter months means that the outdoor air temperature is too low to be introduced. This can result in discomfort to occupants and the need to increase the air temperature via heaters, incurring high energy demand. Typically the air temperature in buildings is maintained by heaters using the thermal characteristics of conduction, convection and radiation to raise incoming air temperature to the desired level [28].

Integrating a heat recovery device into a wind tower would reduce these energy costs. The incoming supply air would be at an initial higher temperature, reducing the temperature increase required from the heating system. Further to this, internal heat gains contribute significant amounts of heating potential to occupied spaces [29]. Heat sources such as occupant body heat, electrical equipment and solar gains all deliver thermal gains to occupied spaces. Some evidence suggests that the internal heat gains of an occupied space can be enough to raise the air temperature to an appropriate level when coupled with heat recovery [30].

In typical situations, heat can be lost from a building through a number of transfer mechanisms. Poor insulation, infiltration of outdoor air through non-airtight building envelopes and inefficient ventilation systems are all causes of heat loss. Used in conjunction with a well-insulated, airtight building, a wind tower integrated with a heat recovery system would channel air out of the exhaust channels. As the exhaust air would be controlled by the wind tower with minimal heat losses elsewhere, heat would be transferred to the incoming

air. Though the concept of this design appears robust, the pressure drop of heat recovery unit remains the major obstacle for development and integration.

As air temperature is altered, relative humidity is also affected. Generally, if air temperature is the only factor affected, as air temperature increases, relative humidity decreases. As temperature decreases, relative humidity increases. Changes to relative humidity can cause problems to building operators. Indoor spaces subject to consistent high humidity and mid-to-high air temperatures can develop bacterial growths that affect occupant health, similar to SBS [31,32]. High humidity adds to occupant discomfort in hot climates as the humidity prevents the evaporation of sweat from skin. Without effective evaporation of sweat, occupants cannot regulate body temperature as effectively, increasing discomfort [33]. Low relative air humidity is equally as undesirable as high relative air humidity. Low relative humidity causes dryness to occupant skin, eyes, nose and throat. This is commonly seen on airliner jets that can supply air at levels typically lower than 25% relative humidity [34]. This highlights that high and low humidity in buildings is not acceptable and passive HVAC systems should equally manage humidity of incoming air. The commonly accepted range of 40-70% is preferable for occupant health and comfort [35].

Mechanical HVAC systems are capable of dealing with humidity levels that are undesirable to occupant health and comfort. The conventional method is to cool air below the dew temperature. Condensate is removed at this stage and the air becomes completely saturated. The air is then reheated, as no additional moisture is introduced to the system, the relative humidity lowers. This is an energy intensive process. Another method is to employ desiccant materials as a method of humidity control. Desiccant materials are materials that have high surface area to volume ratios. The high ratios enable the adsorption of water molecules to the surface of pores within the material [36]. Desiccant materials are deployed in HVAC systems in similar ways to heat recovery devices and often share common structures and designs.

Desiccant materials are used for humidity control and are advantageous for occupant health and comfort. However, integration of these devices into HVAC systems show similar problems to heat recovery devices due to the additional associated energy demand and costs [37]. Redesign of humidity control systems in a similar method to heat recovery devices could prove to be equally as beneficial. High-pressure drop is a problem consistent between heat recovery systems and humidity control systems. Resolution of the cause of the high-pressure drop may lead to improvements for both systems.

At present, heat recovery devices incur a high-pressure drop in the air moving through them. In efforts to increase the maximum heat transfer between airstreams, the surface area of the transfer materials is maximised. This does not provide a significant reason for the high-pressure drop alone. For example, to maximise the surface area given in the available volume of a rotary heat recovery wheel, matrices and honeycomb structures are frequently used, acting as miniscule ducts through which air can flow [38]. This can be seen in Figure 1-4.



Figure 1-4 – Matrix structure of a rotary wheel recovery device used for mechanical HVAC

The structure of some heat recovery devices increases the pressure drop due to the size and arrangement. The high surface area of the transfer material creates additional skin friction between the material and the air, increasing the pressure drop [39]. Further to this, the small size of the openings for the air to flow through creates additional pressure drop increase [40].

Taking these considerations into account, the challenge is to define a novel heat exchanger for integration into a passive ventilation wind tower system. The system had to avoid or limit the factors which most significantly influence a high pressure drop of air flowing through the heat exchanger. Equally important was to maintain a balance of heat recovery and pressure drop, providing a system that has minimal pressure drop across it but recovers no heat was not viable. An allowable pressure drop of 2Pa across the device was targeted. It was envisioned that this pressure drop would be low enough to enable sufficient air to pass through the heat recovery unit, whilst also transferring heat from one air stream to another.

1.1 Aims and Objectives

The overall aim of this work was to develop a recovery device that can be integrated into a passive ventilation system that will not impede the flow of air through the system by limiting the pressure drop across the device, thereby providing adequate air supply rates to occupied spaces. The heat recovery device will enable the use of wind towers for ventilation when external air temperatures are too low to be introduced without first increasing temperature. This will improve the year-round capabilities of wind tower operation and reduce the energy demand on mechanical HVAC systems both in terms of providing ventilation air and in terms of suitable air temperature. A dehumidification recovery device will enable the relative humidity of the incoming airstream to be conditioned as required, reducing the moisture content to more acceptable levels. This will improve occupant health and comfort.

Following the overall aim of the project, the following research objectives were identified:

1. Review existing literature relating to mechanical HVAC, passive ventilation and heat recovery devices
2. Conceptualise and prototype a novel design of heat recovery device suitable for passive ventilation systems
3. Develop a validated CFD model for investigation of pressure drop and temperature change across the recovery device
4. Investigate the effect of varying the internal structure of the novel device on the heat recovery and dehumidification performance
5. Evaluate the effect of the novel design on pressure drop across the device and the impact on ventilation supply rates
6. Assess the overall potential of the design for integration into passive ventilation systems to condition air through heat recovery and dehumidification.

1.2 Project Methodology

This study will follow a systematic approach to the problem described above. A thorough analysis and review of existing literature in related areas will be undertaken. The two major areas of published research that will be reviewed focus on current and in-development heat recovery devices with an emphasis on low pressure drop technologies and wind tower technology and development. Following this, CAD software will be used to generate 3D models that will be used for Computational Fluid Dynamic (CFD) analysis and prototyping. The CFD modelling capable of producing data on the air flow through the recovery device, the pressure drop across the device and the change in condition to air, will be used. ANSYS

Fluent will be the CFD software used for this analysis. The data generated from the CFD model will be validated against an exact replica experimental test using custom made ductwork and 3D printed prototypes, taken from the same geometry files as the CFD models.

The primary investigation conclusions will be drawn from the viability of the device to limit pressure drop to the air streams and the changes in condition of the air in terms of temperature and relative humidity. Figure 1-5 shows the methodology flow chart for the progression of the PhD study.

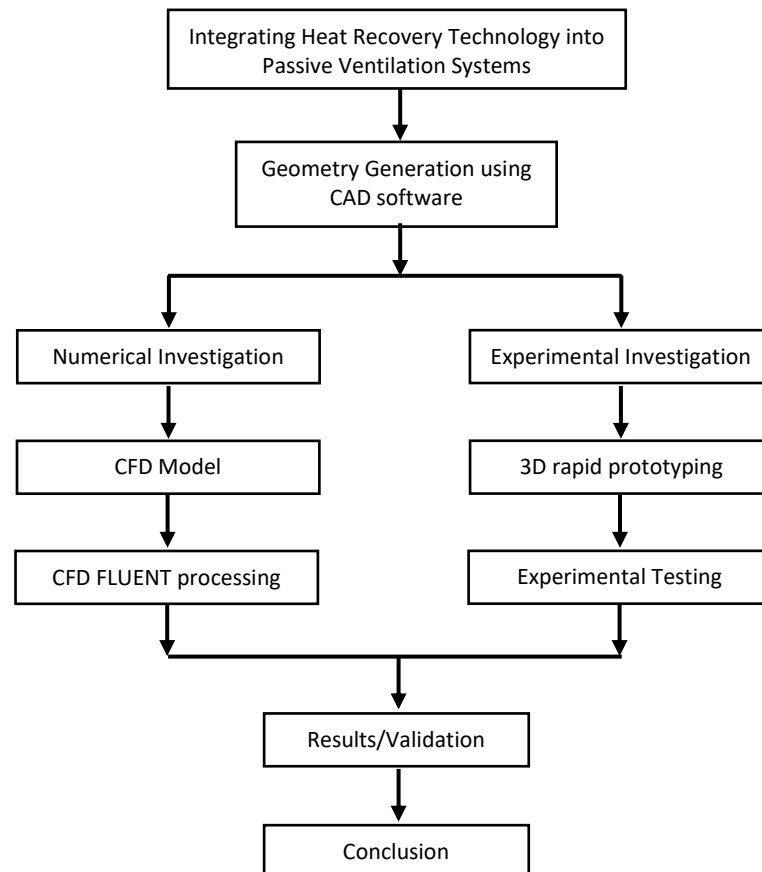


Figure 1-5 – PhD Methodology Flowchart

1.3 Thesis Structure

The aim of the study described within this thesis was to develop a heat recovery device that could be integrated into a wind tower ventilation system without impeding the flow of air through the wind tower by limiting the pressure drop to 2Pa. This research followed a logical methodology for integrating a heat recovery device into a wind tower and determining the performance of the device. Experimental and numerical methods were used to help determine the performance and identify areas of improvement.

The thesis is composed of seven chapters. The order and content of the chapters will lead the reader through the research from concept to the conclusions detailed in Chapter 7. A brief summary of each chapter is listed as follows.

Chapter 1 presented an introduction to the high-energy demand placed on buildings for ventilation and shows examples of alternative technologies. The chapter highlights key objectives and the methodology of the research project.

Chapter 2 presents a thorough and comprehensive review of current literature relating to areas key to this research. The broad areas cover passive ventilation and heat recovery technology. The review analyses numerical and experimental methods of testing to determine the performance of both passive ventilation technology and heat recovery technology. Developments in both areas are focussed on. Low-pressure drop heat recovery devices are highlighted, along with wind tower developments that accelerate air velocity. The contents of the chapter are used to identify the gap in existing research and note the appropriate and most applicable methods of analysis to achieve the research aim.

Chapter 3 provides the numerical methods that will be adopted in the thesis. The chapter will detail the theoretical background of CFD, the generation of meshes and grid verification and boundary conditions.

Chapter 4 presents the method for the experimental testing of the novel heat recovery device. Following geometry generation detailed in Chapter 3, 3D printing is used to manufacture a prototype for testing. The design and setup of the experiment are described.

Chapter 5 describes the validation of the CFD models using the output data from the experimental prototype testing. The accuracy of the CFD simulations in comparison to the experiment are quantified.

Chapter 6 details the results and discussions from the CFD analysis and the prototype testing. Comparisons of air velocity, air temperature and relative humidity are discussed for different configurations of prototype for both numerical and experimental testing.

Chapter 7 provides conclusions to the research derived from the analysis of the results presented in prior chapters. Areas for potential future work to further enhance the research are identified and presented.

Chapter 2

2 Literature Review

2.1 Introduction

This chapter provides a review of research areas that have furthered the development of this thesis. An initial understanding for the need for ventilation in buildings is presented, followed by an overview of the principles that underpin passive ventilation. Historical and modern passive ventilation applications are highlighted, along with reasoning as to why wind tower are the most suitable passive ventilation system for integration with a heat recovery device. Following this, current and future developments of wind tower systems are provided. Several studies, which aimed to improve the ventilation performance of wind tower systems and explore different configurations, orientations and additional components, have been reviewed along with analytical and experimental methods. Heat recovery and dehumidification systems were reviewed analytically in order to identify the key parameters that affect performance and potential integration into passive ventilation systems. Numerical and experimental studies were explored to determine the most suitable methods of analysis. Following the review, a research gap in the existing literature was identified.

2.2 Indoor Air Quality

Continuous ventilation of occupied spaces is vital to maintain adequate indoor air quality (IAQ). The IAQ of a building is measured by examining the levels of various pollutants within the internal atmosphere. Commonly assessed pollutants include carbon dioxide (CO₂), carbon monoxide (CO), nitrogen dioxide (NO₂), sulphur dioxide (SO₂) and formaldehyde (HCHO). The levels of these pollutants within the internal air affect IAQ along with the relative humidity and temperature of indoor air and the air velocity. As IAQ decreases, Sick Building Syndrome (SBS) becomes more prevalent in occupants [41]. Various government organisations and agencies assess IAQ and have made guidelines to which engineers should work to.

Abdul-Wahab *et al.* [42] reviewed the different standards and guidelines in order to summarise the overall guidance for IAQ and the recommended ventilation rates to minimise SBS. Thirty different standards and guidelines from worldwide groups and agencies were

analysed. CO₂ is identified as one of the key indicators of IAQ and the effectiveness of the ventilation system. A general limit of 1000 parts per million is accepted by a number of standards and guidelines with a preferred value of 800ppm given. Moisture content of the internal air is prescribed in many of the standards and guidelines. The moisture content of the air is significant for IAQ for two reasons. Low levels of relative humidity cause increased dryness to eyes and noses, leading to irritation. High levels of relative humidity increase the instances of mould and bacteria growth along with airborne transfer of pestilences. The lower level of relative humidity recommendations is between 30-40% and upper recommendations of 60-70%. The recommendations factor in the season and the way in which air is delivered.

As humans spend a high percentage of their time indoors, building operators must ensure that the conditions are not detrimental to their health by following the standards and guidelines for IAQ. It is estimated that up to 90% of human time is spent indoors [43]. The increased time exposed to indoor environments increases the likelihood of occupants experiencing SBS. Crook and Burton [41] describe SBS as respiratory ill health associated with the built environment. The authors sought to clear the overlap that currently exists between definitions of SBS and building related illnesses. SBS is defined as relating to mucous membrane symptoms (i.e. relating to the eyes, nose and throat), dry skin and symptoms relating to headaches and lethargy. A second part to SBS related to the temporary effects of polluted buildings. Symptoms improve in occupants within hours of leaving the affected area. Building related illnesses are symptoms of mould and bacterial growth that can have substantial impacts on occupant health should the mould spores and bacteria grow to dangerous levels.

Macnaughton *et al.* [44] have recently shown how improved air quality can reduce the effects of SBS on occupants in substantial ways. By comparing reports from occupants in a conventional office space prior to moving to a new office designed to improve air quality, reports of SBS related symptoms reduced. Furthermore, the increased CO₂ concentration in the air was shown to increase occupant heart rate by an average of 2.3bpm and instances of reporting other SBS symptoms increased by 1.43 times.

Seppänen and Fisk [45] compiled a review of ventilation systems and the effect systems had on occupant health and instances of SBS. Seppänen and Fisk [45] focused their attention on mechanical HVAC systems as the most common form of ventilation in buildings. The authors noted that the simple ventilation processes of mechanical HVAC and how air is circulated

could contribute to significant increases of instances of SBS in occupants. The HVAC system itself may be contaminated and so any air passing through the system is contaminated. The external air source that the HVAC system draws inlet air from may be contaminated. A HVAC system using recirculation practices for ventilation may draw air from a contaminated indoor source that is then distributed around the building. Table 2-1 shows the risk factors that the authors attributed to each of the most common ventilation systems. It is clear from the table that mechanical systems pose a greater risk of contamination compared to natural ventilation systems but have a significantly greater degree of control of temperature, humidity and ventilation rates.

Table 2-1 – Suspected risk factors of HVAC types and building features [45]

HVAC system type	Risks
Natural ventilation with operable windows	No particle removal via filtration; poor indoor temperature and control; noise from outdoors; inability to control the pressure difference across the building envelope and exclude pollutant infiltration or penetration of moisture into structure; low ventilation rates during some weather conditions; possible low ventilation rates in some portions of the occupied space
Systems with ducts and fans but no cooling or humidification (simple mechanical ventilation)	HVAC components may be dirty when installed or become dirty and release pollutants and odours; poor control of indoor temperature because of absence of cooling; low humidity in winter in cold climates; high humidity during periods of humid weather; noise generated by forced airflow and fans; draft caused by forced air flows
Systems with ducts, fans and cooling coils (air conditioning systems)	Additional risk factors from cooling coils: very high relative humidity or condensed moisture (e.g., in cooling coils and drain pans) and potential microbial growth; biocides used to treat wet surfaces such as drain pans and sometimes applied to nearby insulation
Systems with ducts fans, cooling coils and humidifiers of various types	Additional risk from humidifiers: microbial growth in humidifiers; transport of water droplets downstream of humidifiers causing wetting of surfaces; leakage and overflow of humidifier water; condensation from high-humidity air; biocides in humidifiers; chemical water treatments in steam generators
Systems with recirculation of return air (recirculation may occur in all mechanical HVAC systems)	Additional risks* from recirculation: indoor-generated pollutants are spread throughout the section of building served by the air handling system; typically higher indoor air velocities increase risk of draft and HVAC noise; supply ducts and filters of HVAC system may become contaminated by recirculated indoor-generated pollutants
Sealed or operable windows (windows may be sealed or operable with all types of mechanical HVAC systems)	Additional risk with sealed windows: no control of the environment if HVAC systems fails; psychological effect of isolation from outdoors. Additional risk with operable windows: more exposure to outdoor noise and pollutants

Decentralized systems (cooling and heating coils located throughout building, rather than just in mechanical rooms)	Additional risk of decentralisation: potentially poorer maintenance because components are more numerous or less accessible. Potentially more equipment failures because of larger number of components
--	---

***However, recirculation facilitates removal of indoor-generated pollutants using air cleaners, e.g., particle filters, and may also decrease concentrations of pollutants near pollutant sources.**

The study reached a clear conclusion in the assessment of SBS instances in mechanically ventilated buildings compared to naturally ventilated buildings. In 16 of 17 assessments, increases in SBS symptom were seen to a statistically significant level in mechanically ventilated buildings when compared to naturally ventilated buildings. Air-conditioned buildings were shown to have the highest instances of SBS symptom levels compared to more simple mechanical ventilation. The authors noted that higher ventilation rates are often cited as a cause for lower instances in SBS symptoms, however the study did not factor ventilation rates into the analysis. The authors acknowledge that the naturally ventilated buildings in the study may report lower instances of SBS due to higher ventilation rates.

Recent literature shows that control and management of IAQ is important in reducing symptoms of SBS in occupants. Continuous ventilation of indoor spaces is necessary to maintain IAQ below the recommended limits of pollutant and contaminant levels. Though it is universally agreed that ventilation improves IAQ, there are differences between researchers as to the most suitable method of ventilation to achieve this. Seppänen and Fisk [45] provided the clearest argument for naturally ventilated spaces to improve IAQ, showing the majority of the buildings assessed in their study showed higher instances of SBS in mechanically ventilated buildings compared to naturally ventilated buildings.

2.3 Passive Ventilation Principles

Reducing the energy demand for ventilation practices has long been seen as a key driver for the reduction of the total energy demand in buildings, and in turn reducing the global dependence on fossil fuels. Fordham [46] argued that more needs to be done to promote natural and passive ventilation as an alternative to mechanical HVAC if this is to be a reality. Fordham [46] noted that 100% natural ventilation of buildings is possible but significant changes in attitude are required, particularly from a building designer point of view. The author further stated that losses of heat through the building fabric are undesirable and as

a building becomes more insulated, natural ventilation is seen as the main area of heat loss that is avoidable.

The effectiveness of “heat reclaim”, as the author noted, can range between 50-75% for use in a mechanical system, extracting thermal energy from the outgoing air via a heat exchanger to be returned to pre-heat the incoming air. Though this is seen as a desirable outcome, it is stated that the energy required by additional fans to move the air through the building due to the increased pressure loss mitigates savings made by the heat exchanger. The author suggested two instances in which the concept would be worthwhile, the first in cold climates where a higher heat load can be reclaimed. Secondly, in a natural ventilation system whereby the pressure loss of the heat exchanger can be reduced to not impede the flow of air and negates the need for additional fans.

Passive ventilation, particularly in the hot, arid climates of the Middle-East, has been used for centuries to deliver fresh air to buildings and as a means of cooling, as noted by Soflaei *et al.* [47]. Whilst it is possible that the exact interactions behind the application of passive ventilation were not understood, manipulation of the fundamentals to provide continuous outdoor air was well handled. Many examples still exist of different ventilation practices, all which are able to operate without mechanical means or electrical input.

The study by Linden [13] is considered a thorough review of the mechanics involved in natural ventilation. In the study, Linden noted the two primary driving forces behind natural ventilation and provided a comparison. Wind driven ventilation, a result of the wind velocity and direction, and buoyancy driven flow, caused by temperature differences of air within a space, provide the dominant forces for ventilation under natural conditions. Linden noted that though wind driven flow is often considered the primary driver, air temperature differences produce a more substantial effect. The aim of this work was to deliver modern designers an understanding of the principles which had long been manipulated by building designers centuries before.

Chenari *et al.* [48] investigated the strategies that lead to sustainable, efficient and healthy ventilation. Schematics for the processes of single-sided ventilation, cross ventilation and stack ventilation are shown in Figure 2-1. Single-sided ventilation is applicable on buildings with deep rooms and partitions where air would not penetrate the full depth of the room. Cross ventilation is used when openings are positioned opposite each other within a building, allowing air to enter from the windward direction and exit from the leeward face. Stack

ventilation occurs when an outlet is positioned at height within a space as air enters from lower levels. The warming air rises and exits the outlet.

These three fundamental forms of ventilation commonly applied to buildings. The review acknowledged that natural ventilation is a strategy worth consideration for delivering fresh air to occupied buildings, but one that can be limited by natural weather cycles. The connection between the outdoor and indoor environments and its effects on ventilation rates is strongly emphasised. The study noted how natural ventilation is dependent on many external effects. The design choices made to the external characteristics of the building and other buildings influence natural ventilation. To this end, the authors suggested that hybrid ventilation, a mixed combination of natural and mechanical ventilation, is a more suitable.

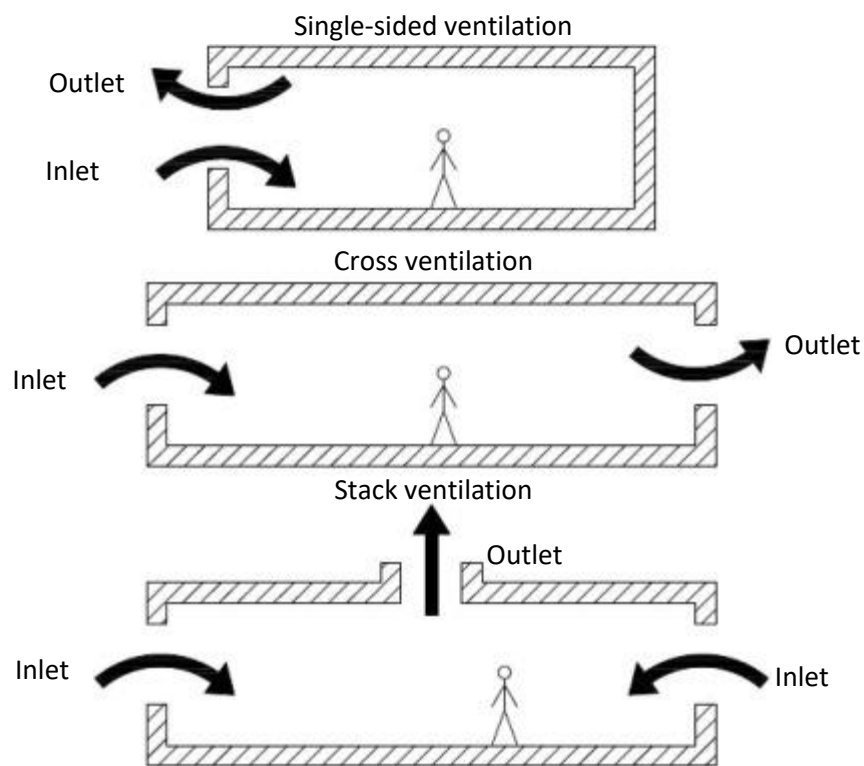


Figure 2-1 – Schematic view of different natural ventilation principles [48].

Single-sided ventilation was determined as the least successful option in terms of delivering air compared to cross ventilation and stack ventilation. The review concluded that natural ventilation combined with mechanical ventilation is a preferable solution. This is due to the high impact that external conditions have on indoor conditions in purely natural ventilation solutions. The central argument to this is based on the inability of natural ventilation systems to pre-treat (heat, cool or dehumidify) the incoming air. A system able to provide pre-treatment of the air would enable greater uptake of natural ventilation in buildings. Furthermore, it is noted that the design of buildings for natural ventilation must be taken in

to account in the early stages of a project for optimal integration, a statement supported by Fordham [46].

Chu and Chiang [49,50] produced studies that were interested in passive ventilation, particularly the effect of wind-driven cross ventilation flow and the design parameters that influenced the efficiency of cross ventilation were studied and analysed. The authors noted that little attention had previously been paid to internal obstacles within a building and the effect these have on ventilation rate. By ignoring the obstacles of the interior of a ventilated space, researchers were consistently overestimating the ventilation effect of cross ventilation. Chu and Chiang [49] corrected for this effect. The blockage ratio, the cross sectional area of the obstacle compared to the cross sectional area of the building, shown in Figure 2-2, and position of the internal obstacle were calculated as the primary influences on the change in ventilation rate. As the blockage was moved closer to the windward or leeward openings, ventilation rates dropped. As the blockage ratio increased, ventilation rates also fell.

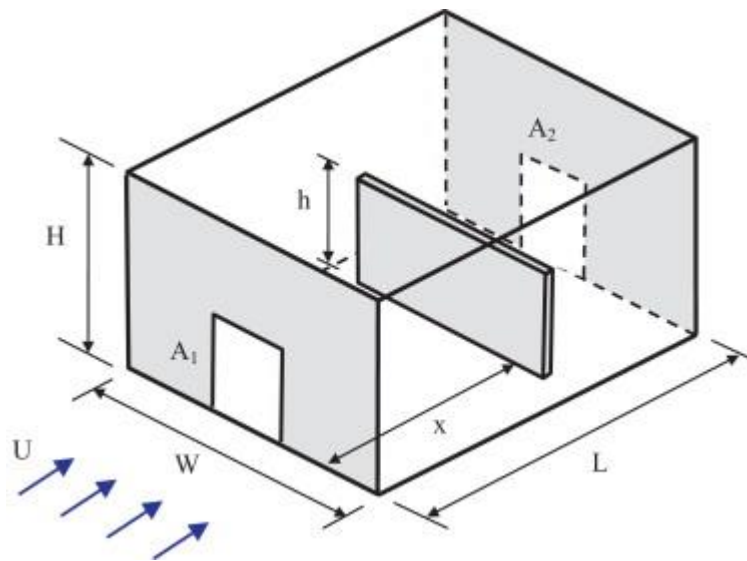


Figure 2-2 – Schematic diagram of the full-scale building with a vertical plate inside [49]

The studies also found that the length and height ratios of the building shape are important to cross ventilation flow. Building shapes with lower length to height (L/H) ratios exhibit higher cross ventilation rates than higher L/H ratios due to the higher-pressure difference between the windward and leeward faces. As the building length increases, internal friction slows the movement of air, reducing the ventilation rate. This was observed in buildings where $L/H > 5.0$. The authors noted that conventional models do not calculate for this and so overestimate ventilation rates. The study also showed that openings for cross ventilation should be positioned opposite each other. Diagonal openings on the windward and leeward

faces of the building resulted in a 15.5% reduction in ventilation for the same test done with openings positioned opposite.

Baines and Turner [51] provided an early theoretical and experimental investigation into the effects of buoyancy driven flow in a confined region. The study used many different examples to represent their confined region and illustrate the flexibility of the theory, including cooling and heating in a model room. Baines and Turner acknowledged the limitations of the theoretical model derived compared to experimental and real-world applications. The effect of turbulence was omitted from the model, some similarities were maintained between the theoretical and experimental model however.

Linden *et al.* [52] studied the mechanics of natural ventilation, focussing on the comparison between mixing and displacement ventilation. Theoretical and experimental models were produced and analysed. Both of these forms of ventilation are driven by changes to the density of the air caused by air temperature. Figure 2-3 shows a schematic of the principles of mixing and displacement ventilation. Warm air exits the room at the ceiling level in both cases. In mixing ventilation, cool air enters the room at high level where it falls due to its high density compared to warm air. As the air falls, mixing occurs. In displacement ventilation, cool air enters the room at a low level. As the temperature of the inlet air increases, it rises, forcing the air at ceiling level out. Little mixing of the air occurs in displacement ventilation.

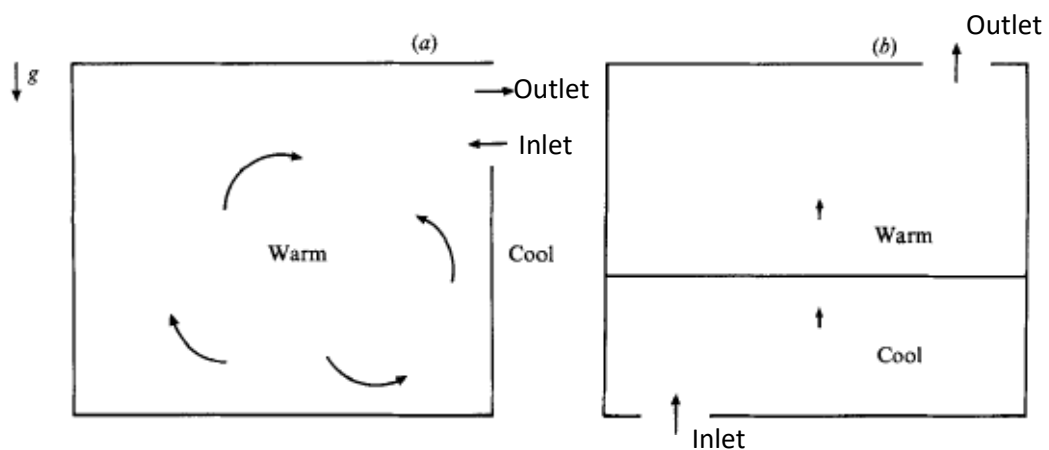


Figure 2-3 – (a) Mixing ventilation and (b) displacement ventilation [52]

Linden *et al* [52] considered two cases. The first, where ventilation is driven by a temperature difference between the internal and external environments. The second, where ventilation is driven by constant internal heat sources considered such as occupant activity, electrical equipment and heating systems. For each case, mixing and displacement ventilation were considered. The work found that the strength of the buoyancy sources affected the strength of the stratification of the air and the air velocity, but did not affect the form of stratification.

Following the derivation of the theoretical models, the authors make the argument for naturally ventilated buildings using the principles described. Temperate and hot climates can be ventilated in summer by removing internal heat from the building, provided the internal temperature is higher than the external temperature. The external temperature should be high enough to not require pre-heating. Displacement ventilation is the preferred method here. In climates where the external temperature is too cold, the authors suggested that mixing ventilation is preferable. This way fresh air is introduced but does not cause thermal discomfort for occupants.

Though many studies have been carried out that look at wind driven and buoyancy driven ventilation in isolation, this separation of ventilation methods is unlikely to occur in real world scenarios. As a consequence of this, Li and Delsante [53] carried out an analysis of natural ventilation that combined wind and buoyancy driven ventilation. The analysis by the authors is thorough in its scope, attempting to unify ventilation rates by considering buoyancy, wind driven flow, solar radiation and heat losses through the building envelope. The schematic for the building used in the study is shown in Figure 2-4. The study is simplified by choosing not to include the thermal mass of the building.

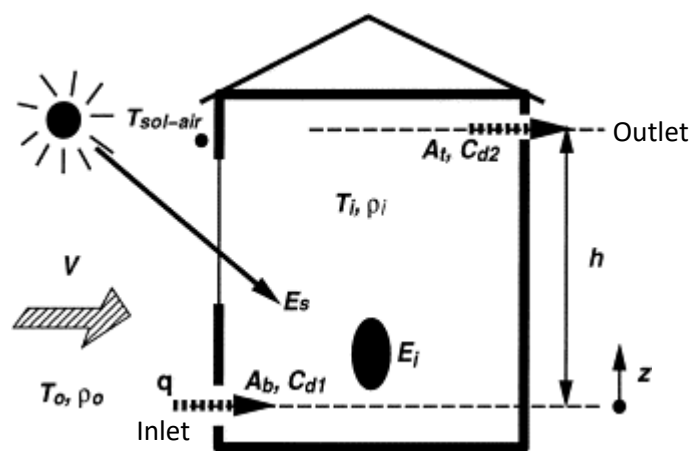


Figure 2-4 – The general notation for a two-opening building with solar radiation [53]

The authors found that the ventilation rate was affected by changes to wind speed, heat sources and losses. When each parameter was analysed individually, the ventilation rate change was noted in comparison to the change in each of the parameters. The greatest effect however, was seen when heat loss was introduced to the model. Doubling the heat loss parameter reduced the ventilation rate by half. The study also noted that the wind driven flow can oppose buoyancy flow. This occurs when the wind direction is opposite to that shown in Figure 2-4, that is in the opposite direction to the outlet. The counter-driving force of the wind has three possible effects on ventilation. Hand calculations that isolated each

parameter showed that buoyancy driven ventilation is greater than the wind driven force and ventilation rates fall but continue out of the same outlet. Wind driven ventilation is the dominant force and cross ventilation occurs out of the lower outlet. The forces balance and ventilation does not occur, it should be noted that this is unlikely to occur. Each of these scenarios result in reduced ventilation rates. Therefore, researchers and designers need to be aware of the potential for zero ventilation rates when designing for naturally ventilated buildings.

Zhai *et al.* [54] carried out a review of analytical and empirical models for natural ventilation performance prediction by looking at current literature available. The authors noted that analytical models are only appropriate for simple, single-zone geometries due to the complexity of the calculations. Because of the interconnectedness of buoyancy driven flow and temperature in natural ventilation models, the reviewed studies solved airflow and thermal models simultaneously. The review considered that analytical models were only appropriate for specific geometries when the correct driving forces were present. Outside of this, analytical models for passive ventilation could not be manually computed.

From the passive ventilation principles derived by researchers, analytical analysis of passive ventilation has become significantly more common. Continually increasing computational power has enabled greater analysis of the flow patterns and thermal effects in passive ventilation systems. Prior to the advent of computer simulations for analysis, hand written numerical solutions were solved for only the simplest scenarios. Linden *et al.* [52] acknowledged the limitations of numerical solutions, particularly for complex three dimensional problems. Computational Fluid Dynamics (CFD) is the study of fluid flow using computational power to iteratively solve the governing equations that underlie fluid dynamics. CFD analysis is now the most common method for solving passive ventilation problems in a time effective manner. The simulations computed using CFD range from the simplest two-dimensional steady-state problems to complex, three-dimensional transient time problems.

Chen [55] compiled a review of literature of the ventilation performance in buildings and the methods used for prediction and analysis of the internal air quality. The study examined a broad range of methods including analytical and empirical models, small-scale and full-scale experimental models and Computational Fluid Dynamics models amongst others. The review found that CFD models had become popular amongst researchers and contributed to the significant majority of the reviewed literature. Coupling CFD models with other research

methods was common, in order to validate the CFD models and improve the accuracy of the simulations.

Chen [55] noted that Computational Fluid Dynamics solves partial differential equations for the conservation of mass, momentum, energy, turbulence and species concentrations. From the solutions of the equations, values for air velocity, pressure, temperature, relative humidity, contaminants and turbulence can be calculated and measured.

The two most common CFD models used are Reynolds Averaged Navier-Stokes (RANS) equation modelling and Large Eddy Simulation (LES) modelling. The differences between CFD models relates to the method and size of the vortices calculated. RANS equations model smaller vortices and average larger, whereas LES models large vortices and averages smaller. The two most common RANS models used are the standard $k - \varepsilon$ and the RNG $k - \varepsilon$ equations as described by Launder and Spalding [56] and Yakhot and Orszag [57] respectively. The equations are shown in Chapter 3. Chen [55] noted that LES is considered the more accurate model compared to RANS when instantaneous airflow and turbulence characteristics are required. However, the computation time required for LES modelling is a minimum of two orders of magnitude longer than RANS models for the same problem. Direct Numerical Simulation (DNS) models also exist. These solve the turbulent flow models for all eddy sizes. This is very computationally demanding and only used when completely necessary. This often leads researchers to use RANS models. Table 2-2 shows a brief comparison of the different turbulent models available in CFD modelling, it should be noted that the table is not exhaustive.

Table 2-2 – Brief comparison summary of Reynolds-Averaged Navier Stokes (RANS), Large Eddy Simulation (LES) and Direct Numerical Simulation (DNS) CFD Models

	Solver Type	Time Dependency	Computational Time and Demand	Mesh Requirements	Conditions for Use
Reynolds-Averaged Navier Stokes (RANS)	Time-averaged	Steady-state or Transient	Low computational demand, low processing time	Good quality mesh required (large – fine)	General purpose CFD equation modelling
Large Eddy Simulation (LES)	Filtering	Transient Only	High computational demand, long processing time	Good quality fine mesh required	High accuracy, transient turbulent flow analysis
Direct Numerical Simulation (DNS)	Complete	Transient Only	Very high computational demand, very long processing time	Excellent quality very fine mesh required	Complete flow analysis requirements

Due to the approximations embedded in the design of CFD governing equations, variability and uncertainty are common. Because of this, one model that accurately simulates one flow may not perform as well for a different type of flow. Zhai *et al.* [58] investigated and tested the most commonly used models or those predicted for use in modelling indoor environments. Here Zhai *et al.* [58] noted that RANS modelling is the most commonly used method for simulation. As average air distribution and characteristics are more useful than instantaneous airflow and turbulence characteristics in building environments, RANS is preferable to LES modelling in most circumstances.

Due to the growing popularity of CFD as an analysis tool, researchers are increasingly becoming more comfortable with the results generated by simulations. Using CFD models for passive ventilation analysis, Hussain and Oosthuizen [59] compared four different RANS models against real-world experimental data to assess the most suitable model for ventilation prediction. Field measurements of the thermal performance of an atrium building were compared against results taken from standard $k - \varepsilon$, RNG $k - \varepsilon$, realisable $k - \varepsilon$ and SST $k - \omega$ turbulence models. The significant difference between the $k - \varepsilon$ and $k - \omega$ model is the treatment of flow at the near wall boundary. $k - \omega$ models require a higher mesh resolution due the improved treatment of flow near the boundary walls compared to $k - \varepsilon$ models. Each of the models tested calculated results with good agreement compared to the experiment data. The SST $k - \omega$ model resulted in the most accurate analysis when compared to the experimental measurements. The study concluded that CFD is a suitable method for analysing passive ventilation flow and thermal characteristics.

The variability of CFD accurately predicting the flow and thermal characteristics of a problem is evident when separate studies are compared. A similar analysis by Liu *et al.* [60] comparing different CFD models to experimental measurements of passive ventilation in an atrium resulted in a different conclusion to Hussain and Oosthuizen [59]. In this study, Liu *et al.* [60] assessed four different CFD models, the laminar model, the indoor zero-equation model, standard $k - \varepsilon$ model and the RNG $k - \varepsilon$ model. The authors note that the RNG model is more accurate than the standard $k - \varepsilon$ model as swirling flows are better calculated due to the additional term used to calculate ε .

The study reported that depending on the area that is assessed, different CFD models provided the most accurate results. The RNG $k - \varepsilon$ and indoor zero-equation model calculated the most accurate results for heated zones where buoyancy was the primary driving force. The results in the atrium suggested that the zero-equation and laminar models were the most accurate. The authors suggested that due to the size of the atrium, the flow is not consistently turbulent throughout the full height, leading to the improved accuracy of the laminar models. This shows that despite CFD models becoming more commonly accepted as methods of analysis and prediction, variation in conclusions between studies is still a frequent result. Cook *et al.* [61] encountered a similar scenario during the study of buoyancy-driven passive ventilation. No clear guidelines had been compiled for methods of use of CFD for passive ventilation. The authors therefore completed work assessing the different models in order to gain understanding prior to producing guidelines for CFD.

As previously noted, coupling CFD models with other research methods enables analysis that is more thorough. Zhai and Chen [62–65] completed a long term study that coupled CFD analysis with Building Energy Simulation (BES) and analysed the impact of the coupling on building design. This provided the authors with greater understanding of the thermal performance of the building. The systems worked complementary to each other, feeding results back and forth to gain a more detailed outcome. The authors' overall aim of the work coupling CFD and BES was to generate guidelines and recommendations for future integration of each piece of software.

2.4 Passive Ventilation Applications

Following the investigation as to why ventilation is required, and the fundamentals of passive ventilation, it is important to examine the systems that utilise these principles. Many methods of passive ventilation exist that take advantage of the pressure differences around

a building, resulting in ventilation. Each of the following applications employed the passive ventilation principles in different ways. In order to integrate a system that is capable of ventilating a building, along with pre-conditioning the air to a suitable level, it is important to explore the options for passive and low energy ventilation. Though building materials can be used to aid the control of air temperature through high building thermal mass and high insulation levels, the effects are not described or explored due to the depth of study available. The focus of work is towards the ventilation applications that deal with this.

The design of courtyards to promote ventilation and cooling is commonly seen as the architectural design with the longest history. Various features of courtyard design work together to provide passive cooling and ventilation to buildings. Safarzadeh and Bahadori [66] established the designs that affected cooling of courtyards most effectively. Tall courtyard walls provided wind shading and prevented the ingress of hot winds into the buildings. South-facing walls and windows provide additional shading to the rest of the building. The planting of trees in the courtyard provided additional shading. The presence of water features, such as ponds or pools, and flora contributed to lowering the temperature and the wind-shading effects of the courtyard walls and trees. These components were designed to minimise the heat gains of the building.

Abdulkareem [67] provided a critical appraisal of courtyard architecture, both as a method of ventilation and the ability to lower the ambient air temperature in the area. The author provided an in-depth study of the impact of courtyards on the ambient temperature. Various systems that are used in conjunction with courtyards, with the aim to improve temperatures, were investigated.

The author was hesitant to promote the return of vernacular architecture over modern mechanical air-conditioning systems. The ability of a courtyard to cool and ventilate a building sufficiently was questioned repeatedly. Instead, the author suggested that proper design of a courtyard should be taken into consideration alongside mechanical air-conditioning systems. This, the author proposed, would allow a hybrid system to be created. The mechanical air-conditioning system would actively cool and ventilate the building, with the courtyard offsetting some of the energy demand from the mechanical system.

The development of courtyards has continued with modern methods and designs. As the urban heat island effect becomes more noticeable in cities around the globe, architects and designers continue to look for methods to reduce temperatures from building sources [68]. Taleghani *et al.* [69] explored the use of courtyards in the Netherlands in urban settings. The

study examined the potential heat mitigation of courtyards and the impact that evaporative cooling has on the ambient air temperature. The orientation and size of the courtyards were altered to attain which was the optimum direction to face and the influence of the size of the courtyard. The outcomes of the research suggested that a North-South orientation minimises the solar gains of a courtyard due to exposure to the shortest period of solar radiation. Furthermore, water pools and vegetation are highly recommended as methods of lowering the air temperature.

As modern architecture develops from traditional designs, methods of providing passive ventilation have also changed. Atria in buildings have become a common architectural feature, serving as a joining space to different stories of a building and as a central space. Examples of common atrium design can be seen in Figure 2-5. Hussain and Oosthuizen [70] investigated design configurations of atria using Computational Fluid Dynamics (CFD). The researchers noted how solar driven airflow is the dominant ventilation principle, due to the large amount of glass used in the construction of most atria. Atria are connected to the adjacent rooms to allow the free flow of air, providing ventilation. Significant amounts of work has been conducted to analyse the interaction between the atria and adjacent rooms.

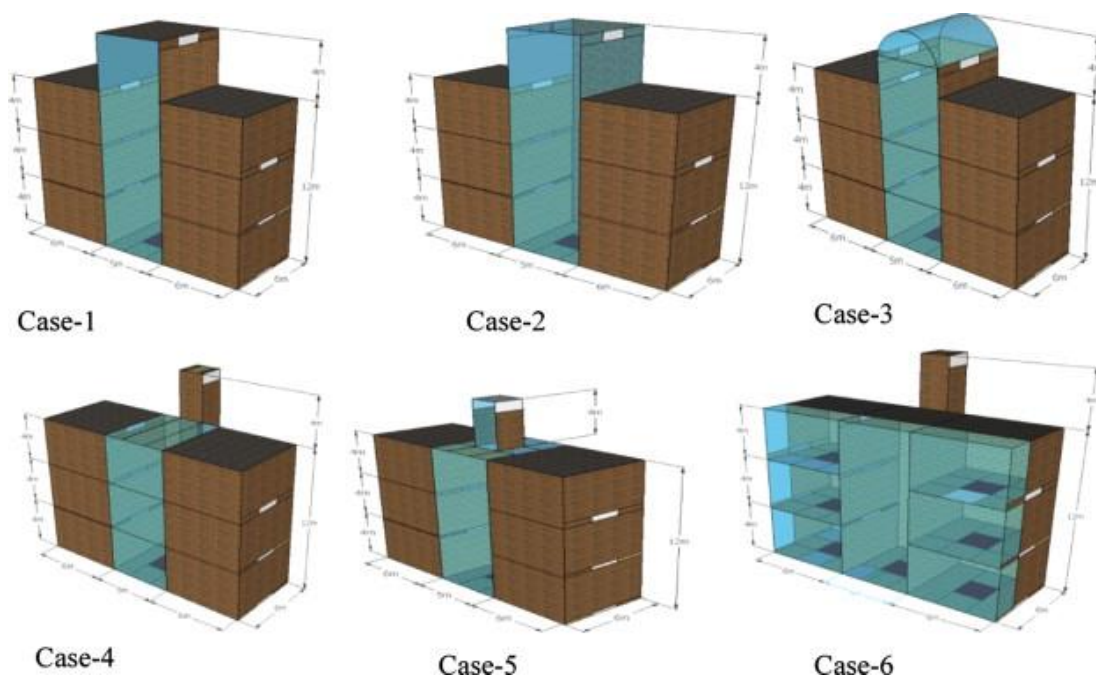


Figure 2-5 – Basic design configurations of an atrium space considered [70]

Many of the design principles that Hussain and Oosthuizen [70] used were originally conceived by Holford and Hunt [71]. The study developed a theoretical model, based on empirical formula of heat transfer and air flow, that is capable of predicting the flow through a building with an atrium based on the buoyancy flow due to thermal stratification caused

by internal heat gains from occupant activity and high solar gains. The authors noted that ventilation of atria improved when thermal stratification was at its greatest, either due to high temperatures of the warm air or deeper layers of warm air.

The study quickly focussed on the differences of ventilated and unventilated atria. That is, atria with direct openings to the external environment at low levels and those without. Figure 2-6 shows an example of this. When the atrium was subject to two openings, one from the external environment and one from the inner building storey, the flow is more complex to analyse and greater mixing occurs of the internal air.

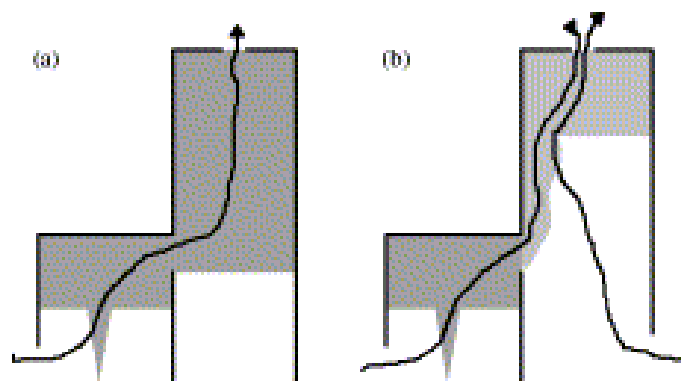


Figure 2-6 – An enclosure with (a) an unventilated atrium, and (b) a ventilated atrium. The arrows indicate the flowpaths through the enclosure. The shading represents the warm air in the upper regions of the room and atrium. The lighter shading in the upper atrium in (b) is representative of the cooler layer which forms due to the direct ventilation [71]

Because of the greater mixing between the outdoor and internal air, which is subject to the heat gains, lower flow rates are observed. When the atrium was unventilated, shown in Figure 2-6a, the layer of the warm air increases in depth, increasing the flow rate out of the atrium and ground floor room, enhancing cooling. The final major conclusion of the work related to the size of openings in the atrium. The opening size at the ceiling height of the atrium has a large effect on the ventilation rate, particularly in ventilated atria. As a simplification, when the ceiling opening is twice the size compared to the lower opening, flow rates doubled.

Moosavi *et al.* [72] provided a thorough literature review of atrium design and the implication of modifying each of the parameters involved in atrium design. The paper intended to understand the developments that have occurred in passive ventilation design, the principles that underpin the ventilation principles of atria and how poorly designed atria have affected the perception and awareness of end users. The review also looked at increasing ventilation rates in atria by combining the passive ventilation system with mechanical systems to create hybrid processes.

The review separated the parameters that affect the performance of atria into thermal performance and ventilation performance. The authors identified thermal performance as reliant on the properties of the openings at low and ceiling height of the atrium, the geometry of the atrium and roof, and fenestration and material properties. Ventilation performance relies on opening characteristics and atrium design. The properties of the openings in the atrium are important and closely linked to both thermal and ventilation performance. The design of inlet and outlet openings in atrium requires careful consideration to maximise performance. The number, size, ratio of inlet to outlet size and placement are key considerations in atrium design. The local climate plays an important role in the design of the atrium. Temperate climates are assessed by a different method than tropical climates. If these factors are not properly accounted for, thermal performance and ventilation is not limited to the atrium. Low ventilation and inadequate temperatures across the entire building are a consequence.

Atria are architectural features that encourage passive ventilation using principles founded on buoyancy driven flow. Similar to the driving mechanicals for ventilation in atria, solar chimneys are a passive ventilation technology that require solar radiance to drive flow rates. Figure 2-7 shows a modified vertical solar chimney arrangement, similar to a Trombe wall design. A vertical channel connected to the exterior of the building is constructed. The channel construction features an internal and exterior absorber wall. Between the absorber walls is an air channel through which air flows. Glazing is added to a Trombe wall to maximise the solar gains.

Solar chimneys are orientated for maximum solar gain on the sun-exposed face. The resulting temperature difference between the temperature within the chimney and the external environment creates flow out of the chimney. By providing an inlet from the adjoining building, ventilation is achieved [73].

Khanal and Lei [74] contributed a review to the state-of-the-art of solar chimneys, examining the effect that buoyancy driven flow has on passive ventilation and how this has been investigated by various research groups over the last 25 years. The authors noted the advantage of solar chimneys ability to ventilate a building on windless days. This is important as the glazing of the solar chimney creates the conditions for buoyancy driven flow in varying seasons when a sufficient temperature difference is achieved between internal and external temperatures.

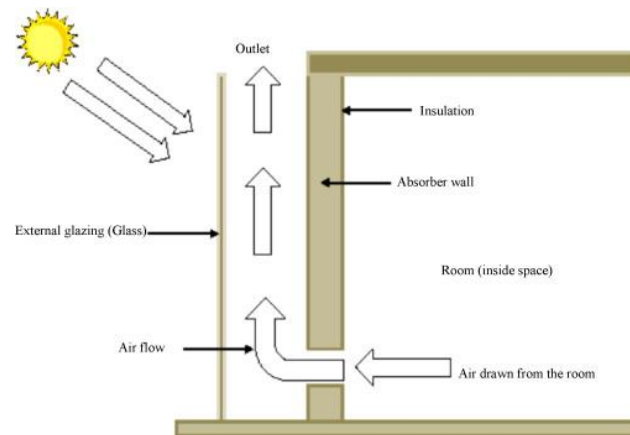


Figure 2-7 – Schematic of solar chimney with vertical absorber geometry [74]

The study assessed the methods of analysis of solar chimneys and the outcomes of research. Analysis was distributed evenly between analytical, experimental and numerical methods, either as a single method of analysis or in combination. The increased use of CFD for analysis in the most recent research was notable to the authors. Citing increased computational power and understanding of flow fundamentals allowing advanced simulations, not solely for the research of solar chimneys but passive ventilation systems more generally. Disparity and contradictions between conclusions of the reviewed research suggested to the team that the complexity of the subject area is not yet fully understood and more in-depth is required.

A separate review was completed by Zhai *et al.* [75] which examined the progress of applications of solar chimneys and the integration of solar chimneys with other technologies to improve performance. Both wall and roof mounted solar chimneys were reviewed. The authors also explored the applications of additional renewable energy systems. Interestingly, Zhai *et al.* [75] examined the concept of solar chimneys as a design that could be exported for other uses. Roof mounted solar collectors that operated with the same principles of solar chimneys showed increases in ventilation and space heating for cooling and heating seasons through different configurations. A combination of vertical wall and roof mounted solar chimneys showed the most beneficial configuration due to the increased temperature gain inside the channel and increased stack pressure due to the increased height. This aided ventilation rates.

The researchers explored additional systems that enhanced the performance of the solar chimneys. Cooling of the incoming air to provide greater comfort to occupants was examined along with active solar systems to enhance ventilation or generate electricity. The review suggests that ventilation and thermal comfort can be achieved by passive means with no

energy demand. By pre-conditioning the incoming air to acceptable levels for occupant comfort, in this case by lowering the temperature, solar chimneys with integrated systems provide adequate ventilation by passive means with no energy requirements.

Ventilation can be applied in alternative ways to encourage reduced energy demand and greenhouse gas emissions. Night ventilation is a method of providing cooling to a building. The thermal mass of the building structure acts as a heat sink during occupied daytime hours, storing thermal energy in the materials used for construction. The building is then ventilated during unoccupied night-time hours. This lowers the thermal energy in the building structure, enabling storage in the thermal mass of the building the following day. This offsets the time at which the interior of the building experiences highest air temperatures, improving thermal comfort to occupants [76].

Artmann *et al.* [76] have been highly active in the area of night ventilation research. The authors noted that the rise of modern buildings featuring extensive glazing, which contribute significantly to solar gains, has led to a significant increase in cooling demand. Particularly in office spaces with high occupation levels. The concept of offsetting the time when the highest air temperature occurs through thermal mass is well understood. The researchers were interested in the applications of passive ventilation to cool the building as opposed to mechanical ventilation and the associated energy costs of such systems. Passive night ventilation relies on the common mechanics of passive ventilation. Cross and stack ventilation are the primary methods due to wind driven and buoyancy flow.

The study suggested that night ventilation is a more practical solution for cooling of the thermal mass of a building in climates where the night-time temperatures are notably lower than day-time temperatures. This encourages the thermal mass of the building to radiate stored heat. Using climatic data from 259 weather-reporting stations in Europe, the most applicable locations for night ventilation were identified. Northern Europe is the most suitable location for night cooling ventilation given the temperature difference of day-time compared to night-time. Areas of Central and Eastern Europe were suitable but Southern Europe was ruled out for solely passive night ventilation as fluctuations in night-time temperature would reduce ventilation rates. Hybrid systems were proposed to mitigate some of the energy costs of mechanical ventilation where solely passive night ventilation was not possible.

Artmann *et al.* [77] continued their research of night ventilation, analysing the parameters which most affect efficiency. The study focussed on the effects of the local climate, building

thermal mass, internal heat gains, air change rates and heat transfer coefficients of the internal surfaces. Each of the parameters was varied in a building energy simulation to assess the impact on the air temperature during the day as compared to the night. A base case model was also simulated to provide context and comparison for each of the varied parameters.

The study concluded that the local climate conditions and ventilation rate during the night were the most important parameters affecting the cooling potential. This led to recommendations for designers and architects to design for passive night ventilation systems to minimise energy demand. The location of the building is very important and so continuous monitoring of weather data was advised. Increasing the thermal mass of the building was an effective option to reduce temperatures. The researchers suggested that maximum thermal mass and contact area for airflow should be designed in.

The manipulation of wind driven flow and the buoyancy effect are the key principles of passive ventilation in the form of cross and stack ventilation airflow. Different technologies and methods have been used to manipulate these forces to ventilate a building without mechanical input for centuries. Closely linked to the traditional courtyard configuration of Middle Eastern vernacular architecture, *baud geer* have been used as a ventilation device and evolved into modern day wind towers [78]. Saadatian *et al.* [16] compiled a comprehensive review of traditional wind tower technology, from the initial construction methods and design uses, through to modern developments and materials.

Bahadori [79] was among the first modern researchers to investigate traditional wind towers. An example of a schematic of a traditional wind tower is shown in Figure 2-8. The work analysed the building ventilation techniques used by traditional wind towers and how it improvements could be made using hand calculations to solve the momentum, mass and energy equations required. The modifications to the traditional wind tower design intended to enhance the cooling potential of the system and reduce dust infiltration through the wind tower into the building. The study was successful in that it was shown that incoming air velocities of 5m/s were achieved, delivering air at 15°C lower compared to traditional designs with less dust infiltration.

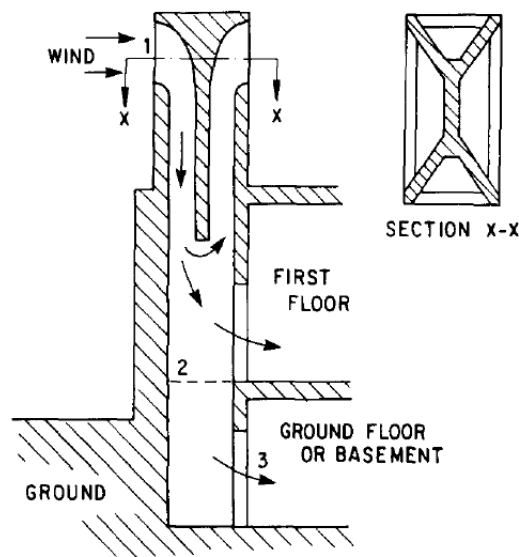


Figure 2-8 – Airflow pattern in a conventional wind tower [79]

Bahadori *et al.* [80] improved on the initial work by further modifying traditional wind towers. Using full-scale prototypes, the group tested two configurations of evaporative cooling wind towers alongside a conventional wind tower. The two configurations were wetted columns within the wind tower and wetted surfaces to the interior of the wind tower to provide cooling. Measurements were taken of the air temperature, relative humidity and airflow exiting each wind tower. The volumetric flow rate of the modified wind towers was lower than the conventional design; a peak of $1.5\text{m}^3/\text{s}$ compared to $1.39\text{m}^3/\text{s}$ and $1.05\text{m}^3/\text{s}$ for the wetted column and wetted surface respectively. The air temperature of the modified designs were $9.4\text{--}12.3^\circ\text{C}$ lower than the standard design. The authors advised that further development of the structures continue, with scope to lower or remove electrical demand due to mechanical ventilation and cooling technologies.

Bouchahm *et al.* [81] used experimental and numerical analysis of wind towers to provide recommendations to improve wind towers. The recommendations included altering the height, modifying the internal configurations of the wind tower and including internal wetted columns the full height of the structure to improve cooling potential. The results of the work showed that increasing the height and maximising the surface area of the wetted columns were the most significant factors in improving the thermal performance of the wind tower, resulting in a temperature difference between the internal and external air of $2.5\text{--}5.5^\circ\text{C}$ compared to $2.5\text{--}4^\circ\text{C}$ of the standard wind tower.

Evidence shows that traditional wind towers are capable of delivering adequate ventilation and modifications encourage cooling potential to be realised. However, Yaghoubi *et al.* [82]

noted that even in areas where wind towers originate, utilisation of the systems for ventilation is at an all-time low. Instead, mechanical air-conditioning systems are now the dominant ventilation system. This represents a cultural shift away from traditional technologies to modern mechanical systems. The shift also reflects the increased global energy demand, particularly for HVAC systems. This provides insight to designers and engineers that practical solutions are required to ventilation and air-conditioning problems and that energy demand reduction should be at the forefront of new solutions.

Table 2-3 shows a comparison of the different passive ventilation systems reviewed. This list is not exhaustive of passive ventilation technologies available. The design principles and potential for integration of heating and cooling technologies has been assessed based on the literature.

Table 2-3 – Comparison of Passive Ventilation Design Principles

	Design Principle	Heating/Cooling Integration Potential
Courtyard Design	Tall courtyard walls provide sun shading. Flora and water features enhance cooling effect by increasing moisture content in the air.	Cooling potential using water features or flora is high, heating would not be appropriate.
Atrium	Large central space of a building, connected to multiple spaces. Warmed air in the atrium draws air from connecting spaces out, replaced by fresh air.	Ventilation principle relies on the stack effect, of warm air exhausting out of a building at height. Integrating heating or cooling would be difficult
Solar Chimney/Trombe Wall	Solar gains increasing internal temperature of air within a chimney, the heated air exits chimney, and is replaced by fresh outdoor air at an inlet at a lower height	Cooling has been integrated into previous systems. Solar gains used for air flow could be used for heating
Night Ventilation	Cool, fresh air is introduced to a building during cooler night time hours, lowering the overall building temperature	Strategy is based around lowering building thermal mass to provide cooling
Wind Towers	Vernacular architectural design mounted to the roof of a building and connected to the space below. Wind driven flow forces air into building, whilst the stack effect exhaust warm internal air out.	Cooling techniques have previously been integrated for an associated pressure drop

Of the passive ventilation applications examined here, wind towers present a suitable choice for further research. The ability to ventilate regardless of wind direction is a strong advantage over other systems such as cross ventilation, coupled with the ability to ventilate using

buoyancy driven and wind driven flow. The low profile of the system is attractive from an architectural and aesthetic viewpoint. Furthermore, the close proximity of the inlet and outlet channels show potential for easy integration of pre-conditioning technology. The lack of pre-treatment to the incoming air in a wind tower is a significant disadvantage but provides scope for research to fill this gap.

2.5 Commercial Wind Towers

Based on traditional baud-geer design principles, commercial wind towers have developed using modern engineering and manufacturing technologies. Commercial wind towers are generally square, rectangular or circular shaped roof mounted stacks. The faces of the wind towers feature louvres that direct air through the wind tower, down a shaft and into the room below. The shafts can be divided into a number of divisions depending on the type of wind tower, commonly one, two or four divisions. At the bottom of the shaft sit dampers and grilles that alter the flow rate of the incoming air and distribute the air around the room. An example of a commercial wind tower can be seen in Figure 2-9.



Figure 2-9 – Experimental testing set-up of the Windvent at Sheffield Hallam University [83]

Wind towers have had significant uptake in buildings with high occupant density such as schools and office environments. High occupancy increases the internal gains from occupant activity and electrical equipment use. The higher the internal gains, the greater potential for

buoyancy and the stack effect. This improves the ventilation supply rates and the air quality of the occupied spaces.

The review of wind tower technology and development by Hughes *et al.* [14] provides a comprehensive overview of the development of passive ventilation strategies from early vernacular architecture, to modern ventilation systems which incorporate the latest scientific and engineering advancements. The review seeks to understand the nature and background of wind towers. Using this understanding, the work considered how greater uptake by consumers would be possible by further enhancing of the technology. The review stated that for a standard 1m x 1m plan area wind tower, that a supply rate between 85 litres per second and 650 litres per second could be achieved for wind speeds between 1m/s and 5m/s. Given the guideline ventilation rates suggest a supply of 10 litres per second per person, this suggests that a wind tower could supply ventilation to 65 people in an occupied space depending on the wind speed [9].

Additionally, the review analyses cooling technologies integrated into wind tower systems. The key parameter examined for each technology was the temperature reduction seen when compared to a conventional wind towers. This is important for future development of wind towers. As wind towers are not currently able to alter the temperature or relative humidity of the incoming air, operational time is limited by external conditions, technologies that improve the operational time are desired. To lower the energy demand from mechanical HVAC systems, passive ventilation technology needs to be as efficient as possible.

2.5.1 Wind Tower Development

Continuous development of wind towers to improve efficiency is necessary to maintain a competitive advantage over mechanical ventilation systems. This is necessary to encourage the adoption of passive ventilation technology over mechanical HVAC, thereby reducing energy demand and saving costs. Computational fluid dynamics (CFD) is the most common technique for rapid development of new components and configurations. The streamlined process of designing, modelling and simulating new components or prototypes compared to small scale or prototype manufacturing aids the development procedure. Far-field testing requires long-term measurement of properties of design. Whilst it is vital to obtain measurements in real world settings, the use of CFD enables better refinement of design prior to far-field testing, saving time and manufacturing costs. This ensures that the final prototype used for testing is as close to the best design as possible.

Increasing the ventilation supply rate through a wind tower is a major focus for wind tower research and development. Ensuring that the minimum supply rate is high enough to provide adequate fresh air allows wind towers to compete against mechanical HVAC systems. The majority of research that has been completed focuses on this. The components that make up a wind tower and affect the supply rate have each been individually optimised. The shape of the wind tower, angle and number of external louvres and design of the internal cross divider have each been investigated. Though the aim of wind tower development is to maximise the supply rates, these must be controlled when external wind velocity increases beyond the level for adequate ventilation. Research was carried out into dampers at ceiling height and how this affects high airflow and circulation.

External louvres provide weather protection to the interior of the wind tower; preventing the ingress of weather and pollution in to the building through the wind tower. The louvres channel airflow through and down into the shaft of the wind tower. The design of the louvres is important as air accelerates or decelerates due to the louvre angle and size. The impact of any design changes to louvres has a significant effect on the overall performance of a wind tower to ventilate an occupied space.

CFD modelling and analysis was employed by Liu *et al.* [84] to evaluate the number and length of louvres for maximum airflow and the ability of a wind tower to distribute airflow uniformly around a building. As the number of louvres increases, the flow through the wind tower increases. A 12.7% increase in airflow rate was observed by the addition of 2 – 3 louvres to a maximum total number of 6 – 8 louvres. Beyond this number of louvres, the airflow rate only increased 1.5%. Figure 2-10 shows the airflow pattern and pathlines around the wind tower and the effect of increasing the number of louvres. Short-circuiting, where air enters and exits the wind tower without circulating around the adjoining room below, was observed in the upper section of the wind tower. Short-circuiting is problematic as the efficiency of the wind tower is reduced. Air is effectively wasted as it moves through the wind tower without entering the room. This highlights the importance of selecting the correct number of louvres and louvre design.

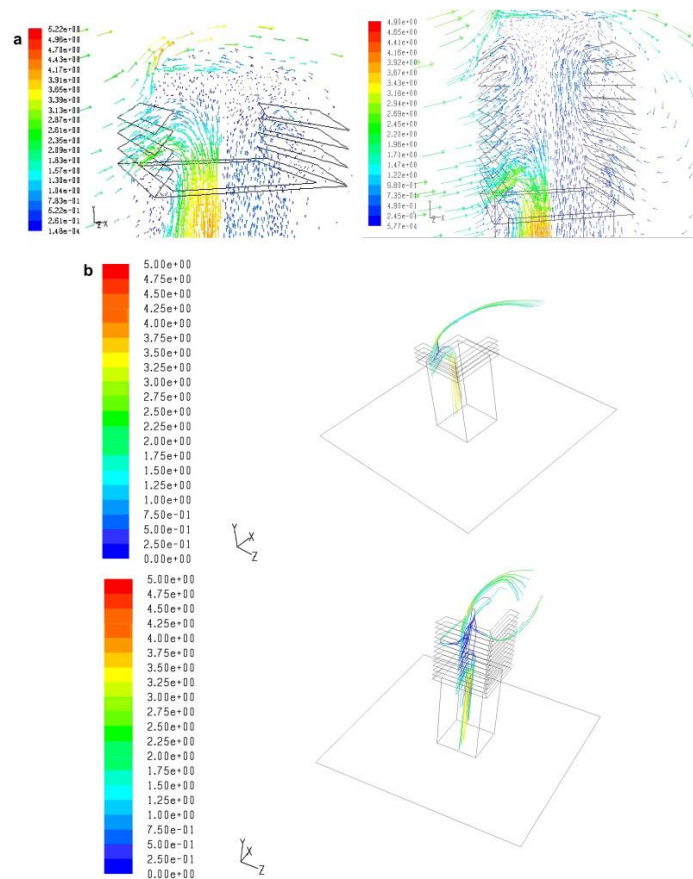


Figure 2-10 – Airflow pattern and pathlines in and around the windcatcher (3-layer louvers and 12-layer louvers) (a) Airflow pattern, (b) Pathline [84]

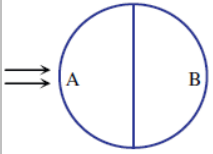
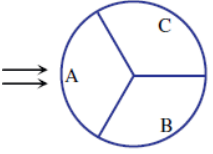
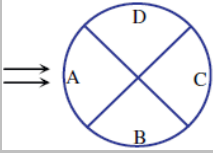
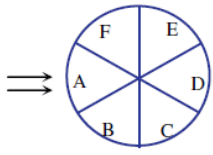
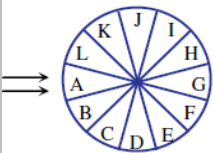
Hughes and Ghani [85] conducted a similar using CFD study assessing the impact of louvre design on supply rates. By varying the angle of louvres incrementally by 5° within a range of 10° - 45° over a set number of louvres, the effect on the airflow rate and pressure distribution within the building was calculated. Measurements showed that at a louvre angle of 35° results in the maximum internal air velocities. Analysis identified the stall angle of the louvre design between 35° - 40° , showing the optimum angle is 35° with the highest internal airflow velocity. Beyond this range, flow separation occurs above the louvres reducing velocity and efficiency. This is proven through comparison of a louvre at 35° and 45° . At 35° , there is a 45% increase in internal thermal comfort of occupants and 42% reduction in trailing edge stall compared to 45° .

The ventilation supply rate through a wind tower is maximised when the pressure difference between the different faces are greatest. Researchers aim to create the largest difference in pressure possible. Because of this, the geometry of a wind towers is a significant factor in the overall performance. Square and rectangular shaped wind towers are most commonly seen and analysed. The large flat surfaces and sharp edges create large zones of high and low pressure. The number of internal divisions within the shaft of the wind tower influence the

supply rates. The incident angle of wind direction on the face of the wind tower has significant effect on the design of a wind tower and optimum performance.

As a response to this, multi-direction wind towers were tested by Montazeri [19] to determine the effect of increasing the number of internal section within the wind tower on the behaviour of the air flow. Five different shapes of wind towers were tested experimentally in a wind tunnel. The results of numerical modelling were validated through comparison with the experiment results. Two-sided, three-sided, four-sided, six-sided and twelve-sided variations were tested by measuring the supply air rate into a test room at different air incident angles. The experiment setup is shown in Table 2-4.

Table 2-4 – Experimental Setup for each of the Designs and Comparison of Flow Rates at Different Wind Angles [19]

Windcatcher model	Wind Direction (deg.)	Openings	Net air flow rate (m ³ /s) at 0° wind angle	Net air flow rate (m ³ /s) at 45° wind angle
Two-sided	0-90		0.029	0.022
Three-sided	0-60		0.026	0.017
Four-sided	0-45		0.024	0.027
Six-sided	0-30		0.021	N/A
Twelve-sided	0-15		0.025	N/A

The maximum efficiency for a typical square four-sided wind tower is at a wind incident angle of 45° to a flat surface. In this scenario, half of the wind tower acts as an inlet and half acts as an outlet. The research aimed to understand if this was universal across all designs.

In standard operation, a large portion of a four-sided wind tower is used to extract internal air. Montazeri [19] proposed that a more efficient use of sections of the wind tower would be for supply. The study tested this using a circular cross section for the wind tower with an increasing number of internal divisions. Experimental testing and numerical modelling proved this idea incorrect; by reviewing previous work, the author found that square and rectangular wind tower was 13% more efficient than the current circular design. This was due to the sharp edges of the square and rectangular shaped wind towers creating flow separation around the wind tower. This increased the suction force, drawing additional air out of the building. Furthermore, at an incident angle of 0° increasing the number of partitions within the wind tower decreases the induced supply rate within the test room. However, as the number of partitions increases the influence of a changing incident angle of the airflow reduces. This provides potential for a system located in an area where the direction of the wind is highly varied.

Maximising the airflow through a wind tower into an occupied space is the major goal for the development of natural ventilation. With this objective in mind, alternative solutions for maximising airflow when the climate does not provide adequate conditions for ventilation are required. Increasing airflow with a low energy solution is possible by using a solar powered fan fixed to the underside of the top hat of a wind tower. Hughes and Ghani [83] and Priyadarsini *et al.* [86] both investigated this concept as a solution to increasing air flow rates during periods of low external wind speed. Hughes and Ghani [83] used CFD techniques to position a low energy fan at the top, middle and bottom of a wind tower shaft and observe the effect on air flow and ventilation rates. This was achieved by modelling a porous jump boundary condition at different heights in the wind tower. Simulations showed that at an external wind speed of 1m/s and an induced pressure of 20Pa from the operation of the fan, the recommended guideline ventilation rates could be met. This improves upon the standard operation of a conventional wind tower not meeting ventilation rates at an external wind speed of 1m/s [87].

Priyadarsini *et al.* [86] tested a similar system experimentally using an open-circuit boundary layer wind tunnel for scale models. The team constructed a model apartment with two positions for wind towers to be located for measurement. A conventional wind tower was tested as a comparison with the active wind tower using the low powered fan. Results showed a 550% increase in internal air velocity for use of the active wind tower compared to the conventional wind. Furthermore, when the wind tunnel was turned off, adequate velocity was achieved through sole use of the fan. This highlights the ability of the active

system to provide cooling and ventilation when no wind is present. The study concluded that the system could further improve efficiency by using a solar panel mounted to roof of the wind tower to power the fan.

Control of the airflow through a wind tower and into the occupied space is necessary to prevent unwanted effects on the occupants. Depending on the conditions such as the indoor temperature, the outdoor temperature, internal pollutant concentration and external wind speed the rate at which fresh air is introduced should be controlled. Dampers at the base of the wind tower unit are able to meet this demand by regulating the flow through the wind tower either through manual or automated control. Continuous monitoring of environmental conditions ensures that dampers are set at the optimum angle for ventilation, pollutant and temperature regulation.

Elmualim [88] and Hughes and Ghani [26] investigated the effect of dampers on the operation of wind towers. Using an experimental setup, shown in Figure 2-11, Elmualim [88] found that dampers and an egg crate grille attached to the base of the wind tower shaft were capable of reducing the airflow rate into the adjoining room when compared. The supply rate was reduced by 20 – 50% at an external wind speed of 1 – 3m/s depending on the angle of the dampers. The damper and egg crate grille improved the distributor of fresh air into the room. The study also used CFD analysis to understand the effect of the dampers. The CFD analysis was validated by the experimental results.

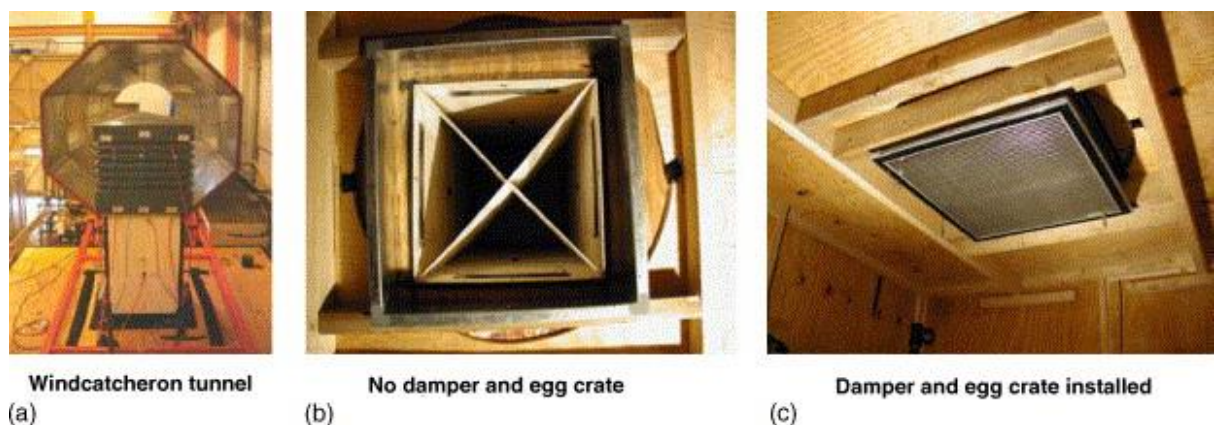


Figure 2-11 – Experimental test set-up in the wind tunnel [88]

Building on this work, Hughes and Ghani [26] used CFD modelling to determine the optimum louver angle in terms of pressure and internal air velocity. The dampers were modelled at angles between 0 - 90° from the vertical plane in 5° increments. Measurements of pressure and velocity distribution around the test room indicated that as the angle of the dampers increases, the pressure drop across the dampers increases and the velocity increases. The

authors explain this by the reduced area available for air to flow. This aids occupant comfort by reducing draughts that may occur during periods of high external wind speed.

2.5.2 Wind Tunnel Testing

Wind tunnel testing is a valuable technique used to gain qualitative and quantitative data from prototypes in a controlled environment. Researchers can use the results from wind tunnel testing to validate solutions from CFD models. Initial hand calculations using empirical formulas for flow rates can be used to focus and guide the CFD design. This occurs less commonly now due to the speed and accuracy of CFD design. In this respect, the two systems work in a complimentary manner. Modelling and simulation is completed using CFD analysis until a design is refined to a suitable degree for use in wind tunnel testing. Researchers generally use wind tunnel testing at a later stage due to the increased time and resources needed for thorough testing compared to CFD analysis. However, modern rapid 3D printing is able to create precise models in a short time, and so wind tunnel testing may become more commonly used for research.

A number of characteristics of a wind tunnel must first be recognised and determined for proper analysis within a wind tunnel. Moonen *et al.* [89] and Moonen *et al.* [90] detailed wind tunnel indicators for flow quality and applications within the test section. Ensuring that wind tunnels used for testing meet these indicators is necessary to ensure that the conditions of the wind tunnel can be replicated appropriately in the CFD modelling. Moonen *et al.* [89] acknowledges that different applications of wind tunnels significantly affect the construction and analysis of the wind tunnel. A uniform flow in both directions is necessary for aerospace applications, whereas building and wind engineering is better suited to a flow that is uniform in the horizontal plane but increases with height in the vertical plane. This is known as an atmospheric boundary layer wind tunnel and represents the changes of wind velocity at increasing height. As schematic of this can be seen in Figure 2-12.

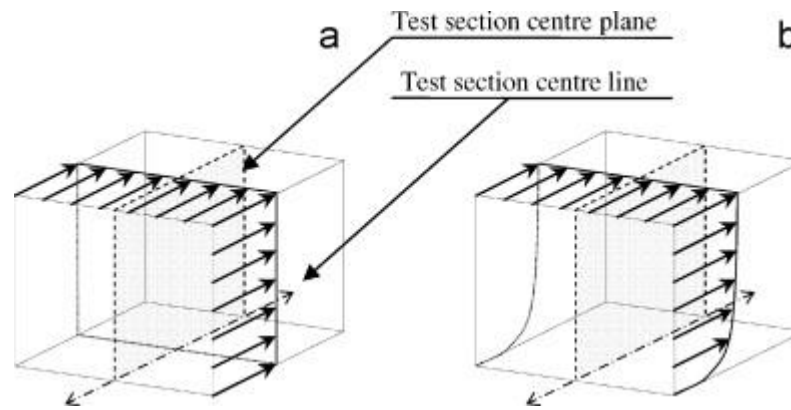


Figure 2-12 – Required flow fields in wind tunnel test sections: (a) entirely uniform flow for aeronautical applications and (b) laterally uniform flow for Wind Engineering studies [90]

Walker *et al.* [91] conducted an investigation into passive ventilation using a wind tunnel for validation of CFD analysis. A proposed building structure that used buoyancy driven flow for ventilation in conjunction with wind towers mounted to the roof of the model building was considered. The results collected from the wind tunnel analysis showed a high level of correlation to the CFD analysis. A scale model of the building tested in the study can be seen in Figure 2-13 and was constructed to fit within the wind tunnel.



Figure 2-13 – Picture of the scaled air model in the test chamber [91]

A major component of the research was the importance of maintaining similarity in wind tunnel testing compared to the full-size building. To ensure the results presented were correct, the research team examined similarity analysis between the proposed full-scale design and the model scale. Geometric, kinetic and thermal similarities are the three characteristics that should be maintained between full size and model scale testing. Geometric and thermal similarity are generally easily achieved by simple scaling of dimensions and the heat loads required. Thermal similarity can become problematic when the required scale heat loads necessary are too great and pose a fire or health risk. Kinetic

similarity is more difficult to achieve in most wind tunnels. Due to the requirement to match the Reynolds number between the two scales, standard wind tunnels are generally not capable of simulating the inlet velocities required to meet the similarity. However, research completed by Defraeye *et al.* [92] showed that as long as fully developed turbulent flow is achieved, even with a lower Reynolds number compared to the full scale model, that similarity is achieved. This is because turbulent flow is independent of Reynolds number above the critical value. Provided that the critical value is reached, the Reynolds number of the models do not need to match for kinetic similarity to be achieved.

Along with the ability to validate CFD analysis, wind tunnel testing provides useful qualitative data in the form of visualisation. This benefits researchers by providing the opportunity to evaluate transient flows which may not be ordinarily possible depending on the CFD analysis performed. This gives researchers a better understanding of the swirl patterns and distribution of internal air.

Montazeri and Azizian [93] and Montazeri *et al.* [94] used wind tunnel testing for the qualitative visualisation of airstreams for one and two sided wind towers respectively. One sided wind towers are more commonly used in areas with a prevailing wind direction and require openings within the building such as windows or doors for the air to exhaust out of. Two sided wind towers provide more flexibility in terms of wind direction and building design as the two sides of the wind tower can be used as the inlet/outlet respectively. The schematic of the two sided wind tower used in the experiment can be seen in Figure 2-14.

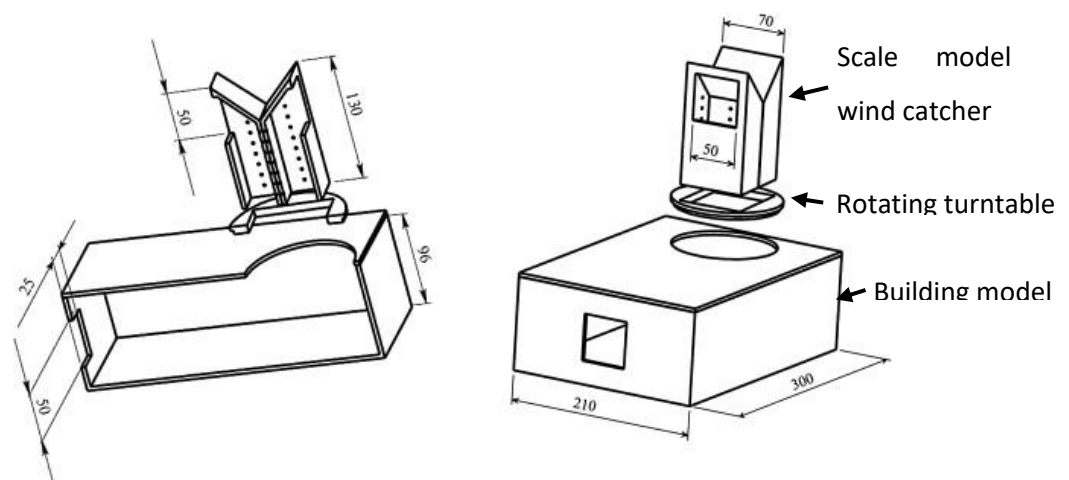


Figure 2-14 – Isometric view of two-sided wind catcher model and its connected house model along with their dimensions and locations of pressure taps. All dimensions are in millimeter [94]

Both studies used a scale of 1:40 for testing in an atmospheric boundary layer open circuit wind tunnel. The effect of the incident wind direction compared to the face of the wind tower

on the ventilation supply rate performance was examined in both studies. The results showed that the pressure coefficient, an indicator of airflow rate, is highly dependent on the wind incident angle. For both models, a wind incident angle of 0° , relative to the opening of the wind tower, provides maximum supply ventilation whereas 90° provides minimum supply ventilation. This highlights the limitations of one and two-sided wind towers, only when the wind direction is at the optimum for ventilation are adequate supply rates achieved. However, in areas where there is a strong prevailing wind direction, one and two-sided wind towers could be beneficial. Four-sided wind towers offer greater flexibility however.

It was also noted by Montazeri *et al.* [94] that short circuiting, where air moves from the inlet to the outlet without entering the occupied space and providing ventilation, is much more prevalent in two sided wind towers, particularly at an incident angle of 60° . This reduces the efficiency of a two-sided wind tower significantly.

As stated previously, Elmualim [88] examined the addition of dampers to wind tower units as a means of controlling air flow through into the occupied space. The presented work on the use of full-scale models in large wind tunnels showed positive results and validation of CFD analysis. The work included the study of ventilation rates into a small room below the wind tower. However, it was noted that with these tests, atmospheric conditions cannot be replicated in a small wind tunnel as the roof of the wind tunnel leads to artificial acceleration of the air. The full experimental setup of the wind tunnel used is shown in Figure 2-15.

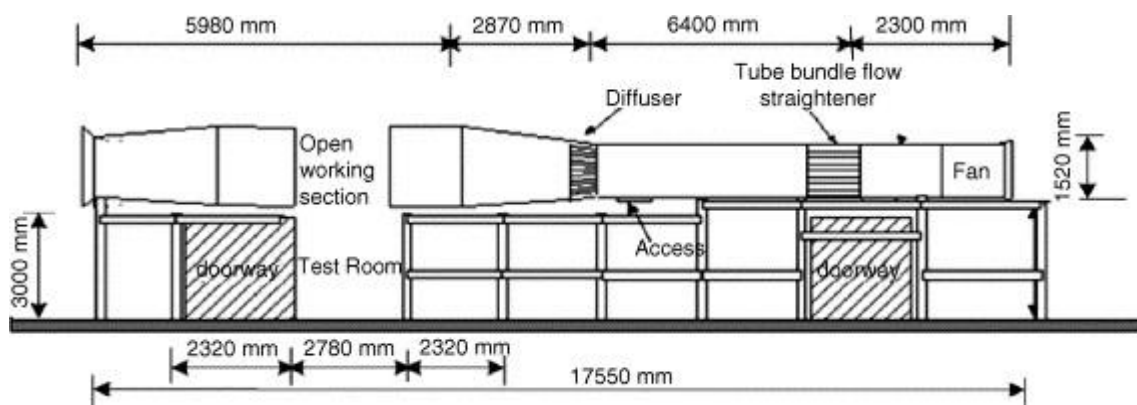


Figure 2-15 – Schematic drawing of the wind tunnel at BSRIA [88]

Despite the versatility and significant developments in wind tunnel technology for replicating real world conditions using atmospheric boundary layer wind tunnels, full scale testing in open-air environments is still necessary to determine the true characteristics of a new technology. Shea *et al.* [95] conducted far-field testing of a four-sided wind tower in order to determine the suitability of the system outside of a wind tunnel. The study found that, as

expected, the ventilation rate varied linearly with wind velocity. Maximum ventilation occurred when the wind angle resulted in two quadrants acting as inlets and two quadrants acting as outlets, an incident wind angle of 45° from a face of the wind tower. When a single quadrant acted as an inlet with the remaining three quadrants acting as outlets, ventilation was at a minimum. Despite this, the wind tower was capable of meeting ventilation requirements for the majority of the time. When measurements were taken from the full-scale prototype and compared to steady-state predictions from CFD models, it was found that the airflow rate was consistently under-predicted by the CFD analysis. This shows that full-scale testing is important for analysis and that reliance on a single modelling method is unreliable and can be expensive in terms of optimising solutions.

The analysis of wind towers deployed on occupied buildings is important to determine, if any, the effect the system has on ventilation supply rates. Jones and Kirby [96] studied 16 different classrooms ventilated by various methods, including wind towers, for a calendar year in order to evaluate the effectiveness of each system. The concentration of CO_2 was used as the measurable parameter for ventilation, as suggested by Building Bulletin 101 [9] which specifies ventilation rates in schools. The analysis of the classrooms fitted with wind towers established that passive ventilation was capable of supplying the required ventilation in summer, particularly when used in conjunction with open windows. However, the CO_2 concentration levels were seen to be too high during winter months due to the closed dampers preventing ventilation. Sensors monitoring internal temperature automated the control of the dampers. As the internal temperature during winter is lower than in summer, the dampers remained closed.

To counter the increasing pollutant build up, the study recommended monitoring CO_2 concentration as the parameter for controlling the dampers with a controlled, continuous airflow of 5l/s/person . Analysis showed that this would incur an energy loss of approximately 62W per person during winter but it was noted that this loss could be offset by heat generated by occupant activity and electrical equipment. The work that was completed by Jones and Kirby [96] is supported by a number of other studies, most notably Clements-Croome *et al.* [7], Kolokotroni *et al.* [23] and Mumovic *et al.* [24].

If the heat lost to the external environment from open dampers in winter could not be generated from electrical equipment, the additional strain on heating systems would increase the energy demand and cost to building operators. In a well-insulated building, the majority of the heat loss would be through the exhaust quadrants of the wind tower. This

presents an opportunity to recover some of the heat from the exhaust air, transferring heat to the incoming airstream. This would increase the temperature of the incoming air, lowering the strain on the heating systems whilst providing fresh air for ventilation at the same time.

Wind towers are a passive ventilation system that require very little energy for operation. Recent innovations have improved the ventilation supply rates of wind towers through optimisation of shape, size and components. The improvements to wind towers have resulted in a system that is capable of deliver the recommended ventilation rates to occupied spaces. However, wind towers are not appropriate for year round use, particularly in cooler climates with cold winters. Open ventilation during winters would result in increased energy demand for heating systems if the internal heat gains of the interior were not enough to overcome the losses. The addition of a device that could transfer heat from the exhaust air to the incoming air would be greatly beneficial to utilise wind towers year round without affecting energy demand. The selection of an appropriate device requires careful decision-making.

2.6 Energy Recovery Ventilation Devices

The use of energy recovery devices in ventilation systems is becoming increasingly common to reduce the heating and cooling demands of buildings. The exhaust air of a building ventilation system is used as either an energy source or sink depending on the climate conditions, time of year and requirements of the building as noted by Sauer and Howell [97]. Heating systems raise internal air temperature. As the air is evacuated by the ventilation system, the energy in the exhaust air can be transferred to the incoming fresh air. This raises the temperature of the incoming air and reduces the energy demand on the heating system during winter. During the cooling season, the exhaust air can be used as a heat sink for the thermal energy in the warmer incoming fresh air, thereby reducing the cooling demand.

Energy recovery systems have been shown to provide a significant reduction of energy demand on the HVAC systems of buildings [11,12]. In the UK, indoor air temperature has increased by 3°C over the previous two decades, this equates to a 20% increase in heating energy consumption [98]. Widespread use of heat recovery devices in ventilation systems to transfer energy to the incoming air could offset this energy increase. Behavioural changes in occupants and the high electrical consumption in office and service sector buildings have resulted in internal heat gains from electrical equipment that are considerable. The

temperature increases from these heat gains provide a reliable heat source that could be recovered consistently by a heat recovery device, reducing the reliance of heating systems.

Exhaust air heat losses through open wind tower dampers during winter, as previously reported by Jones and Kirby [96], could be recovered by integrating energy recovery ventilation devices into the shaft of wind towers. As the inlet and outlet quadrants sit adjacent, access to each airstream would be simple. This reduces the size of the device. The combination of a wind tower and energy recovery device would result in a system capable of freely ventilating a building, along with reducing the energy demand on heating systems.

In general thermodynamic terms, two different forms, sensible and latent heat, define thermal energy. Sensible heat is the dry air temperature that can be recovered. Latent heat is the energy that is recovered from the moisture within the airstream. Sensible only heat recovery devices generally have lower efficiency than total energy recovery devices that are capable of recovering sensible and latent heat [99–101]. Whilst a significant proportion of research focus related to energy recovery devices is on sensible heat recovery, latent heat recovery is equally important. As noted, the internal relative humidity levels can have a significant effect on occupant comfort and health when outside the optimum range. Management of the interior moisture through energy recovery devices would also contribute to lower energy demand as mechanical systems would not be required.

Mardiana-Idayu and Riffat [102] investigated heat recovery device integration into passive ventilation systems. The study assessed the appropriateness of different recovery technologies and potential for integration in passive ventilation systems. Their work concluded that heat pipe heat recovery units were the most effective for passive ventilation due to the lack of moving parts in the system. This was considered important due to the low maintenance requirements and small pressure drop necessary for passive ventilation systems to overcome. Heat pumps were most commonly used in mechanical ventilation systems and rotary thermal wheels were widely used for dehumidification of airstreams. The authors noted that little work had been conducted combining heat recovery and other low carbon technologies such as evaporative cooling and desiccant dehumidification and is worthy of further research.

Building on the work by Mardiana-Idayu and Riffat [102], Alonso *et al.* [103] performed a review of heat/energy recovery devices for uses in zero energy buildings in cold climates. The authors recognised that in cold climates, the variation between outdoor and indoor temperatures can reach up to 40°C and recovering the heat from outgoing exhaust air limits

the energy demand of the building. This is particularly suitable for zero energy buildings which aim to limit energy demand as much as possible. Alonso *et al.* advocate three types of recovery devices, plate heat exchangers, heat wheel and run-around technology, highlighting the merits and disadvantages of each. Considering the cold climate, which the study uses, the parameters to which the devices are assessed include freezing problems and if moving parts can be affected by this, odour transfer, and sensible and latent heat transfer effectiveness. The review concludes that each of the devices has distinct advantages over the others in particular applications and so does not provide a statement solely advocating one device. Though the review by Alonso *et al.* [103] is detailed and thorough, the ventilation method suggested is a mechanical HVAC system and so concerns about pressure drop across the device are not as heavily assessed.

More recently, Cuce and Riffat [104] took a detailed view of heat recovery systems for building applications, theoretical, experimental and simulation analysis as well as thermodynamic performance assessment. The review looked at the technology as a whole, predominately focussing on the integration into mechanical ventilation systems. The authors recognised the high-energy costs that can be associated with mechanical ventilation systems integrated with heat recovery technology due to the need for fans to overcome the additional pressure drop due to the integration of the heat recovery devices. Overall, it was noted that heat recovery systems are designed to reduce the energy consumed for heating, cooling and ventilation in buildings by recovering waste heat.

Shi and Chew [105] and Chan *et al.* [106] analysed different solar-based energy systems and the heat recovery devices that were integrated into them. Shi and Chew [105] determined which parameters most strongly affected the efficiency of each system investigated. For solar-based energy systems, the orientation of the building and the system itself have a significant effect on the efficiency along with local weather conditions, tilt angle, surface temperature and system selection. The depth to which they are buried and the size of ground source-based systems are key to the operating capacity. Chan *et al.* [106] recommended that further research be undertaken to improve the technologies with particular interest in the system efficiency, architectural aesthetic and cost effectiveness. A combined system that was capable of delivering heating and cooling was recommended to be the most effective.

These studies indicate that research into the integration of recovery devices into other technologies has been conducted with positive results. Mardiana-Idayu and Riffat [102] indicate the parameters for recovery systems that should be taken into account when

considering integration with passive ventilation. Ensuring a high recovery efficiency and low-pressure drop induced in the airflow are regarded as the two most significant parameters that should be assessed for passive ventilation integration. Taking these considerations into account, a number of recovery technologies have been reviewed and evaluated based on the recommendations and other parameters affecting passive ventilation integration.

2.6.1 Rotary Thermal Wheels

Rotary thermal wheels are a mechanical means of heat recovery. A rotating porous metallic wheel transfers thermal energy from one air stream to another by passing through each fluid alternately. The system operates by working as a thermal storage mass whereby the heat from the air is temporarily stored within the wheel matrix until it is transferred to the cooler air stream [102]. The matrices are ordinarily constructed in a honeycomb or sinusoidal wave arrangement. This maximises the surface area of the matrix, increasing the contact area between the wheel and the airstream, and theoretically, increasing the transfer. This is demonstrated in the schematic diagram in Figure 2-16.

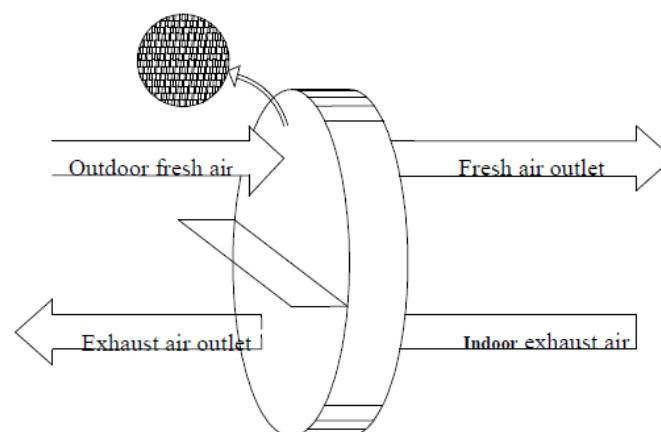


Figure 2-16 – Working principle of wheel heat recovery unit [107]

A number of numerical investigations have been completed in order to conceptually optimise various aspects of the design of rotary thermal wheels [38,108–111]. Mathematical models were developed by different research teams in order to calculate a number of factors of the performance of rotary wheels which were then compared against experimental laboratory work or existing literature. The mathematical models focussed on the heat and moisture transfer through the wheel matrices, the effect of rotation speed on the temperature of airstreams and the individual analysis of a single channel within the honeycombed structure of the matrix. Hemzal [112] carried out experimental research which focussed on the pressure drop in rotary thermal wheels and the effect it had on air flow. Similar data presented below by Yamaguchi and Saito [38] showed that the pressure drop

across the wheel increased as the air velocity increases. Figure 2-17 shows the effect of air velocity on the pressure drop across a 100mm thick wheel and the influence of an entrance region factor on the calculation. As the air velocity at the entrance to the rotary wheel increases, the pressure drop also increases. It is important to take into account for the pressure drop calculation the effect of the small entrance regions have. The effect of these increase the pressure drop by up to 50Pa at an air velocity of 4m/s, Both studies highlight that the integration of the standard structure of a rotary wheel into a passive ventilation system is difficult, as the lack of driving forces to overcome pressure loss would lead to low ventilation supply rates.

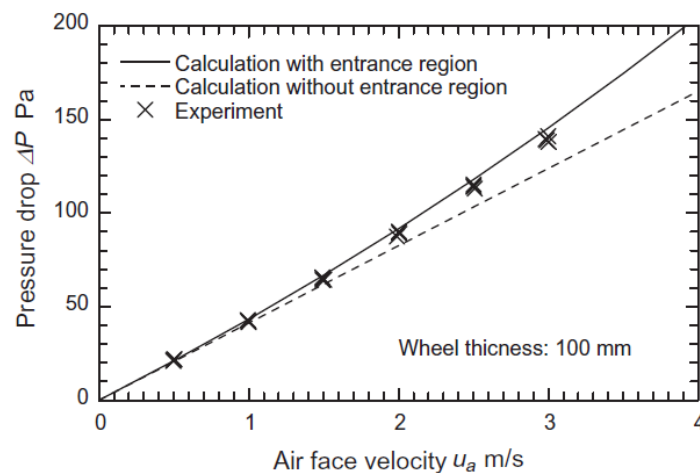


Figure 2-17 – Relationship between pressure drop and air superficial velocity [38]

At present, rotary thermal wheels are commonly used in mechanical ventilation systems to recover the energy from the exhaust air. The total efficiency of rotary thermal wheels is generally above 80%. Juodvalkis *et al.* [113] noted that in mechanical ventilation systems, rotary thermal wheels are commonly coupled with a rotary heat pump. This is done to improve the overall performance of the system for recovery and heating. Figure 2-18a demonstrates that a hybrid system using a rotary thermal wheel, is capable of delivering ventilation with lower input energy compared to an air conditioning system across a range of outdoor air temperatures. Furthermore, the hybrid system delivers air that is cooler and so provides greater thermal comfort to occupants at high outdoor air temperatures, as shown in Figure 2-18b. Further studies show that systems incorporating a rotary thermal wheel are capable of saving significant amounts of energy. In a climate with a high heating degree days value such as Sweden, reducing the energy demand of a building based on the total useable floor area up to 30-42kWh/m² is possible, as shown by Akbari and Oman [114].

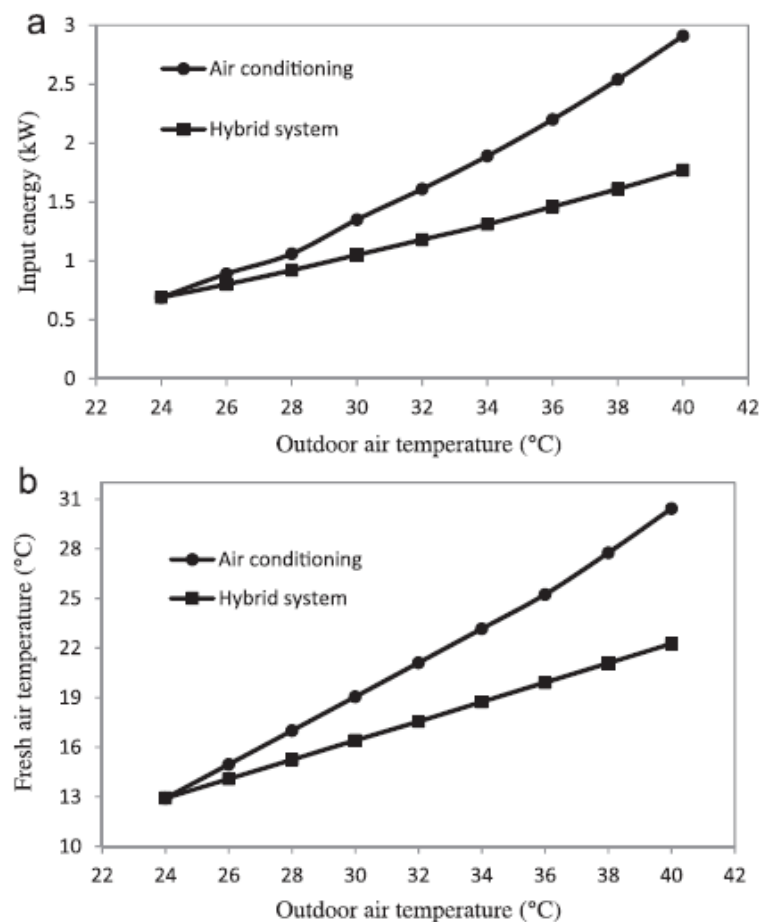


Figure 2-18 – Effect of outdoor air temperature (a) on input energy required, and (b) on fresh air temperature [115]

Rotary thermal wheels have a number of disadvantages that limits the use for heat recovery applications. Rotary thermal wheels are susceptible to parasitic shortcuts, where air moving in one direction recirculates in an unintended direction, known as air short-circuiting. Furthermore, cross contamination of the air streams is a significant factor in the placement of rotary thermal wheels. Roulet *et al.* [116] stated that although seals and purge selectors can reduce the impact of short circuiting and cross contamination, it does not completely remove the problem, making rotary thermal wheels unsuitable for hospitals and other buildings where isolated air streams must be maintained. Furthermore, because of the high-pressure loss experienced across rotary thermal wheels, additional fans are used to maintain high airflow rates into buildings for ventilation. If these fans require more power to operate than is recovered, the total energy demand will increase. This will cause a cost increase due to the variation in the price of energy depending on the source, if these fans require more electrical power to operate than is recovered from gas powered heaters.

Two types of rotary thermal wheel exist. Heat wheels and enthalpy (desiccant) wheels. Though there is geometrical similarity between heat and desiccant wheels, there are differences that effect the operation of each design. In this application, desiccant materials, coated to the surface of the matrix of the wheel, are used to transfer moisture from the airstream with the highest relative humidity to another through the process of adsorption and desorption [117].

Ge *et al.* [118] described the mechanisms of adsorption and desorption in desiccant materials. Desiccant materials have moisture adsorptive properties; the adhesion of gas, liquid or dissolved solids molecules to the surface of a solid. Desiccant materials are highly porous and so have a very high surface area to volume ratio. This makes adsorption possible. Adsorption is a weak interaction and can be reversed. This is known as desorption. The addition of heat, known as regeneration, to the desiccant material encourages the release of molecules from the surface of pores. However, the temperature required for desorption of the water from the surface of the desiccant is generally within the range of 80-120°C which incurs high energy costs from the regeneration airstream [111].

Enteria *et al.* [119] attempted to show that lower regeneration temperatures are capable of maintaining desorption of the silica gel. This was achieved by pre-heating the regeneration air using heat recovery. Reducing the regeneration air temperature as low as possible will result in lower overall energy consumption and increase the attractiveness of the systems to building operators as stated by Fan and Ito [120]. Other research by Intini *et al.* [40] showed that desorption at lower regeneration temperatures may be possible when the velocity of the inlet and regeneration air are properly managed for optimum desorption depending on the local conditions.

It is important that desorption is maintained, allowing the silica gel to continue to adsorb the moisture from inlet air and improving comfort. If the desorption process is interrupted, the silica gel may become completely saturated and no longer be capable of reducing the relative humidity of the airstream through adsorption.

Jai *et al.* [121] and Tashiro *et al.* [36] investigated various desiccant materials which can be used for dehumidification in rotary desiccant wheel systems. The materials were assessed on the volume of water that was adsorbed onto the pore surface compared to the volume of the material. The higher the volume of water adsorbed, the better the material was determined to have acted. Composite materials were used in each study, combining new materials with more commonly used desiccant materials. Jai *et al.* [121] found that the

composite desiccant material showed a 50% improvement in adsorption compared to the conventional design. Furthermore, the optimal regeneration temperature was 80°C compared to 100°C for the conventional design. Tashiro *et al.* [36] saw a similar improvement of composite materials of 39% over conventional desiccant materials. In the case of desiccant rotary wheels used for ventilation, Nui and Zhang [122] stated that silica gel (hydrated silicon dioxide) is the most common desiccant material used for a wide range of applications.

Calay and Wang [115] found that due to the efficient method of moisture removal in desiccant wheels, they are commonly used as a centralised method of air treatment. This method of air treatment is capable of energy savings of up to 60% compared to existing systems. Zhang and Niu [123] found that the optimum rotation speed for a desiccant wheel for dehumidification is significantly lower than a heat wheel. The optimal rotation speed for a desiccant wheel was calculated as less than 1rpm. This increased contact time is necessary for the adsorption of the water molecules on to the surface of the desiccant material.

Ge *et al.* [124] studied solar powered rotary desiccant wheel cooling systems which were separated into two classifications. Separate solar rotary desiccant wheel cooling system and a hybrid system where mechanical vapour compression systems are used for cooling of the airstream. The authors noted that the moisture removal capacity of both classifications of systems is high but the cooling capacity is limited by the cooling technology employed. Both classifications are suitable for use in climates that are hot and humid. Little experimental and far-field testing have been completed which would be beneficial for design and improving simulation models that are primarily used for analysis.

Rotary thermal wheels are an energy recovery device that transfer heat and moisture from one airstream to another by rotating through each airstream. The properties are transported from each airstream through a matrix constructed to maximise surface area. The wheels are commonly made of aluminium and can be coated with additional materials to enhance the performance. The efficiency of rotary thermal wheels is high, with values up to 90% efficiency reported. A number of factors affect the performance of rotary thermal wheels. The rotation speed of the wheel, thickness and material of the matrix, depth of the matrix, velocity of the airstreams amongst other parameters. All these require consideration. Rotary thermal wheels can be treated with desiccant materials to enable dehumidification of airstreams. Moisture is adsorbed to the surface of the desiccant materials where it is then removed from the surface by heat from the opposite airstream.

Though the low profile and high efficiency of rotary thermal wheels would suggest integration into passive ventilation systems would be possible, high pressure drop across the wheel is measured. The small opening of the matrix structure creates high skin friction between the matrix walls and the moving air causes this. To overcome the pressure drop, mechanical HVAC systems use fans to increase the velocity of the airstreams to negate the pressure drop. This incurs additional energy demand and if the energy saving from use of the rotary thermal wheel is less than this, the total energy demand of the system goes up. Integration of rotary thermal wheels into wind tower systems would require reconfiguration of the matrix structures.

2.6.2 Fixed Plate Exchangers

Fixed plate heat exchangers are the most commonly used type of heat exchanger and have been in use and continually developed for a number of decades [102,125]. Thin metal plates are stacked with a small spacing between plates. Two different airstreams pass through these spaces, adjacent to each other. The heat transfer occurs as the temperature transfers through the plate from one airstream to the other. A side view of a fixed plate heat exchanger can be seen in Figure 2-19, showing the interaction of the exchanger and the airstreams. The efficiency of these devices has been shown to be extremely high in transferring sensible heat from one air stream to another. Nielsen *et al.* [126] have noted values of 90% sensible heat efficiency. The high levels of efficiency are attributed to the high heat transfer coefficients of the materials used, operational pressure and temperature range.

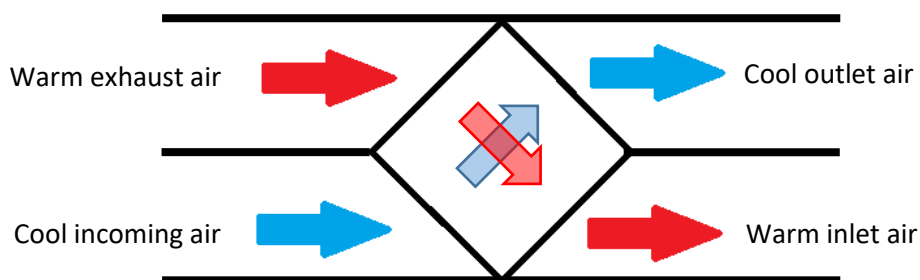


Figure 2-19 – Simple schematic showing the concurrent operation of a fixed plate heat exchanger

The core of fixed plate heat exchangers can be arranged in a number of ways for the airstreams to move through. Cross, concurrent and counter-current flow arrangements are the most common configurations of fixed plate core. Lamb [127] stated that fixed plate heat exchangers operate best under counter-current flow conditions where the two airstreams move in opposite directions. However, the configuration of counter-current flow fixed plate

heat exchangers required substantially more space for ducts and installation than concurrent flow exchangers. Seeing this problem, Nasif *et al.* [128] developed a solution to overcome this problem, both concurrent and counter-current flow arrangements were incorporated into one design, as shown in Figure 2-20. This solution reduces the space required of a standard concurrent flow arrangement but still allows the two airstreams to pass counter-current over a substantial amount of the heat exchanger. This improves the efficiency of the system whilst saving space.

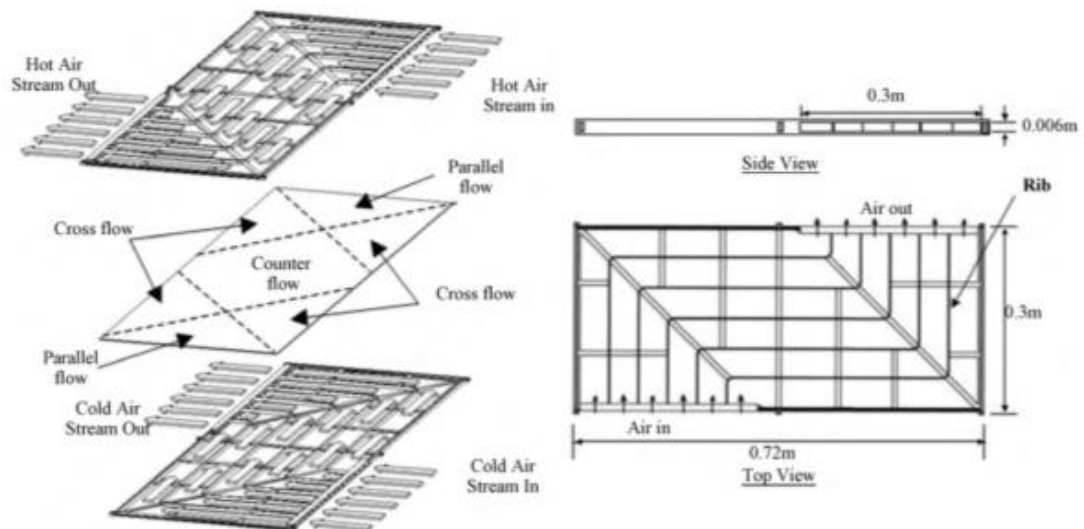


Figure 2-20 – Heat exchanger plastic frame flow channels [128]

Abu-Khader [129] reviewed the recent advances in research of plate heat exchangers. Improvements to the heat transfer efficiency and pressure drop were two of the parameters that the author used to assess the advancements. Abu-Khader [129] noted that significant advancements have been made, with particular attention paid to the design of the plates in the devices. Modifications to the traditionally flat plates used in construction results in improved heat transfer.

Zhang [130] compared corrugated plates to flat plates, an example of this new construction can be seen in Figure 2-21. The authors theorised that triangular corrugations would provide a higher transfer of heat compared to standard flat plates as the mixing effect in between the corrugations would be intensified in the troughs. Furthermore, the thinner material thickness used, due to the increased strength from the shape of the plates, would aid transport from one airstream to the other. There were difficulties in modelling the design in CFD due to the frequent transition from laminar to turbulent flow even at low Reynolds numbers. A low Reynolds $k-\omega$ model was used to solve this problem. The study confirmed the theory of Zhang [130] and showed that the corrugations did increase the efficiency of

the system. A number of complex flows developed in the lower corrugations which aided heat transfer. Recirculation, flow separation and reattachment all developed over time in the corrugations, increasing the transfer.

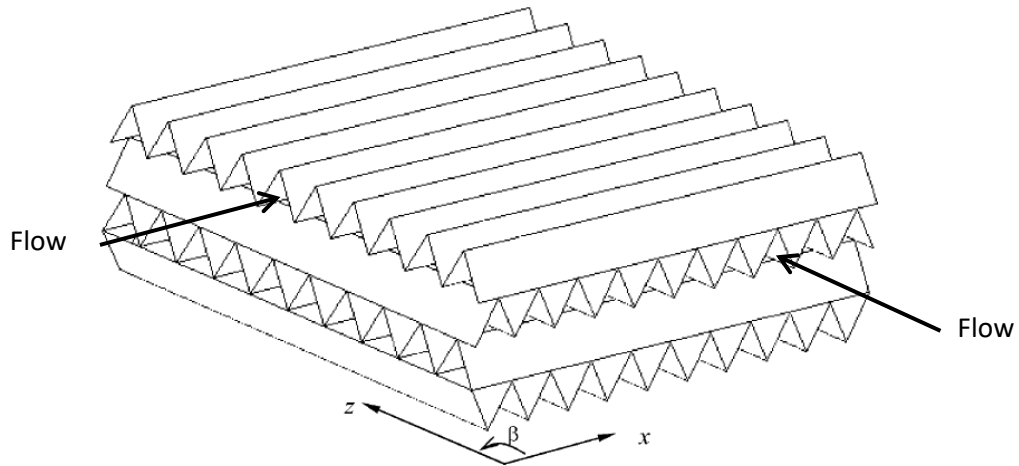


Figure 2-21 – The flow channel geometry for corrugated fixed plate heat exchangers [130]

A common problem that affects fixed plate heat exchangers is the build-up of condensation within the structure. If air is cooled below the dew point temperature during the heat transfer to the opposite airstream, condensation will form. Fernandez-Seara *et al.* [131] reported that this build-up of condensation can seriously reduce the thermal performance and efficiency of the heat exchanger. Further to this, in climates with external temperatures which regularly fall below 0°C, frost and ice formation within the heat exchanger due to the condensate can block the air pathways, preventing the exchanger from operating. Kragh *et al.* [132] developed a solution to this problem by designing a fixed plate heat exchanger which continuously alternated between two modes of operation to prevent the build-up of frost and ice. The new design maintained good operating conditions, even when the external air temperature was significantly below 0°C. The temperature efficiency was measured as 82%.

Fixed plate heat exchangers are the most commonly used heat recovery device, particularly in mechanical HVAC systems. Thin metal plates are closely stacked and two airstreams are passed through the adjacent gaps where convection occurs. Fixed plate heat exchangers are effective heat transfer devices and show high efficiency, up to 80%. However, due to the size of the gaps between metal plates, the pressure drop across a device is high. The high pressure drop means for ventilation systems to adequate supply air to occupied spaces, fans must be used to improve the air velocity. This incurs additional energy demand. Also, fixed

plate heat exchangers are capable of only transferring sensible heat. Latent heat transfer is not possible. Research has improved the use of fixed plate heat exchangers but the applications of these devices in passive ventilation appears to be limited.

2.6.3 Membrane Fixed Plate Exchanger

Though metals and alloys are the most common materials used in fixed plate heat exchangers, the use of these materials limits the plate heat exchangers to solely sensible heat recovery. Research is now also exploring the newer area of porous membranes to act as the plates of the exchanger, which are capable of transferring both sensible and latent heat. By also transferring latent heat from one airstream to another, the energy demand for moisture control, either humidification or dehumidification of the airstream, is lowered. This improves the overall efficiency of the device.

Yaici *et al.* [133] used porous membranes as a material for total energy recovery devices, replacing the metal sheets that were previously used. The results from this study showed that sensible and latent heat recovery is possible with membrane modelling across a fixed plate heat exchanger. Figure 2-22 shows the schematic of a membrane fixed plate exchanger. The membrane is supported between two layers in order to provide structure to the plates; the supports do not interfere with heat or mass transport. Al-Waked *et al.* [134] used CFD analysis to generate a model of a membrane heat exchanger. Two airstreams were modelled adjacent to each other, one for the hot stream and one for the cold stream. The results showed that total energy recovery from fixed plate heat exchangers is an efficient process, transferring heat and moisture through convection and conduction. When the flow is arranged in a counter-flow arrangement, the effectiveness is highest, up to 86% but dropping to 67% as the flow rate of air increases from 30m³/hr to 190m³/hr.

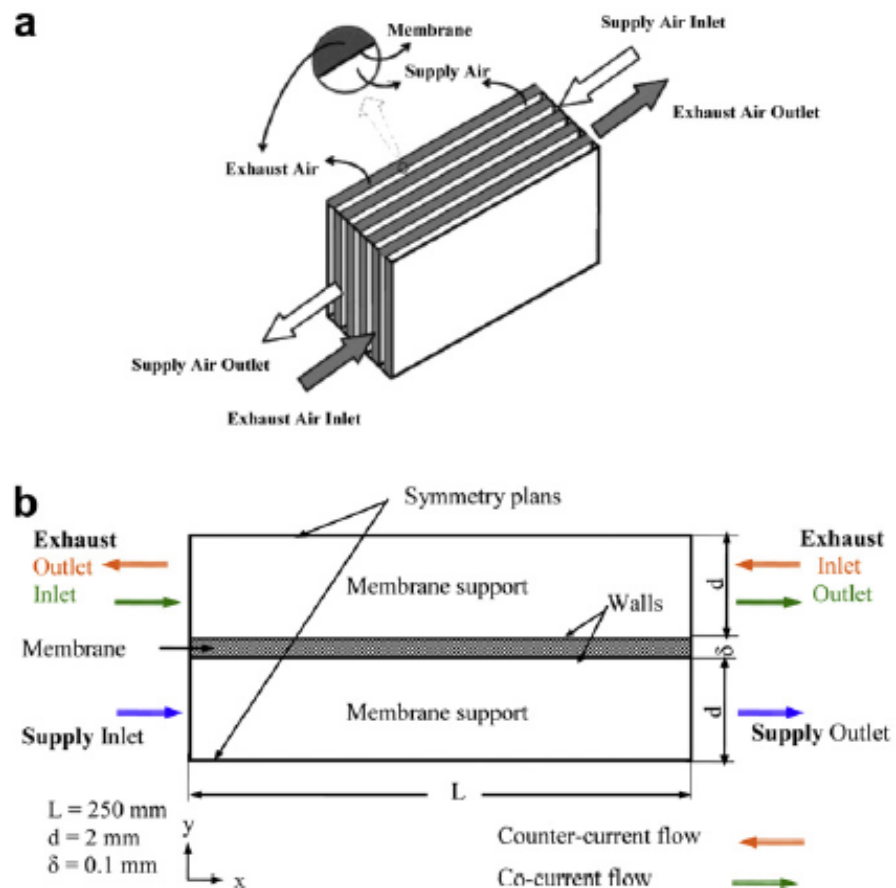


Figure 2-22 – Schematic of a membrane-based energy recovery ventilator: (a) core in counter flow arrangement; (b) schematic of the physical model in a co-current and counter flow arrangements [133].

Research conducted by Zhang [135] has shown that Supported Liquid Membranes (SLM) are a promising area of membrane based fixed plate heat exchanger due to the ability to transfer heat and mass. Zhang and Xiao [136] showed that SLM have a moisture diffusivity coefficient of up to 3-4 orders of magnitude higher than solid membranes; allowing for greater moisture transfer and recovering more latent heat than traditional metal/alloy fixed plates. From research completed by the same group [137] and Min and Su [39], it was determined from a study of different plate materials and characteristics that the plate thickness is the defining factor in the efficiency of the heat exchanger along with channel height between the plates. Zhang and Jiang [101] also found that for reliable performance, the pressure difference across the exchanger must be high with high membrane intensity. Nui and Zhang [122] noted that the efficiency of this form of recovery is similar to highly effective enthalpy rotary wheels but do not have the problems of frost and condensation common with rotary wheels.

Membrane fixed plate heat exchangers are a development from conventional fixed plate heat exchangers. By replacing the metal plates with membrane plates, sensible and latent heat recovery is possible. This improves the efficiency of the system, as a greater total amount of energy is transferable from one airstream to another. However, improvements

have been made to enable total energy recovery; the same pressure drop issues are faced by membrane fixed plate heat exchangers.

2.6.4 Heat Pipes

Heat pipes are a heat recovery device that use a multi-phase process to transfer heat from one airstream to another. Heat pipes are constructed as sealed metal pipes that contain a fluid used for heat transfer. Lin *et al.* [138] explained that heat pipes operate when heat is transferred when the sections of the pipe act as an evaporator and condenser within a wicked, sealed pipe. The fluid inside undergoes constant phase change to transfer heat from the evaporator to the condenser. The fluid within the pipes changes from a fluid to a gas in the evaporator section, absorbing the thermal energy from the warm airstream. The gas condenses back to a fluid in the condenser section where the thermal energy is dissipated into the cooler airstream, raising the temperature. The fluid/gas is transported from one side of the heat pipe to the other through pressure, wick forces or gravity, depending on the arrangement of the heat pipe, as shown in Figure 2-23.

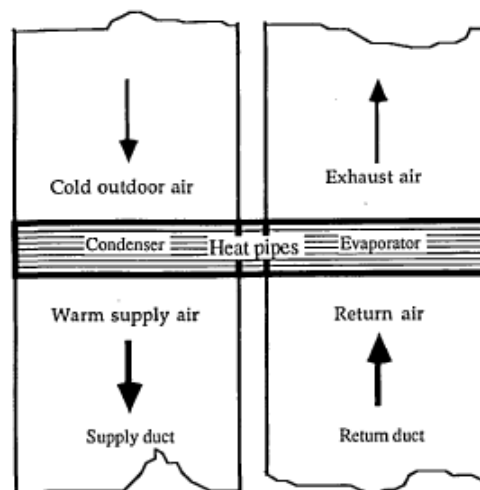


Figure 2-23 – Schematic representation of heat-pipe heat recovery unit in operation [139]

Liu *et al.* [140] reported that heat pipes are an effective method of heat transfer with a varying level of efficiency depending on the fluid mixture used. Two airstreams can be completely separated with zero risk of the flows mixing; this prevents cross-contamination, which is essential in applications such as the food industry and hospitals. No moving parts within the systems results in high reliability, low maintenance and a compact system that can be accommodated easily. As the fluid is free to flow around the heat pipes, the system is capable of recovering heat in both directions, cooling or warming air as necessary depending on the indoor and climatic conditions. The study showed that finned pipes

provide the highest efficiency. This is because of the greater contact surface area between the heat pipe and the air.

As there are no moving parts, no noise pollution generated and high transfer efficiency, heat pipes are suitable choices of heat recovery devices. Heat pipes are capable of sensible heat recovery only. Latent heat recovery is not presently possible; this limits the applications of heat pipes. Srimuang and Amatachaya [141] investigated the application of heat pipes for heat recovery. The work documented the advantages for energy saving and reduced greenhouse gas emissions in industrial applications and potential applications in other sectors. In the same study, Srimuang and Amatachaya [141] examined new types of heat pipe that have been developed. Two-phase closed thermosiphon (TPCT) and oscillating heat pipes (OHP) operate in similar ways to conventional heat pipes, but the method of transport of the internal fluid differs. TPCTs operate using gravity to transport heat when the evaporator section is located below the condenser. This means that the orientation of TPCTs is fixed and the operation is not reversible in both directions. However, TPCTs lack the internal wicking material that makes transport possible in conventional heat pipes but can cause internal resistance to heat transfer, reducing efficiency. OHP transfer heat through capillary action. Turns in the continuous pipe sit within the different airstreams. Evaporation occurs within the tube, forming bubbles that drive flow due to the increase in pressure. These bubbles condense when subject to the cooler airstream, transferring heat. Examples of OHPs can be seen in Figure 2-24. The authors noted that OHPs are cheap to manufacture and have good efficiency.

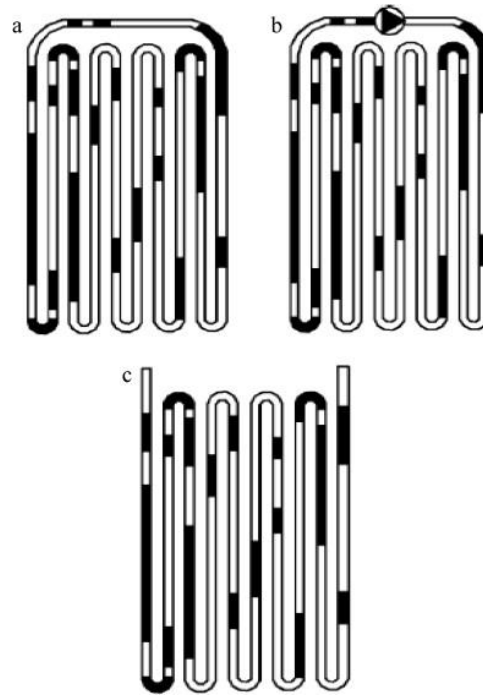


Figure 2-24 - Types of oscillating heat pipes [141]

A number of teams have conducted theoretical and experimental research into heat pipes. Gan and Riffat [139] conducted CFD analysis to understand the pressure drop on an airstream caused by a heat pipe heat recovery system. The most obvious cause of a pressure drop is due to the blockage caused by the physical presence of heat pipes in the ducts, restricting the area through which the airstream can pass. Finned pipes and smaller spacing further increase this effect. The authors found that an indirect cause of the pressure drop comes from the reduced temperature difference between the supply and exhaust air streams after the heat recovery.

Hughes *et al.* [30] completed CFD modelling to determine the most effective arrangement of heat pipes. Both the pitch and distance between heat pipes was varied along with a horizontal or vertical arrangement. This was done to determine which arrangement resulted in the highest heat recovery. Using pure water as the phase change material in the pipes, the distance between the heat pipes relative to each other was altered as well as the number of rows. The optimal pattern of heat pipes determined as a pitch of 0.035m between centres. In this configuration, pre-cooling recovery was calculated at 15.6°C in hot, dry climates modelled to represent conditions similar to the UAE. Pre-heating was calculated at 3.3°C across the heat pipes for milder temperatures, more similar to a climate such as the UK. The results of this study showed that using heat pipes for pre-conditioning of air was possible, for both heating and cooling. As heat pipes are a passive system, no energy input was required for pre-conditioning, highlighting the energy saving potential.

Calautit *et al.* [142] used a similar methodology when modelling heat pipes in a vertical and horizontal arrangement with the pattern described above. This analysis yielded similar results in terms of temperature drop. Reductions in incoming airstream flow rate of 7% and 10% were observed when the heat pipes were arranged in a vertical and horizontal arrangement respectively. Whilst the reduction in internal flow rate is noticeable, it was not sufficient to prevent proper supply rates being provided into the ventilated space.

El-Baky and Mohamed [143] indicated that as the outdoor air temperature increases, the temperature change for both the inlet and exhaust air increases. This led the authors to the conclusion that the highest working efficiency of a heat pipe is achieved when the fresh air temperature is close to the operating temperature of the heat pipe fluid and the temperature difference between the inlet and exhaust airstreams is at its greatest. The authors also varied the ratio of mass flow rate between the inlet and exhaust air. The study tested inlet mass flow rates 1, 1.5 and 2.3 times that of the exhaust air mass flow rate. It was concluded by the authors that the variation in mass flow rate had a positive effect on the evaporator airstream and a negative effect on the condenser airstream. This suggests that increasing the mass flow rate of an airstream has a positive effect on the efficiency of the heat pipe heat exchanger.

Heat pipe heat exchangers are a passive heat recovery device that are capable of transferring heat from one airstream to another with an efficiency up to 80%. Researchers have investigated heat pipes, exploring the parameters to maximise the efficiency. The orientation between horizontal and vertical, the spacing between each unit and the geometry of the pipes are important in determining the heat transfer effectiveness. The temperature of the inlet air was seen to have the greatest effect on the heat transfer from one airstream to the other. The greater the inlet air temperature, and the greater the difference between inlet air temperature and exhaust air temperature, the higher transfer was achieved. Research also showed that heat pipes had a low effect on the pressure drop of airstreams passing through them. This is important in ventilation practices as high pressure drop would reduce the supply ventilation rates.

2.6.5 Run-Around Systems

Run-around systems are a hybrid heat recovery system that incorporates characteristics from other heat recovery technology to form a single device, capable of recovering heat from one air stream and delivering to another a significant distance away. Vali *et al.* [144] showed the general configuration of a run-around heat recovery unit. Two fixed plate heat

exchangers are located in two separate airstreams and are linked by a closed loop containing a fluid that is continually pumped between the two heat exchangers. Vali *et al.* noted that the fluid is heated and cooled continuously as it flows around the loop. The constant flow of the fluid within the loop provides heat recovery. A schematic of a run-around system is shown in Figure 2-25. The constant flow of the fluid through the loop requires pumps to move between the two heat exchangers. Though this is an additional energy demand, using pumps to circulate fluid is less energy intensive than fans to circulate air.

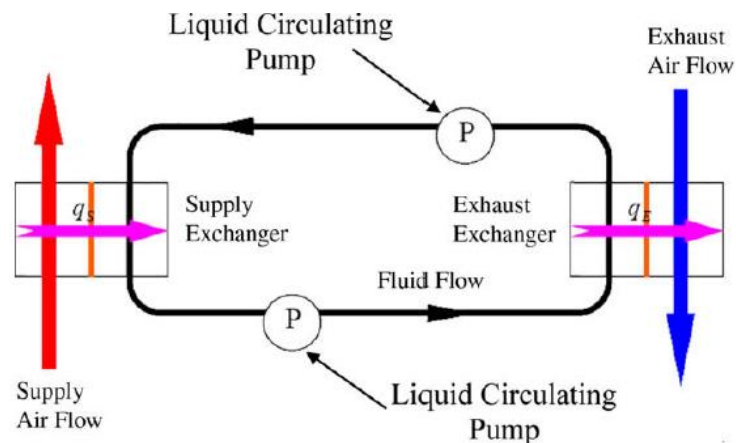


Figure 2-25 – Schematic diagram of a run-around heat recovery system [144]

Hviid and Svendsen [145] designed a simple system to experimentally test the pressure loss of a run-around heat recovery system. It was shown that using two separate air-to-liquid heat exchangers connected by a liquid loop, a pressure loss of 0.74Pa could be attained for a system with 75.6% temperature efficiency. It was shown that the frictional losses within the fluid loop are the most significant factor for determining the size and energy consumption of the pump needed. This work was furthered by Davidsson *et al.* [146] by increasing the efficiency of the systems for a small increase in pressure loss. A temperature efficiency of 80% was made possible with a 1Pa pressure loss measured across the heat exchanger. This demonstrated that efficient heat recovery in passive ventilation systems may be possible by limiting pressure loss.

A number of attempts to improve the design of run-around systems have been conducted by focussing on the fixed plate heat exchangers used in the system. Using a membrane based core in the fixed plate heat exchangers, Mahmud *et al.* [147] found that a total effectiveness of the system of 50-55% was achievable. Because a membrane fixed plate heat exchanger was used, both the heat and water vapour were transferred through the micro-porous layer. A different study by Wallin *et al.* [148] used a coil heat exchanger in place of the fixed plate heat exchanger and also compared the efficiency of a variable capacity heat pump. The coil

heat exchanger increased efficiency from 47% to 65% and the variable capacity heat pump increased the efficiency to 66%.

The combination of a cross and counter-flow plate heat exchanger, as previously discussed, was incorporated into a numerical model of a run-around heat recovery system by Vali *et al.* [144]. The new system design was validated against published literature and was accurate to $\pm 2.5\%$ for both individual exchangers and a system as a whole.

Due to the large size and necessary equipment for the installation of the equipment, retrofit of existing buildings to integrate run-around systems is difficult and expensive. However Emerson [149] showed that early integration into building design can alleviate these problems. Wang [150] stated that this is the most efficient and economical method of designing in a passive ventilation system with run-around heat recovery. Furthermore, these systems contain the heat recovery system within the ductwork that would normally be associated with mechanical ventilation, adding no substantial architectural features to the building.

Run-around systems combine two technologies into a single configuration for heat recovery. Incorporating two fixed plate heat exchangers, connected by a closed loop, two or more airstreams that are not positioned adjacent to one another can be joined for heat transfer. The fixed plate heat exchangers transfer heat to and from the airstream and the loop acts as an intermediary. The high efficiency and low pressure drop of the system mean that high heat transfer can occur and does not impede the ventilation supply rates. Only sensible heat transfer is possible however, latent heat transfer does not occur. As the airstreams do not have to be located adjacent, this gives the system greater flexibility compared to other heat recovery system. However, the flexibility also requires ductwork to accommodate the loop, taking up significantly more room than other systems.

2.6.6 Phase Change Materials

Phase change materials, commonly referred to as PCMs, are a technology that is used to store sensible and latent heat within the structure of the material. PCMs have been increasingly investigated by researchers due to the ability to store energy at a higher storage capacity than standard building materials. By mixing PCMs into common building components and materials, researchers have been also to study the ability to store heat and transfer heating and cooling demands from conventional peak times to off-peak times. Baetens *et al.* [151] and Farid *et al.* [152] have completed reviews of existing literature that

investigate the type of heat storage, classification of PCMs, suitability in buildings and applications to give a broad understanding of PCMs.

Parameshwaran *et al.* [153] analysed PCM thermal energy storage systems in significant detail. Thermal energy storage systems offer the ability to transfer heating and cooling energy from peak time to off-peak times, reducing energy consumption. The authors noted that though PCM components are expensive, the cost of integrating thermal energy storage systems can be offset the earlier that the systems are integrated into building design. The investigation explored a number of parameters affecting PCM use. The two primary types of technology, latent heat energy storage (LHES) and cool thermal energy storage (CTES) were assessed. Given the current research being undertaken and the integration of the technology architecturally, performance assessments of buildings utilising thermal energy storage systems were all explored. Parameshwaran *et al.* [153] concluded by recommending an outline for effective use of thermal energy storage systems in high performance buildings.

Kelly [154] reported that phase change materials can be classified into three main groups; organic compounds, inorganic compounds and inorganic eutectics. Each of these groups has different characteristics which are advantageous and disadvantageous for heat storage applications. PCMs store and release thermal energy by cycling between solid and liquid states as the ambient temperature fluctuates; this process is shown in Figure 2-26. As the temperature rises, the materials changes from solid to liquid, this process is endothermic and so absorbs heat from the ambient air, reducing the local air temperature. As the air temperature reduces, the PCM solidifies and the thermal energy is output to the environment, increasing the local temperature.

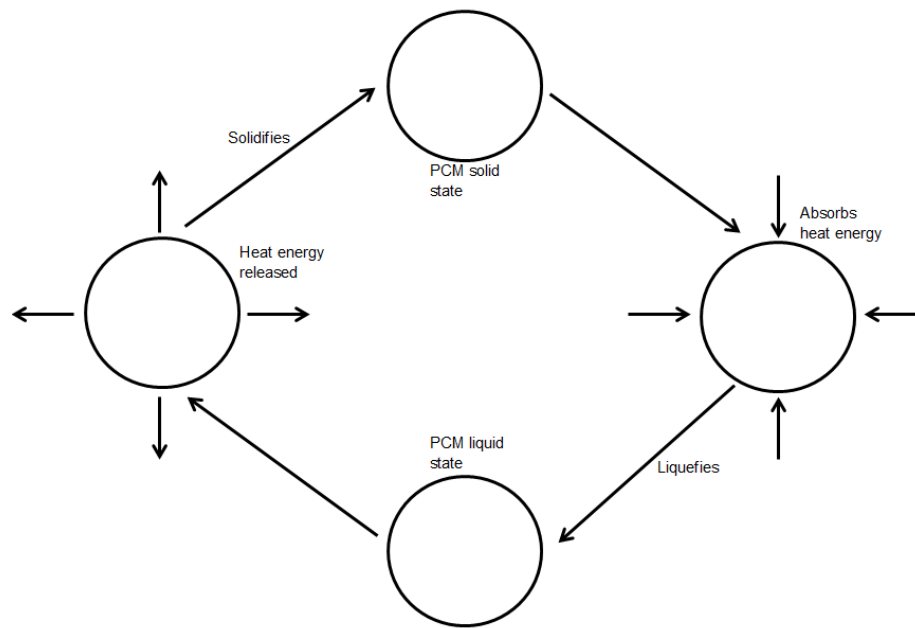


Figure 2-26 – Schematic diagram of heat transfer process of PCMs [154]

This highlights the potential for PCMs to alter the ambient air temperature to more comfortable levels for occupants by cooling or heating the air in a reactive way to climate conditions. By offsetting heat gains during the hottest time of the day, the energy demand on cooling systems would be reduced. This adheres to the concept of thermal lag. As the air temperature drops, the PCM solidifies, releasing heat back to the environment. This is advantageous, particularly in buildings that have occupancy schedules. Commonly, the temperature would reduce once occupants have left, when the release of the heat from the PCM would not affect thermal comfort. This encourages lower energy demand for HVAC systems and requires no energy input for activation.

Kauranen *et al.* [155] noted that the melting and freezing temperatures of the PCMs must be carefully matched to the local climate conditions to ensure the maximum efficiency from the system. The different groups of PCMs have a wide range of melting and freezing points, as shown in Figure 2-27. It is beneficial to select the appropriate group for the local climate. Organic PCMs are generally chemically stable, non-corrosive, non-toxic, do not suffer from supercooling and have a high latent heat of fusion.

The most common organic PCM is paraffin wax. An inexpensive PCM has a wide range of melting temperatures, 20-70 ° C, depending on the composition. However, due to low thermal conductivity, 0.2W/(m . K), and large volume change, up to 70%, there is limited application for paraffin waxes in building materials and components. Inorganic PCMs are phase change materials that are not naturally occurring, such as hydrated salts, but have

properties that make them suitable to store and transfer thermal energy. A high heat of fusion, good thermal conductivity and inexpensive material costs suggest that inorganic PCMs are the ideal material for thermal storage. However, they are corrosive to metals and undergo supercooling and phase decomposition. Eutectic mixtures are multiple solids in various ratios to keep the melting point as low as possible. [151]

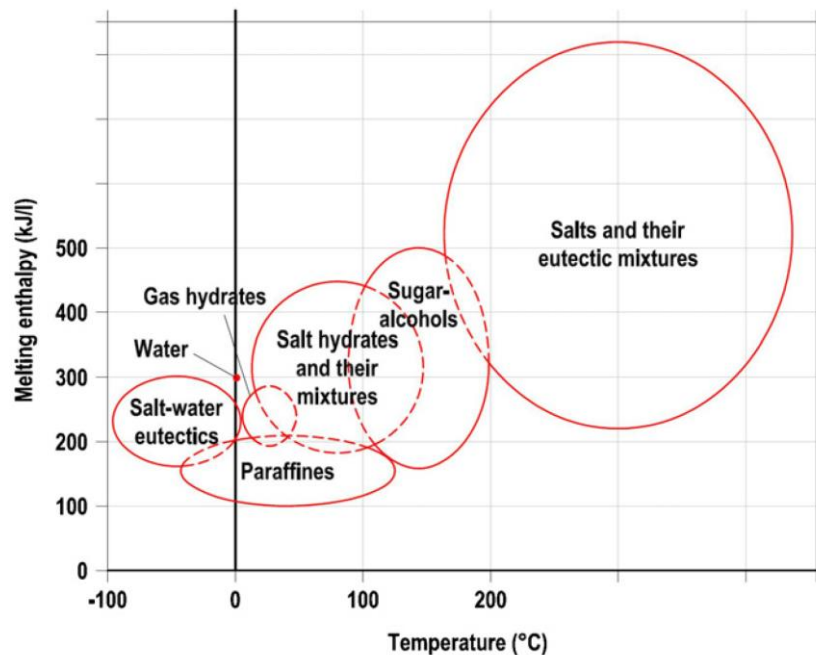


Figure 2-27 – The melting enthalpy and melting temperature for the different groups of phase change materials. [151]

The concept of thermal mass of a building for heat storage, that the physical structure of the building absorbs heat to help cool the air, has long been understood and investigated. A study by Feldman *et al.* [156] of PCMs in comparison to traditional building materials has shown that the thermal storage capacity of PCMs is twelve times higher than standard building materials over the same temperature range. The sensible heat of the wallboard tested was 31kJ for a 1m² piece for a 3.5°C temperature change, compared to 381kJ/kg for the combined material. This would improve the effect of thermal lag without impacting building materials or construction methods.

The pressure drop on airstreams across PCMs has not been investigated to be able to comment on the effect that the material may have. As the PCM can be incorporated directly into the building structure, this would not affect the flow in the same way other heat exchanger technologies do, it can be suggested that there is no pressure loss created by the inclusion of PCMs in the building fabric. This gives PCMs a significant advantage over other heat recovery device and integration into ventilation systems would not be necessary. Alternatively, PCMs could be built directly into the construction of the ventilation system

that would incur no pressure drop. However, as PCMs are integrated into building materials and components, it would be logical to ensure that the majority of the material was located close to the inlets and exhausts of the building. This would ensure that the maximum heat transfer were possible.

2.7 Applications of HRV in Passive Ventilation

The most common heat recovery devices have been identified and examined based on the effectiveness and potential for integration into passive ventilation systems. The key parameter for successful integration with passive ventilation is a low pressure drop. As passive ventilation systems do not generate high air velocities, a high pressure drop cannot be overcome and low supply rates would result.

The integration of heat recovery devices by researchers is explored in the following section. The studies are assessment on the type of device that is integrated, how it was integrated and the result of the study. A number of the studies focus on the integration of the device with a wind tower system. This is a common passive ventilation system that is capable of delivering the recommended ventilation supply rates without any energy demand.

2.7.1 Application of rotary thermal wheel

O'Connor *et al.* [157] studied the effect that a rotary thermal wheel had on the supply air flow rates in to a building when integrated into a wind tower ventilation system. A CFD model was created to simulate the effects on supply airflow rates. The CFD simulation was validated by a scale model experiment conducted in a closed-loop subsonic wind tunnel. The external air velocity was altered to test a range of operating conditions for the combined system. The velocity of the air below the rotary wheel was measured; this provided a useful measurement that could easily be compared. From the air velocity, the flow rates were calculated and values from the CFD and experiment were compared. Although the flow rates were reduced compared to a wind tower that did not include a rotary thermal wheel, the guideline ventilation rates for occupants in a school or office building were met when the external wind velocity was 3m/s and above, this is lower than the average wind speed of the UK (4-5m/s). The calculated air supply rates are shown in Figure 2-28 and compared with the guideline supply rate. Though the results show that the ventilation rates were achieved below the average wind speed, it should be noted that instances where the wind speed is not reach would occur frequently due to the variation in wind speeds.

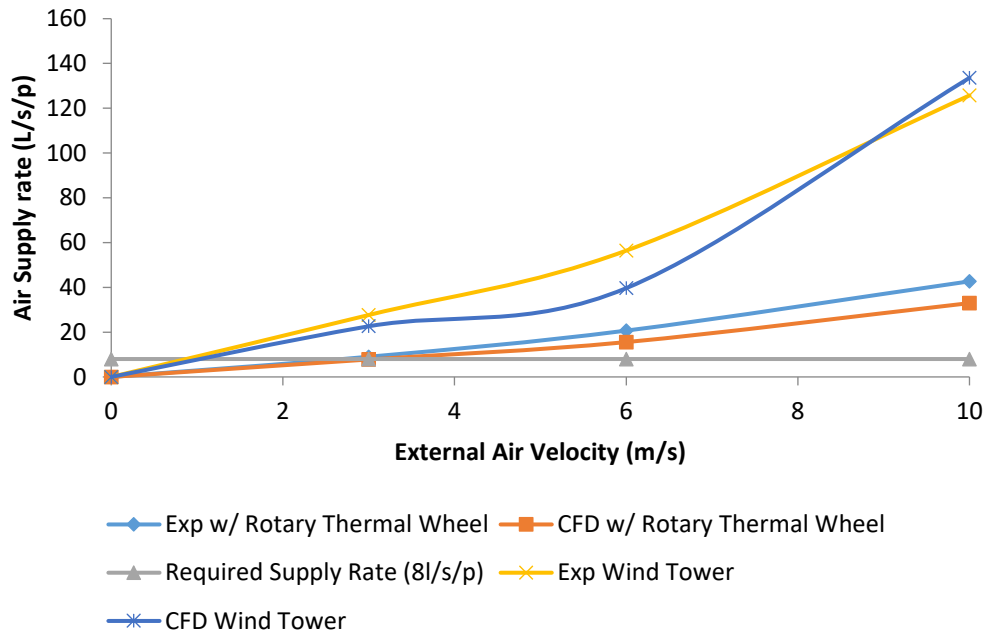


Figure 2-28 – Comparison of air supply rate for a wind tower and a wind tower with a rotary thermal wheel against the guideline supply rate of 8l/s/p. [157]

No full-scale experimental or field test data was completed in this study; therefore, it cannot be conclusively proved that rotary thermal wheels are entirely suitable for integration into a commercial wind tower system. However, despite the reduction to airflow rates in the building after the integration of the rotary thermal wheel, the reduction was not large enough to prevent the ventilation guideline rates being met.

Sufficient research has not yet been conducted to determine the suitability of rotary thermal wheels in natural ventilation, ventilation supply rates can be met but the thermal capabilities of the rotary thermal wheel have not yet been investigated. Further work would be beneficial to increase understanding of the system.

2.7.2 Application of Fixed Plate Heat Exchangers

Mardiana *et al.* [158] integrated a fixed plate heat exchanger into a wind tower passive ventilation system, highlighting the advantages of this type of system as a means of zero energy ventilation which can be simply modified. Full-scale laboratory testing was undertaken in order to determine the effect on the supply airflow and the efficiency of the combined system. The wind tower integrated with the heat exchanger was mounted centrally on a sealed test room. The experimental setup can be seen in Figure 2-29. The external conditions of the wind tunnel were varied, the external wind velocity and air temperature were modified to assess how the combined system performed under different conditions.

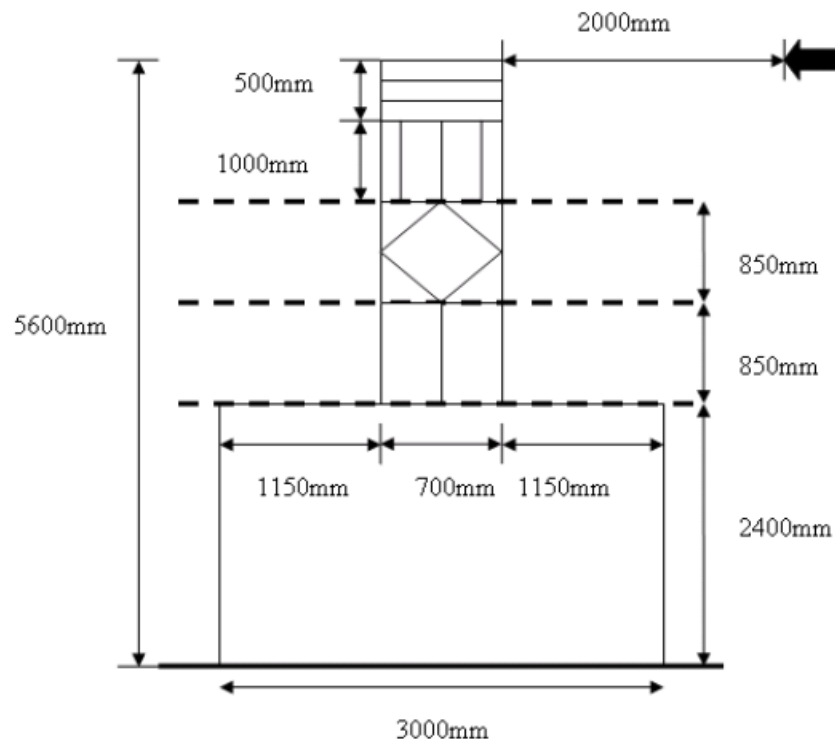


Figure 2-29 – The schematic diagram of experimental chamber and total dimension [159]

The results showed a number of factors were important to the efficient operation of the fixed plate heat exchanger. A maximum temperature change of 5.1°C and 4.6°C were measured for cold and warm air inlet streams respectively. An increase in temperature change was noted as the air velocity increased from 1.2m/s to 3.1m/s for both the warm and cold air inlet conditions. However, the efficiency of the heat exchanger in both conditions reduced. The efficiency reduced from 70% to 50% and 69% to 49% as the external air velocity increased from 1.2m/s to 3.1m/s for the cold and warm air inlet streams respectively. This was due to the shorter contact time between the air and the heat exchanger because of the increased air velocity. It was observed from the experiment that for the warm inlet air, the air temperature reduced as it entered the wind tower. This highlights the system's properties as a means of providing thermal comfort in a warm environment through passive cooling.

The pressure drop across the heat exchanger was measured as the inlet air velocity increased. Pressure drop increased from 7Pa to 30Pa as the inlet air velocity increased from 1.2m/s to 3.1m/s. Ventilation supply rates were not investigated in the paper. However, due to the high pressure drop, it is likely that a significant reduction in air supply rates would occur compared to a wind tower without the fixed plate heat exchanger.

The results from this study indicated that the combination of a wind tower passive ventilation system and a fixed plate heat recovery device could provide an effective combined technology to recover waste heat from exhaust air and cool incoming warm air

with zero energy demand. Though no quantitative data for the ventilation rates within the test room was provided, it can be assumed that due to the high pressure loss across the heat exchanger that these were significantly reduced from standard operation of a wind tower. Further investigation of this combined of technology is essential in understanding the air flow characteristics of the system.

2.7.3 Application of Heat Pipes

More research has been conducted into the integration of heat pipes into passive ventilation than other heat recovery systems. This is due to the low pressure drop to airstreams caused by heat pipes, making the technology a more attractive option for research and development. Wind towers were again used as the passive ventilation system for integration with this heat recovery technology. This further highlights the suggestion that wind towers provide a suitable alternative to mechanical HVAC systems, capable of supplying and exhausting air at the same time.

Shao *et al.* [27] investigated the use of heat pipes in a passive stack ventilation system. A laboratory model was conducted, using lamps and bulbs to generate heat for buoyancy driven flow through the model building structure. Four different heat pipes with different internal fins were tested in order to determine which the most effective heat transfer device was over a range of inlet air velocities. It was found that louvered fins within a heat pipe provided the most efficient heat transfer compared to the other prototypes over the range of air velocities. Further to this, it was noted that increasing air velocity had a negative effect on the thermal efficiency of the heat pipes. As velocity increased, the efficiency decreased. This is due to the reduced contact time between the heat pipe and air, as noted in other studies previously.

Calautit *et al.* [160] used CFD analysis to determine the effectiveness of heat pipes in reducing air temperature in a single-sided wind tower with varying tower height and different fluid types within the heat pipes. Water and ethanol were the two types of fluid that were tested within the heat pipes during the analysis. The heat pipes were also compared to an evaporative cooling system, which was commonly used in traditional bau-d-geer ventilation stacks.

Based on the measured heat transfer rates to the evaporator and condenser sections of the heat pipes, water provided better temperature reduction and heat transfer compared to ethanol. The variation in the wind tower height was not a significant factor in the change in air temperature experienced as air flowed down the wind tower. This is likely due to the

equal contact time between the air and the heat pipes, regardless of the wind tower height. A more compact system using a smaller tower has the same efficiency as a taller tower. The arrangement of horizontal heat pipes within the wind tower reduced the incoming air temperature by 12-15K with a small pressure loss of 5Pa across the heat pipe heat exchangers as can be seen in Figure 2-30.

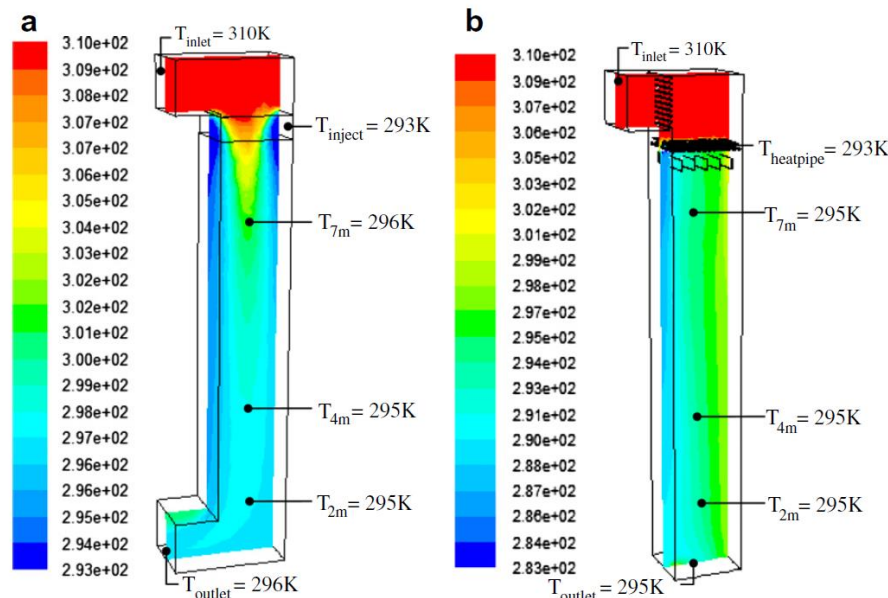


Figure 2-30 – Temperature contour lines of a cross sectional plane in the test channel; (a) evaporative cooling (b) heat pipe device [160]

Riffat and Gan [161] conducted a study of heat pipes for heat recovery in passive ventilated buildings. A laboratory experiment containing a passively ventilated two-zone chamber was constructed which ran alongside a CFD model of the same geometry and dimensions. The CFD model determined that the low pressure drop across the heat pipes, which was difficult to measure in the laboratory experiment. Three different types of heat pipe were tested. The results from the study showed that plain finned pipes in a horizontal, staggered arrangement were the most efficient at transferring heat from one airstream to the other, similar to the arrangement used by Calautit *et al.* [160]. Finned pipes that were arranged in a single line were less efficient due to the reduced contact time between the heat pipes and the air. Though the results presented the optimum configuration of the heat pipes, it was noted that the pressure loss across the bank of heat pipes was the limiting factor in delivering adequate ventilation.

This work was continued by the same team, who then investigated the effect of a solar chimney on the ventilation and heat recovery [162]. By using a solar chimney to warm the

air through different glazing options, it was found that the ventilation rate increased as the chimney wall temperature increased. However, when heat pipes were included in the design in an attempt to recover the thermal energy in the air, it was found that the thermal buoyancy effect was reduced, limiting the ventilation rates. Because of this finding, it was concluded that buoyancy driven passive ventilation in a building would require manipulation of external wind forces to drive ventilation.

2.7.4 Application of Run-Around Systems

Flaga-Maryanczyk *et al.* [163] conducted a study in Sweden which examined a passive ventilation system which integrated a run-around system using a ground source heat pump as the heat source to warm incoming air. A schematic of the design is shown in Figure 2-31.

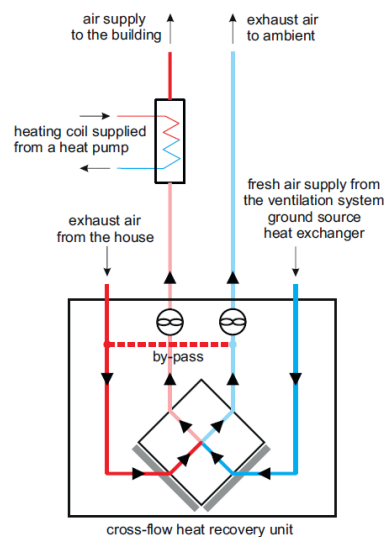


Figure 2-31 – The schematic view of the ventilation system in the passive house [163]

Experimental measurements and weather data were taken from the passive house used in the study. A CFD model of the passive house was created with the measurements taken from the sensors and weather station used as input data. The model was run to calculate the effectiveness of the run-around system and the capabilities of the ground source heat pump.

Ground source heat pumps provide a reliable source of consistent thermal energy when buried 10-20m below the ground surface. The ground temperature is warmer than ambient air in winter and cooler than ambient air in summer, providing both heat source and heat sink. It was found that in February, the coldest month in the climate, that the ground source heat pump was capable of delivering almost 25% of the heating needs of the house and occupants. This reduces demand on the heating system by a significant amount, thereby saving the homeowner energy costs. Scaling of this approach would save users a substantial

amount of money over the year. The work did not include an analysis of the potential greenhouse gas savings from the reduced energy demand.

2.7.5 Application of Phase Change Materials

The majority of research interest in PCMs is the application of phase change material integration into traditional porous building materials such as concrete and wallboards. Kosny *et al.* [164] analysed the thermal performance of buildings which have PCM-enhanced construction materials within the structure. Analysis showed that the addition of PCMs is beneficial in terms of improving the thermal performance and increasing the thermal lag effect.

PCMs can be added to building materials either through direct incorporation at the mixing level or by immersing the building materials in PCMs. Feldman *et al.* [156] found that direct incorporation is the preferred method of addition as only one additional step is required to the mixing process of the materials and shows better heat storage compared to immersion. Though PCMs have a large potential for heat storage, poor thermal conductivity limit the heat transfer rates that are attainable. The enhancement of the heat transfer potential of PCMs was explored by Velraj *et al.* [165] and Stritih [166]. Various methods to increase the charge/discharge rate of heat were investigated by the addition of modifying components compared to standard PCMs. Modifying the components increased the charge/discharge rate of the PCMs, the addition of fins within the PCM was found to be the most influential modification by increasing the contact area between the PCM and the air.

At present, the use of PCMs in passive ventilation systems is extremely limited. The only significant application is the Cool-Phase ventilation system. The Cool-Phase system, shown in Figure 2-32 is a hybrid ventilation system that uses PCMs in thermal batteries to cool incoming air from the external environment before diffusing it into the occupied spaces after occupants have left. The system relies on mechanical, low energy fans to circulate the air through the ducts and across the PCM thermal batteries. The system is quoted as capable of reducing energy use by 90% by replacing conventional HVAC systems which require more energy intensive processes [167].

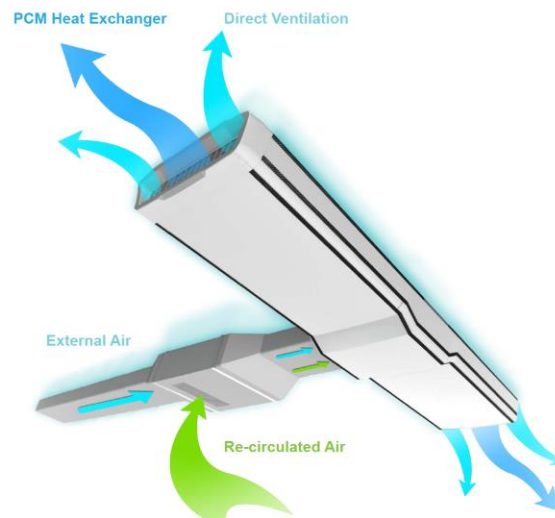


Figure 2-32 – Schematic diagram of operation of Cool-Phase system [167]

A significant drawback of PCM use in a passive ventilation system for heat recovery is the lack of instantaneous or fast heat transfer across different airstreams. Phase change materials are a heat storage technology, whereby the heat is stored within the PCM until the air temperature has fallen to a significant level where it can be released back into the air stream. No research has been conducted into the use of PCMs between two airstreams of different temperature where continuous, instantaneous heat transfer can occur. An investigation into this area would be beneficial for passive ventilation heat recovery research.

2.7.6 Heat Recovery Integration

An overview of the heat recovery technology and their applications that have been explored in this review has been collated in Table 2-5. The heat recovery devices are compared by general advantages and disadvantages, efficiency range, pressure drop, humidity control and energy saving potential. The efficiency is defined as the ability to effectively transfer heat from the source airstream, to the sink airstream, increasing the temperature. Analysing the heat recovery devices in this way means that the most suitable selection for integration into passive ventilation systems can be completed more easily.

Table 2-5 – Summary and details of heat recovery devices

Type of HRV	Advantages	Disadvantages	Performance Parameters	Efficiency %	Pressure Drop (Pa)	Humidity Control	Ref
Rotary thermal wheel	High efficiency Sensible and latent heat recovery Compact design Frost control available	Cross contamination possible Requires adjacent airstreams Mechanically driven, requiring energy input	Rotation speed Air velocity Wheel Porosity	80+	4-45	Yes	[38,102,107–116,123]
Fixed Plate	No moving parts hence high reliability High heat transfer coefficient No cross contamination Compact design Frost control possible Sensible and latent heat recovery	High pressure loss across exchanger Limited to two separate airstreams Condensation build up Frost build up in cold climates	Material type Operating pressure Temperature Flow arrangement	70-90	7-30	Yes	[39,101,102,122,125–128,130–137,158]
Heat pipes	No moving parts, high reliability No cross contamination Low pressure loss Compact design Heat recovery in two directions possible	Requires close airstreams Internal fluid should match local climate conditions	Fluid type Contact time Arrangement/configuration Structure	80	1-5	No	[27,30,138–140,142,143,160–162]
Run-around	Airstreams can be separate No cross contamination Low pressure loss Multiple sources of heat recovery	Multiple pumps required to move fluid Difficult to integrate into existing structures Low efficiency Cost	Exchanger type Fluid type Heat source	50-80	~1	No	[144–150,163]
Phase Change Materials	Easy incorporation into building materials Offset peak energy demands No pressure loss No cross contamination No moving parts Long life cycle	Thermal storage as opposed to instantaneous transfer Expensive Not proven technology Difficulty in selecting appropriate material	Material type Impregnation method	~	0	No	[151,152,154–156,164–167]

Each of the reviewed heat recovery technologies are currently disadvantaged by the high pressure drop experienced when air moves across/through them. This is an important consideration with regard to integration into passive ventilation systems. The pressure drop must be kept as low as possible. CFD analysis has shown the heat pipes have a low pressure drop across the exchanger when the pipes are positioned in an optimised arrangement, 50mm centre to centre distance in the horizontal and vertical directions.. Rotary heat wheels, using scale model testing and CFD analysis, have a pressure loss of similar magnitude to heat pipes at low inlet air velocity. However, run-around systems have a low pressure drop, the large ducting and arrangement of the system is unsuitable for passive ventilation. Furthermore, the low efficiency of the system prevents worthy energy savings due to the energy required by the pumps to move the fluid around the system. Fixed plate heat exchangers are a reasonable heat recovery device for passive solutions. However, integration with a four-sided wind tower is the overall goal. At present, fixed plate heat exchangers only operate between two airstreams.

To maximise energy savings, efficient transfer of heat is required. Heat pipes and rotary thermal wheels provide the highest temperature efficiency. Rotary thermal wheels also provide the added benefit of latent heat recovery and moisture control. Latent heat recovery has been shown to increase the effectiveness of heat recovery devices when coupled with sensible heat recovery.

Rotary wheels and heat pipes can be further enhanced by focussed research into the design of each system. With further research and development of the matrix structure, optimal length of the wheel and the rotation speed, the pressure drop across the wheel may be reduced to levels where passive ventilation is capable at higher inlet air velocities. Heat pipes are capable of high heat transfer rates with a moderately low pressure drop compared to other technology. Further research into the optimum shape and arrangement of heat pipes would provide a suitable technology for integration into passive ventilation systems. Both systems are capable of transferring energy in both directions, summer cooling and winter heating would be possible within a single system providing year round ventilation and thermal comfort.

Analysis of currently literature suggests that the heat recovery devices with the most potential for integration into passive ventilation systems are rotary thermal wheels and heat pipes.

2.8 Summary

The continuous supply of fresh air and exhausting of stale internal air is the most effective way to maintain IAQ, protecting occupant health from the adverse effects of Sick Building Syndrome (SBS). Commonly, this is achieved with mechanical Heating, Ventilation and Air-Conditioning (HVAC) systems. However, a large energy demand is required to operate these systems. Passive ventilation systems offer an alternative ventilation technology to mechanical HVAC systems without the energy demand required.

Passive ventilation systems rely on natural driving forces to circulate fresh air around a building. Though passive ventilation systems are capable of delivering the required supply rates for good IAQ, the temperature of the incoming air is completely dependent on the external conditions. When the outdoor temperature is not at a level to provide thermal comfort to occupants, the use of passive ventilation systems becomes limited to the seasons with moderate temperatures. The use of passive ventilation in winter months in climates similar to the UK would result in high demand on heating systems, potentially offsetting savings from the replacement of mechanical HVAC.

Heat recovery is a technology that has the potential to reduce the energy demand for heating and cooling within buildings by recovering energy from exhaust air in winter months for heating and cooling incoming air in summer months. Heat recovery devices are currently integrated with mechanical HVAC systems. Little work has been completed to integrate heat recovery devices into passive ventilation systems. This would reduce the energy demand needed to condition the air, and remove the energy demand needed to ventilate buildings mechanically.

Integrating heat recovery technology into passive ventilation systems relies on the pressure drop across the heat exchanger remaining as low as possible to prevent reduction in air supply rates. Of the heat recovery technologies reviewed, rotary wheels and heat pipes are the most feasible options for integrating into passive ventilation systems. High efficiency and the ability to transfer both sensible and latent heat are advantageous. Though the present design of rotary thermal wheels and heat pipes do not fulfil the criteria required for integration into passive ventilation systems, further research may make this possible. Further study could lead to an integrated passive ventilation system with heat recovery, resulting in a system capable of lowering the energy consumption of a number of types of building in a number of climates.

2.9 Research Gap

This chapter provided a review of passive ventilation and heat recovery devices. The review covered research topics that included indoor air quality, passive ventilation techniques, wind tower design and development, heat recovery devices and the integration of these devices into passive ventilation systems. The reviewed covered literature that investigated each of the research topics, focusing on numerical and experiment based studies. Based on the previously published work reviewed, a number of outcomes can be concluded:

1. Ventilation is required to provide good indoor air quality (IAQ) to occupants and reduce instances of sick building syndrome (SBS) [41,42,44]
2. Computational Fluid Dynamics (CFD) analysis is a suitable method for simulation of passive ventilation and heat recovery technologies [55,58,59]
3. Validation of CFD analysis using experimental models in wind tunnels is recommended and a commonly used technique [19,26,91]
4. Wind towers are a practical solution to provide passive ventilation to occupied spaces [14,81,84]
5. Heat recovery is an area of technology that can provide substantial energy savings to building operators [102–104]

The literature review provided understanding of wind tower development and the potential for heat recovery technology integration. Following the literature that has been reviewed, several gaps in current research have been identified:

1. No studies have been completed that show the use of wind towers integrated with heat recovery technology.
2. No attempts exist that have attempted to modify rotary thermal wheels to reduce the pressure drop experienced by airstreams.
3. No investigations exist that have attempted to adapt existing rotary thermal wheels for a wind tower ventilation system.
4. No data is available for the heat recovery rates from a rotary thermal wheel when integrated into a wind tower system.
5. No work had explored the integration of a dehumidification device into a wind tower ventilation system.

In order to fill the research gap that has been identified, numerical Computational Fluid Dynamics analysis and prototype experimental testing will be undertaken to create a novel rotary wheel that incorporates a low pressure drop matrix. This will enable integration of heat recovery into a passive ventilation system, which has not yet been completed.

Chapter 3

3 CFD Methodology: Theory and Modelling

3.1 Introduction

Computational Fluid Dynamics (CFD) is a method of modelling flow conditions that uses partial differential equations to solve equations relating to fluid flow in an iterative manner. The geometry of a flow regime is broken down into individual cells, known as a mesh, wherein equations are solved to generate an understanding of the fluid flow. Data from each cell generates and receives data from adjoining cells in a cyclic manner until a stable solution is found, when values within the cells become constant or the change in iteration falls below a predetermined value. As described in Chapter 2, the development of CFD analysis over previous decades has enabled engineers and designers to model unconventional geometry and simulate complex flow patterns.

This chapter provides a brief overview of the theoretical principles that underpin Computational Fluid Dynamics and how these principles interact to provide a solution. Furthermore, the method and process of developing CFD analysis is shown. This process highlights the work path undertaken in this study.

3.2 CFD Principles and Theory

3.2.1 Governing Equations

CFD solvers generate solutions for partial differential equations that relate to various aspects of the flow. Because of the method in which fluid flows, conservations of these properties through the geometry is required. The conservation is handled by the equations interacting with each cell.

The CFD code used in this study, ANSYS Fluent, is amongst the most commonly used CFD software. The use of which has been very well established in literature, as acknowledged in Chapter 2. Due to this, the equations presented here relate to those used in FLUENT v15.0, taken from the ANSYS Fluent Theory Guide [168]. No attempts have been made to modify the standard governing equations provided in the theory guide. The mass and momentum equations are solved for all types of flow. The energy equation is required due to the heat transfer involved in the study. As the flow in the model will be turbulent, the Reynolds-

averaged Navier-Stokes (RANS) and the standard $k - \varepsilon$ model transport equations are required. The following governing equations used in the CFD models will be presented here:

- Mass Conservation Equation
- Momentum Conservation Equation
- Energy Equation
- Reynolds-Averaged Navier-Stokes Equation
- Standard k- ε Model Transport Equation
- Species Transport Equation
- Standard Energy Wall Functions
- Standard Species Wall Functions

3.2.1.1 Mass Conservation Equation

Mass conservation in flow is governed in the CFD models by the following equation:

Equation 3-1 [168]

$$\frac{\partial \rho}{\partial t} + \nabla \cdot (\rho \vec{v}) = S_m$$

The terms for the equation follow. ρ is the fluid density, t is time and \vec{u} is fluid velocity. Incompressible and compressible flows are valid. S_m represents the source term for the mass added to the continuous phase from the dispersed second phase [168].

Equation 3-2 [168]

$$\nabla = \frac{\delta}{\delta x} + \frac{\delta}{\delta y} + \frac{\delta}{\delta z}$$

3.2.1.2 Momentum Conservation Equation

The equation for momentum conservation:

Equation 3-3 [168]

$$\frac{\delta}{\delta t} (\rho \vec{v}) + \nabla \cdot (\rho \vec{v} \vec{v}) = -\nabla p + \nabla \cdot (\bar{\tau}) + \rho \vec{g} + \vec{F}$$

The definitions for the properties of the equation follow: p is the static pressure, $\bar{\tau}$ is the stress tensor, and $\rho \vec{g}$ is the gravitational body force and \vec{F} is external body force. Source terms for model-dependent properties are defined in \vec{F} [168].

The equation for the stress tensor $\bar{\tau}$ value is:

Equation 3-4 [168]

$$\bar{\tau} = \mu \left[(\nabla \vec{v} + \nabla \vec{v}^T) - \frac{2}{3} \nabla \cdot \vec{v} I \right]$$

μ is the molecular viscosity, I is the unit tensor. The effect of volume dilation is equal to $\frac{2}{3} \nabla \cdot \vec{v} I$ [168].

3.2.1.3 Energy Equation

The energy equation is used in CFD modelling to simulate heat transfer in the solutions. Conductive and convective heat transfer is the simplest heat transfer mechanism to model in CFD applications. The energy equation used can vary depending on the requirements of the simulation. The energy equation allows thermal conditions to be set at various boundaries including inlets, outlets and walls. Walls to which thermal conditions are not applied are treated as adiabatic with zero heat flux [169]. Therefore, it is important for properties of wall conditions and materials to be set properly.

Fluent solves the following form of the energy equation:

Equation 3-5 [168]

$$\frac{\delta}{\delta t} (\rho E) + \nabla \cdot (\vec{v} (\rho E + p)) = \nabla \cdot \left(k_{eff} \nabla T - \sum_j h_j \vec{J}_j + (\vec{\tau}_{eff} \vec{v}) \right) + S_h$$

k_{eff} is the effective conductivity ($k + k_t$) k_t is the turbulent thermal conductivity, this depends on the turbulence model being in the model. \vec{J}_j is the diffusion flux of species j . Conduction energy transfer is defined by $k_{eff} \nabla T$, species diffusion energy transfer by $h_j \vec{J}_j$ and viscous dissipation energy transfer is defined as $(\vec{\tau}_{eff} \vec{v})$. Heat gain caused by chemical reactions and volumetric sources are defined in S_h [168].

E is calculated as follows:

Equation 3-6 [168]

$$E = h - \frac{p}{\rho} + \frac{v^2}{2}$$

The equation for ideal gas sensible enthalpy h is:

Equation 3-7 [168]

$$h = \sum_j Y_j h_j$$

The species j mass fraction is Y_j . The equation for h_j is:

Equation 3-8 [168]

$$h_j = \int_{T_{ref}}^T c_{p,j} dT$$

In this study, a pressure-based solver is used, therefore $T_{ref} = 298.15$ K. T_{ref} varies due to the solver and models used [168].

3.2.1.4 Reynolds-Averaged Navier-Stokes Equation

The average and variable components of the properties of the Navier-Stokes equations are calculated from the instantaneous forms of the equations. The average values can be calculated from the ensemble-average or the time-average values. The values for the velocity properties are as follows:

Equation 3-9 [168]

$$u_i = \bar{u}_i + u'_i$$

Where \bar{u}_i is the mean component and u'_i is variable velocity components ($i=1, 2, 3$) [168].

For all other scalar quantities:

Equation 3-10 [168]

$$\varphi = \bar{\varphi} + \varphi'$$

φ represents scalar values such as mass, energy or pressure [168].

The ensemble-averaged momentum equations can be written in Cartesian tensor form. The flow variables are substituted into the instantaneous continuity and momentum equations. Taking a time or ensemble average from the instantaneous equations results in the following averaged equations:

Equation 3-11 [168]

$$\frac{\delta \rho}{\delta t} + \frac{\delta}{\delta x_i} (\rho u_i) = 0$$

Equation 3-12 [168]

$$\frac{\delta}{\delta t} (\rho u_i) + \frac{\delta}{\delta x_j} (\rho u_i u_j) = -\frac{\delta p}{\delta x_i} + \frac{\delta}{\delta x_j} \left[\mu \left(\frac{\delta u_i}{\delta x_j} + \frac{\delta u_j}{\delta x_i} - \frac{2}{3} \delta_{ij} \frac{\delta u_l}{\delta x_l} \right) \right] + \frac{\delta}{\delta x_j} (-\rho \overline{u_i' u_j'})$$

Equation 3-11 and Equation 3-12 show the Reynolds-averaged Navier-Stokes (RANS) equations. The Reynolds-averaged Navier-Stokes (RANS) equations differ from the

instantaneous Navier-Stokes equations, in that the solution variables represent averaged values as opposed to the instantaneous values. The average values can be based on time-averages or ensemble-averages. The RANS equations also include the terms $-\rho \overline{u_i' u_j'}$ that represent the effects of these Reynolds stress values [168].

3.2.1.5 Standard $k - \varepsilon$ Model Transport Equation

Whereas one equation turbulence models generally solve one transport equation, generally for turbulent kinetic energy, turbulent length and time scale are calculated in two-equation turbulence models by solving two separate transport equations. The standard $k - \varepsilon$ model is amongst the most popular two-equation models as it can be used successfully for a number of simulation types. Turbulent kinetic energy (k) and the turbulent dissipation rate (ε) are the two primary properties calculated and the equation is based on the transport equations of these. The exact equation for the turbulent kinetic energy is used for the transport equation, whereas the turbulent dissipation rate transport equation was obtained using physical reasoning [168].

The standard $k - \varepsilon$ model is only applicable for fully turbulent flow as the derivation of the equation assumes that flow is fully turbulent and molecular viscosity effects are negligible and so can be ignored [168].

The transport equations for the turbulent kinetic energy and turbulent dissipation rate are shown:

Equation 3-13 [168]

$$\frac{\delta}{\delta t}(\rho k) + \frac{\delta}{\delta x_i}(\rho k u_i) = \frac{\delta}{\delta x_j} \left[\left(\mu + \frac{\mu_t}{\sigma_k} \right) \frac{\delta k}{\delta x_j} \right] + G_k + G_b - \rho \varepsilon - Y_M + S_k$$

And

Equation 3-14 [168]

$$\frac{\delta}{\delta t}(\rho \varepsilon) + \frac{\delta}{\delta x_i}(\rho \varepsilon u_i) = \frac{\delta}{\delta x_i} \left[\left(\mu + \frac{\mu_t}{\sigma_\varepsilon} \right) \frac{\delta \varepsilon}{\delta x_j} \right] + C_{1\varepsilon} \frac{\varepsilon}{k} (G_k + C_{3\varepsilon} G_b) - C_{2\varepsilon} \rho \frac{\varepsilon^2}{k} + S_\varepsilon$$

G_k and G_b are the generation of turbulence kinetic energy due to the mean velocity gradients and buoyancy respectively. The overall dissipation rate affected by the fluctuating dilation in compressible turbulence is defined by Y_M . $C_{1\varepsilon}$, $C_{2\varepsilon}$, and $C_{3\varepsilon}$ are constants. σ_k and σ_ε are the turbulent Prandtl numbers for k and ε respectively. S_k and S_ε are user-defined source terms [168].

3.2.1.6 RNG $k - \varepsilon$ Model Transport Equation

Statistical analysis was used to alter the standard $k - \varepsilon$ model and include modifications, this led to the derivation of the RNG $k - \varepsilon$ model. RNG stands for renormalisation group theory and is the statistical technique used for the derivation. Improved accuracy when modelling rapidly strained flows is achieved due to an additional term in the turbulent dissipation rate equation. This enhances the accuracy for swirling flows. Turbulent Prandtl and Reynolds numbers are calculated in different methods between the RNG model and the standard $k - \varepsilon$ model. The RNG model uses analytical formulas for the turbulent Prandtl and Reynolds numbers compared to the standard $k - \varepsilon$ model which uses constant values. This enables the RNG model to calculate for low Reynolds number effects. This compares to the standard $k - \varepsilon$ model, which is a high-Reynolds number model. Though the RNG $k - \varepsilon$ model can be used to more accurately and reliably generate solutions for a greater range of flows than the standard $k - \varepsilon$ model, the near-wall region of geometries must be suitably configured [168].

The RNG $k - \varepsilon$ equations are shown below:

Equation 3-15 [168]

$$\frac{\delta}{\delta t}(\rho k) + \frac{\delta}{\delta x_i}(\rho k u_i) = \frac{\delta}{\delta x_j} \left(\alpha_k \mu_{eff} \frac{\delta k}{\delta x_j} \right) + G_k + G_b - \rho \varepsilon - Y_M + S_k$$

And

Equation 3-16 [168]

$$\frac{\delta}{\delta t}(\rho \varepsilon) + \frac{\delta}{\delta x_i}(\rho \varepsilon u_i) = \frac{\delta}{\delta x_j} \left(\alpha_\varepsilon \mu_{eff} \frac{\delta \varepsilon}{\delta x_j} \right) + C_{1\varepsilon} \frac{\varepsilon}{k} (G_k + C_{3\varepsilon} G_b) - C_{2\varepsilon} \rho \frac{\varepsilon^2}{k} - R_\varepsilon + S_\varepsilon$$

G_k and G_b represent the generation of turbulence kinetic energy due to the mean velocity gradients and buoyancy respectively. The overall dissipation rate affected by the fluctuating dilation in compressible turbulence is defined by Y_M . α_k and α_ε are the inverse effective Prandtl numbers for k and ε , respectively. S_k and S_ε are user-defined source terms [168].

The additional term in the ε equation of the RNG model is given by:

Equation 3-17 [168]

$$R_\varepsilon = \frac{C_\mu \rho \eta^3 \left(1 - \frac{\eta}{\eta_0}\right) \varepsilon^2}{1 + \beta \eta^3} \frac{1}{k}$$

Where $\eta \equiv \frac{Sk}{\varepsilon}$, $\eta_0 = 4.38$, $\beta = 0.012$ [168]

3.2.1.7 Species Transport Equation

The local mass fraction for each species in a flow, Y_i , is calculated using a convection-diffusion equation for the i^{th} species. The conservation equation for species transport, therefore, is as follows:

Equation 3-18 [168]

$$\frac{\delta}{\delta t}(\rho Y_i) + \nabla \cdot (\rho \vec{v} Y_i) = -\nabla \cdot \vec{J}_i + R_i + S_i$$

For a chemical reaction producing species i , the net rate of production is R_i . S_i is the rate of creation by addition from the dispersed phase plus any user-defined sources [168].

3.2.2 Flow Solvers: Solution Algorithm

Fluent uses two numerical methods for solving flow problems, pressure-based solvers and density-based solvers. Generally, pressure-based solvers were developed and used for low-speed incompressible flows. Density-based solvers were developed and used for high-speed compressible flows. In this work, pressure-based solvers were used for calculation. Pressure-based solvers manipulate the mass and momentum conservation equations noted above to determine the pressure of a given area of the fluid flow.

Pressure-based solvers can calculate the values for unknowns using two different approaches. The segregated algorithm solves each of the governing equations sequentially. In the coupled algorithm approach equations are solved simultaneously. Though the coupled approach improves the rate of convergence seen in solutions, the additional memory requirement can be up to 2-3 times that of the segregated algorithm. In this study, the segregated algorithm was used.

As mentioned above, segregated pressure-based solver algorithms solve the governing equations sequentially. The solution from each equation feeds into the next. This is efficient in terms of computational memory as only a single equation needs to be stored at a time. However, this increases the solution convergence time as each equation is solved individually. Furthermore, as the governing equations are non-linear and coupled, iterative loops must be carried out until a converged solution is found. The work flow of the algorithm solution steps can be seen in Figure 3-1, this work flow counts as a single iteration.

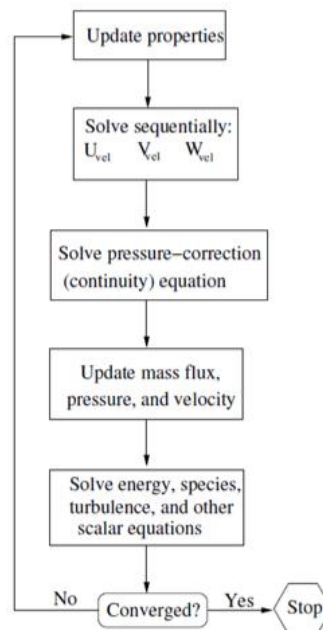


Figure 3-1 – Pressure-based segregated algorithm flowchart [168]

There are four different segregated pressure-based algorithm solvers in Fluent. SIMPLE (Semi-implicit method for pressure-linked equations), SIMPLEC (SIMPLE-consistent), PISO (Pressure-implicit with splitting operators), and FSM (Fractional step method). SIMPLE is the most commonly used algorithm used and used in this study. The algorithm uses the relationship between velocity and pressure corrections to enforce mass conservation and to obtain the pressure field.

3.2.3 Solution Convergence

The convergence of a solution is judged by the decreasing error of the residuals between subsequent iterations. The residuals are dimensionless predetermined outputs from the governing equations. The default convergence criteria set in Fluent is 10^{-3} for all residuals except for energy, which is 10^{-6} . The value for all residuals should fall below these values. Generally these criteria are viewed as accepted for most applications. However, they are not explicit rules for convergence.

Judging the convergence of a solution can be difficult as no set metrics apply for all cases. All inputs of a solution determine the convergence of a model and should be judged accordingly. A common method is to monitor relevant data specific to the problem at hand such as velocity or surface temperature. It is also worth noting that residual values falling below the set criteria level does not guarantee convergence. The solution may still be inaccurate as the residuals reduce but at a lower rate than previous. It is useful to note the trend of the residuals. If the values have reached a plateau, it is commonly acknowledged that the solution has become stable.

3.2.4 Physical Domain

For processing using CFD software, geometry must be created and imported that can be used for flow analysis. ANSYS DesignModeler features geometry creation tools that can be directly fed into the meshing and analysis software for CFD. However, the geometry tools are generally more simplified and less robust than dedicated CAD software. Due to this SolidWorks 2015 was used for the creation of the geometry. SolidWorks is a commercial 3D CAD modelling software that allows for the creation of individual parts and components that can be assembled into complex objects. This provides greater flexibility to users compared to DesignModeler. Furthermore, the files from SolidWorks can also be output to different file formats, specifically the file format required for generating models for 3D printing, details of this will be presented in Chapter 4. This is beneficial as it allows exact replication of the CFD model and a printed experimental model.

The geometry that is created in CAD software and imported to DesignModeler requires further manipulation before CFD analysis can be performed. The geometry represents the solid, physical objects, for CFD analysis the fluid volume must be defined [170]. The fluid volume enables the generation of fluid flow through it. From the fluid volume, the mesh can be generated in which the governing equations are iteratively solved. The process of this can be seen in Figure 3-2.

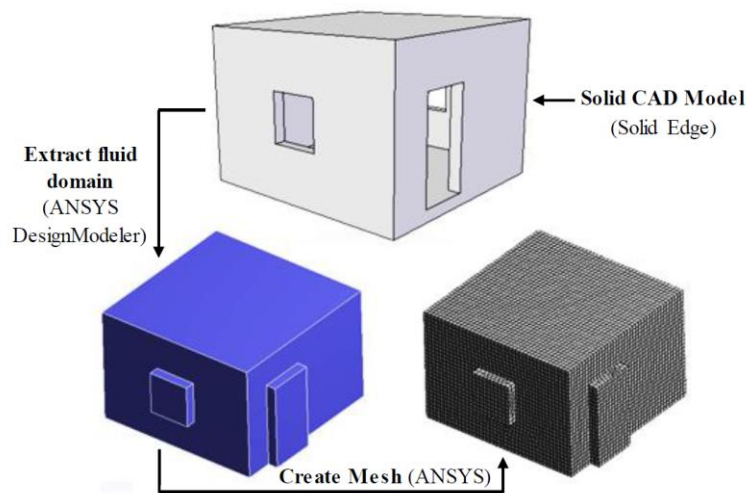


Figure 3-2 – Extraction of fluid domain from a solid CAD model representing a room [170]

3.2.5 Mesh Generation

The role of a mesh in CFD simulation is to provide a grid (structured or unstructured) within which the variables of the governing equations are calculated. The mesh is a representation of the geometry that defines the problem, composed as subdomains of the overall domain

[171]. Subdomains are generally termed as elements, cells or control volumes. Versteeg and Malalasekera [172] have noted that the accuracy of a solution is dependent on the number of cells in a mesh. The higher the number of cells, the greater the accuracy of the solution. However, the larger the mesh, the greater the increase in the computational cost in terms of memory and calculation time. Versteeg and Malalasekera also state that 50% of CFD project time is spent on the characterisation of the geometry and mesh generation. As the mesh has significant impacts on the solution accuracy, time is spent to ensure that the mesh is acceptable for the given geometry and problem.

The generation of the meshes can be categorised into three methods, structured, unstructured and hybrid. Structured meshes apply a regular pattern of cells to geometry where the cells have a regular and repeating shape. Structured meshes are useful for simple geometry where shapes are uncomplicated; the reduced number of cells because of structured meshes improves the computational time of a solution. In complex geometries, unstructured meshes are more applicable than structured meshes. The cells of an unstructured mesh do not follow predetermined design, allowing greater flexibility for cell shape. This allows meshing for irregular shapes and geometry. Unstructured meshes increase the computational time of a solution as meshes have significantly more cells compared to structured meshes. Hybrid meshes are a combination of structured and unstructured meshes, using the most appropriate cell shape required for the geometry.

It is important to select the most appropriate meshing method to generate an accurate solution. The geometry, anticipated flow patterns, computational time and solver type used all require consideration for the meshing method.

3.2.6 Mesh Quality

Assessing the quality of the generated mesh guarantees trust that the calculated solution is accurate, from a meshing standpoint at least. One of the primary methods of measuring the quality of the mesh is skewness. Skewness measures the accuracy of a cell compared to an idealised cell, either triangular or quadrilateral. Examples of ideal and skewed cells is shown in Figure 3-3.

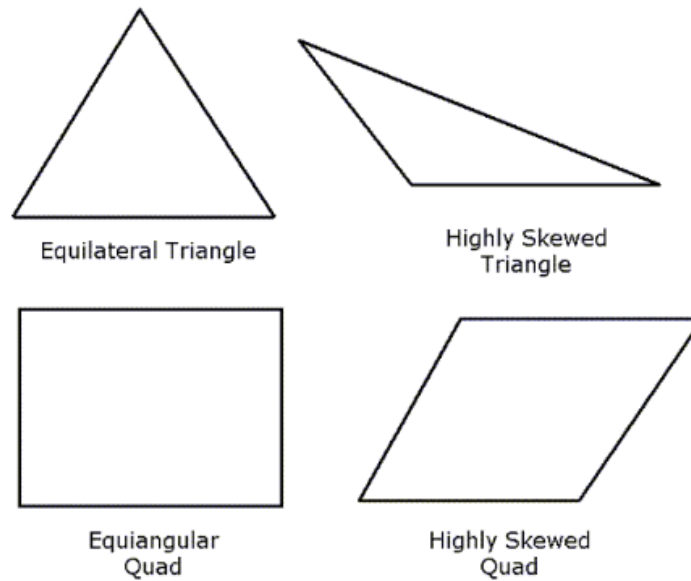


Figure 3-3 – Ideal and Skewed Triangles and Quadrilaterals [173]

The Fluent Meshing User's Guide [173] defines skewness using the following equation for equilateral-volume based skewness, which is used for both 2D and 3D meshes:

Equation 3-19 [173]

$$\text{Skewness} = \frac{\text{Optimal Cell Size} - \text{Cell Size}}{\text{Optimal Cell Size}}$$

This shows how the skewness is a ratio of the actual cell size compared to the optimal cell size, where the optimal cell size is the size of an equilateral cell with the same circumradius. This metric of skewness corresponds to a cell quality, shown in Table 3-1.

Table 3-1 – Range of skewness values and corresponding cell quality [173]

Value of Skewness	Cell Quality
1	degenerate
0.9 — <1	bad (sliver)
0.75 — 0.9	poor
0.5 — 0.75	fair
0.25 — 0.5	good
>0 — 0.25	excellent
0	equilateral

It is noted that for a good quality mesh, a skewness value of 0.4 or below is expected for 3D meshes and that most cells should be good or better. It is acknowledged that a number of cells will fall outside of this range, to poor or bad cell quality [173]. This is especially true for

unstructured 3D mesh cases. Cells that are classified as bad or degenerate are not acceptable as the equations assume that the cells are equilateral, this has significant impacts on the accuracy of the solution.

The ANSYS Theory guide [168] states that wall functions link the solution variables at near-wall cells and the quantities at the wall through a set of semi-empirical formula. The dimensionless wall distance y^+ is used for calculation of the boundary layer at wall surfaces. The value of y^+ is measured from the wall to the centroid of the first adjacent cell. Values of $30 < y^+ < 300$ are generally acceptable for mesh generation in order to capture the turbulent boundary layer profile. In situations where turbulent functions may not have developed or exist, such as at the near-wall conditions of a duct or pipework, an acceptable y^+ value can be lower than the previously prescribed value of 30, generally in the range of $y^+ < 11.25$.

3.2.7 Mesh Adaption

Mesh adaption, also sometimes known as Adaptive Mesh Refinement (AMR), is the process of modifying the current mesh to improve the accuracy of the solution and flow features around complex geometry, without significant impact on the computational time. Different types of AMR strategies exist, mesh refinement methods (h-methods) and mesh enrichment methods (p-methods) are common amongst these. A combined method of mesh refinement and mesh enrichment (hp-methods) also exists and is commonly used. These AMR methods are unstructured adaptive methods, the resulting mesh is unstructured regardless of whether the initial mesh was structured or unstructured.

Chung [174] details the differences between h-methods and p-methods and the combined hp-method. The h-method relies on refinement of cells that are deemed to have poorer quality, where the cells are changed. The most common changes are to divide existing cells into smaller sub-cells to improve flow realisation in these areas. Mesh refinement should be targeted in specific areas of interest with complex flow patterns as computational time can be significantly increased following the use of h-methods. The p-method increases the degree of polynomials or higher order approximations of cells, with the aim to improve the final solution. The hp-method for mesh refinement combines properties from both the h-method and p-method.

Chung states that monitoring error indicators between each mesh refinement iteration is beneficial to determine which mesh is the most suitable. A variable that is determined from the solution accuracy can be chosen as the indicator, such as velocity, pressure or temperature. As the mesh is refined, monitoring of the variable should be undertaken from

the same position in the mesh each time. The mesh can be considered acceptable when the error between subsequent meshes is below the acceptable error level.

3.2.8 Quantification of CFD error and Uncertainties

CFD results are subject to the same processes as other methods of analysis to ensure that engineers and designers have confidence in the outcomes, and are accurate and reliable. The two areas of concern of CFD relate to error and uncertainty of the results. The AIAA Guide for the Verification and Validation of Computational Fluid Dynamics Simulations [175] define error and uncertainty in the following ways:

- Error – deficiencies in a CFD model not caused by a lack of knowledge. Error is characterised by:
 - Numerical errors
 - Coding errors
 - User errors
- Uncertainty – potential deficiencies caused by a lack of knowledge. Uncertainty is characterised by:
 - Input uncertainty, caused by limited information or approximations
 - Physical model uncertainty, caused by poor representation of physical processes or oversimplified assumptions

Versteeg and Malalasekera [172] highlighted the sources of error and uncertainty from CFD simulations and provide methods to quantify error and uncertainty using verification and validation of results. The authors note that it is important to recognise that error and uncertainty are unavoidable and so quantifying using verification and validation allows confidence in models.

Verification is concerned with the quantification of errors in CFD results, as such, it is discrepancies in results from case to case that users should address. This is mainly related to mesh adaption. As the meshes are refined, the error between cases should decrease when inputs other than mesh size and quality remaining constant. Validation quantifies the uncertainty that is affected by the input properties and physical model comparison. Testing the uncertainty of the input parameters requires multiple models to be ran with different input data. The output data should reflect the changes made to the input properties. The most commonly accepted method of validation of CFD models and results is direct comparison with a physical experimental model. The same variables should be measured at the same locations in both CFD and experimental models to reduce uncertainty. Versteeg

and Malalasekera do not define a method to measure the differences between the two data sets. Plotting the data on a graph and visually comparing the data points is suggested but cannot guarantee accuracy. Estimating the physical model values as a base case and comparing the difference to the CFD results to find the percentage error is commonly practiced. Provided the average percentage error is below a prescribed value, a model can be said to be validated.

3.3 Computational Fluid Dynamics (CFD) Modelling

The principles and theory of Computational Fluid Dynamics covered form the methodology and background to the CFD analysis conducted in this study. The following section details the development of the geometry using Computer-Aided Design (CAD) software, through the CFD method of pre-processing, processing and post-processing, to the validation of the CFD solution using comparisons with experimental data.

3.3.1 Problem Identification

The aim of this project was to create a rotary thermal wheel capable of integration with a passive ventilation wind tower system. The purpose of this was to deliver a system that could recover heat from the exhaust airstreams of a wind tower, transferring it to the incoming airstream, thereby increasing the temperature and reducing the dependency on heating systems. Current rotary thermal wheels are not suitable for this purpose due to the pressure drop of airstreams passing through the central matrix structure of the wheel. The honeycomb or sinusoidal wave construction of the wheel causes a high pressure drop due to the skin friction caused by the large surface area in contact with the airstream and the fine gaps between passages for air to move through, as identified in Chapter 2. An example of the matrix can be seen in Figure 3-4.



Figure 3-4 – Sinusoidal wave matrix structure of a rotary thermal wheel

In order to solve this, it was proposed to create an alternative matrix design. The matrix still needed to be capable of recovering heat from the exhaust airstreams to the incoming airstream but with a pressure drop significantly lower than current designs of 150Pa, which did not affect the ventilation supply rates of a wind tower. However, previous work did show a correlation between increased pressure drop and efficiency [38]. The two aims of the design were to minimise the contact surface area between the airstream and matrix, reduce the skin friction and maximise the opening size of the matrix. Both features reduce the pressure drop across the wheel.

As no previous attempts had been made to alter the matrix structure of the wheel, little literature exists to inform the design decisions made. It was necessary to maximise the surface area possible within the allowable volume, whilst maintaining a design that would be easy to manufacture and lower the pressure drop across the device. Two design options were conceptualised that both attempted to overcome the problems with rotary thermal wheels. Both feature large openings and reduced surface area to minimise skin friction. Heat recovery is handled by the thickness of the internal structure walls. Reducing surface area but maintaining volume was thought to ensure that heat transfer would continue due to the thermal mass of the structure.

A concept of concentric circles within the casing of a rotary thermal wheel was envisioned as one of the design options. The circles would radiate out from the centre of the wheel with increasing diameters. The design mirrors that of the sinusoidal wave structure shown above but removing the material between supporting cylinders. Figure 3-5 shows a CAD image of half the proposed design.

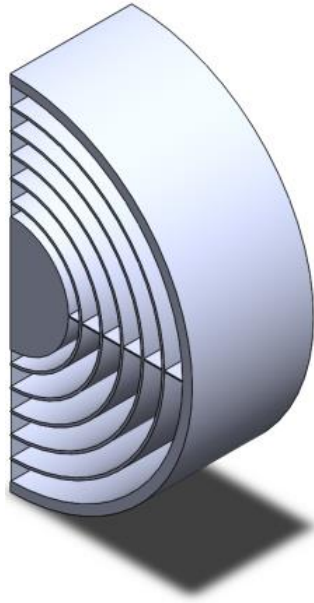


Figure 3-5 – Concept of concentric circles model

The second concept involved blades radiating out from the centre of the wheel, similar to spokes on a wheel. This design was termed the “radial blade” design by the project team. The design is a move away from the traditional structure of a rotary thermal wheel. One advantage of the radial blades design was the potential flexibility of the construction. The blades were designed to slide in and out of the casing, making the design reconfigurable if necessary and improving maintenance ease. Figure 3-6 shows a CAD image of half the proposed design.

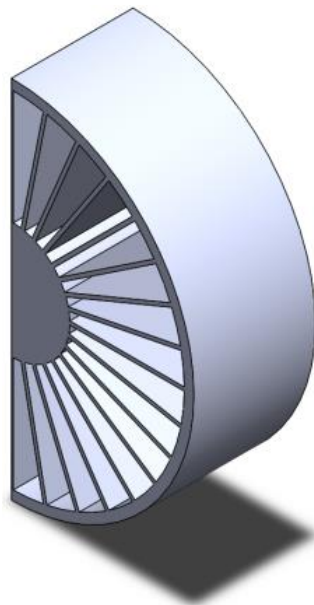


Figure 3-6 – Concept of radial blade model

The radial blade design was chosen as the concept to develop further when the two options were compared. When the geometry of both designs were studied in detail, very little separated the structures. The radial blade concept was eventually chosen purely for ease of construction and material cost. Both designs had similar porosity, which would affect the flow of air through the wheel. The adaptability of the radial blade design, by changing the position of the blades and the angle between them, was viewed as a benefit for testing. Different arrangements could be tested using a single casing into which blades could be fit.

3.3.2 Design Geometry

In total, four different radial blade rotary thermal wheel designs were produced for investigation using CFD, two radial blade designs for heat recovery and two radial blade designs for dehumidification. It was decided that two configurations of radial blades would be examined for each of the systems. The angle between radial blades was altered between 10° and 15° . It was assumed below these values that the blockage presented by the blades would be too high, increasing the pressure drop and at any angle above this, insufficient material would exist for heat/mass transfer. This resulted in configurations of 32 radial blades with 10° angle of separation and 20 radial blades with 15° angle of separation. Figure 3-7 shows the 32 and 20 radial blade configurations.

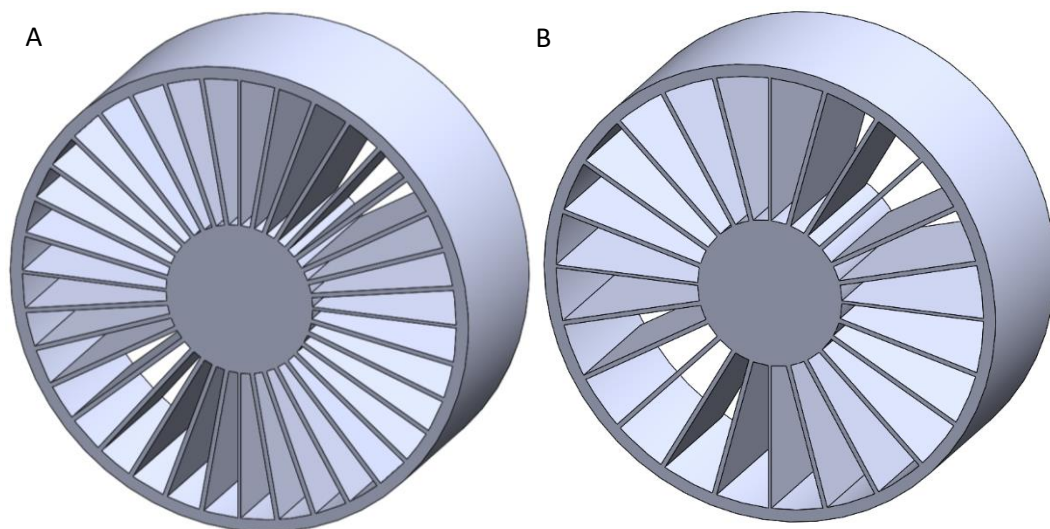


Figure 3-7 – A) 32 radial blade configuration, B) 20 radial blade configuration

To test the properties of the wheels under controlled conditions, it was determined that two adjacent airstreams moving in opposite directions would be used. Though the design of the wheels is aimed at providing heat recovery and dehumidification in a wind tower system, given the complexity of the flows in a wind tower, along with the complexity constructing a

wind tower for experimentation, it was decided that a two-way cross-flow duct would be the most appropriate solution.

As the geometry investigated in the CFD analysis was to be the same size as the physical experiment model, consideration for the construction of the printed model had to be taken into account. Constraints of the printing size resulted in a rotary wheel diameter of 300mm and depth of 105mm for all wheel configurations, Chapter 4 will explore this in further detail.

The wheels were mounted inside a casing that slide into a custom built ductwork of two adjacent ducts. The ducts featured an inlet at one end, covering the whole duct opening and two circular outlets opposite. Fans were attached to the outlets to draw air through the duct from the inlet and out via the exhaust fans. Further explanation of this can be found in Chapter 4. As the casing was required only for mounting of the wheels and the effect of the casing on the flow could be replicated more easily, the geometry was deemed surplus for the CFD model and removed from the modelling. This helped to simplify the mesh and improve computational speed. The experimental versions of the ductwork and casing can be seen in Figure 3-8.

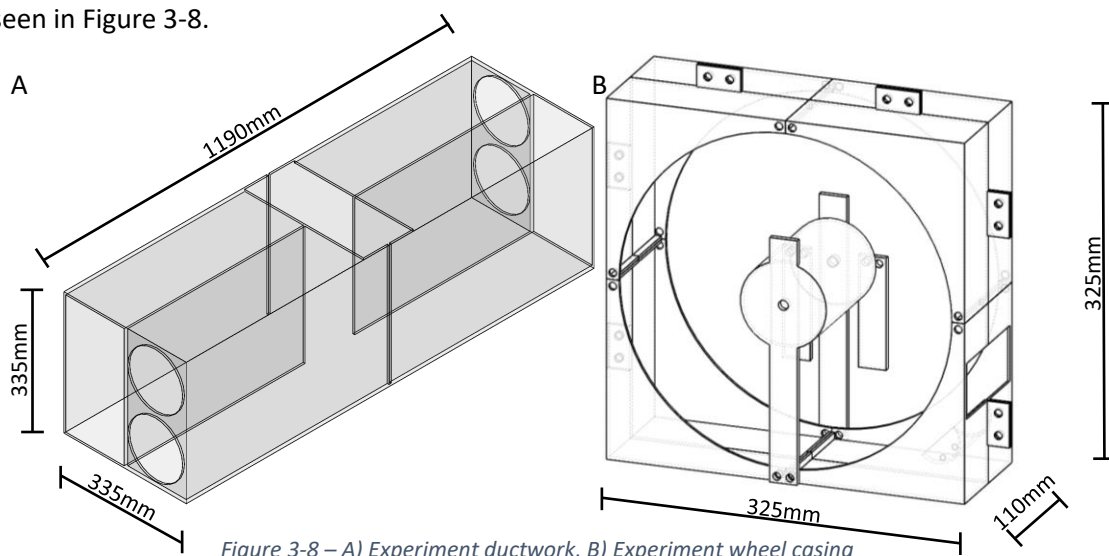


Figure 3-8 – A) Experiment ductwork, B) Experiment wheel casing

3.3.3 CFD Design Geometry

The geometry for the CFD models was simplified to reduce the computational demands and time required for solutions to be derived. The complexity of the ductwork and casing was reduced to make computation quicker, simple channels were modelled as a simplification. It was decided that to model the full experimental design, two airstreams with different inlet conditions moving in opposite directions with the wheel rotating between the airstreams and transferring properties between airstreams, in a single simulation would complicate the boundary conditions required and lead to additional errors in the CFD model design. To simplify the geometry for the CFD simulations, it was decided that only one air channel and

half of the wheel would be modelled at a time. For example, the incoming airstream with the half of the wheel present in that airstream. The simplified geometry used in the simulations is shown in Figure 3-9 for a 32 radial blade example.

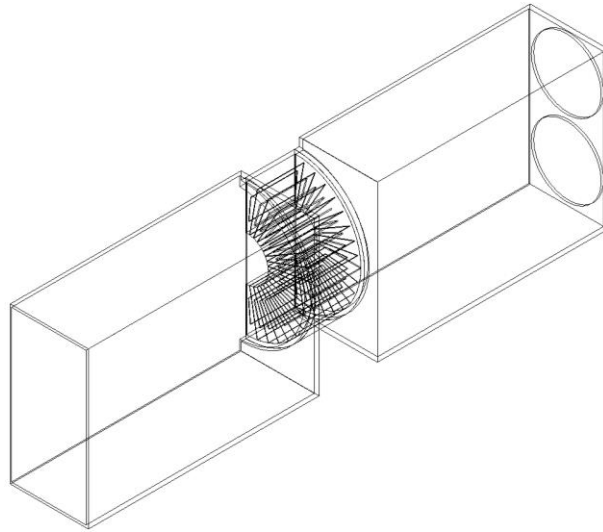


Figure 3-9 – Ductwork and radial blade rotary wheel model used in CFD model

The same geometry was used to represent both the incoming and outgoing airstreams. To model the full experimental system, the inlet boundary conditions that related to the incoming and outgoing airstream of each half of the duct were applied separately. By modelling each airstream separately, the complete system can be modelled in a simplified method when the solutions from the equivalent tests are analysed together. Though this doubles the total number of simulations required, the complexity of the simulations was significantly reduced.

The length of the duct either side of the rotary wheel was 490mm. The total size of the duct was 335x335mm, which included a material thickness of 5mm for the duct walls and an internal divider at the mid-point of 5mm thickness. Each duct therefore had a fluid volume size of 160x325x490mm. In order to mimic the distance between the face of the wheel and the duct where the casing was present in the experimental model, additional geometry was added to the duct. This enabled connection to the wheel face.

The standard dimensions for each of the wheels can be seen in Figure 3-10. In the experimental model the blades, both acrylic and copper, were 100x100mm with varying thickness. The reasoning for the selection of materials will be covered in Chapter 4. For the blades to be inserted into the wheel, 3mm grooves were designed on each side of the wheel structure in which the blades sat. This explains the 94mm length of the blades in the CFD model. Similarly, as the blades were 100mm in length, additional material was required on which the blades could rest, necessitating the 105mm overall depth of the wheel.

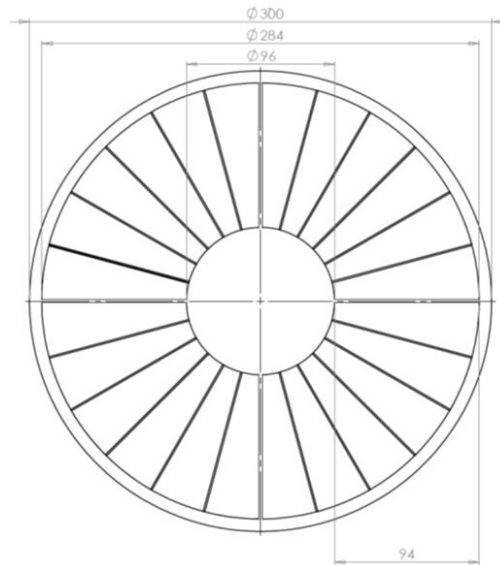


Figure 3-10 – Standard dimensions for radial blade rotary wheel

However, there are differences between the heat recovery and dehumidification configurations relating to the thickness of the blades. The heat recovery radial blades are made of 1mm thick copper sheets, whereas the dehumidification radial blades are 1mm thick acrylic sheets coated in 1mm thick layer of silica gel on either side giving a total thickness of 3mm. Each configuration was modelled with solids to replicate the experiment. The differences in blade thickness gives a significantly different profile to each configuration that affects the flow pattern through the wheel. This can be seen in Figure 3-11.

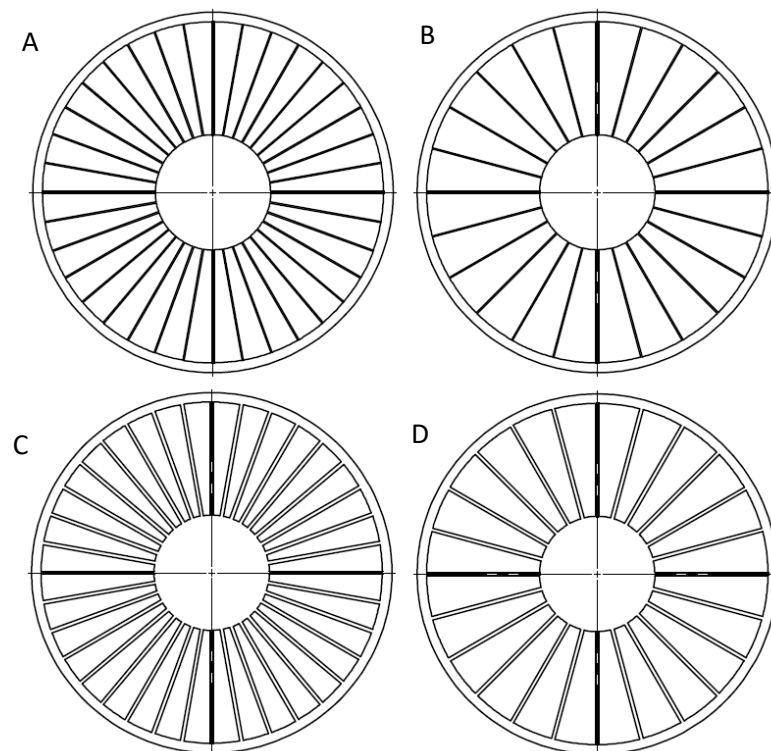


Figure 3-11 – The four configurations of radial blade rotary wheel tested A) 32x copper blades, B) 20x copper blades, C) 32x silica blades, D) 20x silica blades

As the air channels were modelled individually, the effect of the radial blades on the properties of the air as it rotated between the two airstreams had to be modelled in an alternative method. To achieve this, additional volumes were added to each of the geometries of the configurations of the radial blades. The additional volumes were set as fluid volumes within the geometry. The standard geometry representing the experimental model is generated as solids around which the fluid flows and is analysed. However, specific properties and cell zone conditions that relate to heat and mass transport cannot be applied to solid volumes. Therefore, the additional fluid volumes modelled between the radial blades were required. This will be further expanded upon in section 3.3.6.3.6 of this chapter. The fluid volumes matched the volume of the blade sections to maintain consistency between the experiment and CFD simulations. For the heat recovery copper blades, this is 1x94x100mm given the thickness of the copper. For the dehumidification silica gel blades, this is 2x94x100mm for the thickness of silica gel either side of the acrylic blade. The volumes to which fluid properties were applied were positioned between at the mid-distance between blades with half the height but double the thickness of the actual blade. Modelling the fluid volumes with the same dimensions as the radial blades resulted in meshing and solution errors due to the interaction of the solid mesh walls and the fluid mesh walls. Therefore the current method was improvised. The position of the additional volumes between the radial blades can be seen in Figure 3-12.

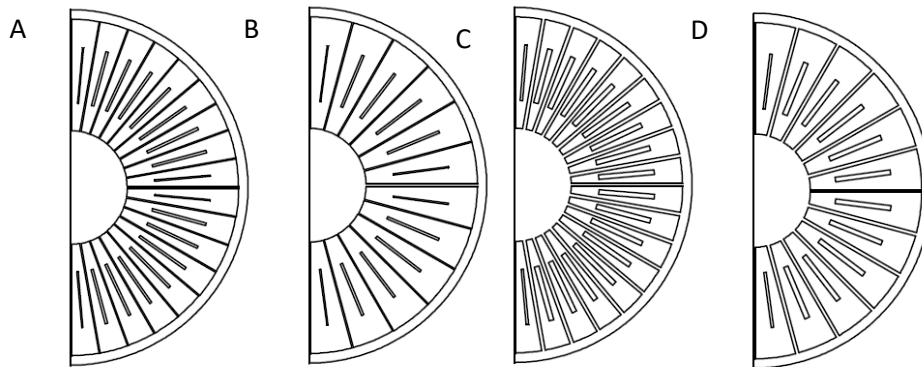


Figure 3-12 – The configurations of radial blade rotary wheel with fluid volumes A) 32x copper blades, B) 20x copper blades, C) 32x silica blades, D) 20x silica blades

The solid bodies of the geometry were imported from the SolidWorks CAD file to ANSYS DesignModeler. Within DesignModeler, the fluid volumes that are necessary for mesh generation for flow analysis are extracted from the solid bodies. The extraction of the fluid volumes can be seen in Figure 3-13.

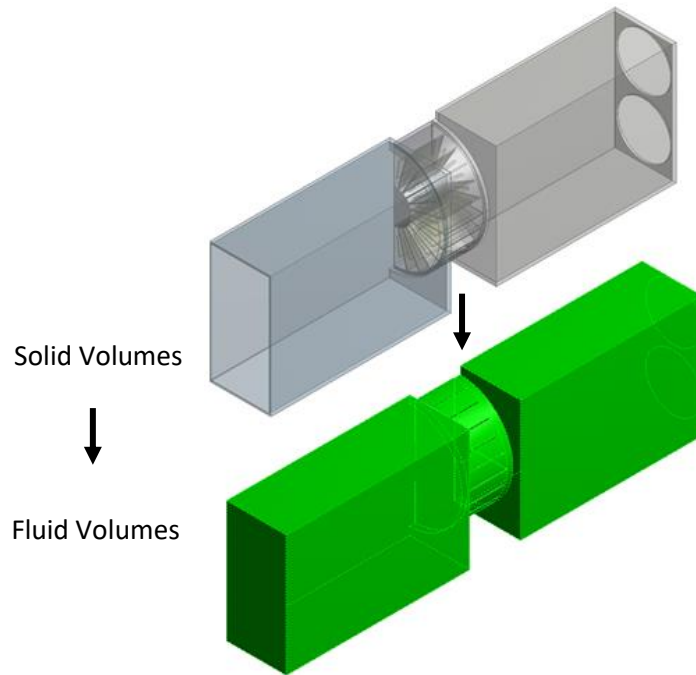


Figure 3-13 – Fluid volume extraction from solid volume geometry

The additional volumes that were added to the solid geometry to represent the volumes of copper in the heat recovery system and silica gel in the dehumidification system were also imported as solid volumes. The properties of these volumes were altered to act as fluid volumes, which enabled the volumes to be grouped as a part with the interior of the duct and rotary wheel. Configuring the additional volumes as fluids allows flow to pass through without affecting properties of the flow, unless further parameters were applied. This will be detailed in section 3.3.6 of this chapter. The position of the additional volumes can be seen in Figure 3-14.

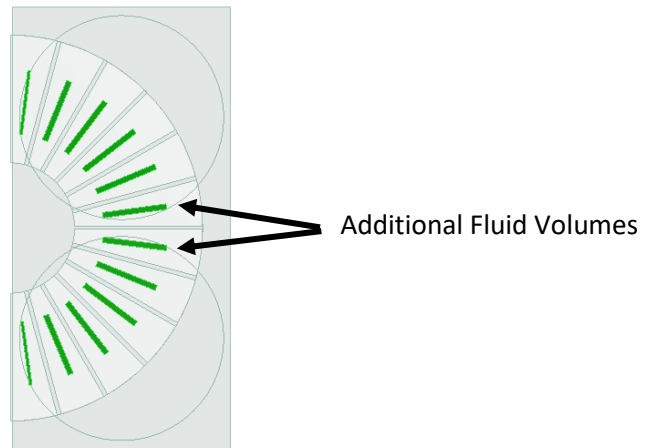


Figure 3-14 – Position of additional fluid volumes representing copper/silica gel volumes (shown in green)

3.3.4 Mesh Generation

The generation of the computational mesh from the fluid volumes is required for the analysis of the CFD model. Mesh quality is an important factor in determining the accuracy of a solution and so many designers spend a significant amount of time ensuring that the mesh is suitable for the simulations. The auto-meshing software incorporated into ANSYS Workbench, the platform software that operates ANSYS products, was used for meshing of the volumes in this work. Auto-mesh provides user control that are capable of delivering high quality meshes but a user-friendly interface.

As the geometry for the each of the configurations varied, each required an individual mesh to be created for simulation. The final meshes for all of the geometries used were unstructured, non-uniform tetrahedral meshes. Face sizing was applied to all surfaces of the geometry, with an element size of 0.0075m for all cases except the 32x silica gel radial blade configuration that required an element size of 0.006m. Though the similarity between the geometry of the configuration was high, the variations in number of blades and thickness of the blades resulted in differences in mesh size. The number of elements in the meshes ranged from 526,038 to 872,588, which is expected given the differences in geometry. The number of nodes in the meshes varied from 102,838 to 171,879, aligning the smallest and largest meshes. The four meshes used for the analysis can be seen in Figure 3-15.

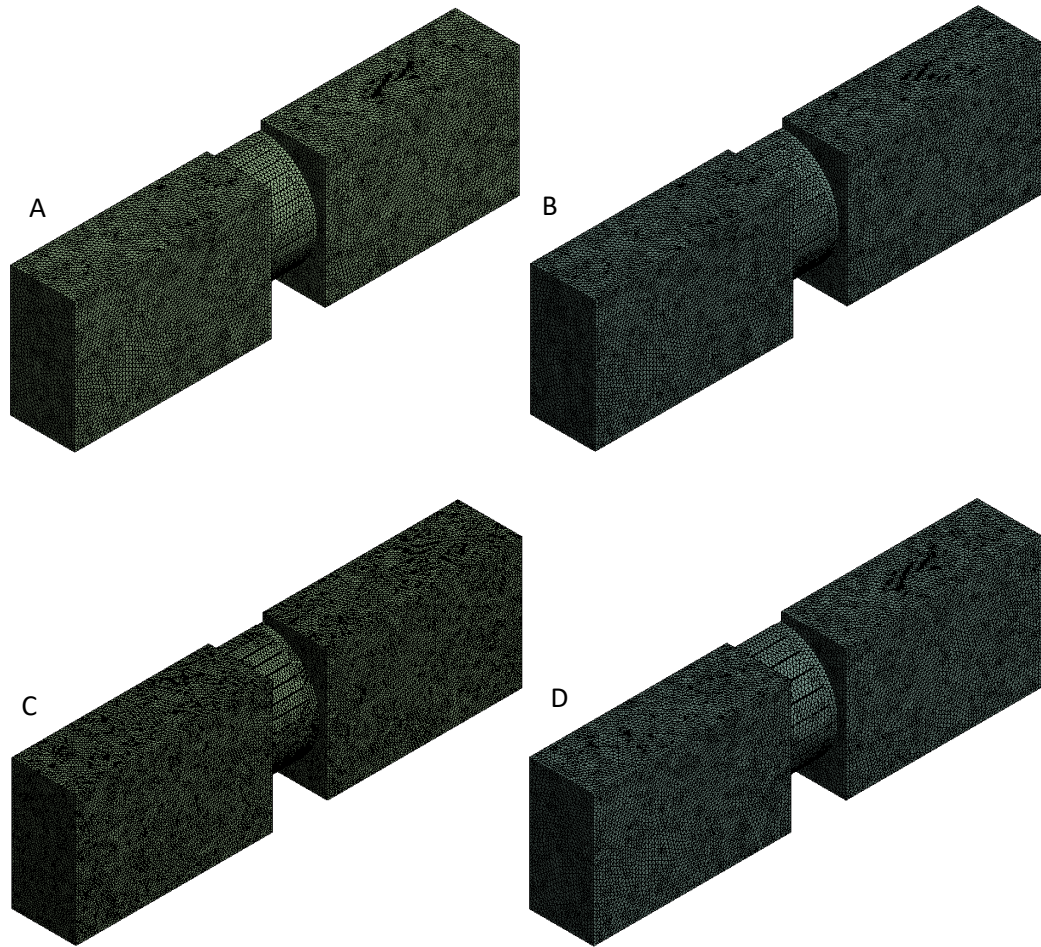


Figure 3-15 – Meshes used for A) 32x copper blades, B) 20x copper blades, C) 32x silica blades, D)20x silica blades

The automatic meshing method involved with the auto-meshing function of ANSYS Workbench employs an algorithm that selects the best choice of cell shape for the given geometry. Typically, when no meshing method is determined for a given geometry, the auto-meshing function will use tetrahedral cells to create a mesh. This is most common in complex shapes, as seen in the half rotary wheel section and ductwork of the geometry. However, in the additional volumes used to present the copper plate and silica gel, hexagonal cells have been created for the simpler shape, shown in Figure 3-16. This reduces the total number of cells in the mesh, reducing the computational time required.

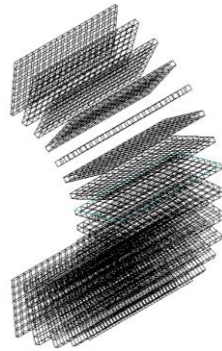


Figure 3-16 – Structured hexagonal mesh for additional silica gel volumes in 32x silica gel radial blade geometry

3.3.4.1 Mesh Quality

It is difficult to judge the true quality of a mesh without direct comparison of the solution with experimental results, even then the boundary conditions and other factors can affect the solution accuracy. There are a number of indicators that can be used to interpret mesh quality however. As previously discussed, the equiangle skew value for a cell determines the shape and spacing of a cell when compared to the idealised shape and cell size. Values closer to zero are the most desirable values for skewness. Figure 3-17 shows the contours of equiangle skew on the surfaces of the fluid geometry for the four different rotary wheel configurations.

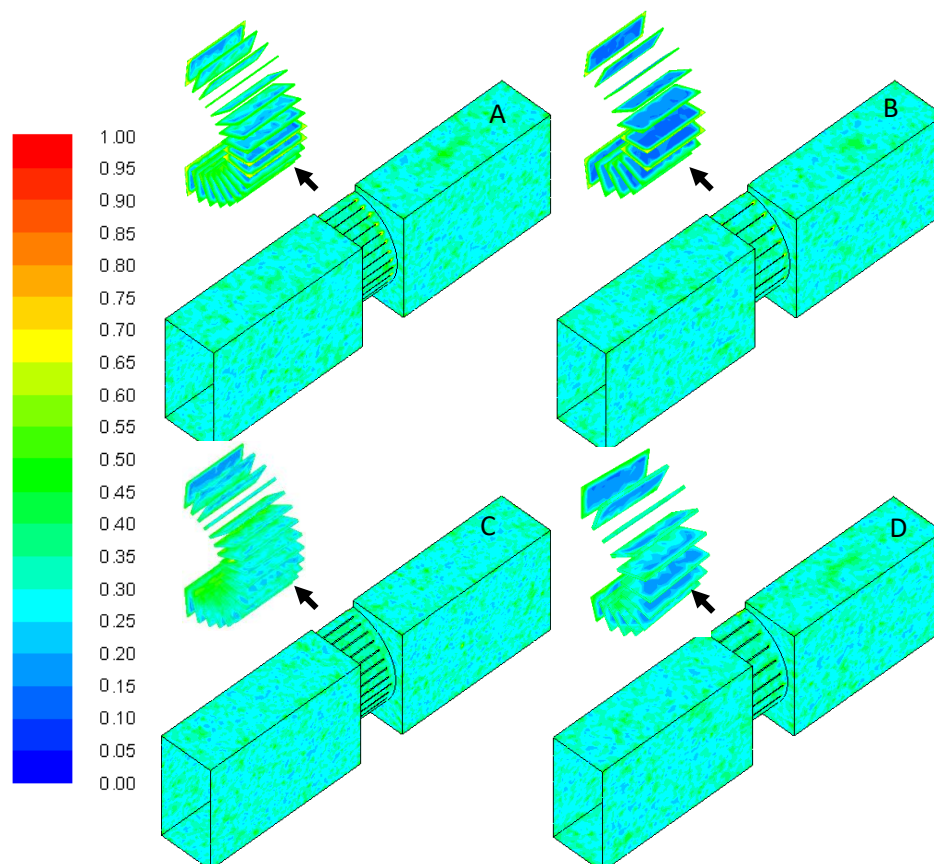


Figure 3-17 – Surface contours of cell equiangle skew for A) 32x copper blades, B) 20x copper blades, C) 32x silica blades, D) 20x silica blades

It is generally accepted for a 3D geometry that the average skewness value for a mesh should be below 0.4 but some cells will deviate above this due to the nature of the cells and complex geometry. The average skew value for each of the complete meshes used for the rotary wheel configurations was 0.32 for all cases. This indicates that the mesh is deemed as good by the ANSYS Theory Guide [168] when considering cell skew values.

A secondary indicator of mesh quality is the y^+ value of the mesh. The y^+ value is the dimensionless value of the distance from the geometry wall to the first calculation node in the mesh. The importance of this value relates to the calculation of the flow at the walls and the wall functions. If the y^+ values are too high, accurate calculation of the effects at the wall cannot be completed. Figure 3-18 shows the surface contours for the y^+ values for the four configurations of rotary wheel. The average y^+ values for the configurations varies between 10.1 - 12.7. This is acceptable as a general range of values given the circumstances of the flow in the models based on previous research [168].

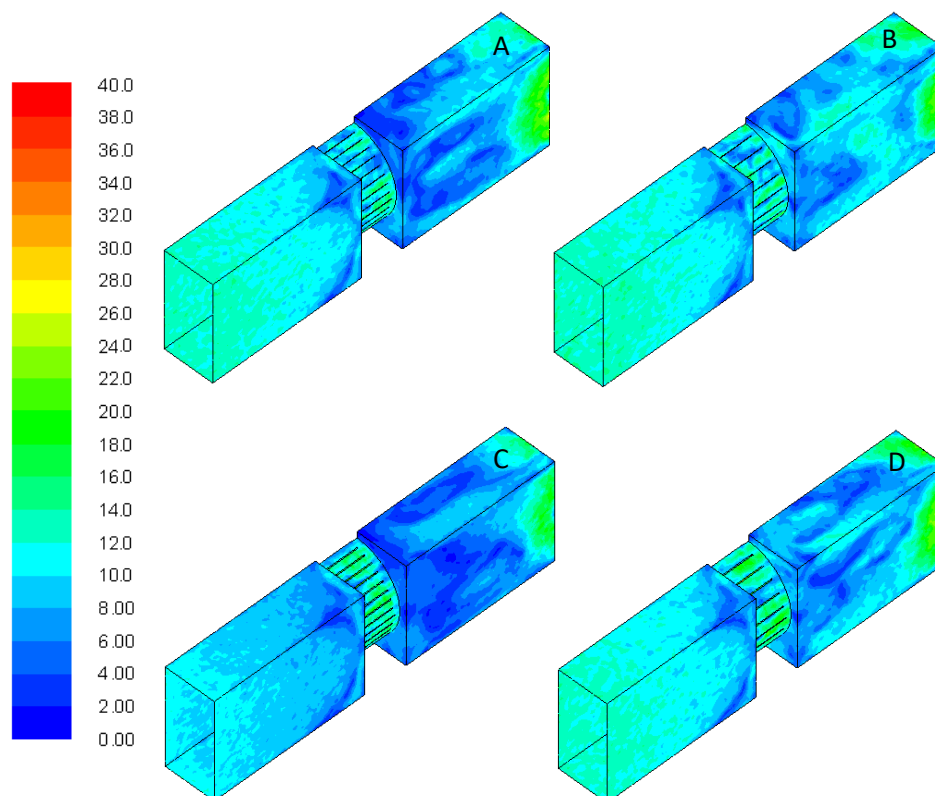


Figure 3-18 – Surface contours for y^+ values for A) 32x copper blades, B) 20x copper blades, C) 32x silica blades, D) 20x silica blades

3.3.5 Mesh Verification

It is necessary to verify that the solution generated from the CFD analysis is independent of the grid quality. To do this, a number of different size meshes were created for configuration

geometries. As mentioned previously, the hp-method for refinement of a mesh combines the h-method for mesh refinement and p-method for mesh enrichment to produce a high quality mesh. The hp-method for adaption was used by reducing the cell element size and increasing the overall mesh size.

As computation of the meshes can take a substantial amount of time to complete, it was decided that the silica gel radial blade configurations would undergo mesh adaption. The results of the adaption would then be used for generation of the meshes for the heat recovery copper blade configurations. As the geometry between the different configurations is largely similar with the exception of the thickness of the radial blades and additional volumes, it was decided that the increased volume size of the dehumidification radial blade configurations would require longer computation time for the mesh generation. Therefore, using the dehumidification configurations for the mesh adaption was deemed logical.

The configurations were initially generated with coarse mesh size and an initial solution generated with simple boundary conditions. From the initial solution, an air velocity flow profile was taken from the centreline of the duct across the full height at 20 equally spaced measurement points. The mesh was refined through successive iterations, each iteration reducing the cell element size and increasing the overall mesh size. For each mesh a solution was generated, with the same boundary conditions as previously used and the flow profile from the centreline measured. The flow profiles for the configurations can be seen in Figure 3-19 and Figure 3-20. The residual plots of the CFD simulations stabilised as the iterations increased and became more stable as the mesh quality improved.

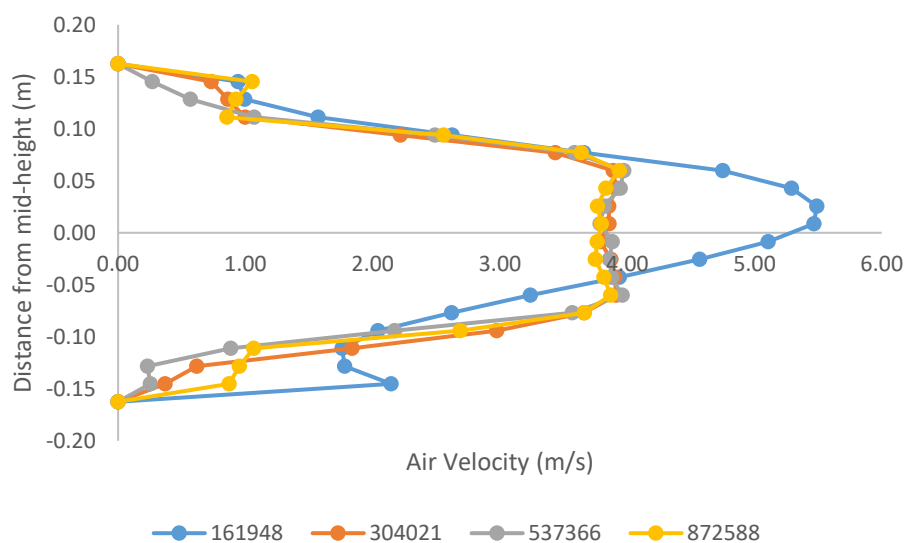


Figure 3-19 – Air velocity flow profile for 32x silica gel configuration for increasing mesh size

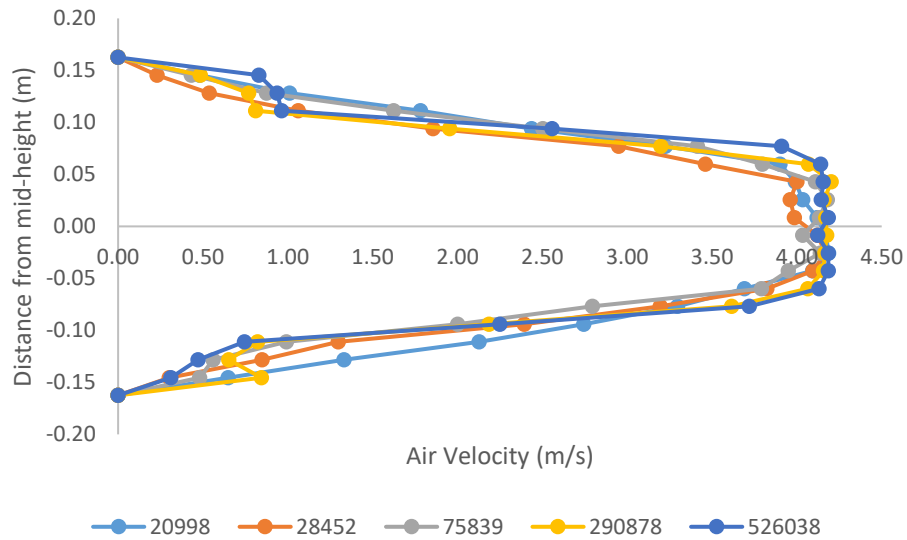


Figure 3-20 – Air velocity flow profile for 20x silica gel configuration for increasing mesh size

For both examples of mesh refinement, the initial mesh and solution yield an inaccurate result when compared to the subsequent solutions. The two graphs show that as the meshes become more refined, the solutions converge and become more similar. The error between the final two meshes at the centre point were 0.29% and 0.37% for the 32x and 20x configurations respectively. This was deemed as an acceptable level of error between the meshes. Figure 3-21 shows the decreasing error percentage between successive iterations of mesh size for the 32x and 20x configurations of rotary wheel.

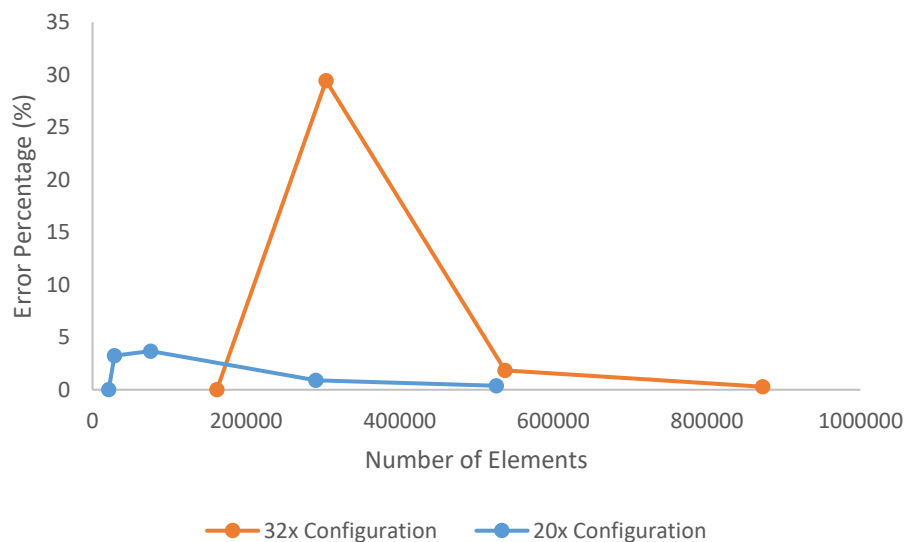


Figure 3-21 – Error percentage of velocity at mid-height in the duct for 32x and 20x configurations of rotary wheel for increasing mesh size using tetrahedral shaped cells

Though it was stated that the cell shape used in the work was predominantly tetrahedral shaped cells, hexagonal cell dominant meshes were also generated as a further aspect of

comparison to find the most suitable mesh type. The same process was used to refine the meshes, decreasing cell element size whilst increasing overall mesh size. Measurements for air velocity flow profile were calculated by running solutions using the same boundary conditions. The change in error percentage across different mesh sizes can be seen in Figure 3-22. Though the meshes generally improved in quality as element size reduced, it was determined that the tetrahedral cell meshes provided preferable solutions in terms of accuracy.

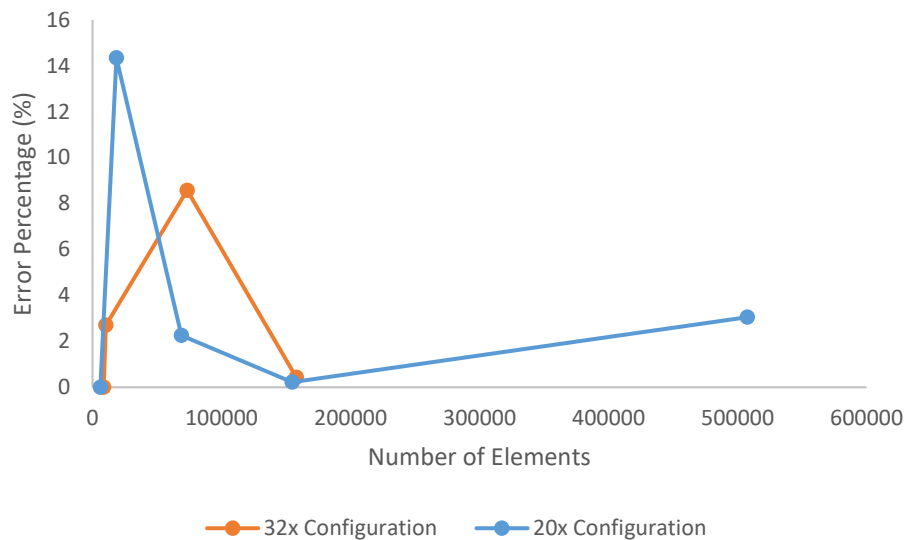


Figure 3-22 – Error percentage of velocity at mid-height in the duct for 32x and 20x configurations of rotary wheel for increasing mesh size using hexagonal shaped cells

3.3.6 Boundary Conditions

For effective simulation and solution of a CFD model to be completed, appropriate boundary conditions must be set for surfaces that influence the fluid flow. Given the experimental aspect of this study, the boundary conditions must also reflect the conditions experienced in experiments. Providing boundary conditions as close as possible to those seen in the experiments ensure that the results generated by the CFD model compared to the experimental results are as close as possible.

As previously mentioned, one airstream duct was modelled at a time, as opposed to the two ducts running with counter-current flow as in the experiment, for simplification of the CFD simulations. This meant that two sets of boundary conditions were required for each simulation with the comparable experiment. The position of the boundary layers was consistent throughout all simulations; the properties and values were adjusted as required. Figure 3-23 shows the placement of the boundary surfaces, these were consistent for all simulations though the values were modified to replicate the conditions for each airstream

and experimental test. The pressure inlet was placed on the vertical surface, opposite the two exhaust fan outlets, mimicking the experiment setup. The fluid volumes that were added between the radial blades are a representation of the volume of radial blade material for each configuration, copper for the heat recovery designs and silica gel for the dehumidification designs. The remaining surfaces were treated as walls. The air temperature and mass fraction of water in the air, measured as a ratio mass of water to mass of air used to calculate the relative humidity for a given air temperature, were set at the pressure inlet. The air velocity was set by setting values for pressure at the inlet and at the outlet. Further details of the steps required to provide the appropriate air velocity for the CFD models can be found in Chapter 5.

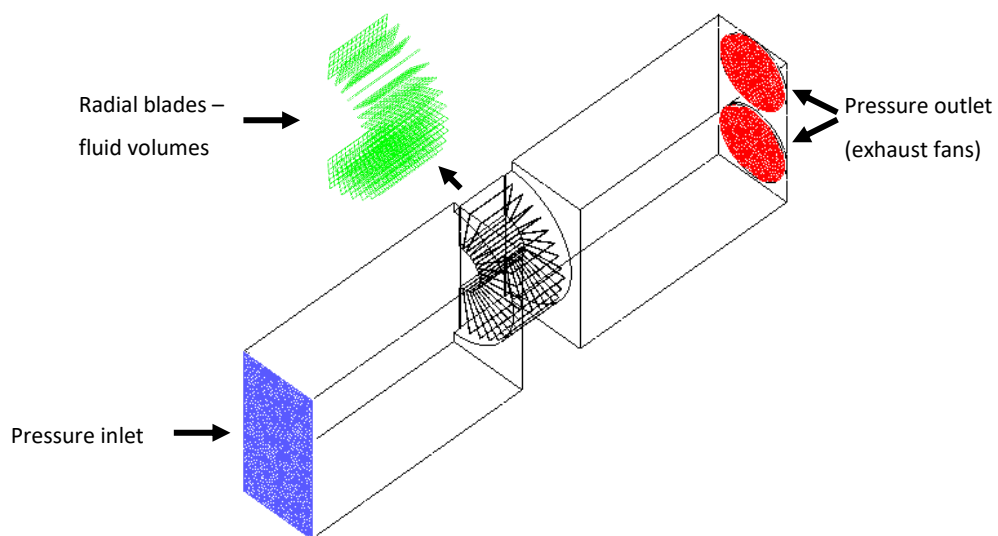


Figure 3-23 – Boundary conditions for flow domain through the ductwork

The plate volumes were added to represent the volume of material of the radial blades of the rotary wheel. By setting the body of the volumes to act as a fluid, flow can pass through the geometry unaffected, unless conditions are applied to the volume. The purpose of this was to set source term functions to the fluid volume cell zones named as the radial blades. Source term functions cannot be applied to a solid volume; therefore, the fluid volumes were necessary. Source terms can be used alter properties of the flow that pass through the selected fluid volume including the momentum, energy, mass and species. Source terms can be used to add properties to a flow but also to remove properties, for example reducing the energy in a flow to reduce air temperature or increasing momentum to accelerate the flow. As source terms can be used to both add and remove properties from a flow, for clarity source terms will refer to the addition of properties and sink terms will refer to the reduction of flow properties.

Source and sink terms were used in the CFD analysis for both heat recovery and dehumidification configurations of the radial blade rotary wheel. The heat recovery wheel only required source and sink term functions for energy values as heat was the only transferred property between airstreams. For the dehumidification wheel, source and sink terms were required for energy, mass and species transport. The species relates to the value of water added or removed from the flow. To maintain calculation stability, the same value of species addition/removal must be input for the mass term.

Separate conditions are required for each airstream for both the heat recovery and dehumidification processes. The airstreams are known as the incoming and outgoing airstreams. The incoming airstream represents the fresh, outdoor air that passes through the rotary wheel. The outgoing airstream is the exhaust air from the internal environment. The airstreams will be referred in this way for clarity.

For the heat recovery rotary wheel, the incoming airstream increased in air temperature, therefore energy source terms were required. For the outgoing airstream, the air temperature reduced, therefore energy sink terms were required. The boundary conditions used for the heat recovery rotary wheel incoming and outgoing airstreams can be seen in Table 3-2.

Table 3-2 – CFD model boundary conditions for 32 and 20 radial blade heat recovery rotary wheel configurations

Input Condition	Value	
	Incoming Air	Outgoing Air
Pressure Inlet	15Pa	15Pa
Exhaust Fan Outlet	2.5Pa	2.5Pa
Inlet Air Temperature	21.36 - 23.92°C	24.70 - 39.81°C
Wheel Rotation Speed	6rpm	6rpm
Energy Source	100,000 - 750,000W/m ³	-
Energy Sink	-	200,000 - 4,800,000W/m ³

The dehumidification rotary wheel required more source and sink terms to be set to replicate the conditions observed in the experiment. For the incoming airstream, source terms were required for energy and sink terms for species and mass functions as the reduction of relative humidity of air causes the air temperature to increase. For the outgoing airstream, sink terms were required for energy and source terms for species and mass functions as an increase in relative humidity of air causes the air temperature to reduce. The boundary conditions for

the dehumidification rotary wheel incoming and outgoing airstreams can be seen in Table 3-3.

Table 3-3 – CFD model boundary conditions for 32 and 20 radial blade dehumidification rotary wheel configurations

Input Condition	Value	
	Incoming Air	Outgoing Air
Pressure Inlet	15Pa	15Pa
Exhaust Fan Outlet	2.5Pa	2.5Pa
Inlet Air Temperature	13.42 - 17.20°C	24.68 - 39.30°C
H₂O Mass Fraction of Air	0.0075 - 0.01195g/g	0.0055 - 0.0065g/g
Wheel Rotation Speed	6rpm	6rpm
Energy Source	250,000 - 2,000,000W/m ³	-
Energy Sink	-	500,000 - 2,375,000W/m ³
Species Source	-	0.00185 - 0.38kg/m ³ s
Species Sink	0.0002 - 1kg/m ³ s	-
Mass Source	-	0.00185 - 0.38kg/m ³ s
Mass Sink	0.0002 - 1kg/m ³ s	-

The values of the boundary conditions are taken from the data measured during the experimental phase of the study. The variation of inlet air temperature for the incoming air streams is a result of the conditions of the internal air of the room the experiments were conducted in. Though attempts were made to control the air temperature, variation occurred. The low air temperature of the incoming air for the dehumidification configurations is a result of the increased relative humidity of the airstream. As the relative humidity was increased, the air temperature dropped. This will be explained further in Chapter 4. The variation of the outgoing air temperature for both configurations was a result of one of the variable of the experiment. By altering the temperature of the outgoing airstream inlet temperature, the transfer capability of the heat recovery configuration and regeneration potential of the dehumidification configuration could be tested.

3.4 CFD Model Limitations

A number of limitations of the CFD models produced for analysis were identified. As only one airstream was modelled at a time, the effect of heat losses through the ductwork of the two airstreams on each other were not accounted for. Furthermore, the energy sources and sinks

used to model the change in air temperature in the fluid zones were set as constant values. However, this would not be the case in the experiments. As the wheel rotates between airstreams, the heat gains and losses in the radial blades will be highest as the wheel enters the airstream and lowest as the wheel is exiting the airstream. The values for the energy sources and sinks did not account for this effect.

3.5 Summary

This chapter provided the theoretical background information relating to the Computational Fluid Dynamics (CFD) used in this study for modelling and simulation. The process and indicators of quality of developing a CFD model to output an accurate and reliable solution has been detailed. Good practice for selection of characteristics and models used in the simulations has been discussed. The need for accurate geometry modelling and computational mesh generation has been covered, along with the solvers and equations used for simulation. Convergence, an indicator for solution accuracy has been explored. Potential sources of errors and uncertainties in the CFD solution have been investigated with steps taken to minimise the effect of such errors and uncertainties.

Using the knowledge gained from the background theory of CFD analysis, four different configurations of radial blade rotary wheel were modelled. Two systems that shared similar geometry were designed for heat recovery and dehumidification of two adjacent airstreams. Each system was modelled and tested with varying number of radial blades. Differences in the material used for the construction of radial blades altered the use of the system. Copper plates for heat recovery and silica gel covered acrylic plates for dehumidification. The rotary wheels were located at the centre of two adjacent ducts with counter-current flow. To simplify the computation of the solution, only one duct was simulated at a time with the boundary conditions altered to replicate each duct condition. Additional volumes were added to the models to represent the volume of the transfer materials, enabling flow to pass through whilst the characteristics were altered. The CFD model, replicating the conditions experienced in the experiments, investigated properties of the flow before and after the rotary wheels.

Chapter 4

4 Experimental Methods

4.1 Introduction

The following chapter introduces the experimental studies that were carried out as part of this work. The experimental testing was used to validate the Computational Fluid Dynamics analysis detailed in Chapter 3. This chapter provides an overview to the experiment design and the parameters of the experiment.

The experiment methodology covered in the chapter detail the design of the experiment, rapid prototyping of the CAD models using 3D printing, experiment setup and the process used for measurement of the experiment properties. The chapter also presents the equipment used for experimental testing, specifying the operating principles, specifications and accuracy of the equipment.

4.2 Experiment Design

As mentioned in Chapter 2, the aim of this project was to design a heat recovery system with a sufficiently low-pressure drop to be integrated into a passive ventilation system. Maintaining a low-pressure drop across the device was important for integration with a passive ventilation system due to the low air velocity of supply air in passive ventilation systems. A device with high-pressure drop would prevent adequate ventilation supply air from being provided. Modifying the matrix of a rotary thermal wheel was identified as a suitable initial phase of the design process. By increasing the space between the materials of the matrix, it was assumed that the pressure drop of the device would be lowered to acceptable levels whilst maintaining the transfer characteristics.

Heat transfer is the result of temperature difference between two different mediums, these mediums can be solids, liquid or gases and the method through which transfer occurs depends on the type of bodies [176]. Given the design of the radial blade rotary wheel, forced convection is the method of heat transfer as air moves over the radial blades of the rotary wheel. As the aim of the radial blade rotary wheel is integration with a passive ventilation system, natural convection due to buoyancy effects would be the method of heat transfer

between the air and the radial blades. The design of the experiment is known as an open system due to the flow of air from the inlet to the outlet.

Under the first law of thermodynamics, the energy entering a system must be the same as the energy exiting the system minus the energy change within the system [176]. Under steady state conditions, that is the absence of change with time, the conservation of energy for an open system, ignoring negligible kinetic and potential energy changes, is described as:

Equation 4-1 [176]

$$\dot{Q} = \dot{m}C_p\Delta T$$

Where \dot{Q} is the rate of net heat transfer through the system, \dot{m} is the mass flow rate through the system, C_p is the specific heat capacity and ΔT is the change in temperature [176]. This equation will determine the effectiveness of the heat transfer of the radial blade rotary wheel.

The concept of the radial blade rotary wheel is shown in the CAD models in Figure 4-1 and is detailed in section 3.3.2. To experimentally test the new design of rotary wheel, prototypes of the wheel and a suitable casing were constructed and inserted into a ductwork with two channels of equal length. To test the properties of the radial blade rotary wheels, the prototype were subject to two counter-current flows with varying properties. By measuring the properties of the flows before and after the wheels in each channel, the performance of the radial blade rotary wheel design was analysed.

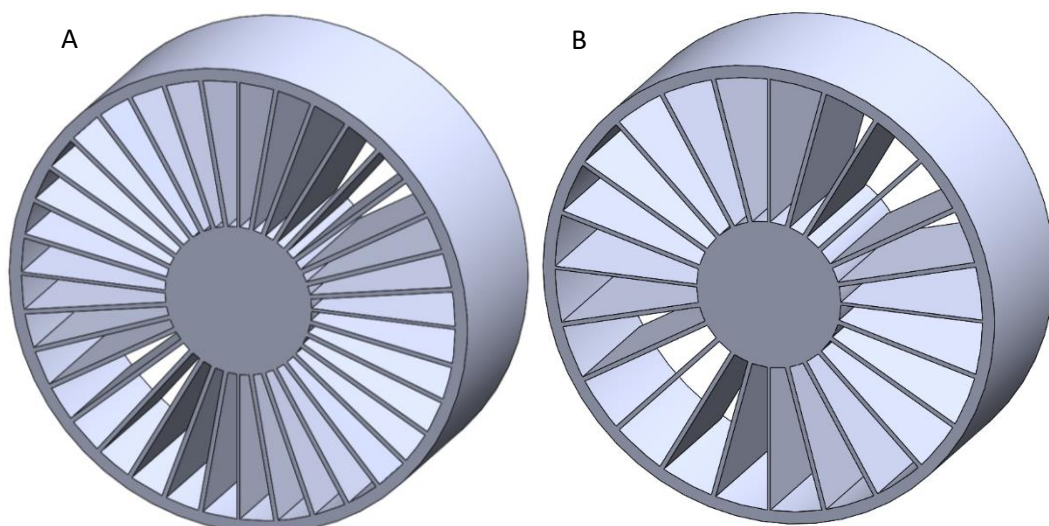


Figure 4-1 – Design of radial blade rotary wheel A) 32 blade configuration B) 20 blade configuration

The properties of the two different flows were varied at the inlet of each duct. The channels of the ductwork were referred to as the incoming air, representing the external air in a full

system, and the outgoing air, representing the exhaust air from an occupied space in a full system. A schematic of the ductwork is shown in Figure 4-2. The inlet air for both the incoming and outgoing channels was conditioned to enhance the differences in properties between the air, increasing the measureable differences before and after the wheel, if any. Measurement points were located at the vertical centreline of each channel at 100mm intervals.

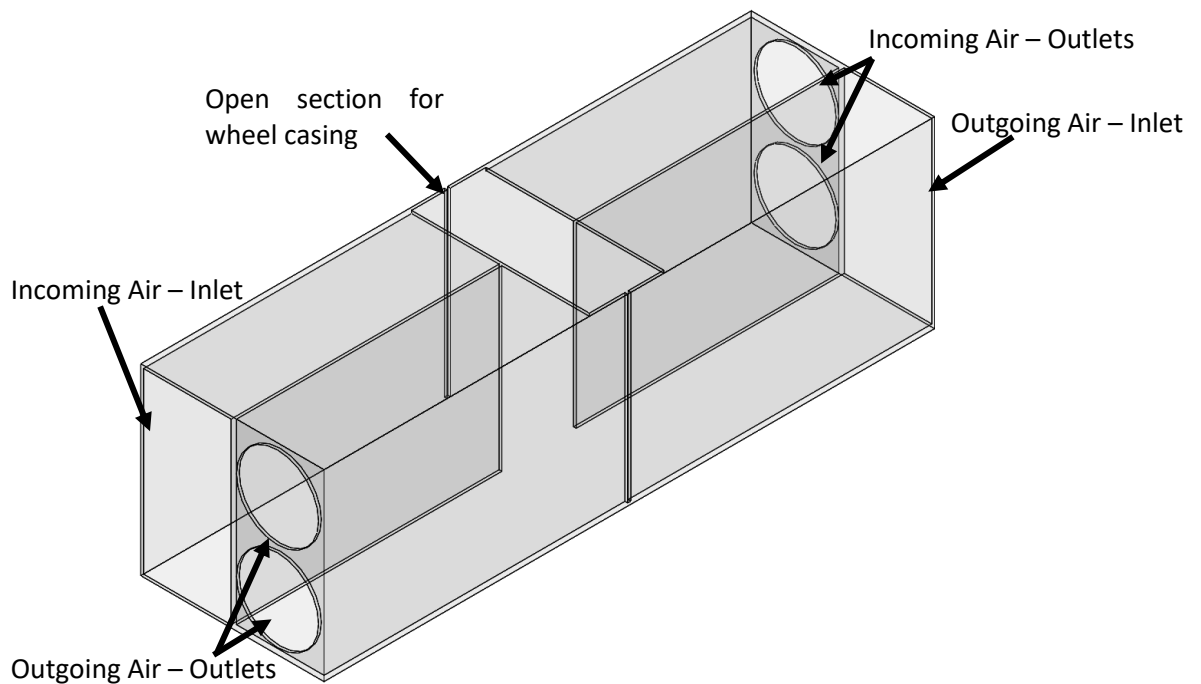


Figure 4-2 – CAD schematic of the ductwork used for experimental testing

For the heat recovery model of the radial blade rotary wheel, the conditions for the incoming airstream at the inlet were dictated by climate conditions of the internal space in which the experiment took place. Sufficient time was taken to measure the ambient conditions, but no additional conditioning was attempted. The outgoing airstream was conditioned using a heat source at the inlet. This enabled a range of inlet temperatures to be provided to the airstream. This was beneficial as the recovery capabilities of the system were tested for a relatively constant incoming airstream temperature and a variable outgoing airstream temperature.

The dehumidification model of the radial blade rotary thermal wheel required that the condition of the incoming airstream be altered to test the moisture transfer capabilities of the system. The relative humidity of the incoming airstream was increased using a sonic humidifier device. The increase in relative humidity of the airstream had the effect to reduce the air temperature. The reduction in air temperature was dependent on the increase in

relative humidity. This was due to the increased saturation level of the air. As more water was held in the air, the temperature reduced. The outgoing airstream conditions were similar to those used in the heat recovery experiment. The heat source at the inlet altered the air temperature over a predetermined range. The source of air for the outgoing airstream was in a closed-loop; therefore, the air had low relative humidity. This was beneficial as it provided a contrast to the high relative humidity of the incoming airstream.

For transfer to occur between the two channels via the rotary wheel, the wheel rotated constantly at a rate of 6rpm, driven by a motor and gear system that was designed into the outer shell and casing of the rotary wheel by a custom-designed system. Typically, heat recovery rotary wheels rotate at a speed between 5-20rpm and desiccant rotary wheels at a speed 5rpm or lower [123]. Given the size of the wheel and the motor available for use, 6rpm was decided as a suitable compromise of rotation speed for both wheels. This is covered in Chapter 3.

The driving forces of the air through the channels was accomplished by mounting four identical axial fans to the channel outlets. Air was drawn from the inlets through the ducts by the axial fans. This was used as the setup to drive the flow because the velocity profile that was established from this arrangement gave the profile with the most uniformity. Further details of how this arrangement was decided upon follow.

The majority of the components of the experiment were non-standard parts and so required design, build and assembly, a large number of which required use of rapid prototyping 3D printing. 3D printing enabled shapes to be fully customised, within printer tolerances, and modifications made to the components quickly realised. Further detail of the 3D design and printing process will be detailed later in this chapter.

The full experiment setup can be seen in Figure 4-3. A number of modifications were made to the experiment setup during initial tests to provide a more accurate test. Separators were attached between the inlet and outlets of the opposite flows; this prevented the recirculation of air from the outlets back through the inlets, negatively affecting the condition of the inlet air. Mesh cloths were placed over the inlets for both channels. During testing of the ductwork, it was shown to improve the uniformity of the flow profile through the channels. Additionally, the mesh cloth increased the relative humidity of the incoming air channel during the dehumidification tests due to the moisture build up in the cloth fabric.

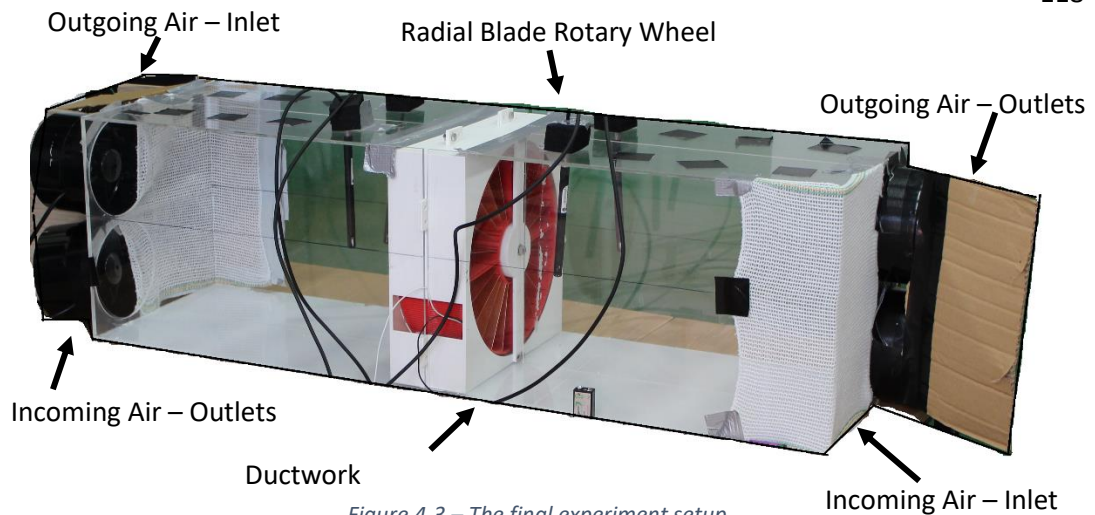


Figure 4-3 – The final experiment setup

4.3 Ductwork Design and Testing

In order to complete the experimental testing of the radial blade rotary wheel, a test ductwork was required. The ductwork required two separate channels to prevent the flows mixing, except for a section at the middle of the ductwork where the rotary wheel could be located. It was necessary for the setup of the channels that the flows could move in a counter-current arrangement. This was to replicate the arrangement of the flow expected in a passive ventilation system.

The design of the ductwork was simple but also balanced by material and construction costs. The dimensions of the ductwork were 335x335x1116mm for the height, width and length respectively, including a 5mm material thickness. The ductwork can be seen in Figure 4-4. This correlated with the dimensions of the casing for the rotary wheels that was 325x325 for height and width, enabling the casing to sit flush in the ductwork.



Figure 4-4 – Acrylic ductwork used in experimental testing

No facilities were available to construct the ductwork within the university. Therefore, the CAD drawings were sent out to specialist fabricators with expertise in bespoke design and high strength acrylic materials. Due to the unique design of the ductwork, the high cost of the construction constricted the length of the ductwork to 490mm either side of the wheel due to material and labour costs. Though a longer channel length would have resulted in a fully developed flow in the channel, it was assumed that the flow profile in the channel could be made uniform.

Flow through the ductwork was achieved by mounting identical axial fans to each of the four outlets of the ductwork, arranged so that air would be drawn from the inlet, through the channel, and exhaust at the outlets.

4.3.1 Ductwork Flow Profile

Understanding the flow profile of the air through the channels of the ductwork was an important consideration for comparison with the CFD model. As the boundary conditions of the CFD model needed to match the conditions of the experiment, knowledge of the flow profile was essential. Furthermore, the unusual driving mechanics of the air flow through the ductwork required exploration to justify the design.

To test the flow profile of the ductwork, each channel was analysed separately. Additional material was added to the section of the ductwork missing to provide a continuous channel for the air to flow. Further material was added to the top section of the ductwork to prevent air escaping. The critical location for the flow profile was judged as the measurement prior to the wheel, positioned 100mm away from the wheel surface. The measurement points can

be seen in Figure 4-5. It was assumed that the flow profile should be fully developed at this point, before interacting with the rotary wheel and so the measurement of the flow at this point was essential. The air velocity at these measurement points, in both the incoming and outgoing channels, was measured at a range of heights. Nine equally spaced measurement locations were set across the height of each channel.

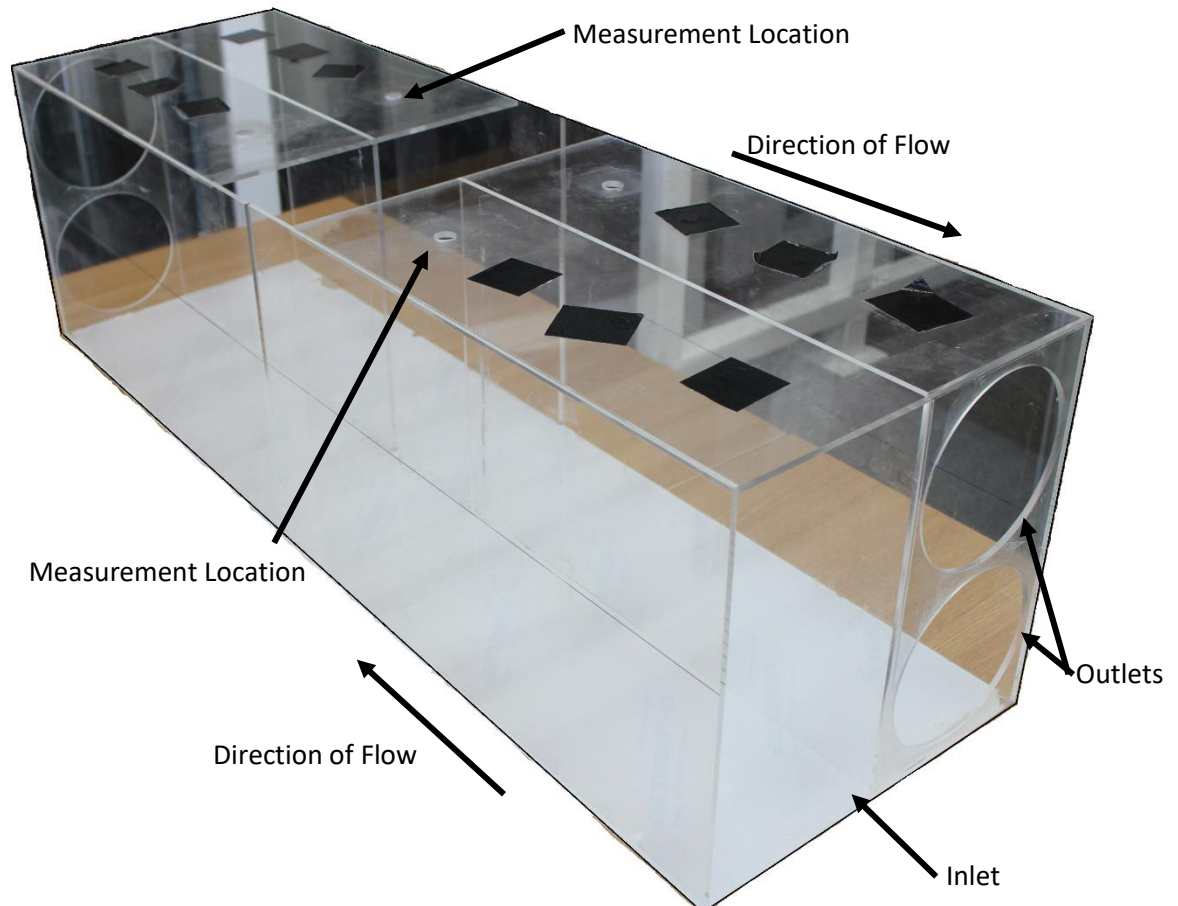


Figure 4-5 – Location of measurement points for ductwork flow profile

A number of methods were attempted to determine the flow profile of the air in the channels. The aim was to find the method that created the most developed flow at the measurement point 100mm before the surface of the rotary wheel.

4.3.1.1 Forward Driven Flow

The original design of the ductwork used forward driven air flow from the axial fans. The fans were mounted in the circular cut-outs used in the final experimental setup. This arrangement gave the flow the full length of the channel to develop. It was assumed that the flow would be fully developed by the measurement points before the location of the rotary wheel.

Figure 4-6 shows the flow profile of the forward driven flow arrangement. Though it was assumed that the arrangement would provide a developed flow at the measurement

location, the results show that the uneven distribution of air velocity across the height of the channel did not yield a uniform flow.

The design of the axial fans is the likely cause for the uneven distribution of the flow along the height of the channel. The central housing of the axial fans holds the motor that generates the drive to the fan blades. This non-rotating area does not generate flow, as it is static. This creates a wake area in front of the housing, generating turbulence as the flow moved forward. In the current arrangement, the channel is not long enough for the flow to develop fully before reaching the measurement location before the surface of the rotary wheel.

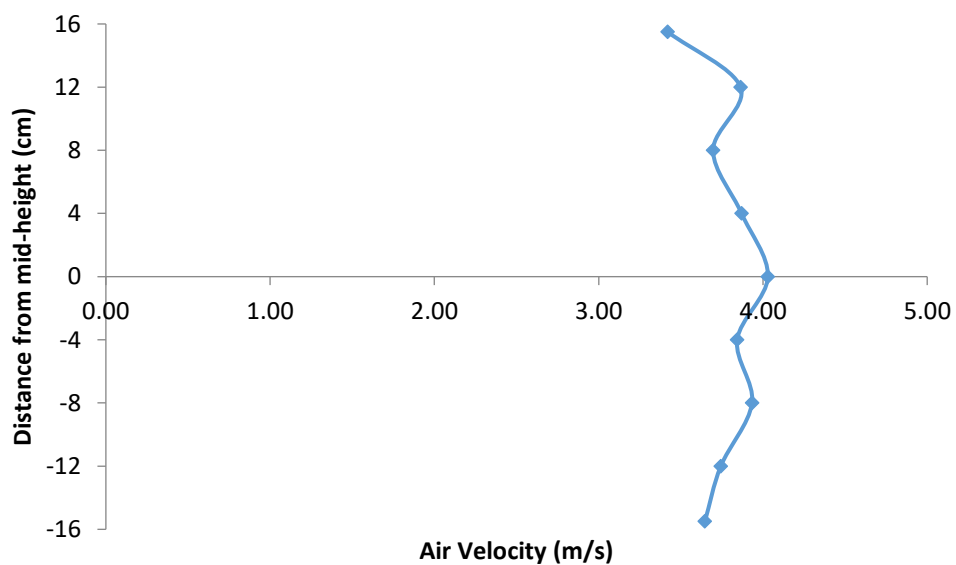


Figure 4-6 – Flow profile of forward driven flow through channel at measurement location with axial fan arrangement

A second method using the forward facing axial fans was used to generate a flow. Mesh cloths were placed over the back opening of the axial fans. It was thought that the openings of the mesh cloths would help to straighten the flow through the fans, providing a more uniform flow profile at the measurement location. The flow profile of the arrangement can be seen in Figure 4-7. The results of the measured air velocity at the measurement location indicate that the uniform flow profile is improved somewhat compared to the arrangement without the mesh cloths.

Between measurement points at 12cm above and 12cm below the mid-height, the flow, shown in Figure 4-7, exhibits the typical profile of turbulent flow in a pipe. Low values of velocity close to the pipe wall, increasing to a maximum at the mid-point. However, the values for the alternative arrangement flow at 16cm above and below the mid-point far

exceed the other values of the profile. These measurement points are located closest to the channel walls and so should have the lowest value. One possible explanation of this is that the flow at the channel walls is separated from the rest of the flow due to the shape and position of the axial fans within the channel. The flow separation may induce high turbulence flow in this area, causing the high air velocities measured. Alternatively, the diameter of the hole drilled for the velocity measurement device is larger than the diameter of the measurement device probe, leaving space between the hole and the probe. Air may escape through this gap, accelerating as it does. This may cause the increase in air velocity at the top measurement point due to the swirling flow of the rotating wheel. The cloth meshes had a significant effect on the flow profile through the duct.

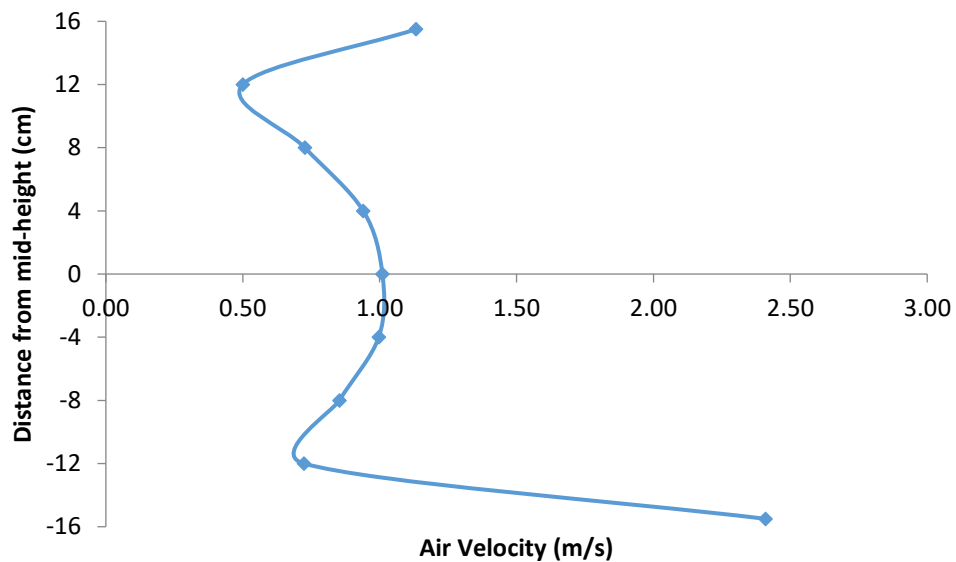


Figure 4-7 – Flow profile of forward driven flow through channel at measurement location with axial fans and mesh cloth arrangement

4.3.1.2 Honeycomb Flow Straighteners

As the initial arrangement of the axial fans did not yield the assumed flow profile through the channel as the measurement location, an alternative method to correct the flow was attempted. Honeycomb flow straighteners are often used in wind tunnels to adjust for flow and turbulence optimisation [177]. Honeycombs channel the air through narrow gaps at regular spacing across the cross-section of the channel, this provides a uniform distribution for the flow.

A honeycomb section was constructed for the channels using straws all cut to the same length of 5cm and joined together to fit the cross section of the ductwork channel. The honeycomb was positioned within the channel at different intervals from the axial fans to

determine the distance from the fans had the greatest effect on the flow profile. The axial fans were still arranged in the way as in 4.3.1.1. Measurements of the air velocity were taken at the nine points previously used. The results of the measurements are shown in Figure 4-8.

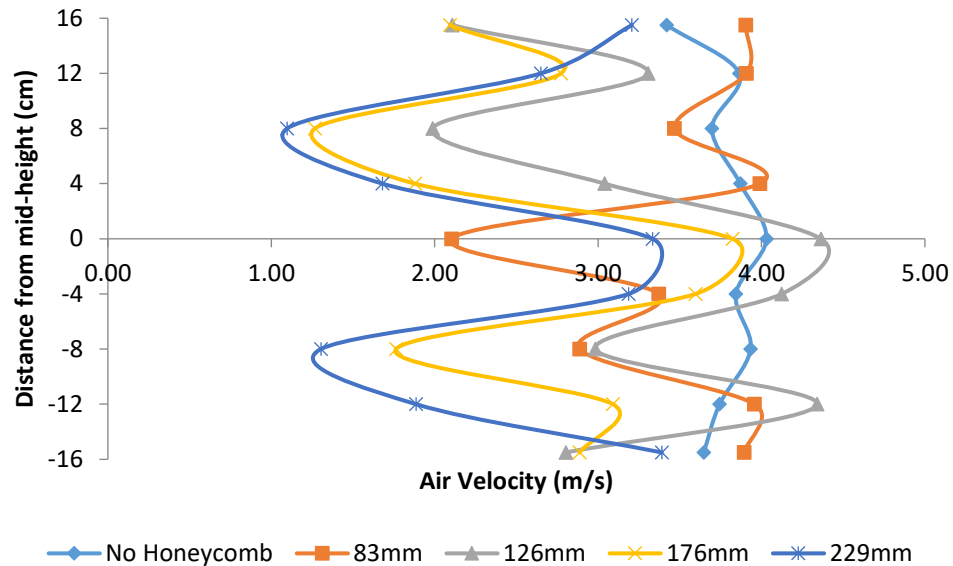


Figure 4-8 – Flow profile of forward driven flow through channel at measurement location with axial fans and honeycomb arrangement

The effect of the honeycomb on the flow profile is drastic. The introduction of the honeycombs into the channel did not improve the uniformity of the profile, regardless of the distance of the honeycomb from the fans. Figure 4-8 shows a comparison between the profile before the honeycombs were included and the profiles after. The variance between values for the no honeycomb test was 0.033 with a standard deviation of 0.18 compared with a high of 0.858 variance and 0.93 standard deviation of values when the honeycomb was placed 229mm from the fans. This suggests that the values for the air velocity before the inclusion of the honeycomb were significantly more similar than when the honeycombs were introduced. When the honeycomb was placed 83mm from the fans, the variance of the measurements was 0.410 and the standard deviation, 0.64, both much higher than without the honeycombs. Both variance and standard deviation are indicators of the distance of values from the mean. The greater the values, the greater the spread of values. The high spread of air velocity values for all the honeycomb arrangements show that the inclusion did not improve the profile of the air in the channel

4.3.1.3 Suction Driven Flow

As the forward driven flow and honeycomb arrangements did not yield a flow profile that was deemed suitable for experimental testing, a third method was attempted. The axial fans

were mounted in the opposite direction than the first two arrangements. This meant that air was drawn from the inlet, through the channel, and out of each of the fans at the outlet. In addition, the mesh cloths covered the inlet area as this had shown to improve the profile of the forward driven flow arrangement. The setup of this can be seen in Figure 4-9.

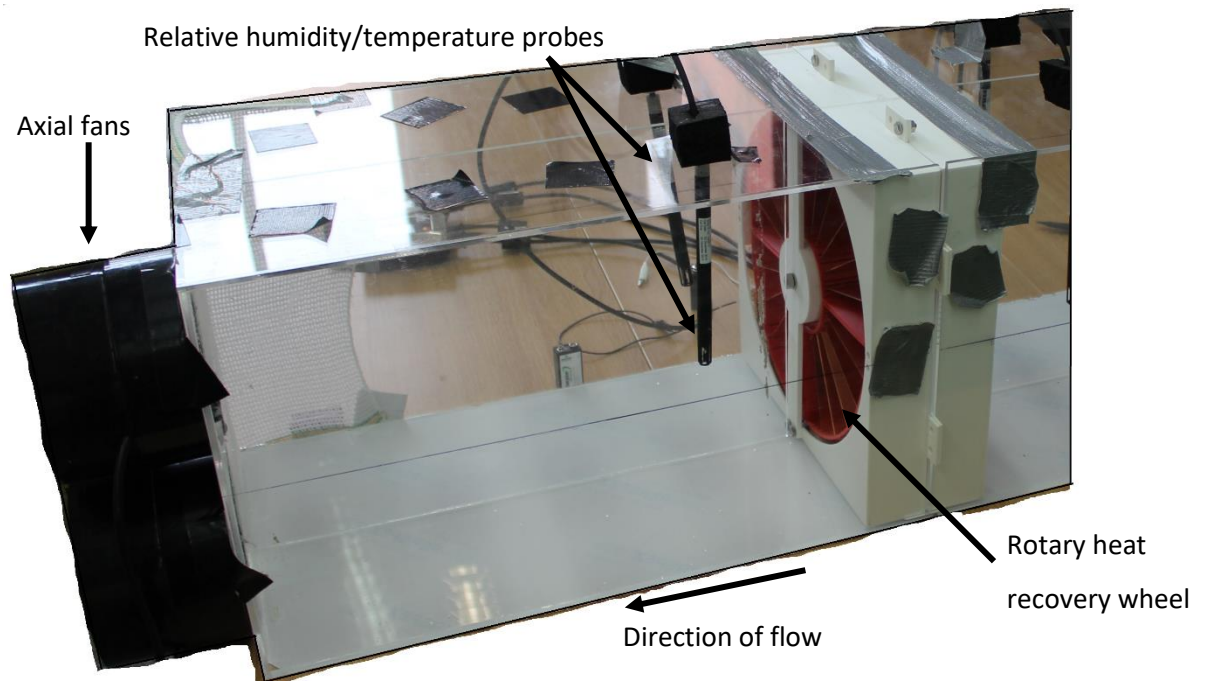


Figure 4-9 – Experimental setup of suction driven flow by outlet mounted fans (rotary wheel was not mounted for calibration tests)

The air velocity was measured across the same nine points at the measurement location 100mm from where the surface of the rotary would be located during the experiment for both the incoming and outgoing airstreams. The measurements can be seen in Figure 4-10 and Figure 4-11.

The two flow profiles from the suction driven flow were more evenly distributed than the previous attempts to create a suitable flow profile. The variance for the air velocity values in the incoming airstream was 0.01 with a standard deviation of 0.08. The variance for the air velocity in the outgoing airstream was 0.02 with a standard deviate of 0.13. This is significantly better than the values seen in the previous examples and shows the even distribution of air velocity across the height of both the channels. The high values for air velocity at the channel walls seen in the forward driven flow arrangement with the mesh cloths is not present in the data.

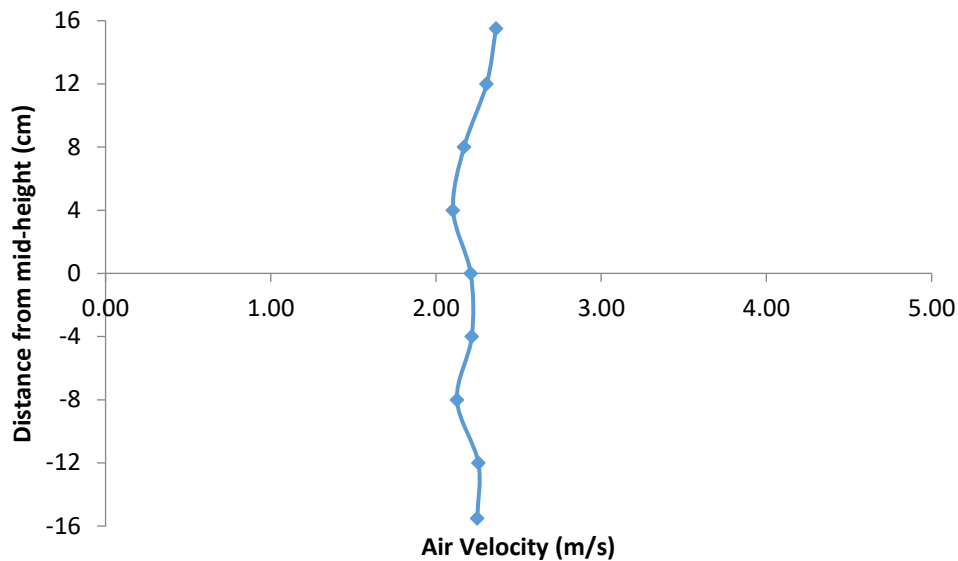


Figure 4-10 – Flow profile of suction driven flow through the incoming airstream channel at measurement location

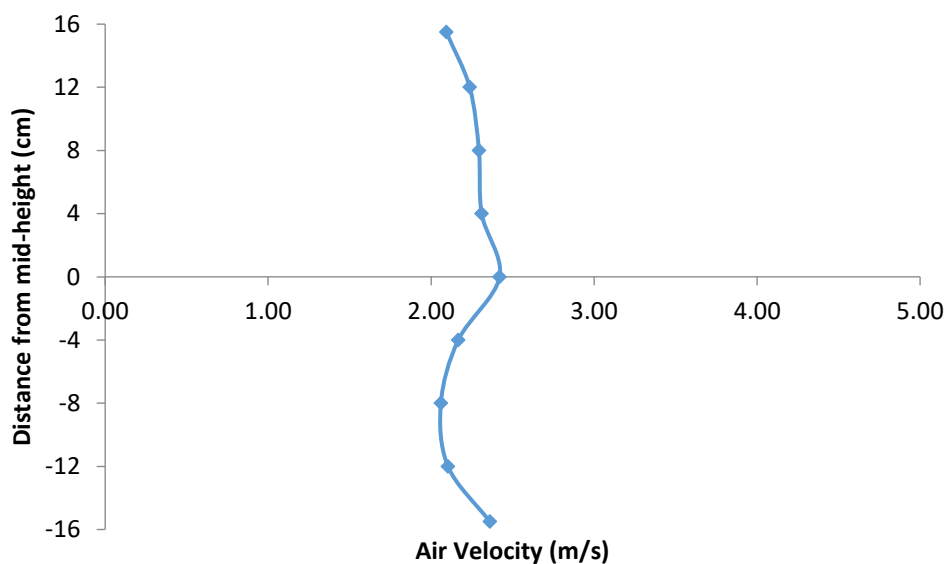


Figure 4-11 – Flow profile of suction driven flow through the outgoing airstream channel at measurement location

The difference between the flow profiles of the incoming and outgoing airstreams is likely due to the setup at the inlets of each channel. As previously mentioned, the inlet air for the incoming channel is drawn from the internal environment of the laboratory. The inlet air for the outgoing channel is pre-heated to increase the air temperature of the air. This is achieved by feeding air from a closed-loop subsonic wind tunnel in the laboratory. The wind tunnel uses an electric heater to change the temperature of the air. This air was fed to the inlet of the ductwork so that a range of outgoing inlet air temperatures could be tested. Though the

pipes feeding the air from the wind tunnel were positioned 300mm from the inlet of the outgoing air channel, the differences between the flow profiles for the incoming and outgoing airstreams are likely a result of this.

4.3.2 Ductwork Flow Calibration

As the suction driven flow arrangement was the most suitable for use in the experiment, it was important to calibrate the Computational Fluid Dynamics model to replicate the same flow conditions. The values for the air velocity for the incoming and outgoing airstreams provided benchmark values for the CFD results to be compared against. The closer the CFD measurements, the more accurate the final solution.

The geometry of the empty channel was created and imported into Fluent for meshing and simulation. As the conditions for each airstream were kept constant, the geometry was reflective of both the incoming and outgoing airstreams as the conditions for temperature and relative humidity did not affect the flow profile. The mesh of the channel can be seen in Figure 4-12. To give an accurate comparison between the benchmark results from the channel testing and the CFD results, the position of the nine measurement points within the channel were replicated in the CFD model. The inlet and outlet conditions of the model were altered a number of times to find the boundary conditions that resulted in the solution with the lowest error compared to the benchmark values.

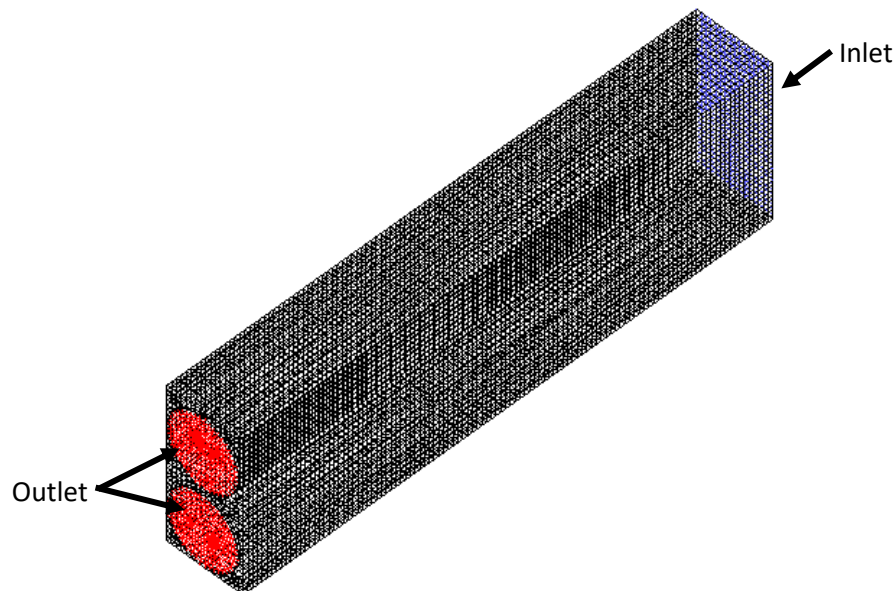


Figure 4-12 – Mesh of ductwork channel used for CFD calibration

The boundary conditions for the inlet and outlets of the CFD model were set as pressure-inlet and exhaust-fan respectively. Configuring the boundary conditions to have pressure as

the base unit encouraged air to flow through the channel. Previous attempts to use velocity-inlet settings did not result in a flow through the channel. As the inlet was open to the environment, the gauge pressure at the inlet is 0Pa. The pressure values for the exhaust-fan boundary conditions were increased until the error between the benchmark experimental and CFD results was deemed suitably low.

Figure 4-13 shows the comparison between the two benchmark air velocity profiles compared to the CFD model with the lowest total error percentage. The total error percentage between the CFD results and the airstreams was 7.24% and 7.31% for the incoming and outgoing airstreams respectively. The error percentage was achieved by setting the inlet pressure to 0Pa to simulate the atmospheric pressure at the inlet and 10Pa at each of the exhaust fan outlets. These were obtained by altering the values at the pressure boundaries until the values with the lowest error were found

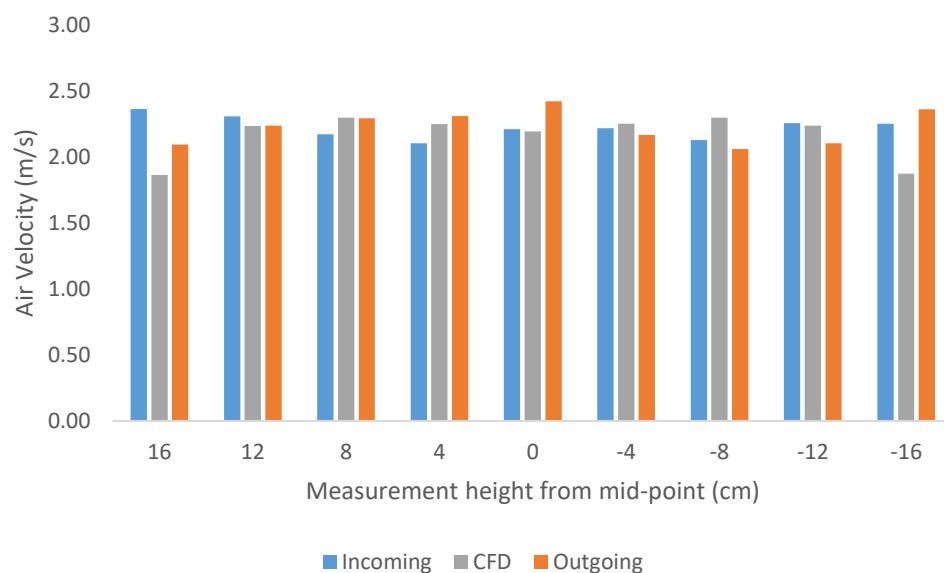


Figure 4-13 – Comparison of incoming and outgoing airstream velocity with CFD simulation

The results show that the CFD follows a similar trend as each of the benchmark data sets. The CFD results show a more typical trend for flow in a pipe whereby the air velocity closest to the wall, the values at -16cm and 16cm, have the lowest values. These measurement points show the greatest error percentage compared to the benchmark results. This is likely due to a combination of the inaccuracies of the experiment setup and the flow recirculating at the holes drilled for measurement in the experiment.

The streamlines of the flow in the CFD model are shown in Figure 4-14. It can be seen that the flow moves through first half of the channel uniformly. The closer the flow to the channel

walls, the slower the velocity. The flow reaches a maximum velocity at the mid-height of the channel. The flow accelerates as it approaches the outlets where the fans are located.

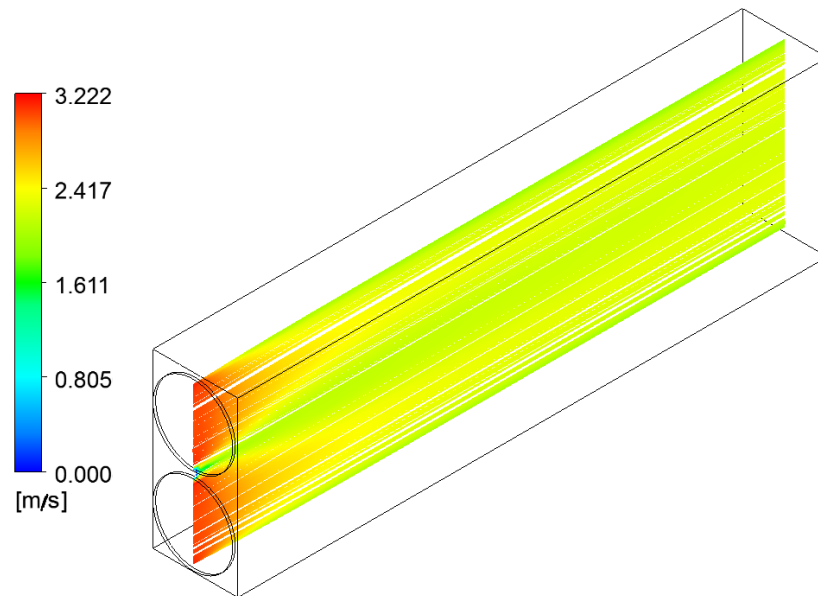


Figure 4-14 – Streamline contours of flow through ductwork channel using experiment boundary conditions

4.4 Experimental Model

For the experimental model to accurately validate the CFD simulations, the geometry of the prototype and the conditions of the experiment must match the simulations as closely as possible. Constructing the prototype to match the computational model would be difficult using traditional prototyping methods. To ensure high levels of accuracy, substantial amounts of time would also be required for detailed construction. Solely relying on CAD geometry files would provide the potential for mistakes.

To overcome these potential problems, rapid prototyping using a 3D printer was used. The geometry file used for the creation of the CFD model was exported to the printing software, ensuring that the prototype was constructed with the exact same dimensions as the CFD model. Furthermore, the 3D printing allowed for alterations to components of the experiment to be manufactured quickly, reducing the lead up time and improving the total testing time.

The HP Designjet 3D printer, shown in Figure 4-15, was used for the rapid prototyping of the components of the radial blade rotary wheel design. The Designjet 3D printer is a commercially available 3D printer that uses recyclable acrylonitrile butadiene styrene (ABS) plastic as the model material. This series of printers build layers of partially melted ABS

plastic upon each other to create a 3D model. This process is known as additive manufacturing or fused deposition modelling (FDM).



Figure 4-15 – HP Designjet 3D Printer

The layers of ABS plastic are built up individually as the printing head moves along two axes in the required shape. Once a layer is completed, the modelling base moves in the vertical direction, ready for the next layer of printing. This is more clearly seen in Figure 4-16. The printing head moves along the x and z axes for a single layer, before the modelling base is repositioned in the y-axis to print the next layer. As the layers build up, the model takes shape.

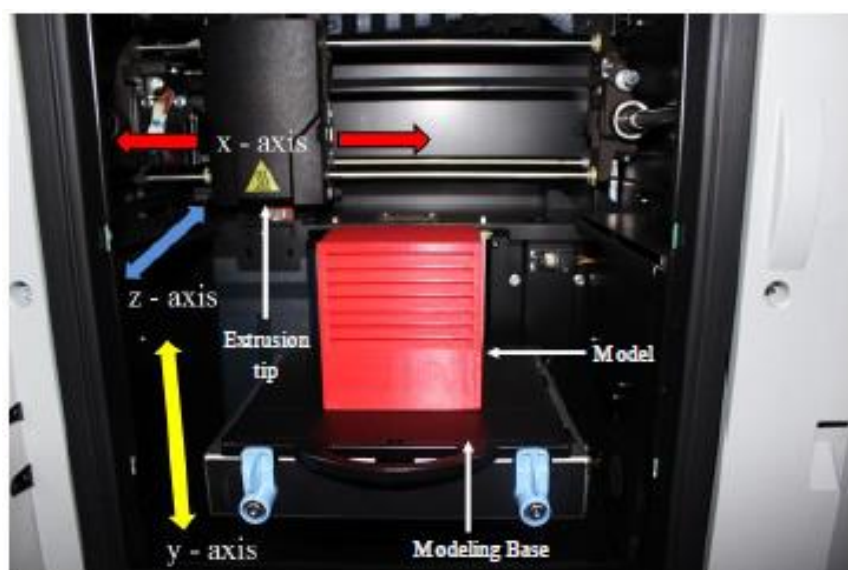


Figure 4-16 – Printing bay of HP Designjet 3D Printer [170]

In order for 3D models to be constructed, support to the model material may be required as the height of the model increases. Layers of a water soluble support material is extruded as required, the dual extrusion nozzles of the printing head enable the two types of material to be printed on the same layer. The support material can be easily removed, either in a water solution or gently removed from the model material provided no damage to the model is caused. Examples of the two types of material in the spools can be seen in Figure 4-17.

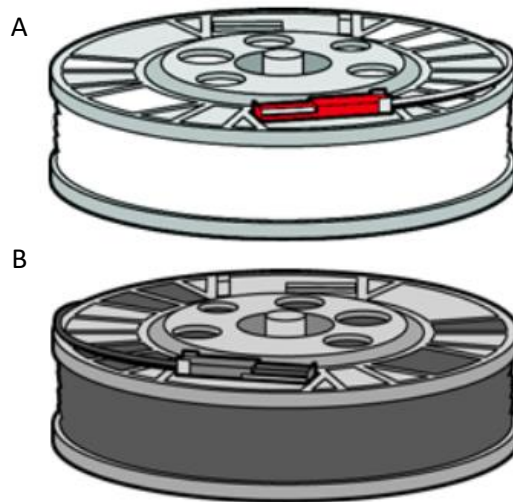


Figure 4-17 – Schematic of A) model material spool B) support material spool

4.4.1 Radial Blades

Two types of radial blade were used for the experiment. Copper blades were used for the heat recovery configuration of rotary wheel and silica gel covered acrylic blades were used for the dehumidification configuration. An example of the copper blade used can be seen in Figure 4-18 and an example of the silica gel covered acrylic blade can be seen in Figure 4-19.

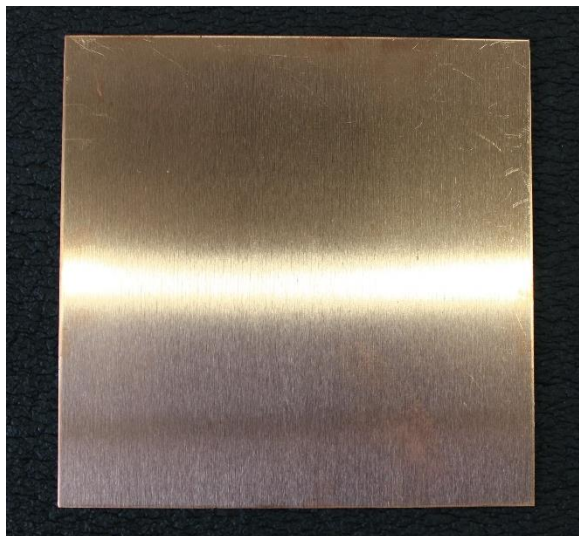


Figure 4-18 – Heat recovery radial blade made of copper metal

The copper radial blade was made from 99% pure copper, allowing for some impurities of the material. Each blade measured 100x100x1mm. The total dimensions of the blade open to the airstream was 94x100x1mm. The blade was inserted to 3mm slots in the inner rotary wheel shell at each end for stability. Aluminium, or an aluminium alloy, is typically used in heat recover rotary wheels due to the moderately high thermal conductivity, cheap price and low density. A comparison of properties of copper and aluminium are shown in Table 4-1.

Table 4-1 – Material property comparison

	Copper	Aluminium
Symbol	Cu	Al
Density	8.96g/cm ³	2.70g/cm ³
Thermal Conductivity	401W/ (m.K)	237W/ (m.K)
Malleability	High	High
Ductility	High	High
Corrosion Resistance	High	High

As a significant amount of aluminium is required to construct a matrix for a rotary wheel, the low price and weight is attractive. As the radial blade design limits the amount of material used in the configuration to minimise the pressure drop across the device, a material with high thermal conductivity is required. Copper was chosen for this reason. As less material is used in the construction of the radial blades, the relatively high density and cost of copper is offset.

Silica gel beads were bonded to the faces of a 100x100x1mm acrylic sheet. A 3mm gap was left at either end of the acrylic sheet to allow the dehumidification radial blades to fit in the guide slots of the inner rotary wheel shell for stability. The silica gel beads had an average diameter of 1mm. This gives the total thickness of the dehumidification radial blades as 3mm. Acrylic was chosen as the base material for the radial blades due to the low density and chemically inert properties of the material. Furthermore, acrylic provided a good bond between silica gel beads and acrylic surface.

Silica gel was chosen as the desiccant material for dehumidification for a number of reasons. Silica gel has a specific surface area of 800m²/g. The high surface area to volume of silica gel provides a high rate of adsorption for water molecules. The high surface area to volume also encourages desorption of the water molecules at lower regeneration temperatures compared to other desiccant materials. This is beneficial in dehumidification rotary wheels

as lower regeneration temperatures result in lower energy demand for a ventilation system, as the air does not have to be raised to as high a regeneration temperature

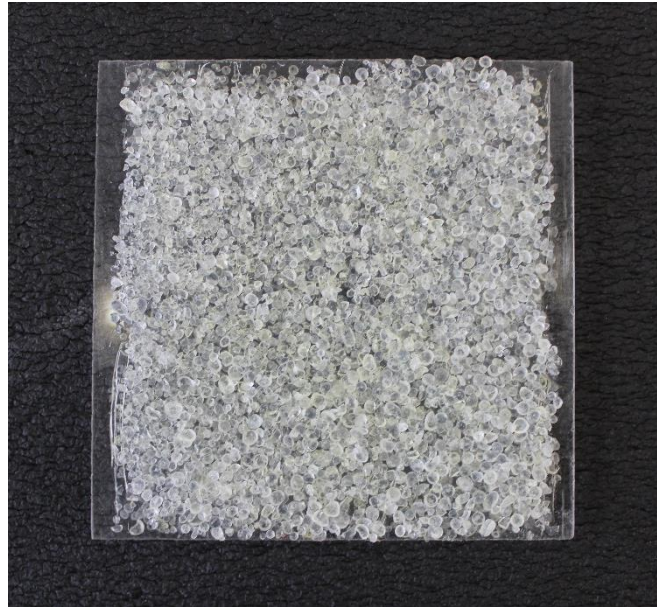


Figure 4-19 – Dehumidification radial blade made of acrylic and silica gel

Thirty-two of each of the copper and silica gel radial blades were required for the experiment. All blades were uniform with small variation of the silica gel radial blades due to the adhesion of the silica gel beads to the acrylic blade.

4.4.2 Inner Rotary Wheel Shell

The inner shell of the rotary wheel was designed to house the heat recovery and dehumidification radial blades. Given that the testing of the radial blades rotary wheel aimed to test configurations of 20 and 32 blades, an adaptable system capable of housing both configurations was desirable from a material use and manufacturing time viewpoint. A schematic of the inner shell of the rotary wheel can be seen in Figure 4-20. The radial blades were designed to sit in the slots of the shell at the correct spacing for the configuration.

The outer diameter of the inner shell was 145mm. As the radial blades were designed to be 100x100mm in shape, the shell was configured to house these. 3mm deep slots were created in the shell within which the blades could sit securely. A lip at the bottom of each slot supported the blade, holding it securely and preventing it from slipping out.

Four inner shells were manufactured to make up the inner rotary wheel shell using the Designjet 3D printer, made from the ABS plastic and following the process described. This ensured consistency of the construction from part to part and high accuracy from the geometry CAD files.

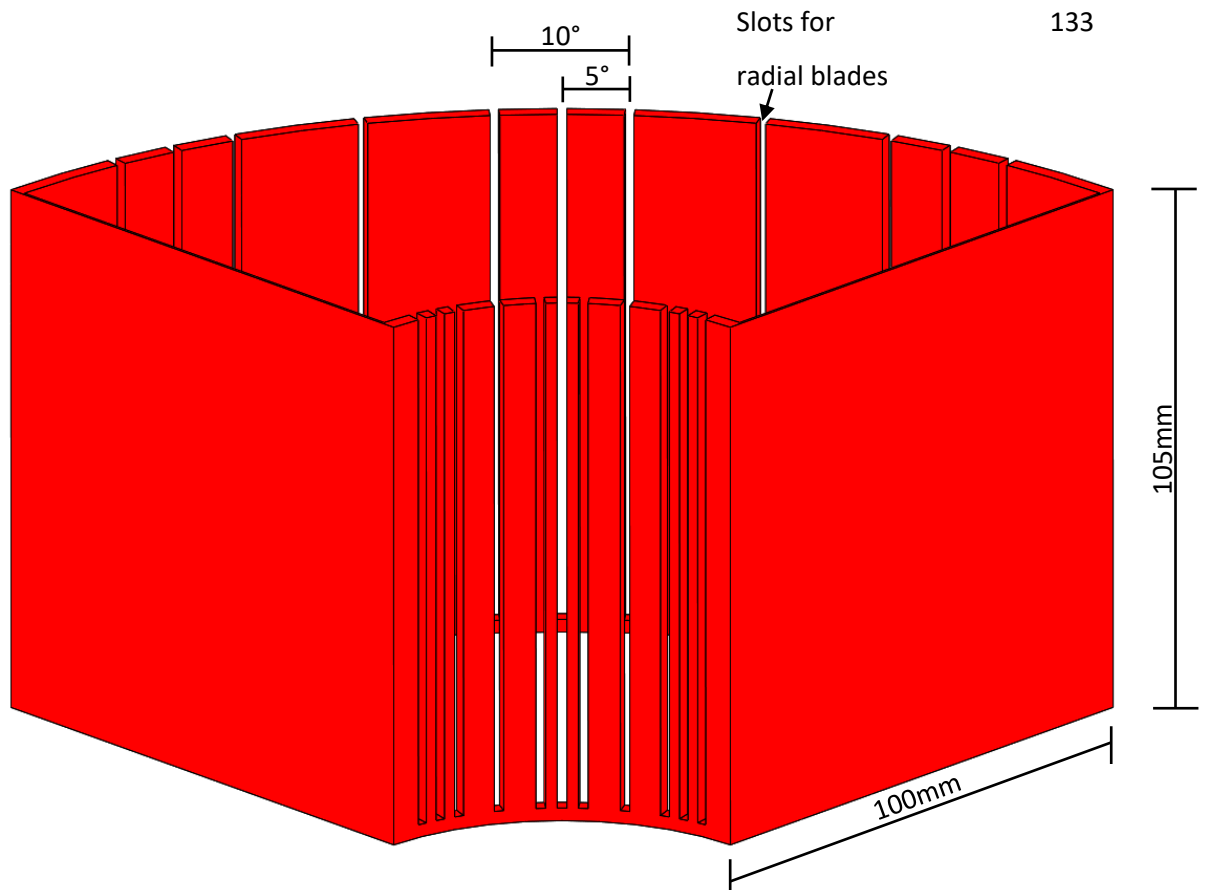


Figure 4-20 – Inner rotary wheel configuration

The rotary wheel shell was required to house 32 and 20 radial blades at equal spacing. Therefore, the angles between the radial blades was required to be consistent. For 32 blades in a configuration, eight blades were required per quarter of wheel. The angle between blades was set at 10° to accommodate the eight blades. For the 20 blade configuration, five blades per quarter were required. Therefore, the angle between blades was set at 15° . The arrangement of slots for the blades can be seen in Figure 4-21.

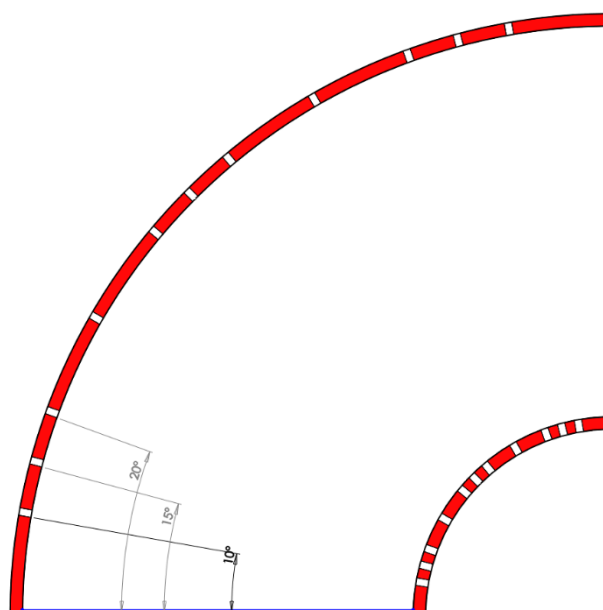


Figure 4-21 – Angles of inner wheel configuration

4.4.3 Outer Rotary Wheel Shell

The rotary wheel was split into two sections, the inner rotary wheel shell and the outer rotary wheel shell. The inner rotary wheel shell was designed to fit inside the outer rotary wheel shell. This allowed the rotary wheel to be reconfigurable, saving material costs and manufacturing time. 3D printing was used for the manufacturing of four outer shells, made from ABS plastic. The printing allowed for high accuracy and consistency between each component, which was important for assembly of the wheel. The inner shell components were designed to fit exactly in the outer shell with minimal tolerance. The accuracy of the 3D printing process allowed this.

The outer diameter of the shell was 150mm from the centre point. This was the maximum size possible for printing in the DesignJet 3D printer. One end of the outer shell featured an inner lip; this prevented the inner shell from sliding through and provided support for the assembly. The shape of the outer shell can be seen in Figure 4-22.

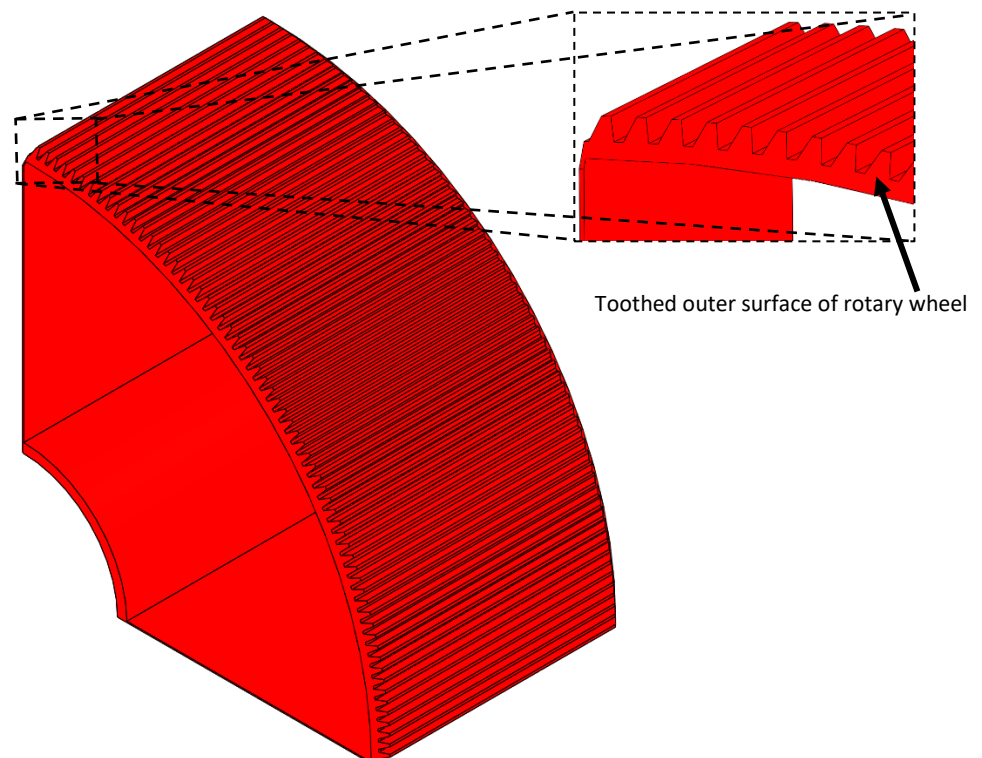


Figure 4-22 – Outer rotary wheel configuration including close up of toothed outer shape for rotation by gear

A toothed gear attached to a small battery powered motor provided the rotation of the rotary wheel. The initial design for the outer wheel shell featured a smooth surface, however, this did not provide the necessary grip to rotate the wheel. Therefore, the outer shell was designed to match the teeth on the gear, allowing smooth rotation of the wheel. The final shape of the outer surface of the wheel is shown in the inset of Figure 4-22 and the toothed

gear is shown in Figure 4-23. The motor rotated at 200rpm with a 6mm shaft for rotation. The diameter of the toothed gear was 40mm. Given the 300mm diameter of the rotary wheel, this meant that the wheel rotated at a constant speed of approximately 6rpm.

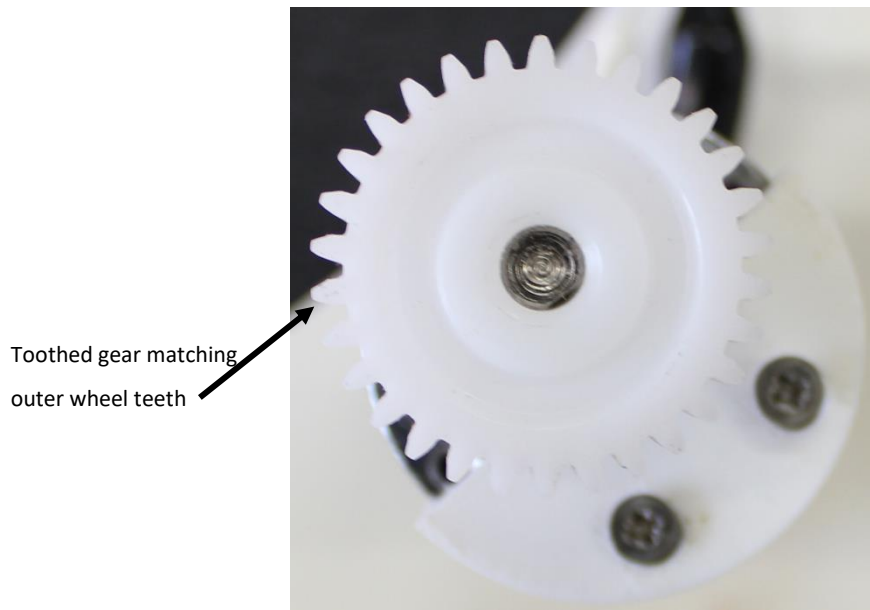


Figure 4-23 – Toothed gear used for rotation

4.4.4 Rotary Wheel Casing

A suitable casing was designed to hold the rotary thermal wheel in place in the ductwork for experimental testing. The case was printed using the Designjet 3D printer and made from ABS plastic. The front and inside view of the casing can be seen in Figure 4-24.

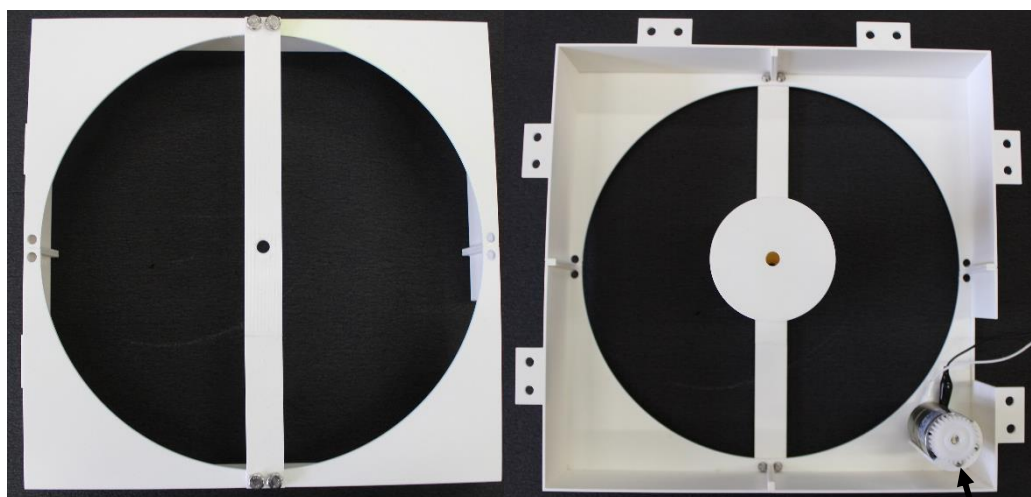


Figure 4-24 – Front and inside view of rotary wheel casing

Motor used for rotation

Each side of the case was printed as individual quarters and glued together to form each half. The quarters were not exact copies as differences were required. The motor was secured in the case by a mount designed to house half of the motor in one of the lower quarters. This

can be seen in the bottom right corner of Figure 4-24 and Figure 4-25. In addition, a gap was left to accommodate the leads required for the motor.

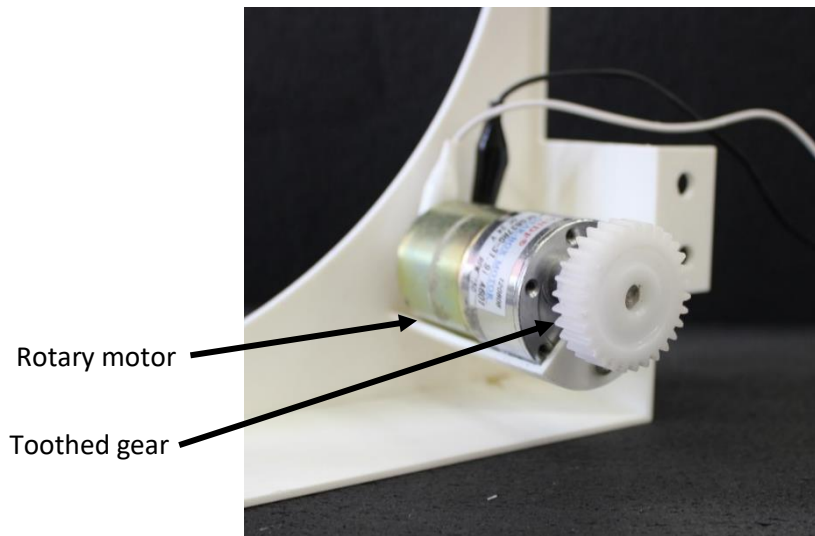


Figure 4-25 – Motor located in mount with toothed gear in position

The halves of the case were attached together by nut and bolts that fixed to brackets designed into the case quarters. This secured the case properly. The rotary wheel rotated around a central shaft in the case. The diameter of the shaft was 78mm. The shaft connected through either side of the case by a vertical brace strut that provided additional strength to the casing. The assembly of the case can be seen in Figure 4-26.

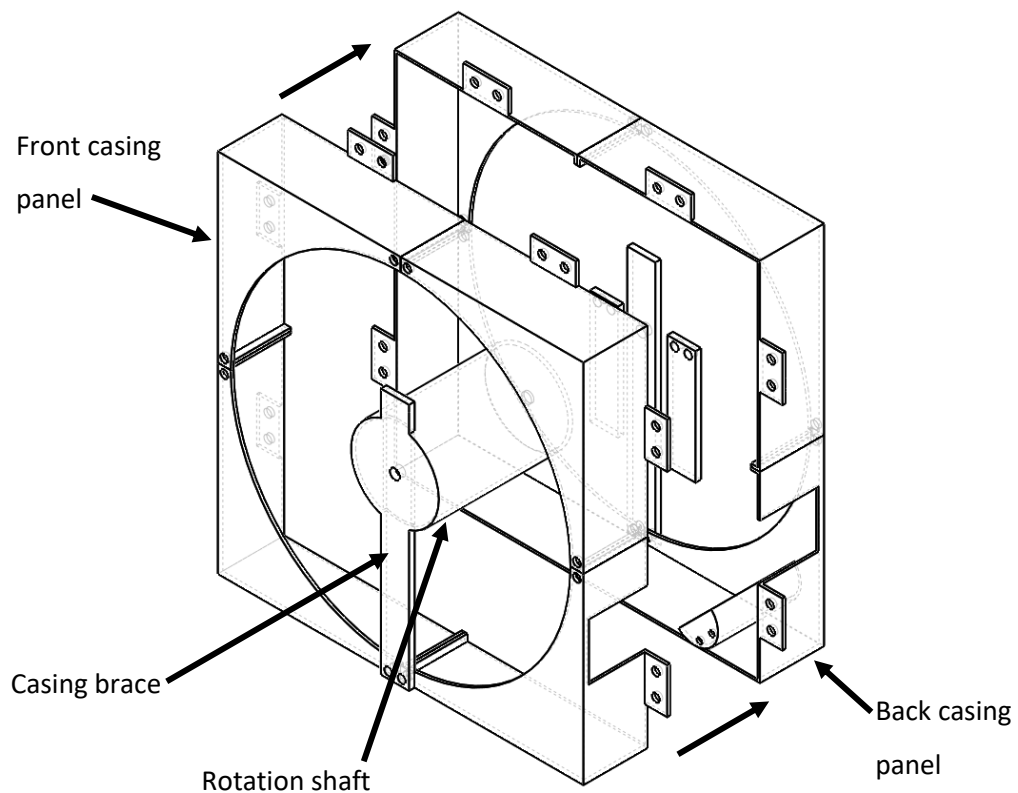


Figure 4-26 – Assembly of rotary wheel casing

4.4.5 Rotary Wheel Assembly

As different configurations of rotary wheel were required for the experiment, easy adaption of the components of the rotary wheel was necessary. The four outer rotary wheel shells were glued together to form a complete wheel. The four quarters were aligned precisely to give the wheel smooth transitions from quarter to quarter and a consistent rotation rate. The radial blades sat in the slots of the inner rotary wheel shell in the desired arrangement, 32 or 20 blades for their heat recovery or dehumidification. Once the correct number of radial blades were inserted in the inner shell, the blades and inner shell were slid into the outer shell. An example of this can be seen in Figure 4-27. Four sets of inner shells were filled with radial blades and secured in the outer shell.

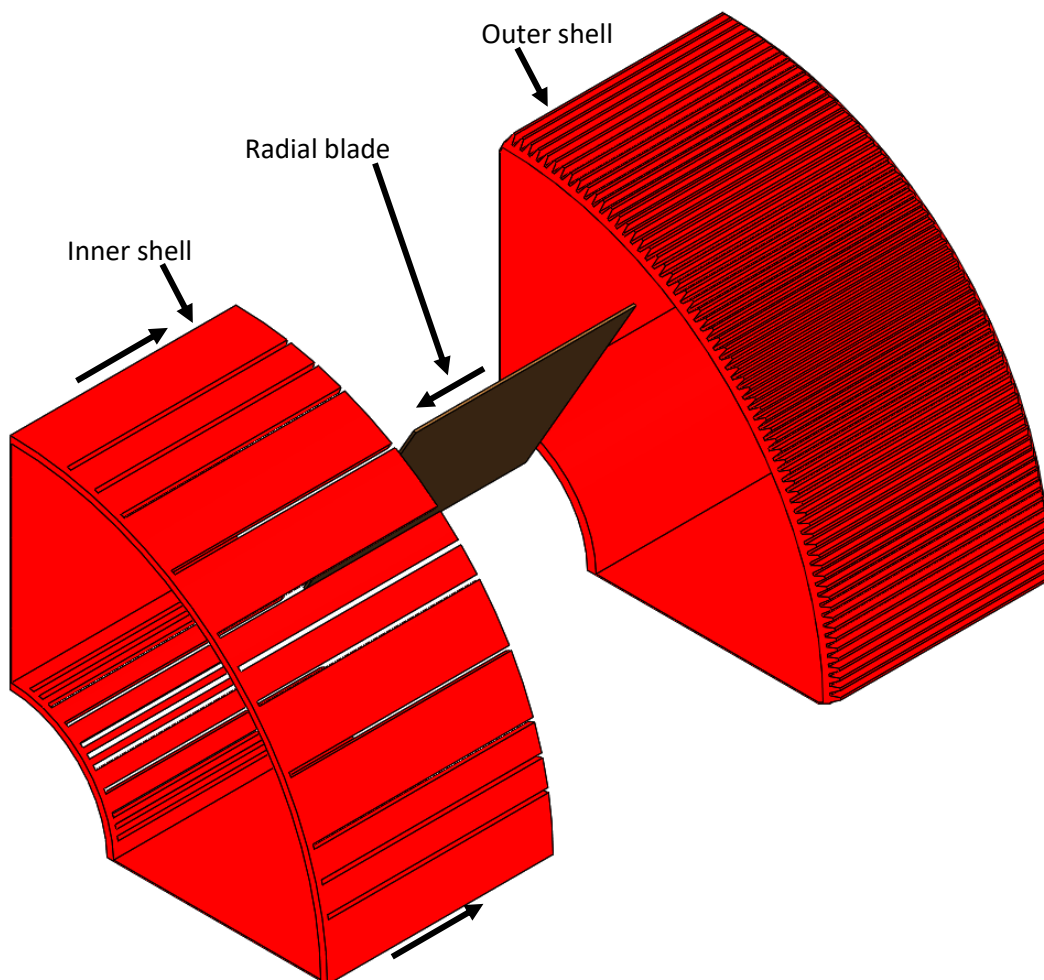


Figure 4-27 – Assembly of inner and outer rotary wheel shells with copper plate radial blade

The configurations of rotary wheel were easily changed for the required experiment. The radial blades were held securely in the rotary wheel by friction. Examples of the heat recovery and dehumidification wheels can be seen in Figure 4-28. The radial blades were equally distributed in the inner shell for even flow through the rotary wheel.

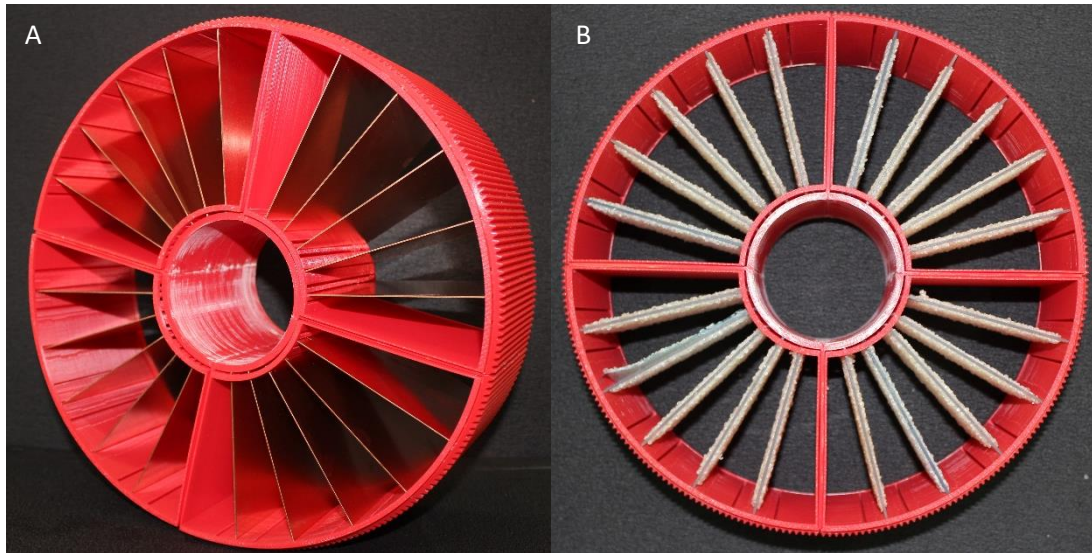


Figure 4-28 – A) 20 radial blade heat recovery rotary wheel, B) 20 radial blade dehumidification rotary wheel

The assembly of the rotary wheel into the casing can be seen in Figure 4-29. Once the radial blades and inner shell have been fit into the outer shell, the rotary wheel is mounted on the rotation shaft of the casing. The diameter of the rotation shaft was designed to allow free rotation of the wheel without any interference. The brackets of each half of the case are then fixed together, completing the assembly of the rotary wheel and casing.

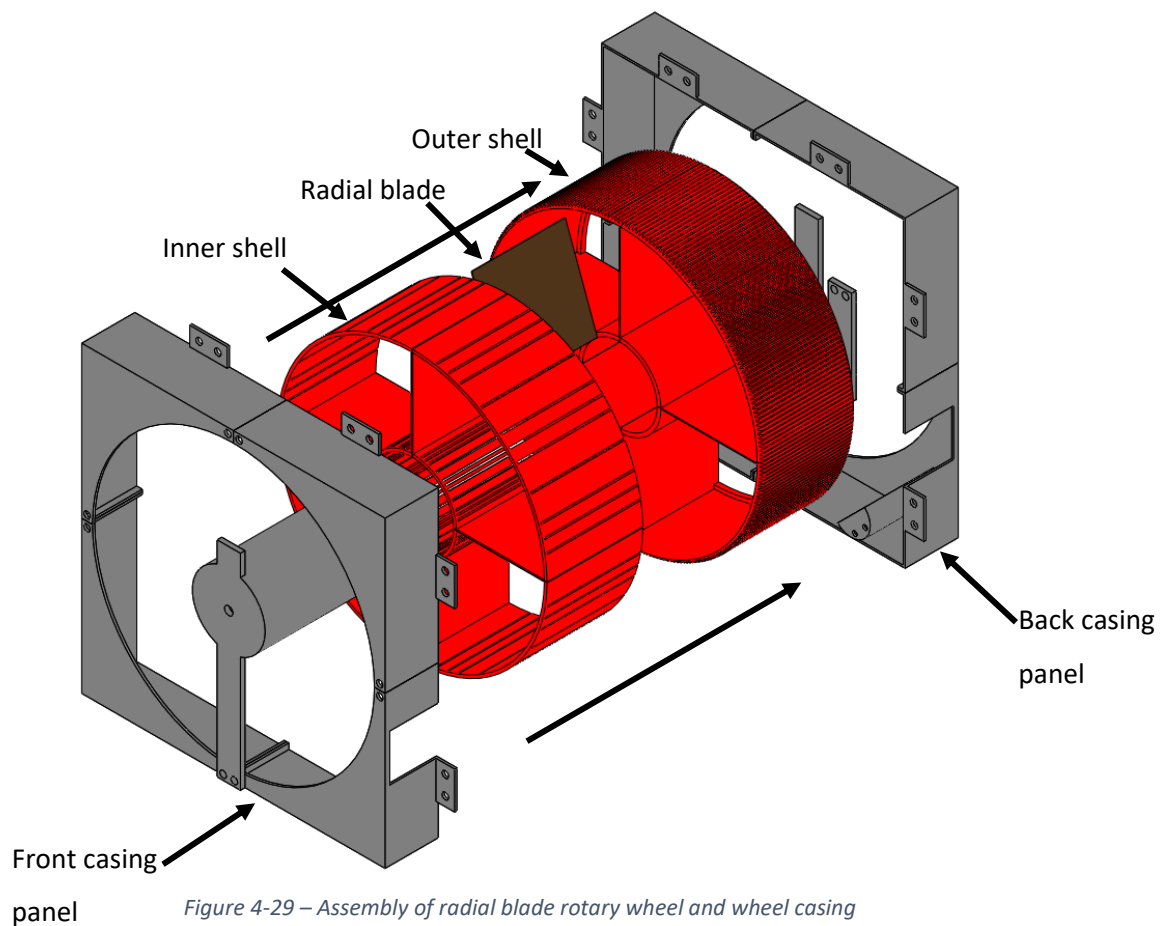


Figure 4-29 – Assembly of radial blade rotary wheel and wheel casing

The assembled rotary wheel and casing was designed to fit directly into the ductwork. The spacing between channels was designed to accommodate the additional bracing of the casing. The method for mounting the casing into the ductwork can be seen in Figure 4-30.

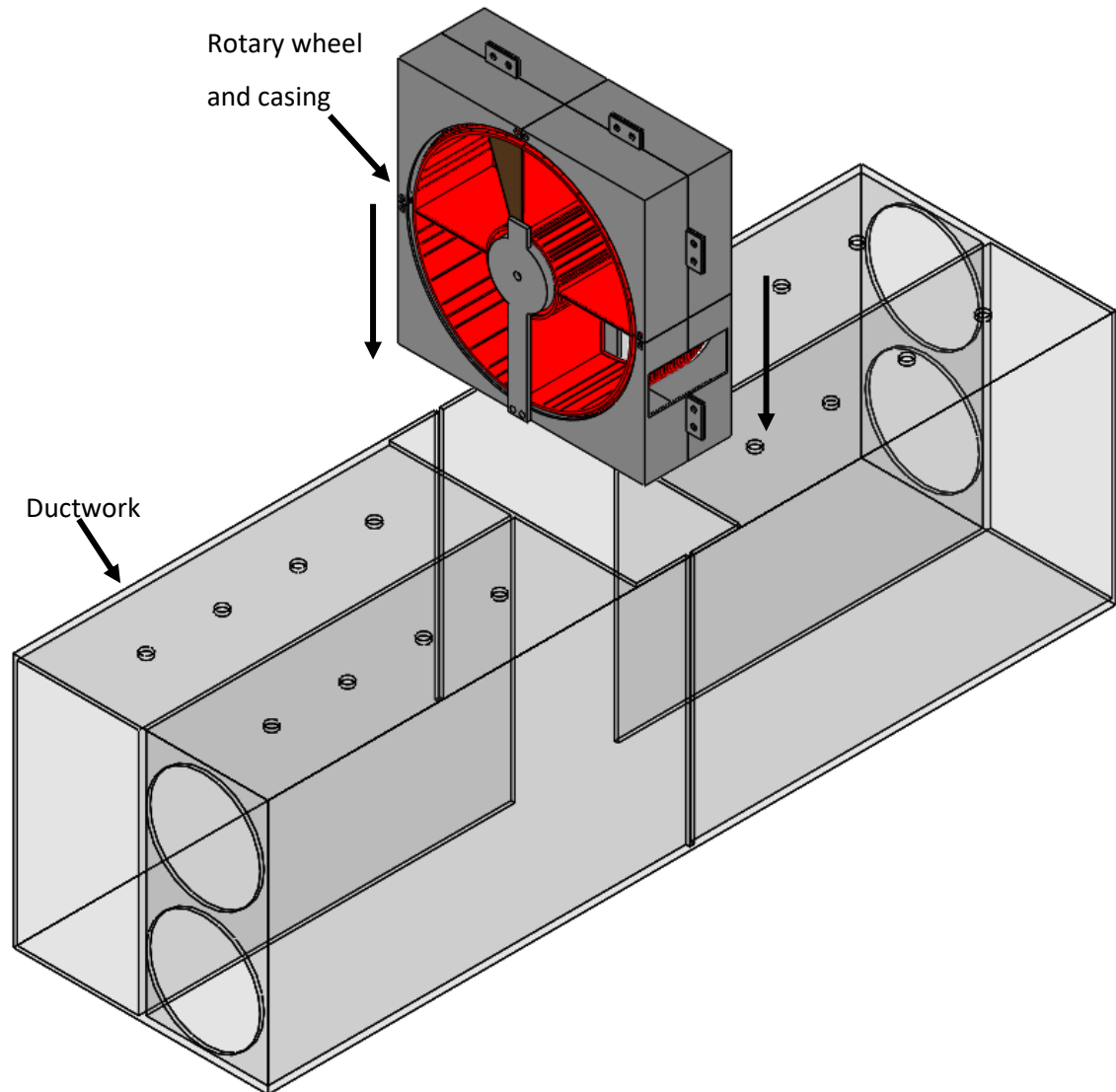


Figure 4-30 – Assembly of rotary wheel and casing into experimental ductwork

4.5 Experimental Setup and Measurement Procedures

An example of the final setup for the experiment can be seen in Figure 4-31. As two different configurations of rotary wheel were tested in the experiment, different measurement locations for the data collection were required based on the property measured and the equipment used for the data acquisition.

The important characteristics that were required to assess the performance of the rotary wheel configurations were air velocity before and after the wheel, air temperature before and after the wheel, and specifically for dehumidification configuration, the relative humidity

before and after the wheel. It was important to measure the properties in both the incoming and outgoing air channels to properly assess the wheel performance.

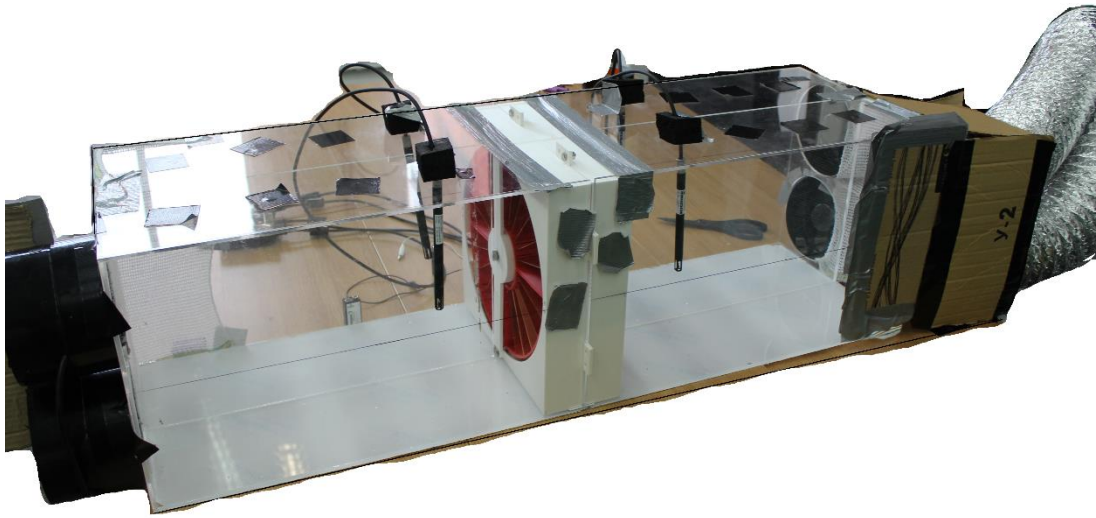


Figure 4-31 – Final experiment setup

4.5.1 Air Velocity Measurement

Measurements of the air velocity before and after the rotary wheel in both the incoming and outgoing air channels were taken for all configurations of radial blades. The position of the measurement locations can be seen in Figure 4-32.

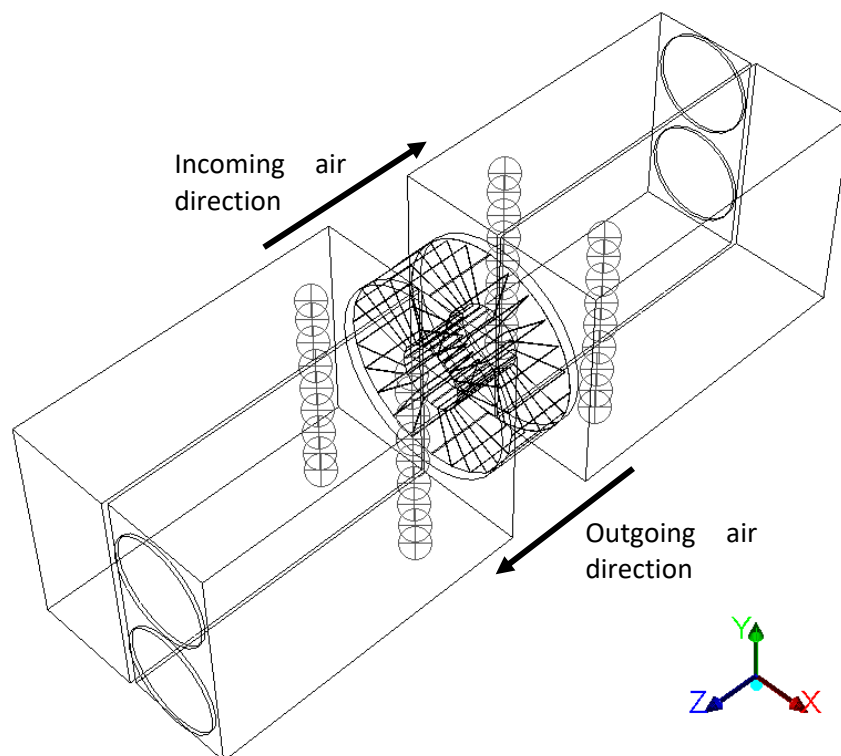


Figure 4-32 – Air velocity measurement locations

Measurements for air velocity were taken to assess the impact the rotary wheel configurations would have on supply air ventilation rates in a passive ventilation system. As high pressure drop across a device results in low ventilation rates, it was necessary to measure the air velocity before and after the wheel, designed to minimise the pressure drop across the device.

Thirty-six measurement locations were chosen for air velocity. This was to provide a flow profile across the channel and understand the effect of the wheel on the profile. The measurements were taken across the height of the channel, along the centreline of each channel. The co-ordinates of the measurement locations for each of the channels can be seen in Table 4-2. The origin of the co-ordinate system is at the centre of the rotary wheel, on the face in the direction of outgoing air flow.

The air velocity was measured only in the direction parallel to the flow; therefore, recirculation and turbulent effects were not taken into account. A time-averaged value for air velocity was taken at each measurement location by measuring the air velocity for a total of 20 seconds, three times. This was done to average the variation of the turbulent flow conditions in the ductwork. Extended testing times would have increased the effect of this and would be considered in future work.

Table 4-2 – Co-ordinates for air velocity measurement locations (x, y, z)

	Incoming Air Before Wheel	Incoming Air After Wheel	Outgoing Air Before Wheel	Outgoing Air After Wheel
P1	-0.08725, 0.1525, 0.115	-0.08725, 0.1525, -0.22	0.08725, 0.1525, -0.22	0.08725, 0.1525, 0.115
P2	-0.08725, 0.12, 0.115	-0.08725, 0.12, -0.22	0.08725, 0.12, -0.22	0.08725, 0.12, 0.115
P3	-0.08725, 0.08, 0.115	-0.08725, 0.08, -0.22	0.08725, 0.08, -0.22	0.08725, 0.08, 0.115
P4	-0.08725, 0.04, 0.115	-0.08725, 0.04, -0.22	0.08725, 0.04, -0.22	0.08725, 0.04, 0.115
P5	-0.08725, 0.00, 0.115	-0.08725, 0.00, -0.22	0.08725, 0.00, -0.22	0.08725, 0.00, 0.115
P6	-0.08725, -0.04, 0.115	-0.08725, -0.04, -0.22	0.08725, -0.04, -0.22	0.08725, -0.04, 0.115
P7	-0.08725, -0.08, 0.115	-0.08725, -0.08, -0.22	0.08725, -0.08, -0.22	0.08725, -0.08, 0.115
P8	-0.08725, -0.12, 0.115	-0.08725, -0.12, -0.22	0.08725, -0.12, -0.22	0.08725, -0.12, 0.115
P9	-0.08725, -0.1525, 0.115	-0.08725, -0.1525, -0.22	0.08725, -0.1525, -0.22	0.08725, -0.1525, 0.115

4.5.2 Relative Humidity and Air Temperature Measurement

Values for relative humidity and air temperature were recorded at the same measurement locations due to the measurement equipment used in the experiments. This is detailed later in Chapter 4. Air temperature before and after the wheel was measured in both incoming

and outgoing channels for both heat recovery and dehumidification rotary wheels. Relative humidity was measured in only the dehumidification rotary wheel experiments, before and after the wheel in both air channels. Measurements for air velocity were made separately to air temperature and relative humidity. This was because of the time required for air temperature and relative humidity measurements. Air velocity measurements were completed after this.

The measurement locations in each channel can be seen in Figure 4-33. Relative humidity and air temperature are important characteristics for assessing the performance of the rotary wheel. Transfer of heat from the outgoing airstream to the incoming air is the goal of the heat recovery rotary wheel. Reducing the relative humidity of the incoming airstream by transferring moisture to the outgoing air is the goal of the dehumidification wheel. Monitoring of these properties, therefore, is necessary to characterise the success of the radial blade design.

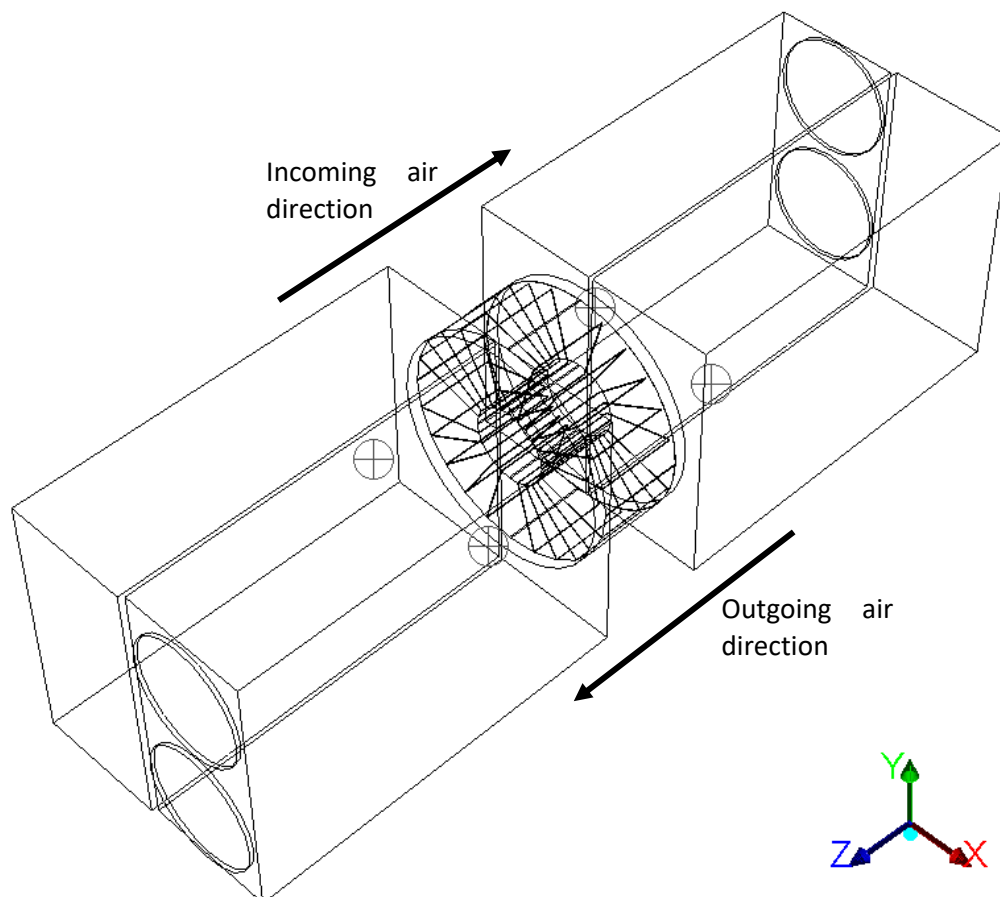


Figure 4-33 – Relative humidity and air temperature measurement locations

The co-ordinates for the measurement points for relative humidity and air temperature can be seen in Table 4-3. The origin of the co-ordinate system is at the centre of the rotary wheel,

on the face in the direction of outgoing air flow. Only four points were available for relative humidity and air temperature measurement due to the equipment used.

Table 4-3 – Co-ordinates for relative humidity and air temperature measurement locations (x, y, z)

	Incoming Air Before Wheel	Incoming Air After Wheel	Outgoing Air Before Wheel	Outgoing Air After Wheel
P1	-0.08725, 0.00, 0.115	-0.08725, 0.00, -0.22	0.08725, 0.00, -0.22	0.08725, 0.00, 0.115

Due to the time dependent nature of the transfer mechanisms for heat recovery and dehumidification, both properties were measured over a long time period. Simultaneous measurements were made at all four data collection points, every 5 seconds for a one-hour period, this resulted in 720 measurements. The advantage of monitoring the properties over a long time period allowed for slow changes in the condition of the air to be noticed. Dehumidification and heat transfer are not instantaneous effects and so measurement over an hour is preferable.

4.6 Experimental Test Equipment

The experimental test was designed to assess the performance of the radial blade rotary wheel design in terms of air flow profile, heat transfer and dehumidification. In order to measure the air velocity, air temperature and relative humidity before and after the rotary wheel, the following test equipment was used:

- Testo 425 hot-wire anemometer
- Testo humidity/temperature probe (12mm)
- Testo 176 P1 absolute pressure data logger

4.6.1 Hot-wire Anemometer

Hot-wire anemometers measure air velocity and air temperature by calculating the change in electrical resistance of a thin wire or foil that is electrically heated. As air moves over the wire/foil, the temperature changes. The change in temperature is then equated to the air velocity and air temperature of the flowing air.

Hot-wire anemometers are commonly used in low velocity wind tunnel and duct experiments. Hot-wire anemometers are accurate and have fast response times; however, the uncertainty of measurements increases as the air velocity measured increases. This generally limits the use of such devices to low velocity experiments and scenarios.

The Testo 425, shown in Figure 4-34, was the hot-wire anemometer used in this experiment. The probe of the anemometer is a fixed probe in that it cannot be changed or replaced; the diameter of the probe is 7.5mm. The anemometer uses a NTC sensor to measure air velocity and air temperature. The telescopic handle of the anemometer extends the reach of the probe to 820mm. The telescopic reach of the probe handle meant that air velocities at different heights in each of the experiment channels could be recorded. The technical specifications of the hot-wire anemometer can be seen in Table 4-4.



Figure 4-34 – Testo 425 hot-wire anemometer

Table 4-4 – Testo 425 hot-wire anemometer specifications

Probe Type	Thermal	NTC
Velocity	Measuring Range	0 – 20 m/s
	Accuracy	0.03 m/s +5%rdg
	Resolution	0.01 m/s
Temperature	Measuring Range	-20 – 70 °C
	Accuracy	±0.9 °C
	Resolution	0.1 °C

4.6.2 Humidity and Temperature Sensor Probe

Relative humidity and air temperature were measured using the Testo Humidity/Temperature probe. This type of probe measures relative humidity and by using the capacitive effect. A strip of metal oxide is placed between two electrodes, as the relative humidity changes, the electrical capacity of the metal oxide changes when moisture in the air collects on the surface of the strip, this change is monitored and used to calculate the relative humidity by considering the air temperature. The air temperature is measured in a similar way as the hot-wire anemometer mentioned previously. Relative humidity and air temperature sensors have a number of applications, specifically in areas where control and monitoring of moisture content is important such as museums and art galleries, storage facilities and large-scale HVAC systems.

The Testo Humidity/Temperature probe, shown in Figure 4-35, was used in the experiment to record relative humidity and air temperature in the channels. A probe was positioned 100mm from each face of the rotary wheel in both channels. Four probes were used in total. The probes did not have telescopic handles and so did not extend to the full height of the channel. Therefore, the probes were secured at the mid-height of the channel. The diameter of the probe head was 12mm. The technical specifications of the humidity/temperature probe can be seen in Table 4-5.



Figure 4-35 – Testo humidity/temperature probe with and without cover

Table 4-5 – Testo humidity/temperature probe specifications

Probe Type	Capacitive	
Relative Humidity	Measuring Range	2 – 98 %rH
	Accuracy	±2 %rH
	Resolution	0.1 %rH
Temperature	Measuring Range	-20 – 70 °C
	Accuracy	±0.3 °C
	Resolution	0.1 °C

4.6.3 Data Acquisition System

A Testo 176P1 absolute pressure logger, shown in Figure 4-36, was used to record the measurements for relative humidity and air temperature. The data logger featured five channels for recording pressure, air temperature and relative humidity with internal sensor for pressure. Two data loggers were used and two humidity/temperature probes were attached to each data logger. The values were stored internally in the data logger, which was then connected to a PC where the data could be downloaded. Setup of the data logger was also completed using PC software.



Figure 4-36 – Testo 176P1 absolute pressure data logger

4.7 Experimental Limitations

The repeatability of an experiment is important for confidence in the resultant data accuracy and reliability. Repeating the experimental tests at different times that result in similar outcomes is possible with a well thought out and properly setup experiment. The variability in experiment results should be a consequence of the accuracy and resolution of the experimental test equipment, as shown in Table 4-4 and Table 4-5.

The setup of this experiment was designed such that little error could enter the system. The different configurations of the rotary wheel were established and checked before each test for stability and condition. A heater with adjustable controls regulated the outgoing air inlet temperature. A single speed motor, preventing changes in rotation speed, managed the rotation of the rotary wheel. The speed of the wheel was monitored regularly to ensure consistency. Variability of the incoming air inlet conditions could not be controlled given the interior conditions of the laboratory. Internal conditions of the laboratory were monitored prior to the beginning of a test.

A number of limitations are inherent in the design of the experiment. The single rotation speed of the motor used prevented the effect of rotation speed on the heat transfer, dehumidification and air velocity from being tested. It is likely that the rotation speed will have a substantial effect on these properties. The lack of insulation between the air channels may result in heat losses from the acrylic ductwork. This will affect the results for air temperature measurements by artificially raising or lowering the temperatures depending on the airstream affected. The cross contamination effect of the rotary wheel would enhance this. As the rotary wheel was not a sealed system, air could move between the incoming and outgoing airstreams through the gaps between the case and wheel. In addition, as the wheel rotated between the airstreams, air could move through the space between blades from one airstream to another. This would enhance the effect of losses from the system.

Though relative humidity could be raised, control over the conditions at the incoming airstream inlet was not possible. The air temperature of the incoming air was dependent on the local conditions of laboratory. Though these were largely stable across all the test days, the ability to vary these conditions would have enabled greater assessment of the performance of the rotary wheel.

4.8 Summary

This chapter detailed the experiment that was used to validate the CFD model previously described. The design of the experiment and the methods used for the design, modelling and construction of the experiment components have been covered. The technologies used, 3D CAD modelling and 3D printing, are detailed. Analysis of the components, specifically the ductwork used for the air flow, is provided. The measurement procedures for characterising the air flow and rotary wheel performance is covered, along with the equipment required for measurement.

Chapter 5

5 Validation of Computational Fluid Dynamics (CFD) Model

5.1 Introduction

The following chapter provides the validation of the CFD numerical simulations by comparison with the results of the experimental testing. Validation of a CFD simulation is important to ensure reliability and confidence in the generated results. The data taken from the experiments is used to validate each of the radial blade rotary wheel configurations, along with the two different radial blade arrangements for each configuration. The data from the CFD models and experiments were compared using tables and graphs; this gives an understanding of the trends and direct error comparison of each of the data sets. For the validation of the CFD model to be accurate, the data measurement locations for the experimental and CFD models are required to be the same. The details of these are shown in Chapters 3 and 4.

5.2 Heat Recovery Configuration Validation

The validation of the heat recovery configuration CFD simulation focussed on two parameters; the air velocity before and after the wheel in both the incoming and outgoing airstreams, and with the air temperature before and after the wheel in both airstreams. As previously mentioned the incoming and outgoing airstreams were modelled separately to simplify the computational mesh and the calculation of the solution.

5.2.1 Air Velocity

Validation of the air velocity in the CFD model by results taken from the experiment is necessary to provide confidence in the CFD simulations. Contours of the air velocity in the incoming air channel for the 32-blade arrangement of the heat recovery configuration are shown in Figure 5-1. It can be seen that the air before the rotary wheel is generally moving at a uniform velocity. As the air enters the wheel, it accelerates due to the constriction of space between the radial blades. As the air exits the wheel, the velocity is still moving at a higher velocity than before the wheel. A number of recirculation zones exist in the channel after the wheel, given the shape of the channel and the rotary wheel; this is expected due to flow separation as air exits the wheel.

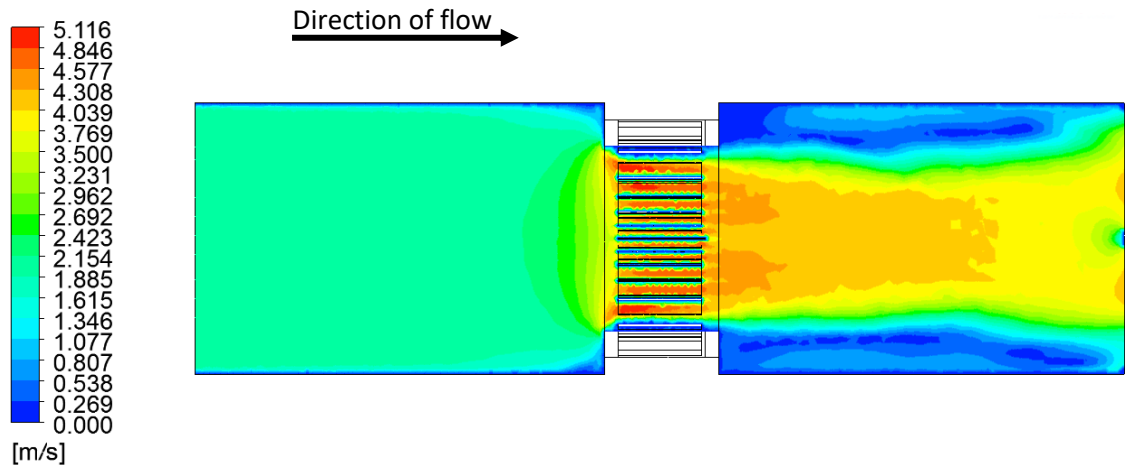


Figure 5-1 – Side elevation of incoming airstream velocity contours for 32 radial blade configuration

The graphs shown in Figure 5-2 and Figure 5-3 compare the measurements of air velocity taken from the CFD model with those of the experiment. The results are recorded from the same measurement locations. Figure 5-2 shows the air velocity measurements 100mm before the face of the rotary wheel. The flow before the wheel is expected to be evenly distributed as fully developed flow in a pipe, low velocity close to the walls with a maximum at the centre point. This is in agreement with the two trendlines shown in the figure. The two trendlines show similar profiles. The average error for the air velocity before the wheel is 12.5% and 24.6% after the wheel. Given the turbulent airflow exiting the rotary wheel, a higher error between the experiment and CFD model results after the wheel is not unexpected.

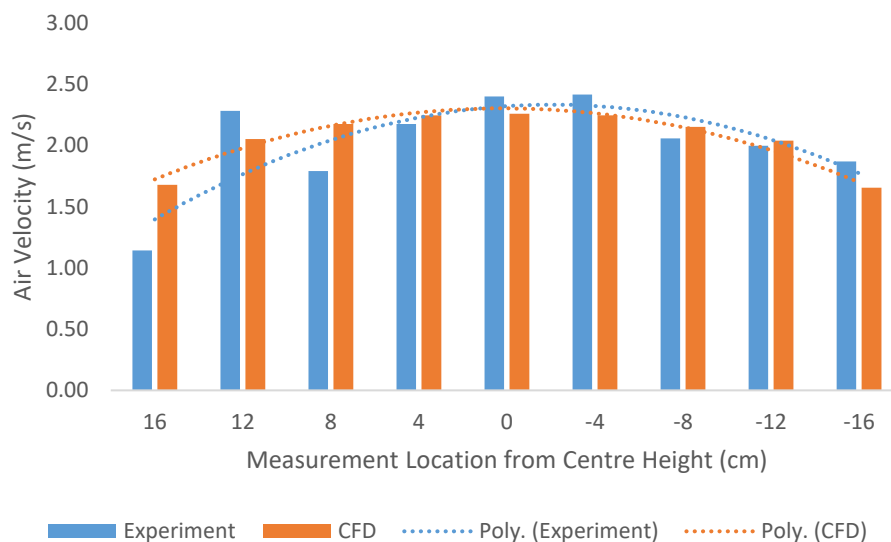


Figure 5-2 – Comparison between experiment and CFD air velocity in the incoming airstream before the 32 blade rotary wheel

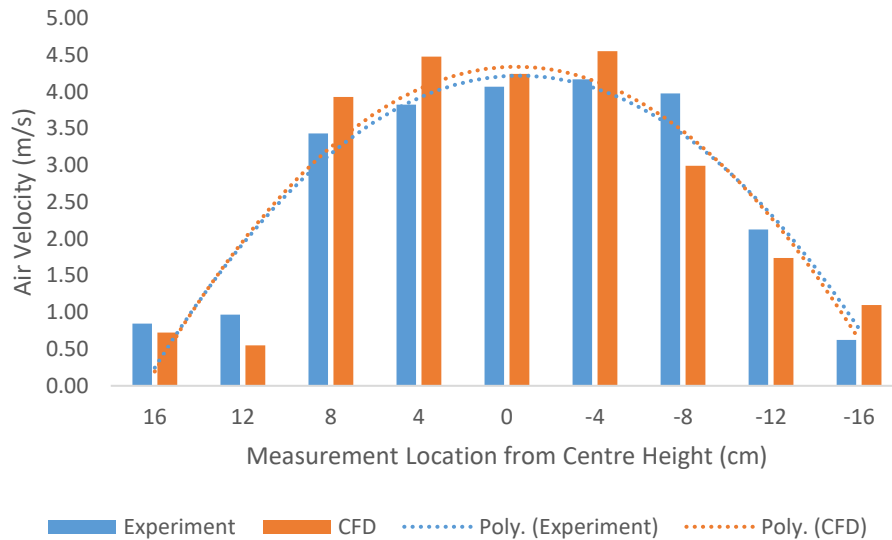


Figure 5-3 – Comparison between experiment and CFD air velocity in the incoming airstream after the 32 blade rotary wheel

Contours of the incoming airstream velocity for the 20-blade arrangement of the heat recovery configuration are shown in Figure 5-4. The flow profile before, inside and after the wheel is similar to that seen for the 32-blade arrangement. The flow before the wheel is distributed like a fully developed flow in a channel and accelerates through the wheel. A surprising feature of the 20-blade arrangement is that the maximum air velocity achieved by the flow is higher than that in the 32-blade arrangement, 5.12m/s compared to 5.20m/s. Given the larger open area of the 20-blade configuration, it may be that recirculation occurs in the 32-blade arrangement, reducing the flow through the wheel.

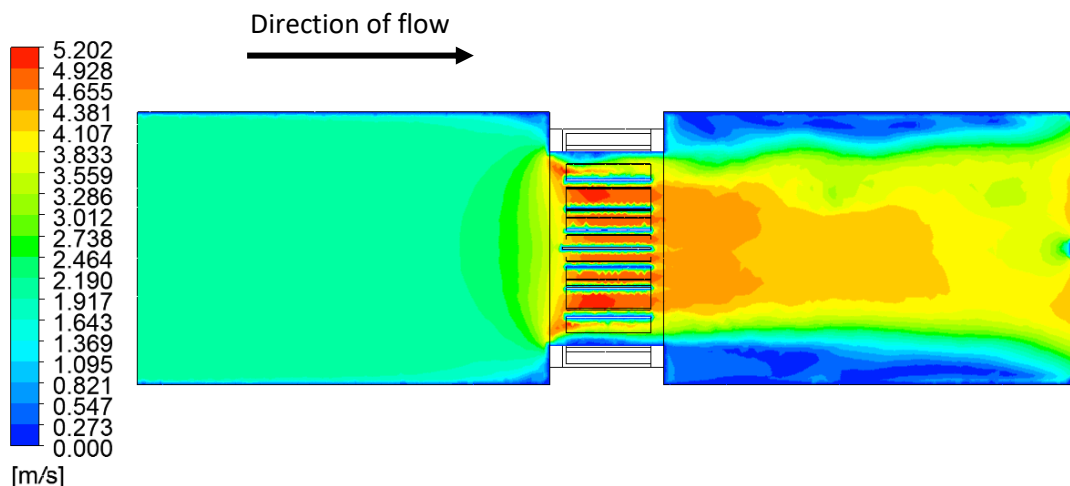


Figure 5-4 – Side elevation of incoming airstream velocity contours for 20 radial blade configuration

The graphs Figure 5-5 and Figure 5-6 show the air velocities for the experiment and CFD simulation before and after the rotary wheel for the 20-blade heat recovery configuration in the incoming airstream. The experiment and CFD results show similar trends for both sets of

data. However, sizeable differences are obvious in the data. The CFD results follow simple trends both before and after the wheel. The experimental results show greater variability, increasing the error between the data sets. The error between the experimental and CFD results before the wheel is 36.5% and 27.5% after the wheel. Though this is higher than the error of the 32-blade arrangement, the trends of the data are similar enough to compensate for the higher error percentage.

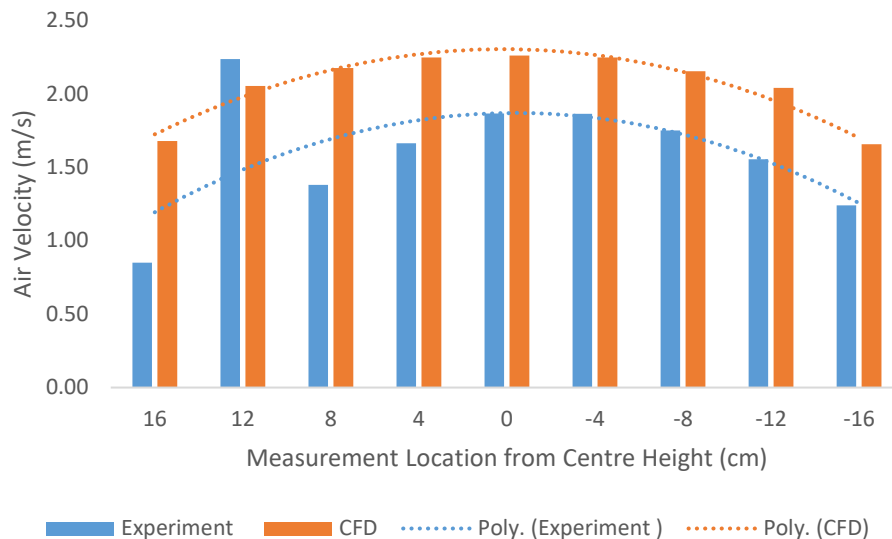


Figure 5-5 – Comparison between experiment and CFD air velocity in the incoming airstream before the 20 blade rotary wheel

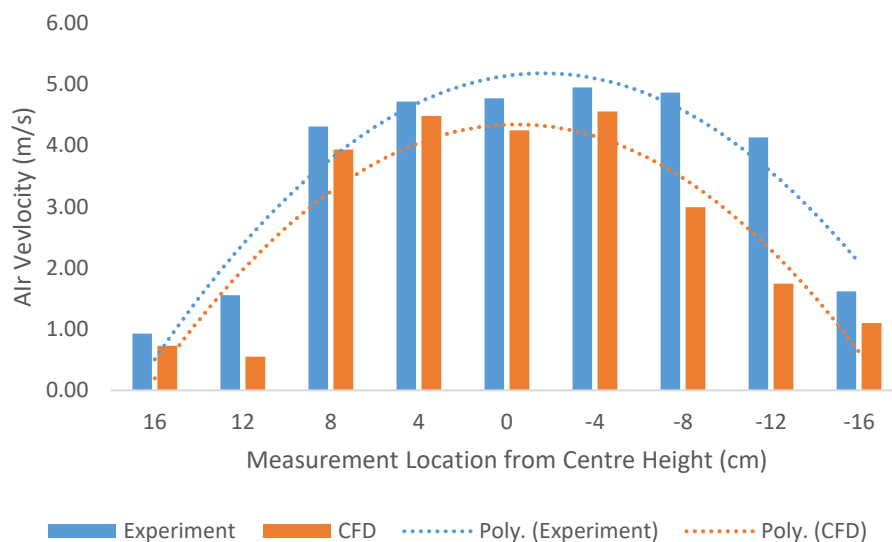


Figure 5-6 – Comparison between experiment and CFD air velocity in the incoming airstream after the 20 blade rotary wheel

The high error for the air velocity results before the wheel, Figure 5-5, are influenced by the high error of two points. The measurements 16cm and 8cm above the centre point have

error of 97.58% and 57.81%; all the remaining measurement points have error lower than 35.21%. The high error at these two points is likely a result of inaccuracies in the experiment given the consistency of the CFD results and trend of the other experiment results.

In terms of air velocity at the measurement locations, the CFD models under or overestimated the values compared to the experimental results, particularly in the 20-blade arrangement. The average error percentage between the experimental data compared to the CFD results was higher for the 20-blade arrangement compared to the 32-blade arrangement. However, the flow profile, shown by the trendlines on the graphs, show that the overall profiles are similar across all instances.

5.2.2 Air Temperature

The air temperature before and after the rotary wheel is the second parameter measured in both the experiment tests and CFD models used for validation of the CFD simulations. Validation of the CFD models using air temperature is significant given the purpose of a heat recovery wheel to increase the temperature of the incoming airstream, accuracy of the CFD models will help to further the development of the concept.

Figure 5-7 shows contours of air temperature in the incoming airstream for test HR-32-1. As the air flows through the channel before the wheel, the air is uniform in temperature. The inlet air temperature was taken from the conditions monitored in the experiment. As the air temperature before the rotary wheel is a fixed value from the experiment, it was not used for comparison with the CFD validation. As the flow passes through the rotary wheel and interacts with the energy source volumes representing the copper plates, the air temperature increases. Given the spacing of the blades, not all of the air is exposed to the blades, limiting the volume of air that increases in temperature.

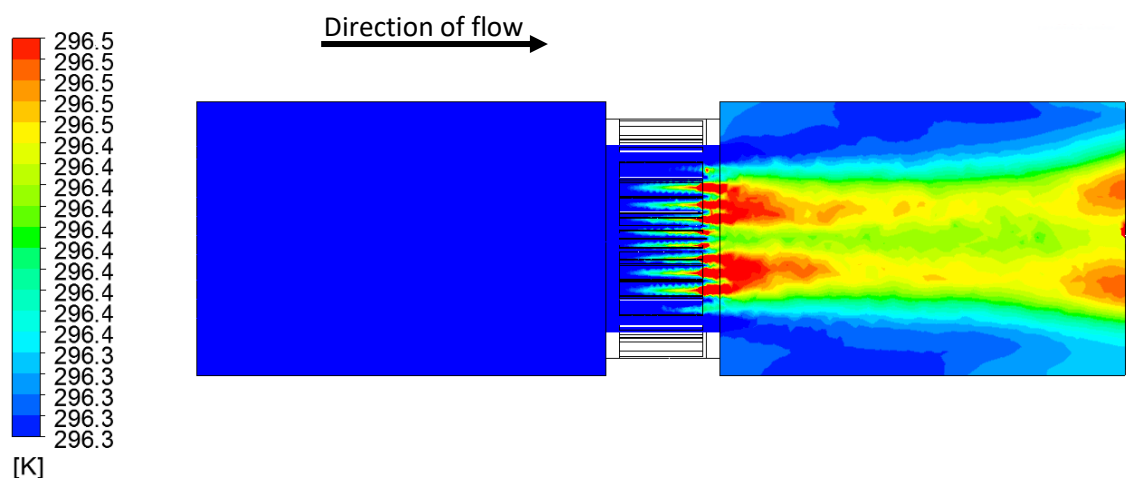


Figure 5-7 – Side elevation of incoming airstream temperature contours for 32 radial blade configuration

The contours show that the increased air temperature is concentrated in the middle of the flow stream. Figure 5-8 and Figure 5-9 show the comparison of air temperatures from the experiment and CFD results for the incoming and outgoing airstreams respectively. The measurements show the air temperature 100mm after the heat recovery rotary wheel. The different tests represent the changes to the outgoing airstream inlet temperature, ranging from 25-40°C.

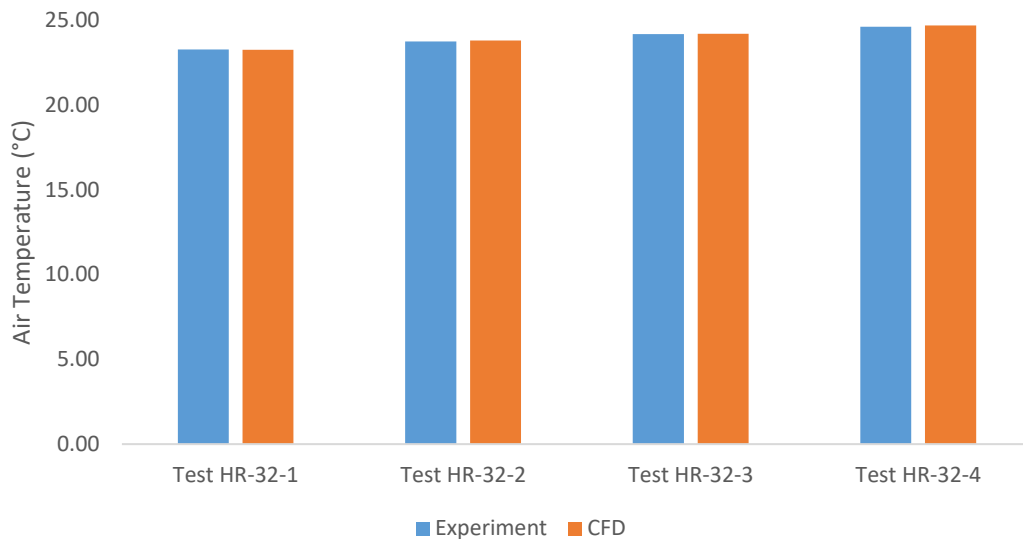


Figure 5-8 – Comparison between experiment and CFD air temperature after 32 radial blade rotary wheel configuration in the incoming airstream

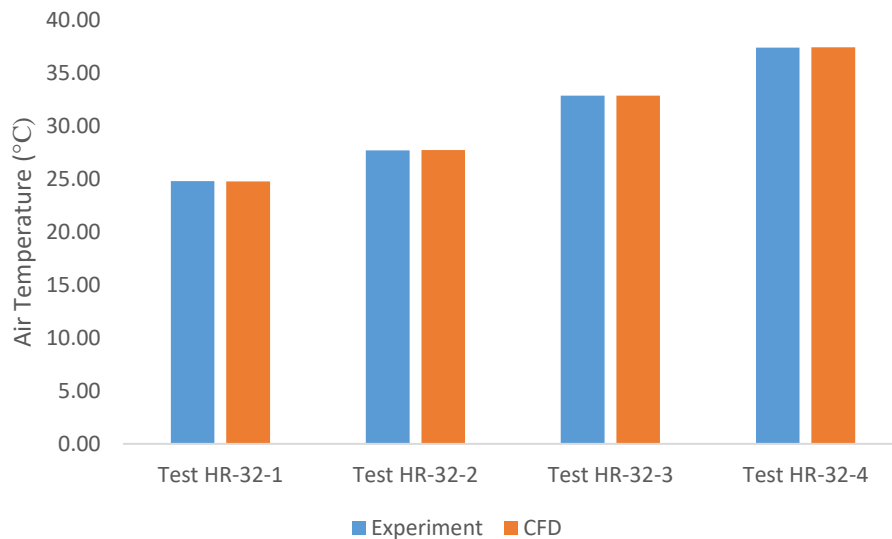


Figure 5-9 – Comparison between experiment and CFD air temperature after 32 radial blade rotary wheel configuration in the outgoing airstream

The air temperature data presented in the two graphs show the small difference between the experiment results and CFD model. Table 5-1 shows the data from the two sets of data.

The error percentage between the changes of air temperature before the wheel compared to after the wheel are low for both the incoming and outgoing airstreams, averages of 0.16% and 0.07% respectively. The low values for percentage error between the air temperatures after the rotary wheel show that the CFD model accurately predicts the thermal conditions of the experiment.

Table 5-1 – Comparison of experiment and CFD air temperatures before and after the 32 radial blade rotary wheel configuration

Incoming Airstream						
	Inlet Air Temperature (°C)	Experiment (°C)	CFD (°C)	Inlet – Exp Change	Inlet – CFD Change	% Error
HR-32-1	23.13	23.28	23.26	0.14	0.13	0.06
HR-32-2	23.43	23.74	23.80	0.31	0.37	0.23
HR-32-3	23.72	24.18	24.20	0.47	0.48	0.07
HR-32-4	23.92	24.61	24.68	0.68	0.76	0.29
Outgoing Airstream						
	Inlet Air Temperature (°C)	Experiment (°C)	CFD (°C)	Inlet – Exp Change	Inlet – CFD Change	% Error
HR-32-1	25.04	24.78	24.77	-0.26	-0.27	0.03
HR-32-2	29.40	27.69	27.72	-1.72	-1.68	0.11
HR-32-3	34.90	32.86	32.87	-2.04	-2.03	0.03
HR-32-4	39.79	37.39	37.43	-2.40	-2.36	0.12

Figure 5-10 shows the contours of air temperature for incoming airstream of the 20-blade heat recovery rotary wheel configuration. The profile of the flow through the channel is similar to that of the 32-blade arrangement. However, the channel of warmed air after the wheel is narrower than the 32-blade arrangement; also, the maximum temperature achieved by the arrangement is lower, 295.8K (22.65°C) compared to 296.5K (23.35°C). Given the lower number of blades for heat transfer this is the expected outcome, the lower contact area between the blades and air results in a smaller channel of air warmed to a lower temperature.

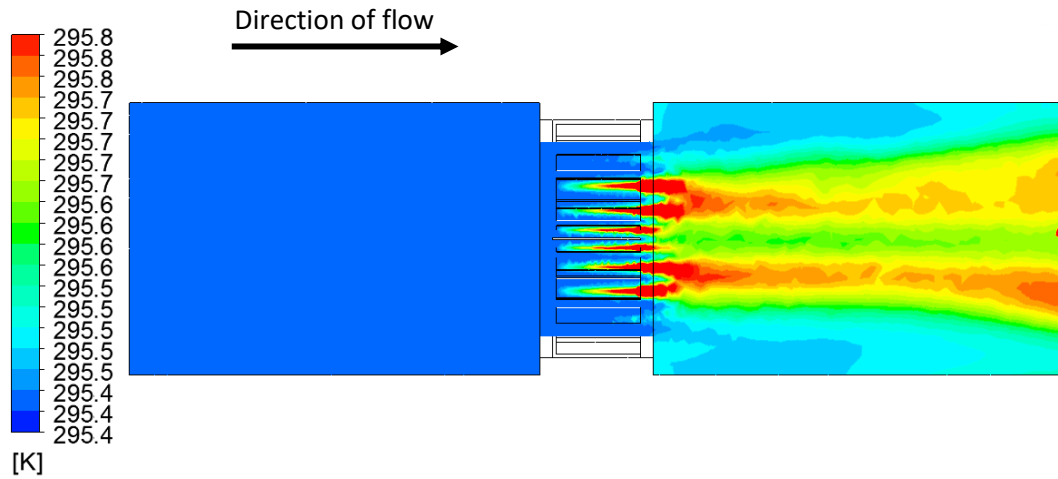


Figure 5-10 – Side elevation of incoming air temperature contours for 20 radial blade configuration

Figure 5-11 and Figure 5-12 show the comparison between the air temperature after the rotary wheel of the experiment and CFD model in the incoming and outgoing air channels for the 20-blade heat recovery configuration. The air temperature measurements between the two data sets show a high level of similarity with low percentage error. The average percentage error for both the incoming and outgoing channel measurements was 0.14%. The measurements of air temperature for the incoming and outgoing airstreams can be seen in Table 5-2. The low average error between the experiment and CFD results highlight the accuracy of the CFD model in simulating the thermal effects of the heat recovery rotary wheel.



Figure 5-11 – Comparison between experiment and CFD air temperature after 20 radial blade rotary wheel configuration in the incoming airstream

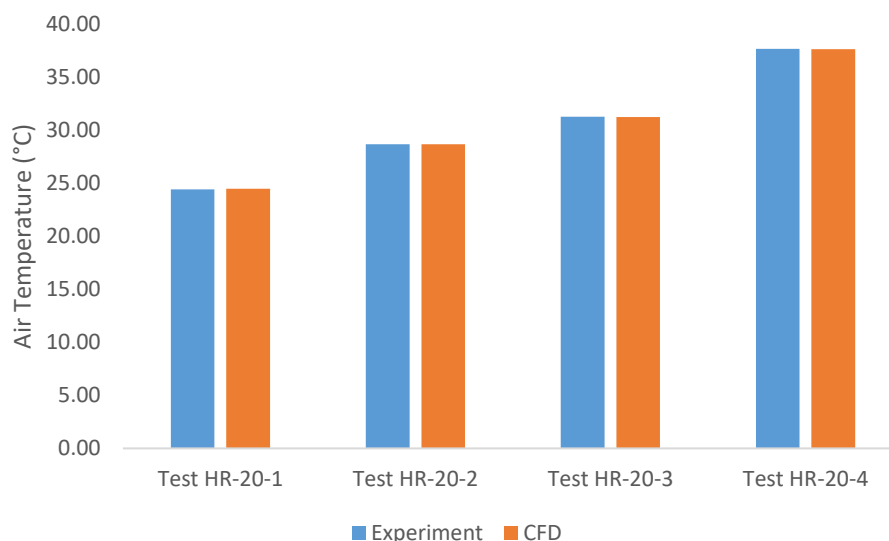


Figure 5-12 – Comparison between experiment and CFD air temperature after 20 radial blade rotary wheel arrangement in the outgoing airstream

Table 5-2 – Comparison of experiment and CFD air temperatures before and after the 20 radial blade rotary wheel configuration

Incoming Airstream						
	Inlet Air Temperature (°C)	Experiment (°C)	CFD (°C)	Inlet – Exp Change	Inlet – CFD Change	% Error
HR-20-1	22.28	22.46	22.47	0.18	0.19	0.03
HR-20-2	22.81	23.06	23.01	0.25	0.20	0.20
HR-20-3	21.36	21.78	21.73	0.42	0.37	0.23
HR-20-4	22.14	22.68	22.70	0.54	0.56	0.10
Outgoing Airstream						
	Inlet Air Temperature (°C)	Experiment (°C)	CFD (°C)	Inlet – Exp Change	Inlet – CFD Change	% Error
HR-20-1	24.70	24.44	24.50	-0.26	-0.20	0.25
HR-20-2	29.73	28.70	28.68	-1.02	-1.05	0.08
HR-20-3	34.82	31.29	31.25	-3.53	-3.57	0.12
HR-20-4	39.81	37.69	37.65	-2.12	-2.16	0.11

5.3 Dehumidification Configuration Validation

The validation of the dehumidification rotary wheel configuration CFD simulation focussed on three parameters; the air velocity before and after the wheel in both the incoming and outgoing airstreams, the air temperature before and after the wheel in both airstreams and the relative humidity of the air before and after the wheel in both airstreams. As with the heat recovery configuration, the incoming and outgoing airstreams were modelled separately to simplify the computational mesh and calculation of the solution.

5.3.1 Air Velocity

Contours of the air velocity in the incoming air channel of the 32-blade dehumidification rotary wheel are shown in Figure 5-13. The flow pattern of air through the channel is similar to that seen in the heat recovery configurations but with some minor differences. Given that the size of the blades in the dehumidification rotary wheel are 3mm thick compared to the 1mm thickness of the heat recovery blades, the lower value for maximum velocity is expected due to the reduced free volume for air to flow through. The 32-blade dehumidification configuration features a greater recirculation zone after the wheel than the comparable heat recovery configuration. This is likely due to the effect of the increased blade thickness.

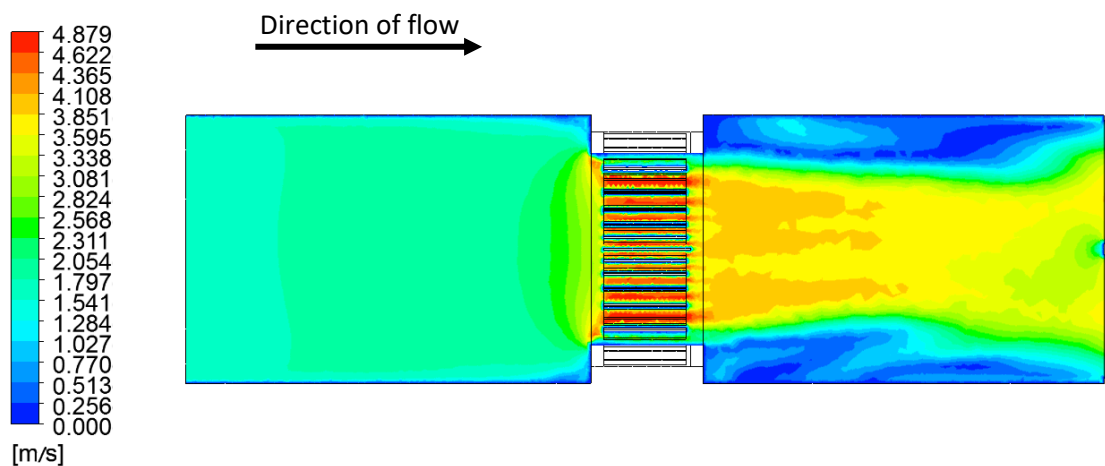


Figure 5-13 – Side elevation of incoming airstream velocity contours for 32 radial blade configuration

Figure 5-14 and Figure 5-15 show the comparison between the experiment and CFD measurements of air velocity before and after the wheel in the incoming airstream respectively. The air velocity measurements before the wheel show similar trends across the height of the air channel but an increasing percentage error between the data sets as the measurement locations approach the centre point.

The average percentage error between the experiment results and CFD data is 28% for the measurements prior to the wheel, with a maximum error of 60%. Though this is a high error percentage, the comparable trends of results indicate that the CFD analysis provides a good guide for the air velocity values.

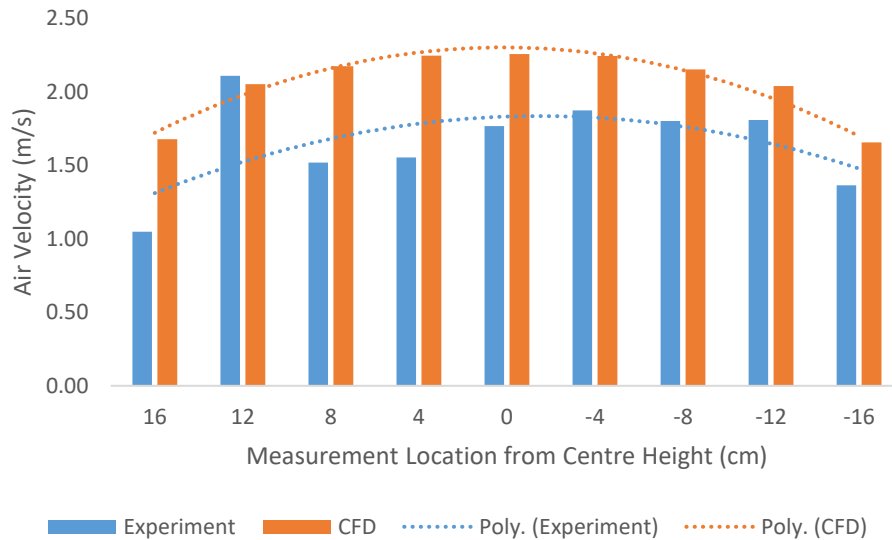


Figure 5-14 – Comparison between experiment and CFD air velocity in the incoming airstream before the 32 blade rotary wheel

The trend for the air velocity measurements after the wheel, shown in Figure 5-15, show a closer trend profile between the experiment and CFD results than the measurements before the wheel. However, the average percentage error is 32.8%, higher than the percentage error of the measurements before the wheel. This is likely influenced by the high error shown at the second measurement point, 12cm from the centre point. The CFD analysis under-predicts the air velocity by a margin of 78%, this greatly affects the average percentage error value. Though the CFD simulation under and over-predicts the air velocity, the air velocity profiles across the height of the channel are similar to those seen in the experiment.

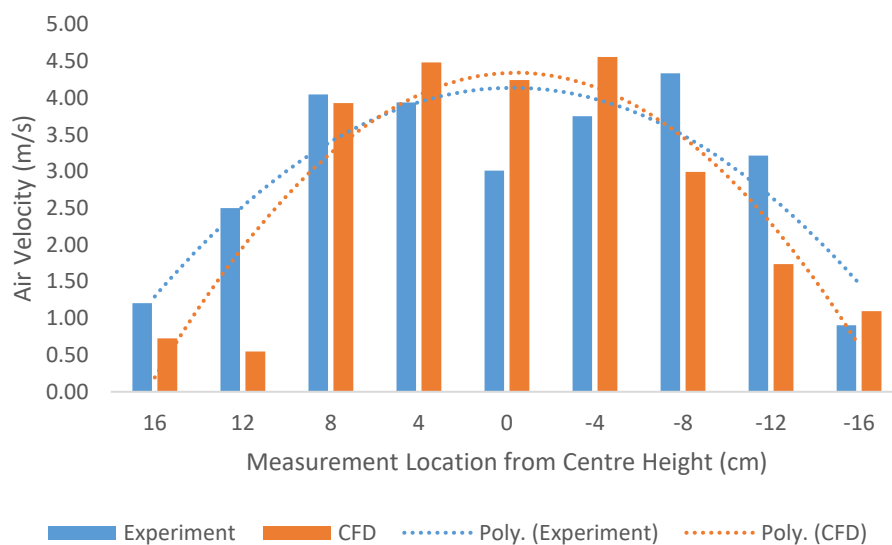


Figure 5-15 – Comparison between experiment and CFD air velocity in the incoming airstream after the 32 blade rotary wheel

Figure 5-16 shows the contours of air velocity of the incoming airstream for the 20-blade dehumidification rotary wheel. The profile of flow through the wheel is similar to the previous arrangements and configurations. Similar to the heat recovery wheel configuration, the air velocity reaches a higher maximum in the 20-blade arrangement compared to the 32-blade arrangement.

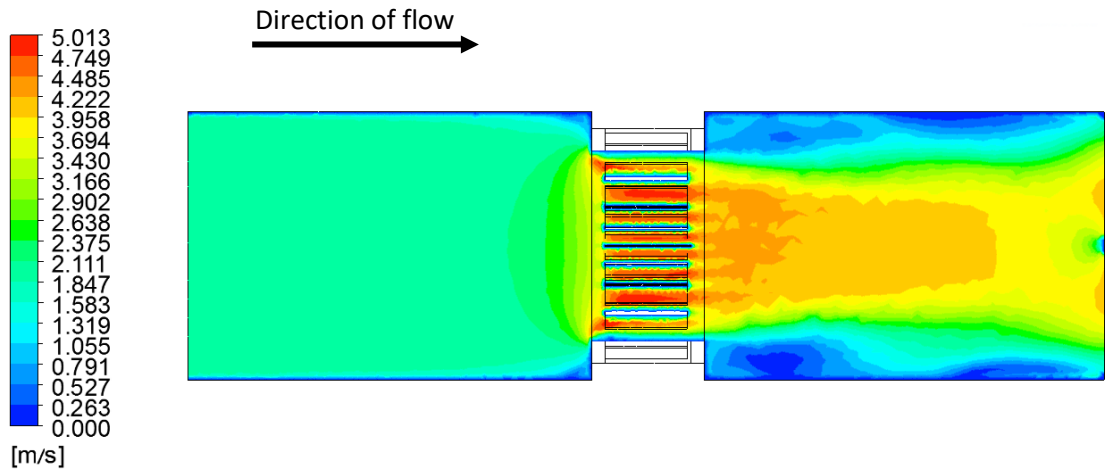


Figure 5-16 – Side elevation of incoming airstream velocity contours for 20 radial blade configuration

The trendlines for the air velocity data for the experiment and CFD results, shown in Figure 5-17 and Figure 5-18, show good agreement between the two datasets. The graphs show the results following similar patterns. In each case, the CFD analysis overestimates the air velocity compared to the experimental results. The average error for the air velocity before the wheel is 13.9% and 20.9% for the air velocity after the wheel. This is the lowest combination of error for the air velocity measurements for any arrangement or configuration.

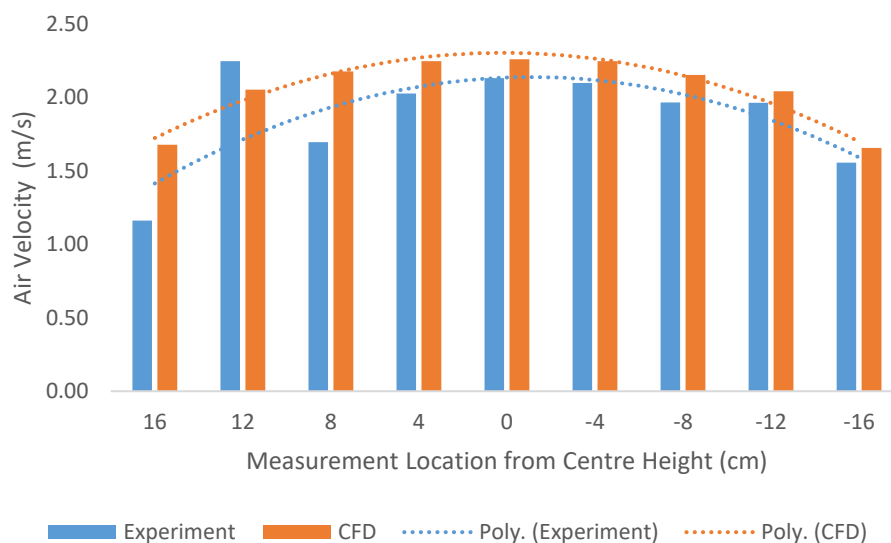


Figure 5-17 – Comparison between experiment and CFD air velocity in the incoming airstream before the 20 blade rotary wheel

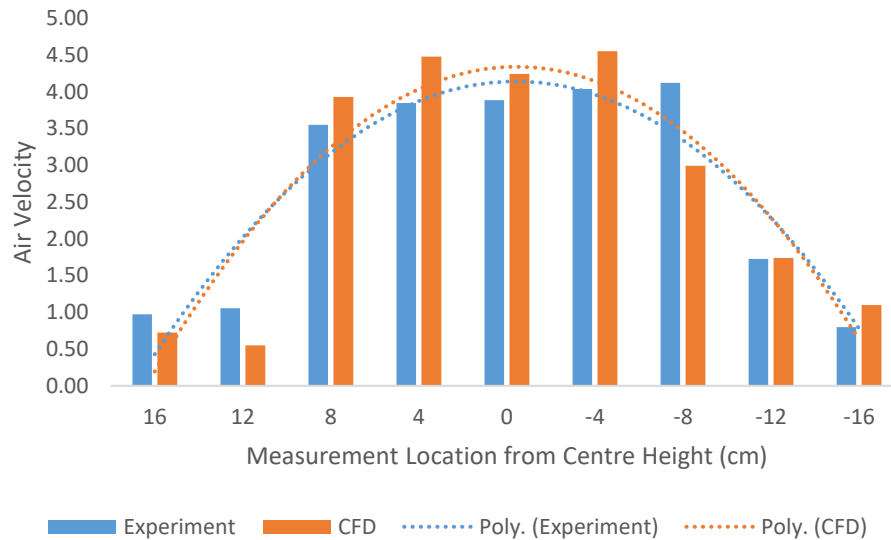


Figure 5-18 – Comparison between experiment and CFD air velocity in the incoming airstream after the 20 blade rotary wheel

The comparison of air velocity measurements between the experiment and CFD analysis for the dehumidification rotary wheel configuration show similarity. The trendlines for the majority of the profiles show good agreement. When the average error percentage between the two datasets was calculated, agreement was less obvious. The CFD simulations over or underestimated the air velocity predictions, up to 97.58% error compared to the experiment results. However, this may be due to inaccuracies with the experiment data measurement.

5.3.2 Air Temperature

Experimental measurements of air temperature for the same setup were used for the validation of the dehumidification rotary wheel configuration CFD models. The change in temperature between the inlet temperature before the rotary wheel and the air temperature in the channel after the wheel were compared between the experimental results and the CFD analysis.

Figure 5-19 shows the incoming air channel and the contours of static temperature for the 32-blade dehumidification rotary wheel configuration. The change in temperature experienced after the wheel is experienced in a similar region to the increase in velocity after the wheel, where the two contours feature similar patterns. This shows that both properties are affected by the radial blade thickness and spacing.

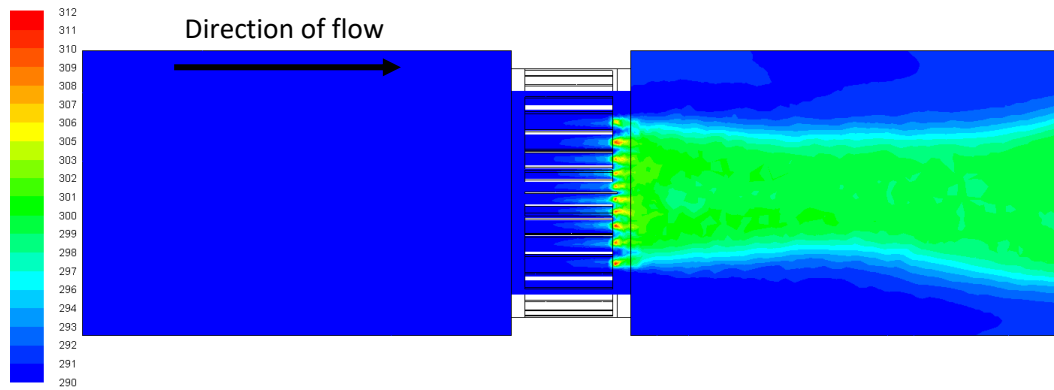


Figure 5-19 – Contours of air temperature in the incoming airstream for the 32 radial blade dehumidification rotary wheel configuration

Figure 5-20 and Figure 5-21 show the comparison of air temperatures after the wheel for the experiment and CFD results in both the incoming and outgoing airstreams. The results show high similarity between the two datasets for all measurements. The average error of the change in air temperature is 0.94% for the incoming air and 1.47% for the outgoing air. This is a low error count between the experiment results and CFD analysis, providing support for the validation of the CFD analysis.

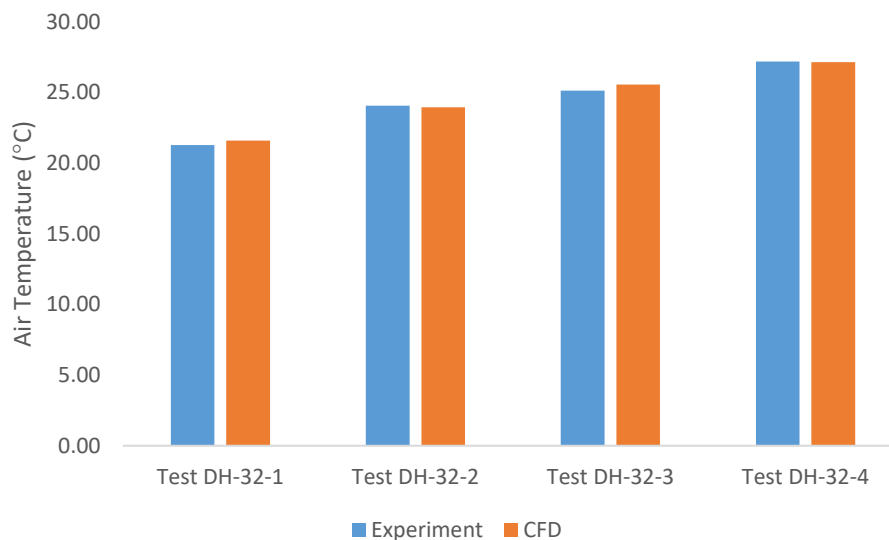


Figure 5-20 – Comparison between experiment and CFD air temperature after 32 radial blade rotary wheel configuration in the incoming airstream

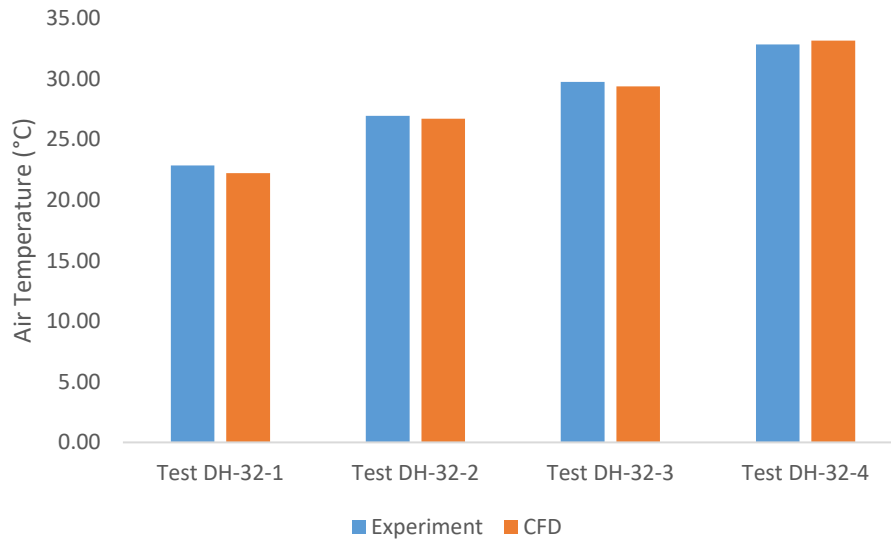


Figure 5-21 – Comparison between experiment and CFD air temperature after 32 radial blade rotary wheel configuration in the outgoing airstream

Table 5-3 shows the details of the air temperature measurements for the experiment and CFD models for the 32 radial blade dehumidification configuration. The inlet temperatures for the two methods of analysis were the same as the inlet temperature measured in the experiment and used as the input for the CFD simulations. The experiment and CFD results show little variation in measurements after the rotary wheel.

Table 5-3 – Comparison of experiment and CFD air temperatures before and after the 32 radial blade rotary wheel configuration

Incoming Airstream						
	Inlet Air Temperature (°C)	Experiment (°C)	CFD (°C)	Inlet-Exp Change	Inlet-CFD Change	% Error
DH-32-1	17.08	21.27	21.60	-4.52	-4.19	-1.54
DH-32-2	17.35	24.05	23.95	-6.60	-6.71	0.42
DH-32-3	16.63	25.13	25.55	-8.92	-8.50	-1.68
DH-32-4	17.00	27.18	27.15	-10.15	-10.18	0.13
Outgoing Airstream						
	Inlet Air Temperature (°C)	Experiment (°C)	CFD (°C)	Inlet-Exp Change	Inlet-CFD Change	% Error
DH-32-1	24.83	22.86	22.23	1.97	2.60	2.74
DH-32-2	30.83	26.97	26.72	3.86	4.11	0.92
DH-32-3	34.52	29.75	29.38	4.77	5.14	1.25
DH-32-4	38.84	32.86	33.18	5.98	5.66	-0.98

Figure 5-22 shows the contours of static temperature for the 20-blade dehumidification configuration for the incoming airstream. The contours show the increase in air temperature

as the flow moves across the silica gel volumes and through the rotary wheel. The pattern is similar to that of the 32-blade arrangement but with a narrower profile. The increase in temperature is lower than that of the 32-blade arrangement.

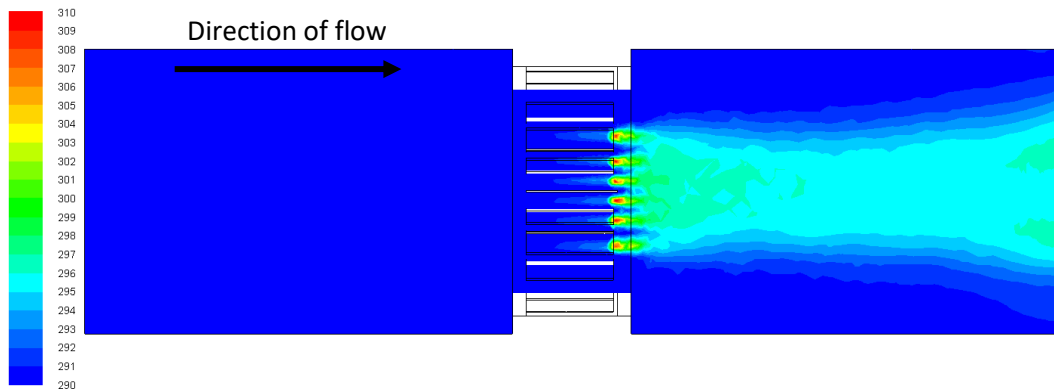


Figure 5-22 – Contours of air temperature in the incoming airstream for the 20 radial blade dehumidification rotary wheel configuration

The two graphs shown in Figure 5-23 and Figure 5-24 compare the results of air temperature measurement in the experiment and CFD analysis for the incoming and outgoing air channels in a number of tests. The graphs show that the air temperature measurements are similarly matched for all the data points. Figure 5-23 indicates the increase in air temperature as the air flows through the adsorption section of the wheel, whereas Figure 5-24 demonstrates the decrease in air temperature as the air flow through the desorption section of the wheel.

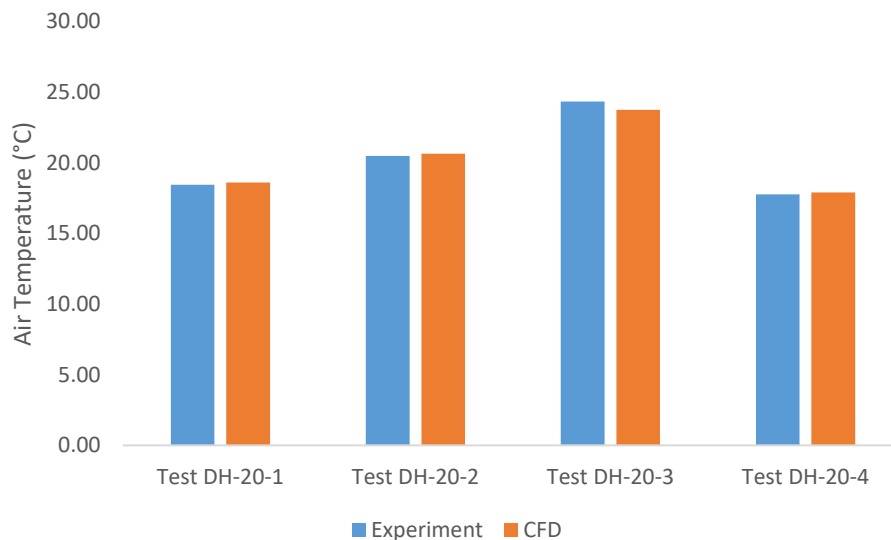


Figure 5-23 – Comparison between experiment and CFD air temperature after 20 radial blade rotary wheel configuration in the incoming airstream

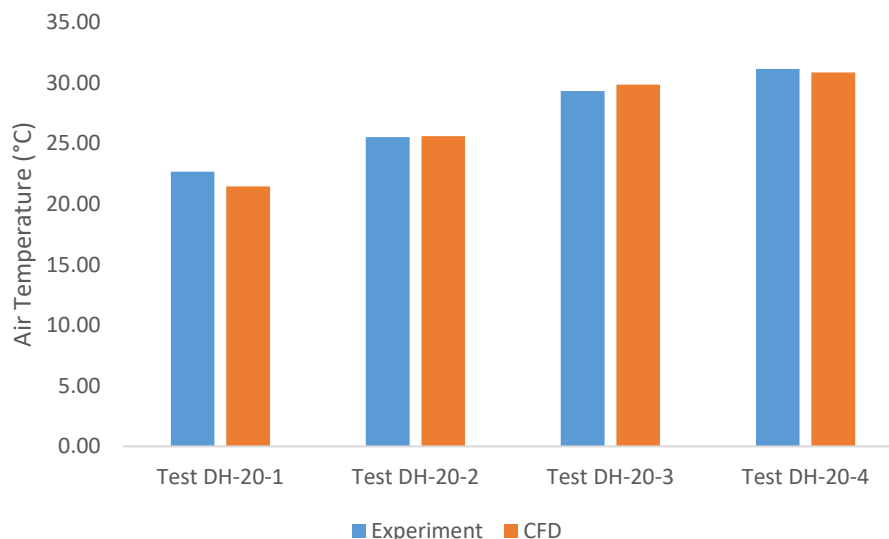


Figure 5-24 – Comparison between experiment and CFD air temperature after 20 radial blade rotary wheel configuration in the outgoing airstream

Table 5-4 displays the data of the measurements of air temperature from the experiment and CFD analysis. The average error between the experiment and CFD analysis is 1.18% for the incoming airstream and 2.10% for the outgoing airstream. This shows that the CFD simulations were able to accurately predict the changes in air temperature affected by the silica gel volumes when compared to the experiment data, helping to validate the CFD analysis.

Table 5-4 – Comparison of experiment and CFD air temperatures before and after the 20 radial blade rotary wheel configuration

Incoming Airstream						
	Inlet Air Temperature (°C)	Experiment (°C)	CFD (°C)	Inlet-Exp Change	Inlet-CFD Change	% Error
DH-20-1	13.57	18.45	18.59	-4.88	-5.02	0.76
DH-20-2	14.21	20.48	20.64	-6.27	-6.43	0.79
DH-20-3	16.85	24.34	23.75	-7.49	-6.90	2.43
DH-20-4	17.11	17.76	17.89	-0.65	-0.78	0.74
Outgoing Airstream						
	Inlet Air Temperature (°C)	Experiment (°C)	CFD (°C)	Inlet-Exp Change	Inlet-CFD Change	% Error
DH-20-1	25.02	22.68	21.47	2.34	3.55	5.34
DH-20-2	29.74	25.54	25.62	4.20	4.12	0.33
DH-20-3	35.43	29.32	29.87	6.11	5.56	1.87
DH-20-4	39.45	31.15	30.88	8.30	8.57	0.87

By using air temperature measurements taken from the experiment test data to validate the CFD simulations, good similarity between the data can be seen with a low percentage error. The graphs show agreement between the trends of data, increases and decreases in air temperature where expected. The average error values for all arrangements and configurations are below 2.10% with a maximum error percentage of 5.34%. The low error percentage and good agreement between the data sets for air temperature provide a strong argument for validation of the CFD models.

5.3.3 Relative Humidity

The purpose of the dehumidification rotary wheel configurations was to provide a design of rotary wheel that is capable of dehumidifying an airstream to a suitable degree whilst minimising the pressure drop across the device to enable integration with a passive ventilation system. Therefore, validation of the CFD analysis of the adsorption and desorption process using the experiment data is important to confirm the accuracy of the simulations.

Contours of relative humidity are shown in Figure 5-25. The incoming airstream relative humidity shows a decrease as the flow moves through the channel due to adsorption. This is clearly shown by the contours. As the flow exits the rotary wheel, the relative humidity has dropped from close to 100% to 32%; the 16 radial blades in the adsorption section of the wheel cause this. The column of air that is affected by the adsorption of the water molecules is focussed around the centre of the channel. This mirrors the patterns shown in the air velocity and temperature contours.

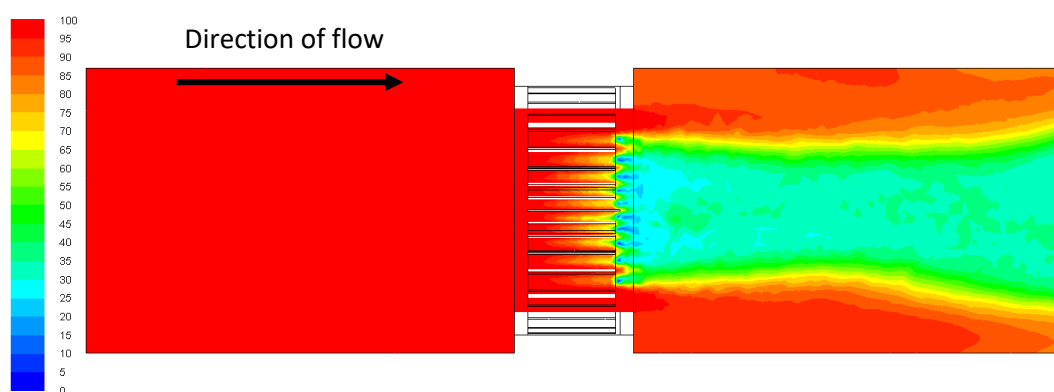


Figure 5-25 – Contours of relative humidity in the incoming airstream for the 32 radial blade dehumidification rotary wheel configuration

The graphs shown in Figure 5-26 and Figure 5-27 compare the measurements of relative humidity after the rotary wheel in the incoming and outgoing air channels taken from the experiment and CFD simulations. The comparison of the two datasets shows good

agreement, with low error between them. The relative humidity in both channels increases as the tests change. This is due to the change of temperature of the inlet air in the outgoing airstream. Further explanation of this will be given in Chapter 5.

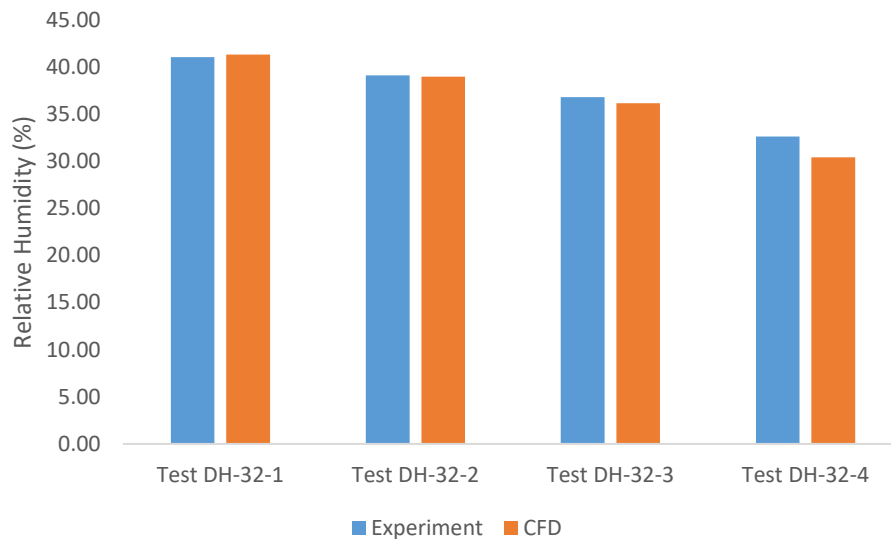


Figure 5-26 – Comparison between experiment and CFD relative humidity after 32 radial blade rotary wheel configuration in the incoming airstream

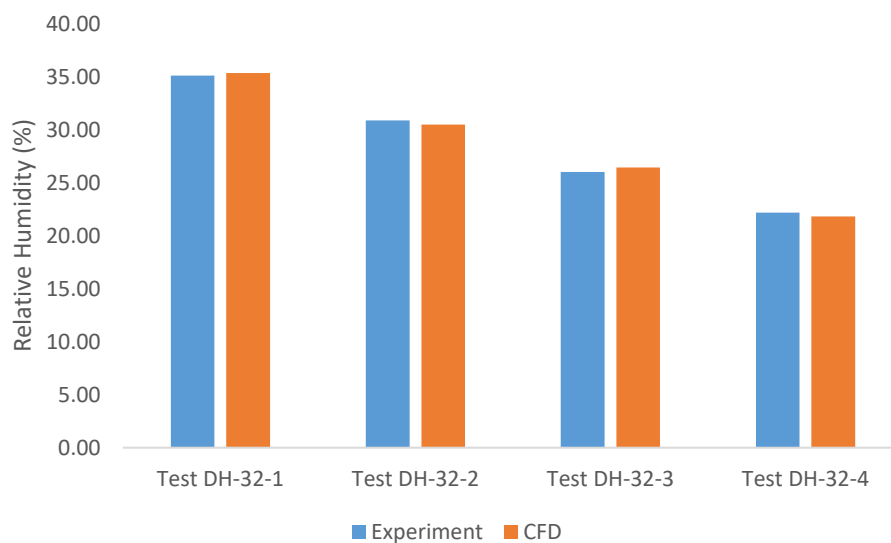


Figure 5-27 – Comparison between experiment and CFD relative humidity after 32 radial blade rotary wheel configuration in the outgoing airstream

Table 5-5 shows the data for the relative humidity for the experiment and CFD analysis before and after the rotary wheel in both the incoming and outgoing airstream. The change in relative humidity measurements before and after the wheel are similar for the experiment and CFD analysis. The average error percentage for the incoming airstream was 2.37% and 1.27% for the outgoing airstream. These are low error values between the experiment and

CFD results, strengthening the case for validation of the CFD simulations using the experiment data.

Table 5-5 – Comparison of experiment and CFD relative humidity before and after the 32 radial blade rotary wheel configuration

Incoming Airstream								
	Experiment		CFD		Exp Change	CFD Change	% Error	
	Before Wheel	After Wheel	Before Wheel	After Wheel				
DH-32-1	95.83	41.06	95.63	41.34	54.77	54.29	0.69	
DH-32-2	98.49	39.11	98.51	38.99	59.38	59.52	0.31	
DH-32-3	99.07	36.82	99.26	36.17	62.25	63.09	1.76	
DH-32-4	99.63	32.62	99.46	30.43	67.01	69.03	6.71	
Outgoing Airstream								
	Experiment		CFD		Exp Change	CFD Change	% Error	
	Before Wheel	After Wheel	Before Wheel	After Wheel				
DH-32-1	29.36	35.11	29.40	35.35	-5.75	-5.95	0.69	
DH-32-2	23.13	30.86	23.16	30.48	-7.74	-7.32	1.24	
DH-32-3	18.53	26.03	18.52	26.43	-7.49	-7.91	1.56	
DH-32-4	15.24	22.17	15.33	21.82	-6.93	-6.49	1.58	

Contours for relative humidity for the 20-blade arrangement of the dehumidification rotary wheel are shown in Figure 5-28. Notable differences between the contours for the 20-blade and 32-blade arrangement can be seen. The inlet relative humidity is lower than that of the 32-blade arrangement and the air after the rotary wheel has higher relative humidity. Though the differences in the relative humidity values are obvious, the overall flow profile is similar.

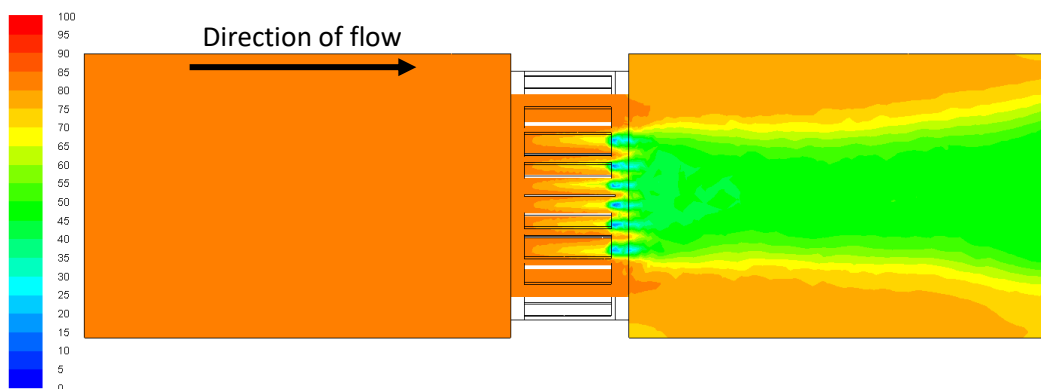


Figure 5-28 – Contours of relative humidity in the incoming airstream for the 20 radial blade dehumidification rotary wheel configuration

The comparison of relative humidity from the experiment and CFD analysis for the incoming and outgoing airstreams, shown in Figure 5-29 and Figure 5-30, demonstrate that the two datasets are in good agreement for the majority of the measurements. The values follow the same trend for each of the test cases in both the incoming and outgoing channels. The average error, calculated as the error between the relative humidity value after the wheel in the CFD model compared to the experiment, for the incoming air was 3.17% and 3.92% for the outgoing air.



Figure 5-29 – Comparison between experiment and CFD relative humidity after 20 radial blade rotary wheel configuration in the incoming airstream

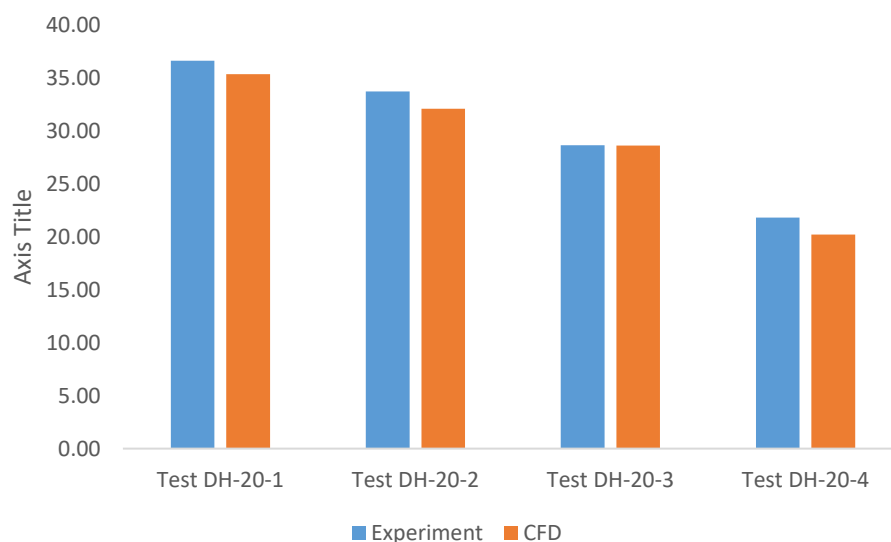


Figure 5-30 – Comparison between experiment and CFD relative humidity after 20 radial blade rotary wheel configuration in the outgoing airstream

Table 5-6 shows the detailed measurement data of the relative humidity in both the air channels for the experimental testing and the CFD analysis. The average error percentage for both the incoming and outgoing airstreams are affected by high error values in a single test. The maximum error of 8.98% in the incoming airstream and 7.36% in the outgoing airstream increase the average error substantially.

Table 5-6 – Comparison of experiment and CFD relative humidity before and after the 20 radial blade rotary wheel configuration

Incoming Airstream								
	Experiment		CFD		Exp Change	CFD Change	% Error	
	Before Wheel	After Wheel	Before Wheel	After Wheel				
DH-20-1	88.04	74.38	88.48	74.36	13.66	14.12	0.02	
DH-20-2	87.47	57.51	87.88	56.39	29.96	31.49	1.96	
DH-20-3	81.44	45.61	81.80	41.52	35.82	40.28	8.98	
DH-20-4	63.49	60.94	63.38	59.90	2.55	3.48	1.71	
Outgoing Airstream								
	Experiment		CFD		Exp Change	CFD Change	% Error	
	Before Wheel	After Wheel	Before Wheel	After Wheel				
DH-20-1	28.69	36.58	28.35	35.33	-7.90	-6.98	3.43	
DH-20-2	23.33	33.70	23.10	32.07	-10.36	-8.97	4.82	
DH-20-3	17.00	28.61	17.04	28.59	-11.61	-11.55	0.07	
DH-20-4	12.52	21.80	12.56	20.19	-9.27	-7.63	7.36	

Validation of the CFD model by comparing relative humidity measurements taken from the experimental testing was necessary due to the importance of moisture control to the performance of the dehumidification rotary wheel. The comparison of relative humidity values after the wheel in both air channels for each of the test cases ran showed that the CFD models were capable of accurately predicting the moisture response of the rotary wheel. The average error between the experiment data and CFD data was 3.92% or below for each of the four conditions monitored. Furthermore, the trends of the results closely matched one another, increasing the argument for validation.

5.4 Quantification of CFD Uncertainties

Due to the nature of numerical CFD analysis of a problem and experiment setup and measurement, the introduction of uncertainties in the design and errors in the result values is generally unavoidable. Therefore, validation of the CFD models by using the experiment

testing enables the accuracy and reliability of the results to be quantified through comparison, as argued by Li and Nielsen [178]. Validation of the CFD models was accomplished by calculating the percentage error between the results of the experimental testing and CFD analysis. The data measured from the experiments was assumed as the baseline measurement with error calculated as the percentage difference to the CFD values at the same measurement location.

Furthermore, comparisons of the trends of the data were used as additional validation. Chen and Srebric [179] state that the validation of a CFD model can be conducted when the error between the experiment results and CFD analysis is judged to be adequately low, and also if the trends predicted by the simulations match those of the experimental work. Given that the maximum average percentage error between the datasets was 36.5%, with the majority of the results lower than this, and the trends of each of the properties measured matched closely, it can be established that the CFD models of the heat recovery and dehumidification rotary wheels were validated.

5.5 Summary

Validation of the CFD models was required to quantify the confidence in the numerical solutions. This was achieved through comparison of data measured from each arrangement and configuration of the rotary wheel between the CFD analysis and the experimental testing. The air velocity, air temperature and relative humidity were the properties that were measured and compared for validation. Strong agreement was found between the experimental results and CFD solutions, the low error and high correlation of trendlines showed that the CFD models were capable of accurately predicting the correct solution when compared with experimental testing.

Chapter 6

6 Results and Discussions

6.1 Introduction

The following chapter details the results of the experimental testing and CFD simulations for the radial blade rotary wheel novel design. As noted in chapter 5, the CFD solutions were validated using the results of the experimental test. Therefore, the accuracy and reliability of the numerical analysis are deemed suitable.

The boundary conditions used to generate the solutions for the CFD analysis were taken from the measurements of the experimental tests. The calculated models of the CFD analysis were used to show that the experimental setup of the radial blade design could be accurately replicated in simulation, improving the development of the design in the future by using CFD simulations. The results for each measured characteristic from the experimental testing of both configurations of the rotary wheel are presented, followed by the CFD results. The error between the CFD results and experiment values is calculated, followed by the corrected values for the cell zone conditions.

The heat recovery wheel, designed with 1mm thick copper plates is evaluated by examining the values of air velocity, air pressure and air temperature before and after the wheel in the two air channels. The performance of the dehumidification wheel, using 3mm thick silica gel coated acrylic plates, is measured by collecting data of the air velocity, air pressure, air temperature and relative humidity of the incoming and outgoing airstreams.

Along with the two configurations of radial blade rotary wheel that are considered, results for different wheel arrangements are given. The number of blades in the heat recovery and dehumidification configurations were tested at 32 evenly spaced blades and 20 evenly spaced blades. The changes to the number of blades was to determine the effect of the blades on the properties and performance of the rotary wheel.

The tests for each of the arrangements are numbered as follows: arrangement type-number of blades in configuration-test number. HR designates a heat recovery arrangement and DH designates a dehumidification arrangement, 32 or 20 blades are specified, followed by the test number, 1-4, to correspond to each of the inlet air temperatures of the outgoing

airstream. For example, HR-32-1 refers to the 25°C inlet air temperature for the 32 blade heat recovery configuration.

The rotary wheel arrangement and configurations were subject to varying inlet conditions. The outgoing inlet air temperature was altered to understand the effect of outgoing air temperature on wheel performance. The condition of the incoming inlet air was determined by the conditions of the interior of the laboratory. These were measured before the start of each test for record.

6.2 Heat Recovery Rotary Wheel

The purpose of the design of the heat recovery rotary wheel was to transfer heat from the outgoing airstream to the incoming airstream. This would increase the air temperature of the incoming airstream, reducing the demand on conventional heating systems. Integrating the heat recovery wheel into a passive ventilation system required redesign of the matrix structure to lower the pressure drop across the device. The results of the testing of the radial blade rotary wheel for heat recovery are presented here. The air velocity before and after the device was measured across the height of the channel for both the incoming and outgoing airstreams. This was used to understand how the wheel affected the flow profile. The inlet air temperature of the outgoing airstream was increased from 25 to 40°C in 5°C intervals. The air temperature was measured before and after the rotary wheel in both air channels. This was done to assess the heat transfer across the wheel and the thermal energy held within the radial blades.

Different arrangements of heat recovery radial blades were tested under the same outgoing airstream inlet air temperature conditions. Arrangements of 32 blades and 20 blades were used to assess the performance of the heat recovery rotary wheel. The two arrangements of the blades were used to monitor the changes to air velocity and air temperature.

6.2.1 Flow Visualisation

Visualisation of the flow through the ductwork and the rotary wheel provides a greater understanding of the interaction of the flow and the radial blades. This could not be achieved with the experimental testing and so visualisation of the flow using the CFD solutions is preferable.

The contours of air velocity in both the incoming and outgoing air channels for the 32-blade heat recovery rotary wheel are displayed in Figure 6-1. The contours for the tests are shown,

where the inlet air temperature of the outgoing airstream 25°C in Test HR-32-1. Little variation between the different test cases and air channels was seen in the contour profiles. The inlet profile of each of the contours showed the same pattern, low velocity close to the channel wall, increasing to a maximum at the channel mid-height.

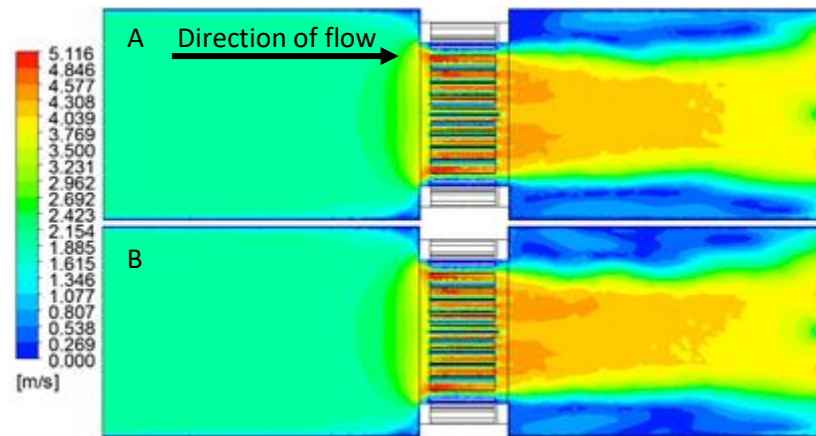


Figure 6-1– Contours of air velocity for the 32 radial blade configuration A) Test HR-32-1 incoming air, B) Test HR-32-1 outgoing air

An area of increased velocity can be seen immediately before the wheel in both of the test contours. This is likely due to a recirculation effect of the air at the wheel surface. The rotation of the wheel prevents some of the forward moving air from entering the volume between the radial blades of the wheel. This air is reflected by the rotating radial blades, increasing the velocity in this area.

The remaining air that is able to enter the rotary wheel accelerates through due to the constriction of the air channel. The air velocity reaches a maximum value for the test case between the radial blades. As the air exits the rotary wheel, a reduction in velocity is noticeable. The air moves in a band equal to the height of the rotary wheel, causing a recirculation wake close to the channel walls of the ductwork. The shape of the rotary wheel as the air exits causes this profile to develop. Changing the design of the rotary wheel on the leeward face in relation to the direction of flow could help to diffuse the air over a greater area. This would be beneficial in slowing down the velocity if required or if the air required further treatment spread over the area of the ductwork channel.

Little variation between the different test cases was seen from the contours of air velocity. Despite the changes to air temperature at the outgoing air inlet, the velocity was unaffected. This is the expected case. Though the density of air is directly related to the temperature, the changes to air temperature across a range of 15°C are not enough to contribute to changes in the air velocity or flow profile.

The contours of air velocity for the 20-blade heat recovery rotary wheel test are shown in Figure 6-2. Test HR-20-1 displays the air velocities for an outgoing inlet air temperature of 25°C. A similar flow profile can be seen from the contours of air velocity for the 20-blade configuration when compared to the 32-blade configuration. This is as expected given the similarity of the overall geometry between the two configurations.

A fully developed flow profile can be seen before the rotary wheel, as also seen in the 32-blade configuration. The flow is fully developed from the inlet of the air channels, this is not representative of actual flow conditions as the flow profile would develop over the length of the channel as it approached the rotary wheel. The same area of recirculation zone can be seen from the increase in air velocity at the wheel entrance. The size of the area is similar to that of the 32-blade configuration, suggesting that the recirculation is less a factor of the geometry of the wheel configuration and related more to the rotation speed of the wheel.

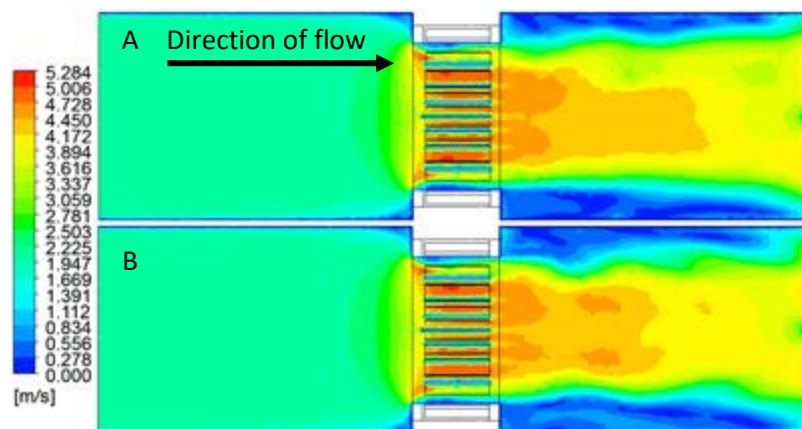


Figure 6-2 – Contours of air velocity for the 20 radial blade configuration A) Test HR-20-1 incoming air, B) Test HR-20-1 outgoing air

The contours for the 20-blade configuration show an acceleration of the air velocity as the air travels through the rotary wheel. The cause of this will be the same as that seen in the 32-blade configuration, the contraction of volume for the air to flow through necessitates the increase in air velocity. The maximum air velocity seen in the 20-blade configuration is higher than that seen in the 32-blade configuration. This is an unexpected result. Conventional knowledge would suggest that the 32-blade configuration would result in the highest air velocity value as the air is constricted the most. The reverse of this appears to be true given the air velocity contours of the 32 and 20-blade configurations. The increased volume between radial blades of the 20-blade configuration may have a lower recirculation effect prior to the wheel. This allows a greater volume of air to pass through the wheel, requiring a higher velocity to exit the wheel.

Greater variation of the flow profile after the rotary wheel is observed in the tests compared to the 32-blade configuration. The size and shape of the flow wake after the rotary wheel are similar between the incoming test channels compared to the outgoing test channels. Equally, the outgoing airstream test show similarity. This suggests that for the 20-blade configuration, the introduced air at the outgoing airstream inlet has a more significant and noticeable effect. This is likely due to the increased volume between radial blades.

The effect of the radial blade rotary wheel design on air velocity for the 32 and 20-blade configurations was analysed based on the flow visualisation. The contours indicate that air accelerates through the rotary wheel due to the contraction of the volume available for flow. Though the air velocity through the rotary wheel increases in both instances, the highest air velocity is measured in the 20-blade configuration as opposed to the expected 32-blade configuration. This suggests that the increased volume available for air to flow through in the 20-blade configuration reduces the backflow of air immediately prior to the rotary wheel. As more air is able to pass through the rotary wheel, higher air velocities are required.

The contours for both radial blade configurations show that after the wheel, the values for air velocity are higher than before the rotary wheel. The momentum gained from the acceleration through the rotary wheel is maintained after the wheel. This is encouraging for integration of the radial blade rotary wheel into passive ventilation systems, maintaining high air velocities after the device is essential for the supply rates to occupied buildings. However, given the relatively short length of the channel after the rotary wheel, further investigation of the air velocities is required. Rapid deceleration of the air after the initial 500mm would result in low supply rates, making the radial blade rotary wheel ineffective for passive ventilation.

6.2.2 Air Velocity

Measurements for the air velocity in both the incoming and outgoing air channels in the experimental testing were taken for each of the tests conducted. The air velocity was measured 100mm before and after the rotary wheel, at nine different heights along the centreline of the channel. Figure 6-3 shows the average values and flow profile from the trendline for the air velocity at the nine measurement heights for tests HR-32 before and after the rotary wheel in the incoming airstream. The average air velocity is shown due to the small variation shown in values for each separate test.

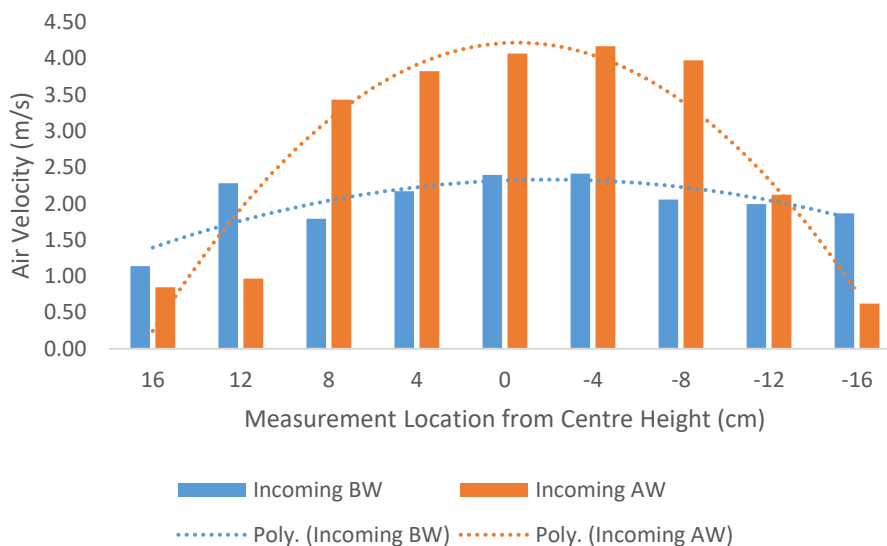


Figure 6-3 – Average air velocity for tests HR-32-1 to HR-32-4 measured before and after the rotary wheel in the incoming airstream

The trendlines added to the values of air velocity in Figure 6-3 present an overall flow profile before and after the rotary wheel in the incoming air channel. The flow before the wheel, represented in blue in the graph, shows more similar velocity values compared to the values after the wheel. This corresponds to the contours shown in the analysis of the CFD simulations. The flow before the wheel exhibits similarity with a develop flow profile in a channel, low velocity at the points closest to the wall increasing to a maximum at the channel mid-height. The points at 12cm above the mid-height and 16cm below the mid-height do not follow the trend as expected, with higher velocities than expected. The velocity at 12cm above the mid-height is more than double that at 16cm above the mid-height. The cause of this increase in velocity may be due to the geometry of the wheel case affecting the air flow. The measurement height corresponds to the height at which the gap in the casing for flow to pass through the wheel starts. This may cause acceleration of the flow as it moves quickly through the wheel.

The acceleration of the air through the rotary wheel can be seen by comparing the air velocities and trendlines. The increase in velocity matches that seen in the CFD contours of air velocity and gauge pressure for the same tests. The flow accelerates through the contraction of the radial blades; this velocity is maintained at the measurement points after the rotary wheel.

Though the contours of gauge pressure from the CFD analysis of the 32-blade heat recovery rotary wheel presented a pressure drop average of 10.03Pa, higher than the desired pressure drop of 2Pa for integration with a passive ventilation system, the air velocity measurements

from the experiment do not show a significant reduction in air velocities after the wheel. This suggests that adequate supply rates could be achieved with the radial blade heat recovery rotary wheel.

Figure 6-4 shows the average air velocity in the outgoing airstream before and after the rotary wheel for tests HR-32-1 to HR-32-4. Similar values for air velocity and flow profiles are presented.

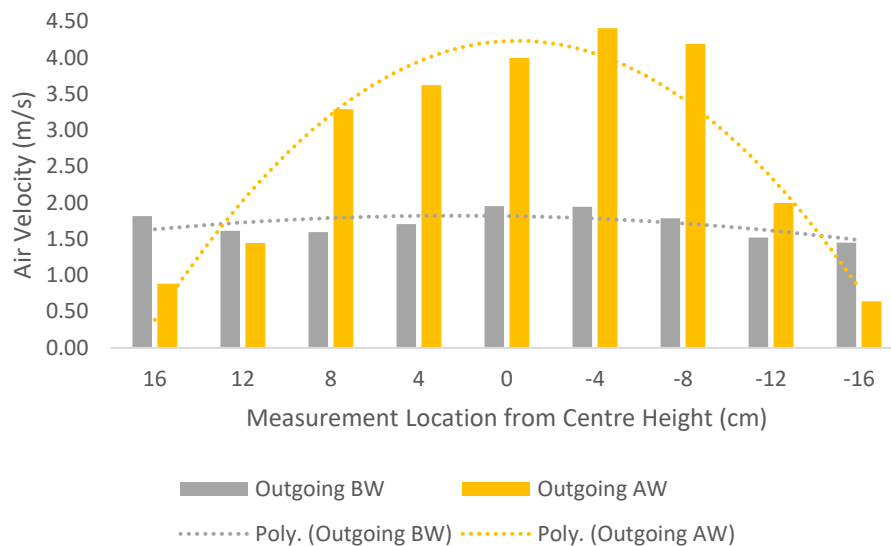


Figure 6-4 – Average air velocity for tests HR-32-1 to HR-32-4 measured before and after the rotary wheel in the outgoing airstream

The flow profile before the rotary wheel in the outgoing airstream features more uniform velocity measurements compared to the incoming airstream profile before the wheel. A small amount of variation can be seen in the velocities across the height of the channel, the general trend of low air velocity close to the channel wall and maximum velocity at the channel mid-height is maintained, reflected in the trendline, but the trend is not as pronounced as in the incoming airstream.

The acceleration of the air flow through the rotary wheel, maintaining the gained velocity after the wheel can clearly be seen in the graph. The trendline of the flow after the wheel shows a symmetrical distribution of air velocity either side of the mid-height. However, the values of air velocity do not reflect this. The velocity at the two measurement points directly below the mid-height are higher than the velocity at the mid-height. This is not the expected result and suggests a bias to the lower half of the channel. As the flow through the ductwork was achieved through suction forces of the axial fans, differences in the setup of the fans may have introduced errors to the flow profile. However, the same measurement points in

the incoming airstream are higher than the mid-height velocity. This suggests that the error is due to the experiment setup. Despite the unsymmetrical profile of the flow after the wheel, the expected pattern of slower flow closer to the channel wall is achieved.

An unexpected result of the air velocity measurements for the 32-blade configuration is the measured air velocity before the rotary wheel is lower in the outgoing airstream compared to the incoming airstream. As the two airstreams were setup with the same axial fan designs, it was predicted that the velocities would be similar. This was the calculated result in the CFD analysis and shown in the flow visualisation. However, the variation in air velocities is likely due to the influence of the ductwork used at the inlet of the outgoing airstream. The ductwork fed the inlet air to the outgoing air channel at an increased temperature for testing of the heat transfer across the rotary wheel. It was assumed the effect of the fed air would be negligible to the air velocity in the channel as the ductwork was positioned 300mm from the inlet. Future testing would benefit from testing the air velocity of radial blade configuration without the influence of the heat supply ductwork.

Figure 6-5 presents the average values for air velocity from the nine measurement points before and after the wheel in the incoming air channel for the 20-blade heat recovery rotary wheel configuration. The velocity profiles before and after the wheel match those seen in the 32-blade configuration in the incoming airstream. The value at 12cm above the mid-height before the wheel peaks above the other values, offsetting the trend. This supports the suggestion that the experimental setup introduces the error of velocity measurement at this point. The other values for air velocity before the wheel match closely to the trendline, indicating the flow profile similar to a fully developed flow in a channel. The values for air velocity measured before the wheel are lower in the 20-blade configuration compared to the 32-blade configuration. This is potentially due to the recirculation of air at the face of the wheel; the higher number of radial blades causing backflow as air is not able to flow through the wheel. This is supported by the images for flow visualisation. As the hot-wire anemometer cannot distinguish between forward and backward flow, recirculation of the flow would not be registered.

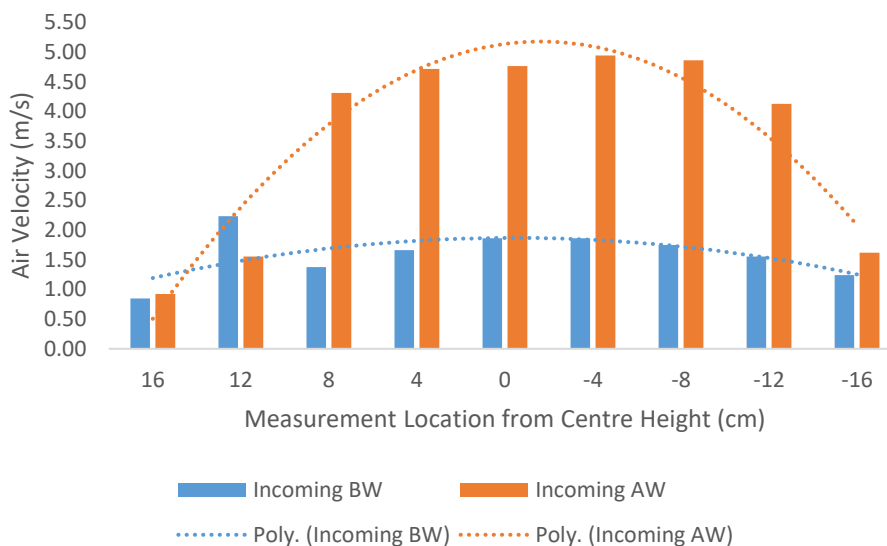


Figure 6-5 – Average air velocity for tests HR-20-1 to HR-20-4 measured before and after the rotary wheel in the incoming airstream

The acceleration of the flow from the measurement before the rotary wheel to the measurement location after the wheel is greater for the 20-blade configuration compared to the 32-blade configuration. Moving from lower velocity before the wheel to greater air velocity after the wheel, the 20-blade configuration agrees with the CFD simulations with regard to these results. The cause of the higher velocity after the rotary wheel has been theorised previously. Given the greater opening volume of the 20-blade configuration, a greater volume of air is able to move through the rotary wheel, accelerating as it does so.

The pattern for the values for air velocity measured after the rotary wheel is similar to that seen in the incoming and outgoing airstreams for the 32-blade configuration. The general shape of the profile is comparable to a flow in a channel, low velocity at the channel walls and higher at the centre point. However, higher velocity is measured at the two measurement points directly below the centre point; this pattern is repeated in the previous two analysis cases of the experiment measurement. The setup of the experiment, specifically the axial fans at the outlet, are most probably the cause of the error. If the axial fans were not positioned and mounted accurately at the outlets of the ductwork, the lower axial fan may have greater influence on the flow through the channel. However, as the error was consistent in both the incoming and outgoing airstreams of the 32-blade configuration, the positioning and mounting of the axial fans is unlikely to be the source of the experimental error.

Figure 6-6 shows the average values for air velocity before and after the rotary wheel in the outgoing airstream for the 20-blade configuration. The profiles of the air flow taken from the

trendlines added to the graph indicate that the flow for this setup is not stable and consistent with the results from other setups. The parabolic shape of the flow profile before the wheel is not evident; instead, the profile appears linear with almost consistent velocity across the height of the channel. This could suggest a highly turbulent flow for this set of measurements, compared to the flow profiles seen before which are more similar to a laminar flow. A typically turbulent flow profile would have more consistent measurements for air velocity at different heights along the channel compared to the parabolic shape of laminar flow. The profile indicates lower air velocity in the outgoing airstream compared to the incoming channel. The velocity at the point 12cm above the mid-height is the highest value measured before the wheel. This was the case in the incoming airstream for the 20-blade configuration also. This implies that the cause is related to the geometry or setup of the 20-blade configuration. However, the difference between the maximum values at 12cm above the mid-height is less pronounced in the outgoing airstream compared to the incoming air.

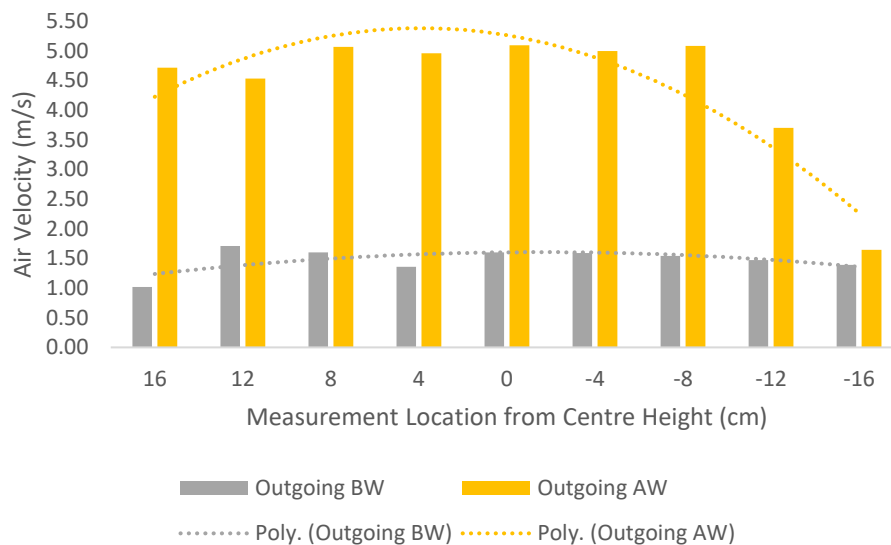


Figure 6-6 – Average air velocity for tests HR-20-1 to HR-20-4 measured before and after the rotary wheel in the outgoing airstream

As seen in the previous cases, the velocity of the air increases as it moves through the wheel and exits the other side. The increase in velocity is similar to the increase in the incoming airstream; however, air velocities errors are obvious. The values for velocity 16 and 12cm above the mid-height exceed the expected results significantly. Given the results from the previous measurement, it was predicted that the air velocities would be similar; however, the high velocities at the two points are counter-intuitive. Furthermore, the two measurement directly before the mid-height are higher than the velocity at the mid-height,

repeating the pattern seen previously. The source of these errors is difficult to determine, as the points below the mid-height are consistent between each of the tests conducted, it can be assumed an experiment error inherent in the design. The source of the error for the two points in the outgoing airstream of the 20-blade configuration could be a result of faulty test equipment.

The air velocity measurements for the radial blade heat recovery rotary wheel configurations used in the experiments show that as the air moves along the length of the channel, the velocity increases due to the contraction of the free volume through which the air can move. This agrees with the solutions calculated in the CFD analysis. Though the trends for air velocity in each of the test cases and airstreams appear to follow the anticipated pattern for flow in a channel, a number of discrepancies have been highlighted that deviate from the profiles expected. The cause of the errors have been determined as experiment setup inaccuracies relating to the positioning and mounting of the axial fans used for suction driven flow through the ductwork.

Though errors in the air velocity were measured in the experimental testing of the radial blade heat recovery rotary wheel configurations, the results were comparable to the CFD analysis as demonstrated by the validation of the models in the previous chapter. Further refinement of the experiment setup with regard to the driving force for flow and channel length would likely improve the flow distribution through the ductwork.

6.2.3 Air Pressure

The design of the radial blades for a rotary wheel was to provide a recovery device capable of integration with a passive ventilation system due to the low pressure drop experienced by air flowing through the device. Current recovery devices required fans to accelerate the air through the recovery device as the pressure drop was too great to overcome whilst being able to adequately supply the required ventilation rates in a passive ventilation system. A low pressure drop recovery device could be integrated into a passive ventilation system without affecting supply rates but providing the benefits of a recovery device.

The increased volume between radial blades compared to a standard rotary wheel was predicted to decrease the pressure drop across the device. Reduced skin friction between the moving air and the walls of the recovery device, along with larger openings at the wheel faces, would prevent high pressure areas from being generated, lowering the overall pressure drop.

Figure 6-7 shows the contours of gauge pressure in the incoming and outgoing airstreams for the 32-blade heat recovery rotary wheel configuration for test HR-32-1. The pressure contours provide a similar set of results to the air velocity contours and can be used to understand why the velocity acts and behaves as it does in the previous images.

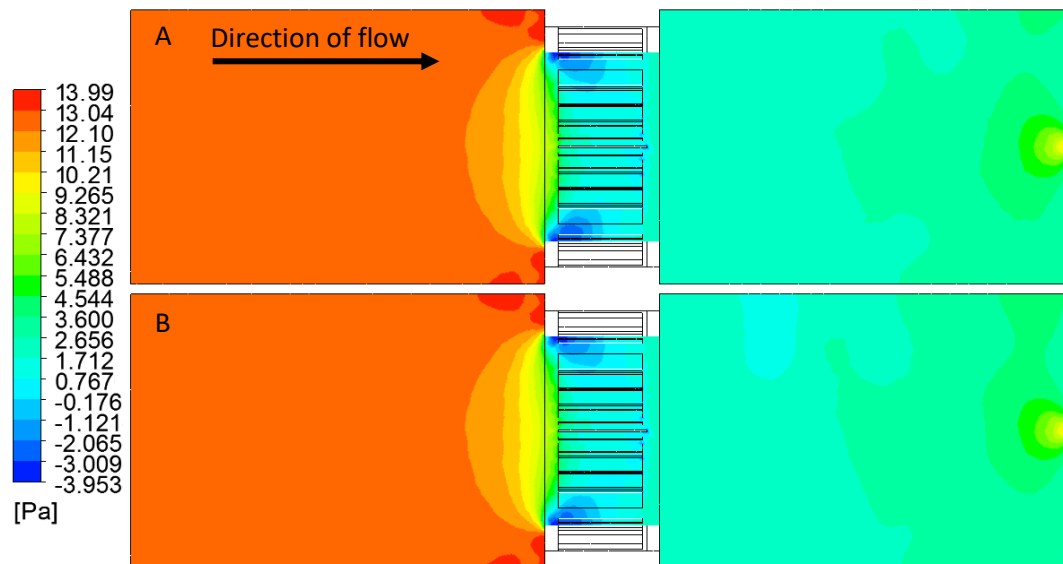


Figure 6-7 – Contours of gauge pressure for the 32 radial blade configuration A) Test HR-32-1 incoming air, B) Test HR-32-1 outgoing air

As the flow develops as it moves along the channel, the air pressure before the rotary wheel is approximately 12Pa. This decreases at the area immediately before the rotary wheel, the same shape and area where the air velocity increases in Figure 6-1. Pressure and velocity are related characteristics, as pressure increases, velocity decreases and as pressure decreases, velocity increases. The decrease in pressure immediately before the rotary wheel and in the volumes between radial blades reflects the increase in air velocity seen in the previous images. As the air exits the rotary wheel, the gauge pressure values remain similar to those inside the rotary wheel, indicating little to no change in air velocity.

Table 6-1 shows the measurements for gauge pressure taken from the CFD analysis of the 32-blade rotary wheel. The measurements were made 100mm before and after the wheel at the mid-height of the channel along the centreline. The pressure drop across the device was calculated for each test to determine if the change in inlet air temperature of the outgoing airstream had an effect. It can be seen, similar to the air velocity contours, that the change to inlet air temperature does not appear to have a significant effect on pressure measurements.

Table 6-1 – Gauge pressure measurements before and after the rotary wheel in the incoming and outgoing airstreams for the 32 radial blade configuration

	Incoming			Outgoing		
	Before Wheel (Pa)	After Wheel (Pa)	Pressure Drop (Pa)	Before Wheel (Pa)	After Wheel (Pa)	Pressure Drop (Pa)
HR-32-1	12.16	2.13	10.03	12.16	2.14	10.02
HR-32-2	12.16	2.13	10.03	12.21	2.27	9.94
HR-32-3	12.16	2.13	10.03	12.19	2.20	9.99
HR-32-4	12.19	2.15	10.04	12.12	1.97	10.15

The values for gauge pressure are consistent for each of the tests, in both of the air channels. Little variation is present before and after the wheel, which suggests that the changes to the inlet air temperature of the outgoing airstream have little effect on the gauge pressure. The average calculated value for pressure drop across the device for the 32-blade configuration is 10.03Pa. This is above the targeted value of 2Pa for passive ventilation systems to meet adequate supply rates. However, it is a significant reduction compared to standard rotary wheels, where pressure drop can be as high as 150Pa.

Contours of gauge pressure for the 20-blade configuration in the incoming and outgoing airstreams can be seen in Figure 6-8. The contours provide a similar profile to that seen in the 32-blade configuration. The uniform high pressure distribution before the wheel indicates the developed flow, with the area of lower pressure and increasing air velocity just before the rotary wheel. Areas of higher pressure above and below the rotary wheel in the channel indicate the recirculation zones as a result of the shape of the channel and wheel casing.

The low pressure as the air enters the rotary wheel shows that the air accelerates as the volume constricts with no other path for the air to flow. It is interesting to note that the maximum negative pressure for the 20-blade configuration is higher than that of the 32-blade configuration. This mirrors the values of air velocity. Given the relationship of velocity and air pressure in the continuity equation, this is expected. The negative pressure, shown by the contours in dark blue at the upper edges of the rotary wheel, extend to a smaller area but with greater value for the 20-blade configuration. Despite the greater volume of free space between radial blades, the area of negative pressure is smaller.

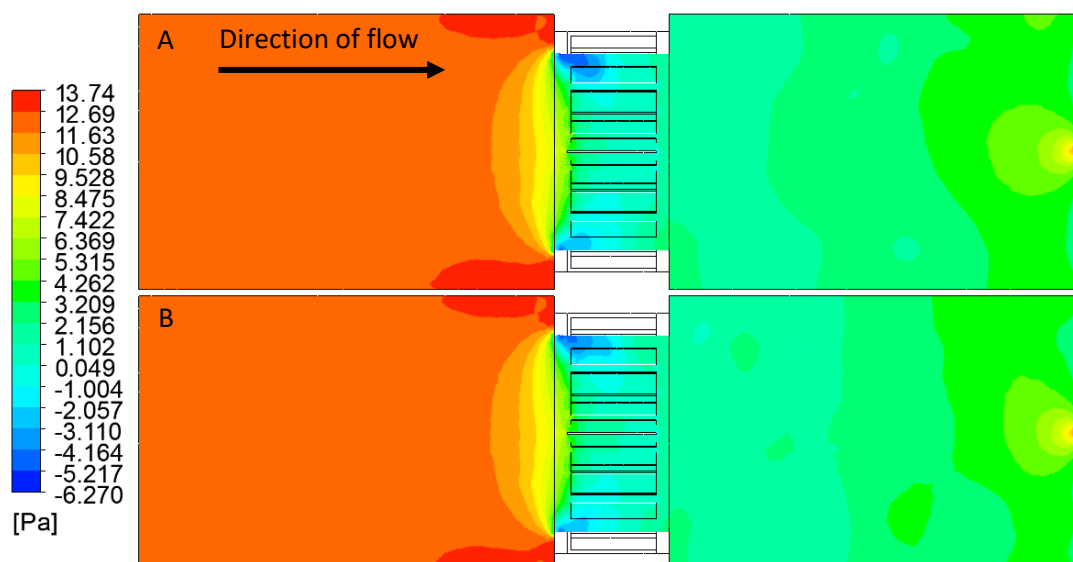


Figure 6-8 – Contours of gauge pressure for the 20 radial blade configuration A) Test HR-20-1 incoming air, B) Test HR-20-1 outgoing air

As the air exits the rotary wheel, the values of gauge pressure are similar to that in the space between the radial blades. However, unlike the 32-blade configuration, as the air moves down the length of the channel after the wheel, the pressure begins to increase. This suggests that the air is slowing, an example of pressure recovery, which would affect the ventilation rates as mentioned above.

Table 6-2 shows the gauge pressure measurements before and after the 20-blade rotary wheel in both the incoming and outgoing airstreams. The increase in air temperature at the outgoing airstream inlet has little effect on the gauge pressure values before and after the rotary wheel.

Table 6-2 – Gauge pressure measurements before and after the rotary wheel in the incoming and outgoing airstreams for the 20 radial blade configuration

	Incoming			Outgoing		
	Before Wheel (Pa)	After Wheel (Pa)	Pressure Drop (Pa)	Before Wheel (Pa)	After Wheel (Pa)	Pressure Drop (Pa)
HR-20-1	12.04	1.93	10.11	12.02	2.02	10.00
HR-20-2	12.01	1.96	10.05	11.99	1.94	10.05
HR-20-3	11.98	1.96	10.02	12.03	2.25	9.78
HR-20-4	11.99	1.87	10.12	12.03	2.02	10.01

Little change to the pressure values exists between the successive tests. The average pressure drop across the device in both airstreams was calculated as 10.02Pa, again significantly higher than the target value of 2Pa for passive ventilation integration, but

substantially lower than the 150Pa pressure drop common with rotary wheels. The average pressure drop is almost identical to the average pressure drop across the 32-blade configuration of the radial blade, suggesting that the number of blades has little direct effect on the pressure drop across the device.

It is possible that the rotation speed of the rotary wheel is a more significant factor affecting pressure drop than the number of radial blades in the rotary wheel design. The same rotation speed of 6rpm was maintained throughout the testing for both heat recovery configurations due to the single speed motor used. Further testing of the heat recovery rotary wheel, increasing and decreasing the rotation speed of the wheel in order to analyse the effect on the pressure drop would be worthwhile. This would also effect the air velocity profile of the heat recovery rotary wheel.

Though the average pressure drop across the heat recovery radial blade rotary wheel for the analysed tests is higher than the anticipated value of 2Pa, the overall reduction to pressure drop due to the novel design is substantial. This suggests that the design can be further improved to further reduce the pressure drop. Despite the higher than anticipated pressure drop averages, the values for air velocity after the rotary wheel are high and show acceleration of the flow after the wheel compared to before the wheel. Additional testing would be required of a longer test section to ensure that the higher air velocities are maintained along the length of a channel, along with various rotation speeds of the rotary wheel to understand the effect on pressure drop.

The aim of a low-pressure drop across the radial blade heat recovery system was to ensure that the integration into a passive ventilation system would not be limited by low supply rates that do not meet the minimum guidelines levels. Though the pressure drop across the device was higher than anticipated, the velocity flow rates were maintained at a high value. The results from the experiment tests and CFD simulations showed that the air accelerated through the wheel, maintaining the higher velocity as it exited. This is encouraging for passive ventilation integration as the supply rate guidelines may be met regardless of the higher than expected pressure drop.

The lowest average air velocity after the wheel is given for the incoming airstream for the 32-blade configuration. Calculating an air supply rate using the average air velocity and area of the channel gives 141.12 litres per second. Given the guidelines provided in Building Bulletin 101 [9] for adequate supply rates if 8 litres per second per person, the radial blade design rotary wheel is capable of providing supply air for 17 people in an occupied space. A

number of considerations should be taken with this analysis however. Axial fans providing a suction force, dissimilar to a passive ventilation system, drive the air velocity in this analysis. The air velocity in a passive ventilation system is likely to be lower than the values experienced. However, the standard dimensions of a wind tower system, the passive ventilation system considered for integration, has a larger opening area for ventilation than the ductwork channel area. This would increase the total volume of supply air able to pass through the system.

6.2.4 Air Temperature

The transfer of heat from one airstream to the other is the key performance indicator for a rotary thermal wheel. The performance of the radial blade rotary wheel with regard to this was tested using CFD simulations that used the boundary conditions taken from the experiment tests. The inlet air temperature for each of the air channels was measured from the experiment test. The temperature of the incoming airstream was dependent on the internal conditions of the laboratory. Given the internal environment of the laboratory, the incoming air inlet temperature was relatively stable for each of the tests. As previously mentioned, the inlet air temperature of the outgoing airstream increased from 25°C to 40°C from test HR-32-1 to test HR-32-4 for the 32-blade configuration and test HR-20-1 to test HR-20-4 for the 20-blade configuration.

The change of air temperature in the airstreams was modelled in the CFD analysis by assigning fluid volumes with the same geometry as the copper blades energy source and energy sink terms. The source and sink terms can be set to alter the characteristics of the flow. Energy source terms were set for the incoming airstream to model the increase in air temperature and energy sink terms were set for the outgoing airstream to model the decrease in air temperature. The values for the source and sink terms were increased depending on the change in temperature experienced by the airstream.

The distribution of the air temperature in the channels can be seen in the contours of air velocity for the 32-blade configuration in Figure 6-9. The contours show the air temperature in both the incoming and outgoing airstreams for test HR-32-4 when the inlet temperature for the outgoing airstream was set to 40°C. The visualisation of the air temperature distribution is useful to provide a clearer assessment of the impact of the blades on the air. Due to the experimental limitations, the measurements were made at only one point before and after the wheel in each airstream at the channel mid-height and 100mm from the face of the rotary wheel in each direction. The visualisation provides a view of the distribution

along the full height and length of the channel. The effect of the source and sink terms representing the radial blades can clearly be seen. An increase of 0.76°C in the incoming airstream can be seen in Figure 6-9A and a decrease of 2.36°C in the outgoing airstream can be seen in Figure 6-9B.

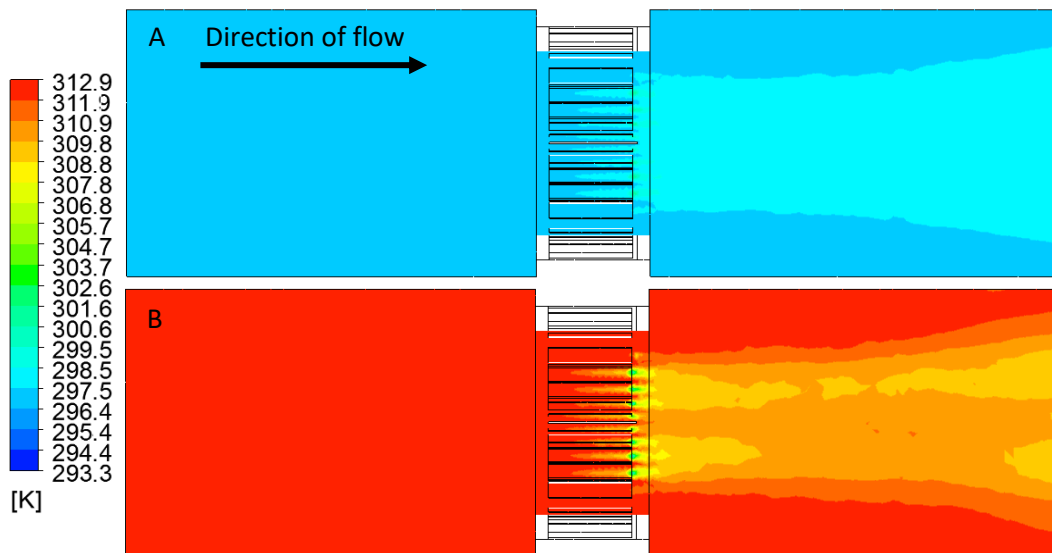


Figure 6-9 – Contours of air temperature for the 32 radial blade configuration A) Test HR-32-4 incoming air, B) Test HR-32-4 outgoing air

In the experimental tests, the temperature in the incoming and outgoing air channels was measured before and after the heat recovery rotary wheel for the 32 and 20-blade configurations. The measurements for air temperature were collected every 5 seconds for 1 hour, giving 720 readings. Before the readings were taken, the inlet air temperatures were allowed to stabilise. The values for air temperature that follow are averaged values from the recording period. The averages were used for analysis, as the temperatures were relatively stable across the recording period; also, the averages give a representative value for longer run times of the system.

Figure 6-10 shows the change in air temperature measured across the rotary wheel for the incoming and outgoing airstreams for test HR-32-1 to HR-32-4. The data from the graph shows the expected trend from the experiments. As the inlet temperature of the outgoing airstream increased from 25°C in test HR-32-1 to 40°C in test HR-32-4, the changes to air temperature in each of the airstreams increase. The difference between the changes to air temperature in the incoming and outgoing airstreams can be perceived as the ability of the radial blade rotary wheel to recover heat.



Figure 6-10 – Temperature change before and after rotary wheel for incoming and outgoing airstreams for 32-blade arrangement

It can clearly be seen in the graph that despite the temperature change increasing as the inlet air temperature of the outgoing airstream increases, the temperature change in the incoming and outgoing airstreams are not equal. The copper radial blades in the outgoing airstream conduct more thermal energy than is released in the incoming airstream. This shows that a significant amount of energy remains in the copper blades as it rotates around. By adding the values of air temperature change from each airstream together, the amount of thermal energy remaining in the radial blades can be calculated.

Table 6-3 shows the values for the average air temperature before and after the rotary wheel in the incoming and outgoing airstreams along with the temperature change. The temperature change in the incoming airstream increases linearly as the inlet air temperature of the outgoing air increases. A large increase in temperature change occurs in the outgoing airstream between test HR-32-1 and HR-32-2, when the outgoing air inlet temperature changes from 25°C to 30°C. This large increase in temperature change is not reflected in the temperature change of the incoming airstream. It is possible that above a minimum value, the copper material is able to more efficiently conduct heat. It is also possible that if the surface temperature of the copper blades reach a minimum value, convection from the radial blades to the incoming airstream is more easily achieved.

Table 6-3 – Air temperature measurements for the incoming and outgoing airstreams for 32-blade arrangement

	Incoming			Outgoing		
	Inlet Air Temperature (°C)	After Wheel (°C)	Temperature Change (°C)	Inlet Air Temperature (°C)	After Wheel (°C)	Temperature Change (°C)
HR-32-1	23.13	23.28	0.14	25.04	24.78	-0.26
HR-32-2	23.43	23.74	0.31	29.40	27.69	-1.72
HR-32-3	23.72	24.18	0.47	34.90	32.86	-2.04
HR-32-4	23.92	24.61	0.68	39.79	37.39	-2.40

The maximum difference between the temperature changes in the experimental incoming and outgoing airstreams is 1.72°C in test HR-32-4; the differences for tests HR-32-1 to HR-32-3 are 0.12, 1.40 and 1.58°C respectively. These values represent the thermal energy stored within the radial blades of the heat recovery rotary wheel. The similar inlet air temperatures for the incoming and outgoing airstreams for test HR-32-1 may contribute to the low temperature changes measured in the test. Lower inlet air temperature for the incoming airstream may result in greater heat transfer from the outgoing airstream to the incoming air.

The CFD simulations were designed to replicate the conditions of the experiment. The boundary conditions were calculated from the measured values in the experiment testing. The cell zone conditions of the volumes representing the radial blades for energy source/sink terms were altered to give a result similar to the experiment values. Table 6-4 shows the percentage error of the air temperature values of the CFD analysis measured after the rotary wheel compared to the experiment results for the corresponding test and measurement location. The table also shows the value for the energy source and sink terms used for the fluid volumes. The source and sink terms have been adjusted based on the percentage error of the CFD, the resultant adjusted values for energy source and energy sink can then be used to predict the exact values measured in the experiment.

Table 6-4 – Percentage error for CFD model compared to experiment results for air temperature after the wheel. Heat source and heat sink values for incoming and outgoing airstreams and adjusted values for error

	Incoming				Outgoing			
	% Error	Energy Source (w/m ³ s)	Adjusted for %Error	Adjusted Source (w/m ³ s)	% Error	Energy Sink (w/m ³ s)	Adjusted for %Error	Adjusted Sink (w/m ³ s)
HR-32-1	0.06	100000	64	100064	0.03	-200000	-70	-199930
HR-32-2	-0.23	277000	-643	276357	-0.11	-1250000	1436	-1251436
HR-32-3	-0.07	360000	-248	359752	-0.03	-1500000	476	-1500476
HR-32-4	-0.29	565000	-1620	563380	-0.12	-1750000	2041	-1752041

Figure 6-11 shows the contours for air temperature in the incoming and outgoing airstreams for the 20-blade configuration, specifically in test HR-20-4 when the outgoing airstream inlet temperature was set to 40°C. The same effect on the air temperature noted in Figure 6-9 for the 32-blade configuration can be seen in the 20-blade configuration. The incoming airstream increases in temperature after the rotary wheel and the outgoing air temperature decreases in temperature after the rotary wheel. The change in temperature for both airstreams is lower when compared to the 32-blade configuration and the size of the affected area is smaller. This is expected given the fewer blades in the 20-blade configuration and lower volume of copper for heat transfer. The low increase in air temperature in the incoming airstream is difficult to determine due to the scale used. The low temperature increase affects two bands above and below the mid-height of the channel.

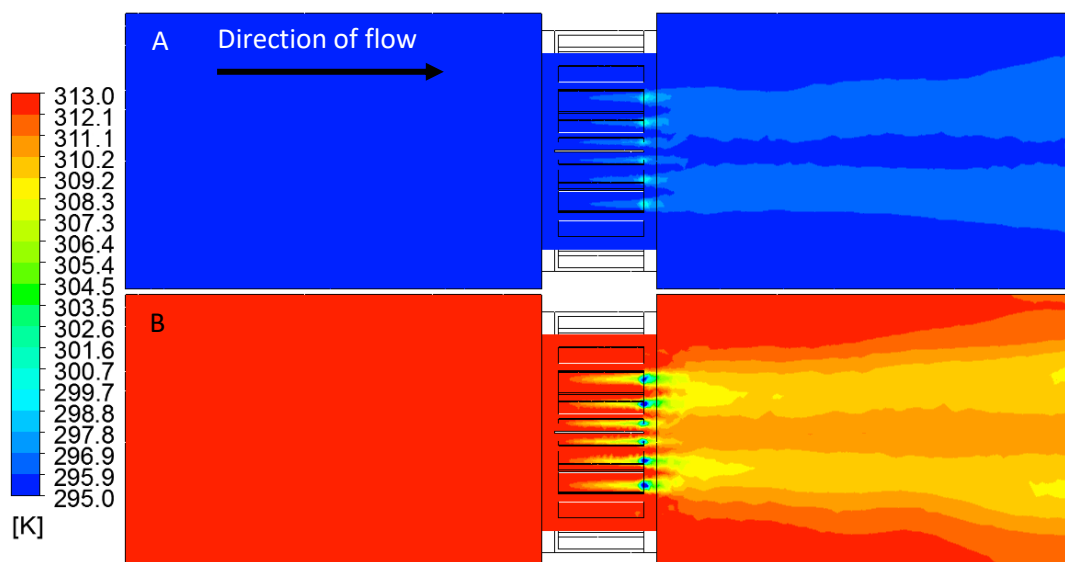


Figure 6-11 – Contours of air temperature for the 20 radial blade configuration A) Test HR-20-4 incoming air, B) Test HR-20-4 outgoing air

Figure 6-12 shows the temperature change for the incoming and outgoing airstreams for tests HR-20-1 to HR-20-4 of the 20-blade configuration of the heat recovery rotary wheel

based on the measurements for air temperature in the experimental tests. The graph for the incoming and outgoing airstreams show the same trend as the 32-blade configuration where temperature change increases as the inlet air temperature of the outgoing air increases. Furthermore, the values for temperature change are generally lower in the 20-blade configuration compared to the 32-blade configuration. This was the expected outcome given the lower volume of material available for heat conduction. However, the temperature change in the outgoing airstream for test HR-20-3 is significantly higher than all other measurements. The temperature change of 3.53°C is larger than all other measurements, including those in the 32-blade configuration; it is likely that this is a result of experimental error. It is possible the error was caused by interference from a cold source, such as an unexpected opening in the ductwork, increasing the temperature change. Given the linear trend for the 32-blade outgoing airstream values, an approximate temperature change of 1.30-1.50°C would be more appropriate.

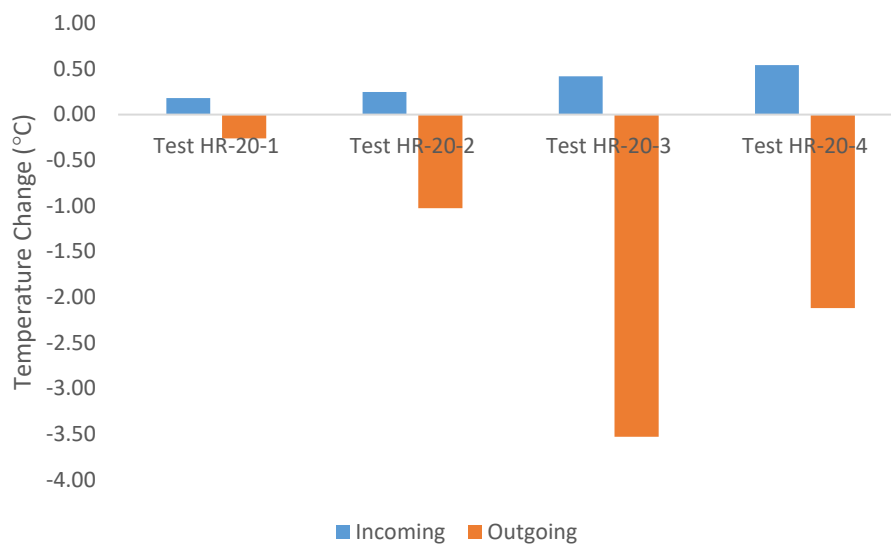


Figure 6-12 – Temperature change before and after rotary wheel for incoming and outgoing airstreams for 32-blade arrangement

The change in air temperature across the heat recovery device in the outgoing airstream is higher than that in the incoming airstream, as shown in Figure 6-12. Equation 6-1 is the heat balance equation that relates the mass flow rate \dot{m} , specific heat capacity C_p and temperature change for an airstream ΔT . Given the continuity between the two airstreams, the equation suggests that the values for each airstream must be balanced.

Equation 6-1

$$Q = \dot{m}C_p\Delta T$$

However, given the measurements from the experiment, this is not the case. Balanced values for temperature change in both airstreams would suggest a 100% efficient heat recovery device. Therefore, losses are the cause of the difference between temperature changes in the airstreams and must be accounted for. Losses caused by the lack on insulation of the ductwork will have a significant effect, as heat is lost through the duct walls. Furthermore, as mentioned in Chapter 2, rotary wheels are susceptible to cross contamination of airstreams due to the design of the system and the lack of seals. This means the air is able to move between the ductwork channels. This will also have a significant effect on the losses of the system and affect the measurements of air temperature by the probes. Other losses may be due to the recirculation of air from the outlets to the inlets. Increasing the distance between them or ensuring separation would improve this. These losses account for the difference in temperature change between the incoming and outgoing airstreams.

Table 6-5 shows the average values for the air temperature and temperature change for the incoming and outgoing airstreams for the 20-blade configuration. The incoming airstream temperature change follows a similar pattern to that seen in the 32-blade configuration, a linear increase as the inlet air temperature of the outgoing airstream increases. The values of temperature change for the incoming air can be calculated as 79-89% of the values of temperature change for the 32-blade configuration in the incoming airstream. Given that the material volume of 20-blade configuration is 62.5% of the material volume of the 32-blade configuration, this suggests that the material volume does not have as large an effect on the temperature transfer from the outgoing airstream to the incoming air.

Table 6-5 – Air temperature measurements for the incoming and outgoing airstreams for 20-blade arrangement

	Incoming			Outgoing		
	Inlet Air Temperature (°C)	After Wheel (°C)	Temperature Change (°C)	Inlet Air Temperature (°C)	After Wheel (°C)	Temperature Change (°C)
HR-20-1	22.28	22.46	0.18	24.70	24.44	-0.26
HR-20-2	22.81	23.06	0.25	29.73	28.70	-1.02
HR-20-3	21.36	21.78	0.42	34.82	31.29	-3.53
HR-20-4	22.14	22.68	0.54	39.81	37.69	-2.12

However, a number of conditions may affect the temperature change for the incoming air. The inlet air temperature of the incoming air was lower in all instances of the 20-blade configuration testing compared to the 32-blade configuration. It is possible that the lower

incoming air inlet temperatures increased the heat transfer across the rotary wheel, artificially improving the performance of the 20-blade configuration. The lowest incoming air inlet temperature is 21.36°C compared to 23.72°C in the 32-blade configuration, a difference of 2.36°C. This corresponds to the erroneous value of temperature change for the outgoing airstream in test HR-20-3. This may have affected the temperature change value, increasing the temperature change due to the lower incoming air inlet temperature.

The differences in temperature change between the incoming and outgoing airstreams for the 20-blade configuration are lower than that of the 32-blade configuration. The values for tests HR-20-1, -2 and -4 are 0.08, 0.78 and 1.58°C respectively. This indicates that the number and material volume of radial blades has an effect on the heat energy stored in the radial blades. The high temperature change of the outgoing airstream in test HR-20-3 results in a difference of 3.11°C, which does not follow the trend of the other values.

Table 6-6 shows the percentage error for the air temperature measurements of the CFD analysis compared to the experimental test for the 20-blade configuration of the heat recovery rotary wheel. The energy source and sink terms were adjusted for the error for each of the tests and the adjusted values are shown. Using the adjusted values, the air temperatures measured from the experiment would be output from CFD simulation.

Table 6-6 – Percentage error for CFD model compared to experiment results for air temperature after the wheel. Heat source and heat sink values for incoming and outgoing airstreams and adjusted values for error

	Incoming				Outgoing			
	% Error	Energy Source (w/m ³ s)	Adjusted for %Error	Adjusted Source (w/m ³ s)	% Error	Energy Sink (w/m ³ s)	Adjusted for %Error	Adjusted Sink (w/m ³ s)
HR-20-1	-0.03	250000	-65	249935	-0.25	-269500	679	-270179
HR-20-2	0.20	270000	546	270546	0.08	-1400000	-1152	-1398848
HR-20-3	0.23	490000	1131	491131	0.12	-4800000	-5583	-4794417
HR-20-4	-0.10	750000	-717	749283	0.11	-2890000	-3237	-2886763

CFD analysis was used to provide the solutions for air temperature measurements of the radial blade heat recovery rotary wheel recorded before and after the rotary wheel in the incoming and outgoing air channels for the 32 and 20-blade configurations. Using energy source and sink terms, the CFD simulations predicted that the air temperature would increase in the incoming airstream and decrease in the outgoing airstream. These predictions have previously been validated by comparison with the experimental results.

The expected trend of increased temperature change for both airstreams as the outgoing airstream inlet temperature increased was realised for both configurations. Though the temperature change increased as the outgoing inlet air temperature increased, the temperature change was not equal between the incoming airstream and outgoing airstream. The temperature change in the outgoing airstream was significantly higher than the incoming airstream for both configurations. This shows the radial blade design is effective at conducting heat from the outgoing airstream but less effective at releasing this energy to the incoming airstream. This suggests that significant thermal energy is stored within the radial blades. Increasing the ability of the radial blades to dissipate the stored thermal energy in the radial blades would greatly increase the performance of the radial blade heat recovery rotary wheel.

Furthermore, as the outgoing inlet air temperature increased from 25°C to 30°C, the most significant increase of the value of temperature change in the outgoing airstream was observed. From 0.26 to 1.72°C in the 32-blade configuration and 0.26 to 1.02°C for the 20-blade configuration. This would suggest that either there is a lower temperature threshold at which the copper radial blades are able to more effectively conduct heat from the airstream, or that a minimum temperature difference between the airstreams must be achieved for significant temperature change. When the inlet air temperature for the outgoing airstream was set 25°C, the average inlet air temperature for the incoming channel was 23.13°C and 22.28°C for the 32 and 20-blade configurations; this gives an inlet air temperature difference of 1.87°C and 2.72°C respectively. Given that the temperature increase of the incoming airstream for each test was 0.13°C and 0.19°C, the view that the temperature difference between airstreams affects the change in temperature for an individual airstream provides a stronger argument.

Given the relatively high inlet temperature of the incoming airstream, further investigation would be advised. As the radial blade rotary wheel was design for integration with a passive ventilation system, the incoming air temperature represents the external air conditions and temperature. Common air temperatures in the UK and northern Europe, the areas where heat recovery would be most beneficial in winter months, would be significantly lower than the temperatures measured in here.

6.3 Dehumidification Rotary Wheel

By applying the radial blade design to a dehumidification wheel, two goals were set. The first was tied to the initial goals of the overall radial blade design; reduce the pressure drop across the device to a sufficient level to allow integration with a passive ventilation system, enabling sufficient supply rates to be achieved. The second was to provide a system with a low regeneration temperature for the desorption of water molecules from the silica gel blades of the dehumidification rotary wheel. The regeneration temperature required for current dehumidification rotary wheels can be in excess of 100°C, requiring substantial amounts of energy to raise the temperature to these levels. Lower regeneration temperatures would reduce the total energy demand required for the system. Low pressure drop across the device would further enhance this.

The radial blade dehumidification rotary wheel was tested by using the same ductwork and experimental setup as the heat recovery rotary wheel. The relative humidity of the incoming airstream was maintained as close to 100% as possible, the inlet temperature of the outgoing airstream was increased from 25°C to 40°C in 5°C increments. This acted as the regeneration temperature for the dehumidification wheel. As relative humidity is related to air temperature, the air temperature of the incoming air inlet and relative humidity of the outgoing airstream were dependent on the properties that were controlled in each airstream. The relative humidity, air temperature and air velocity were measured experimentally, before and after the wheel in each airstream. The CFD simulations recorded the same characteristics along with the air pressure.

Two configurations of radial blades were used to assess the performance of the dehumidification rotary wheel. Configurations of 32 and 20 silica gel coated acrylic blades were arranged to evaluate the adsorption and desorption of water molecules in the airstreams. Due to the increased thickness of the dehumidification blades compared to the copper plates used in the heat recovery wheel, measurements of the air velocity were taken to understand the effect the difference in geometry would have. The tests are numbered DH-32-1 to DH-32-4 for the 32-blade configuration of the dehumidification rotary wheel and DH-20-1 to DH-20-4 for the 20-blade configuration.

6.3.1 Flow Visualisation

Flow visualisation allows the distribution of air around the ductwork to be seen without interrupting the flow. CFD analysis shows the air velocity distribution in the channel and between the radial blades of the rotary wheel. Understanding this interaction further

improves the evaluation of the rotary wheel by examining how the contraction of volume between blades affects the flow.

Contours for air velocity for the 32 radial blade configuration of the dehumidification rotary wheel are shown in Figure 6-13; both the incoming and outgoing airstreams are shown. Previous experience in assessing the air velocity for the heat recovery rotary wheel showed that the effect of inlet air temperature change on the flow profile through the channel is limited. As such, a single test case is shown here, representative of the overall profile of the flow from the inlet, through the channel and rotary wheel, and exhausting at the outlet. The contours show the expected profile, similar to that seen in the heat recovery analysis.

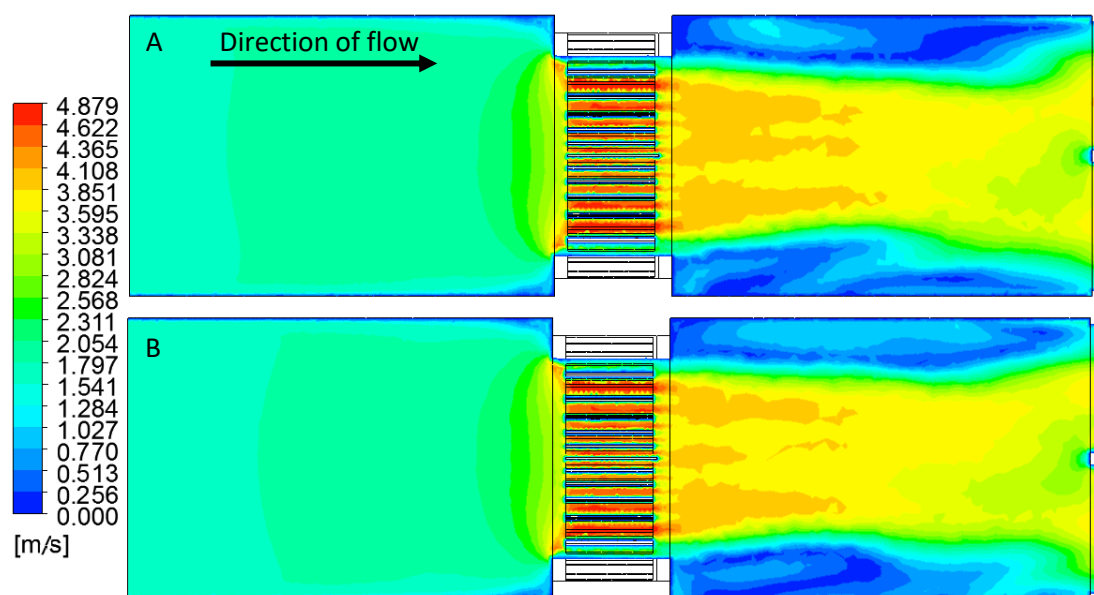


Figure 6-13 – Contours of air velocity for the 32 radial blade configuration A) Test DH-32-4 incoming air, B) Test DH-32-4 outgoing air

The air moves through the channel before the wheel in a fully developed manner, low velocity close to the channel walls with higher velocity at the mid-height. As the flow approaches the rotary wheel surface, the flow accelerates in the area directly prior to the wheel entrance. This is likely a result of the recirculation effect of the flow and reduced air pressure due to the contraction of the channel volume. The air accelerates through the radial blades of the rotary wheel, maintaining the increased velocity after the rotary wheel. As expected, given the increased thickness of the radial blades of the rotary wheel, the maximum air velocity for the dehumidification rotary wheel configuration with 32 blades is lower than that of the heat recovery rotary wheel with the same number of blades. This pattern agrees with the current theory that the reduced space between the radial blades constricts the flow, slowing the air down.

Large recirculation areas after the wheel can be seen at the walls of the channel. The recirculation zones are thicker and extend further down the length of the channel compared to the heat recovery radial blade arrangement. The recirculation zones are seen in the air velocity contours of each of the arrangements and configurations. This is related to the sudden change of shape, from the cylinder of the rotary wheel to the rectangular shape of the channel. This causes flow separation points at the edge of the rotary wheel. The increased size of the recirculation zones for the 32-blade dehumidification configuration is a result of the increased thickness of the radial blades.

Figure 6-14 shows the contours for air velocity in the incoming and outgoing channels for the 20-blade configuration of the dehumidification rotary wheel. The development of the flow profile along the length of the channel is similar to that seen in the 32-blade configuration. The effect of the recirculation prior to the wheel appears to be greater in the 20-blade configuration; a larger area of increased velocity can be seen before the wheel. As the previous analysis of the heat recovery rotary wheel demonstrated, the greater volume of air for the air to flow through increased the velocity. This explains the increased size of the high air velocity area before the wheel.

The acceleration of the air through the rotary wheel is greater in the 20-blade configuration compared to the 32-blade configuration, reaching a maximum velocity 0.13m/s higher in comparison. The cause of the higher air velocity in the 20-blade configuration has been discussed in the heat recovery rotary wheel analysis. Furthermore, the 20-blade configuration is able to maintain the higher velocity over a greater distance, shown by the orange coloured contour after the wheel. This extends a significantly longer distance compared to the 32-blade configuration, suggesting that pressure drop across the wheel is lower and air velocity can be maintained.

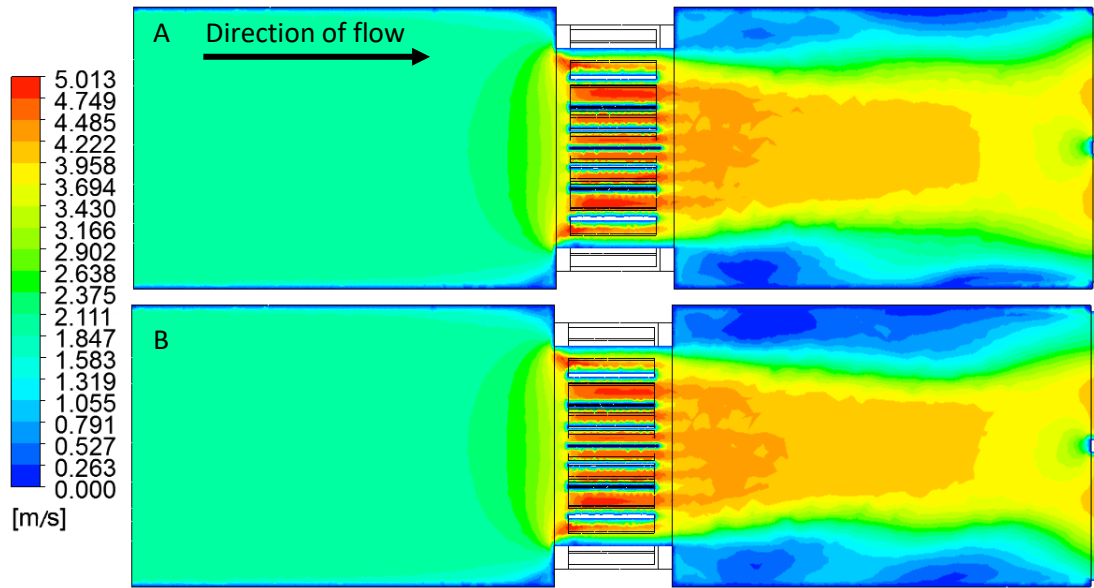


Figure 6-14 – Contours of air velocity for the 20 radial blade configuration A) Test DH-20-4 incoming air, B) Test DH-20-4 outgoing air

6.3.2 Air Velocity

The air velocity in the incoming and outgoing channels was measured 100mm in both directions from the face of the dehumidification rotary wheel. Measurements were taken at nine different heights along the centreline of the channel before and after the rotary wheel to give a flow profiles across the full height and an understanding of the effect the wheel has on the flow. Figure 6-15 shows the measurements for average air velocity and flow profile for tests DH-32-1 to DH-32-4 in the incoming airstream of the 32-blade dehumidification rotary wheel configuration.

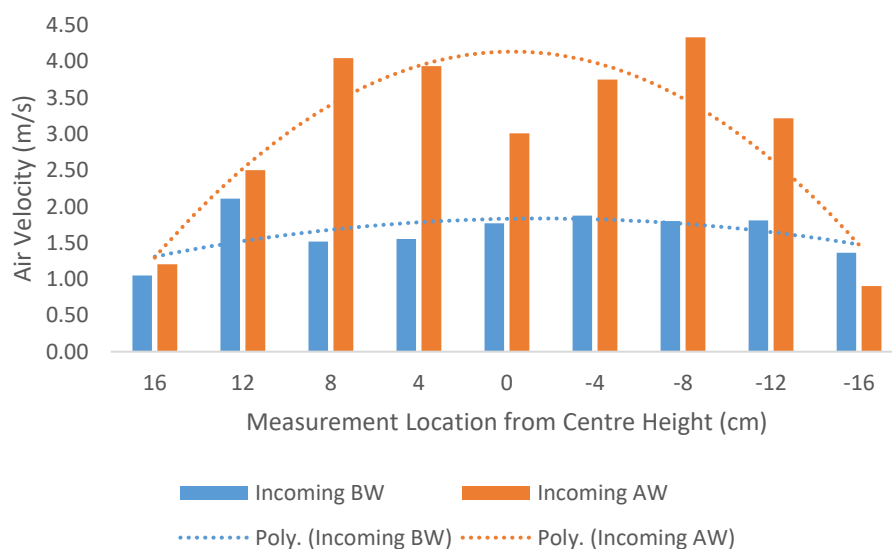


Figure 6-15 – Average air velocity for tests DH-32-1 to DH-32-4 measured before and after the rotary wheel in the incoming airstream

The velocities and flow profile before and after the rotary wheel varies considerably, not only along the height of the channel but also compared to the 32-blade heat recovery rotary wheel. The velocities measured before the wheel show a similar pattern to the expected profile, along with the measurements seen in the equivalent heat recovery tests. The trendline shows the flow appears similar to the fully developed profile along a channel. However, a number of ordinarily unexpected characteristics can be seen in the graph, though these characteristics have been observed in the experimental air velocity analysis of the heat recovery rotary wheel. The measurement for air velocity 12cm above the channel mid-height is the highest compared to the rest. This has been shown to occur regularly throughout the experimental measurements for air velocity.

The acceleration of the air flow through the rotary wheel is evident from the measurements shown. The velocity measurements before the rotary wheel are lower than the measurements after the rotary wheel for all except one case. The CFD flow visualisation shows the acceleration of the air through the contracted volume of the radial blades, and as the air maintains the increased velocity as it exits the wheel. This holds true with the experimental results. However, despite the trendline for the flow after the wheel showing the developed profile as expected in a channel, the measurements of air velocity show this to be inaccurate. The air velocity at the four measurement points either side of the channel mid-height location display higher values than at the mid-height, where conventional knowledge and experience would suggest the maximum air velocity would be located. Given the setup of the experiment, where the two axial fans are positioned at the outlets of the channels to provide flow through a suction driven force, the points of higher velocity above and below the mid-height is understandable. As a similar effect was noted for the heat recovery radial blade arrangement, the increased thickness of the dehumidification radial blades can be assumed to have a greater effect on the flow.

Figure 6-16 shows the measurements for average air velocity and the flow profile before and after the dehumidification rotary wheel from the outgoing airstream from testing of the 32-blade configuration. The profile generated from the values of air velocity before the rotary shows a linear trend, with a negative gradient from the upper section of the channel to the lower section. This is unusual, as the expected trend would show a parabolic shape with the highest value at the channel mid-height and the lowest values closest to the walls. Though no significant variation exists in the values, the deviance from the expect trend shows an experimental error, either a measurement error or setup error. As the experiments were

setup with the same method each time, measurement error from inaccurate placement and positioning of the hot-wire anemometer is more possible.

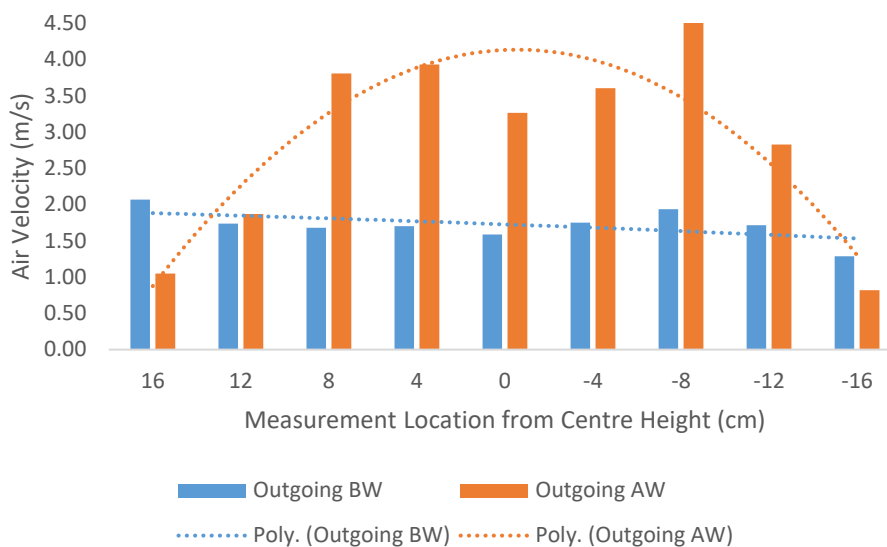


Figure 6-16 – Average air velocity for tests DH-32-1 to DH-32-4 measured before and after the rotary wheel in the outgoing airstream

However, the measurements from the same location of the 32-blade heat recovery configuration show equally as high a velocity measurement. In both cases, the velocity before the wheel is notably higher than the velocity after the wheel. This suggests that the cause is a setup error inherent in the experiment. Due to the geometry around the rotary wheel and in the channel, the measurements of velocity at the channel walls are less significant than the other measurement locations. The dimensions of the rotary wheel case extend such that recirculation areas are generated either side of the case close to the channel wall, the main volume of flowing air is directed through the centre of the channel around the mid-height. Therefore, air velocity errors outside this column are less consequential. The pattern of air velocities for the outgoing air before the wheel may be due to the effect of the ductwork providing the air at the outgoing channel inlet. The ductwork fed air from a heater to the outgoing air inlet was positioned 300mm from the inlet; with the aim to provide warmer air without disturbing the air flow through the channel. The measurements of air velocity suggest that this was not the case.

The air velocity measurements after the wheel show the acceleration that has previously been observed in all experimental tests and CFD simulations. The pattern of air velocities values for the outgoing airstream after the wheel is similar to that of the incoming airstream. Though the values differ marginally, the trends are comparable. The outgoing airstream also features a low mid-height air velocity, where the four velocities either side have higher

values. This suggests that the thicker plates of the dehumidification rotary wheel create this effect on the air flow. As the mid-height measurement location aligns with the central rotation shaft of the rotary wheel, no air flows directly at this height. The flow must re-join as it exits the separate sections of the rotary wheel. As the measurements are taken 100mm away from the wheel surface, the flow may not have sufficient space and time to fully develop, causing the pattern in the air velocities shown in the figure.

Figure 6-17 shows the average air velocities before and after the rotary wheel measured in experimental tests DH-20-1 to DH-20-4 for the 20-blade dehumidification configuration in the incoming airstream. The trends of the flow profiles before and after the rotary wheel more closely match the expected pattern of flow through a channel. The values for air velocity before the wheel are higher in the 20-blade configuration compared to the 32-blade configuration. This follows the pattern that was seen in the heat recovery air velocity analysis. As with the heat recovery rotary wheel, this is likely due to the greater volume between radial blades through which air can flow. This is reflected in the gauge air pressure contours in the CFD solutions previously discussed. The trendline of the air velocity values appear to follow the profile of a fully developed flow in a channel. The values measured 12cm above and below the mid-height are higher than the trend would dictate. Causes of this have previously been discussed.

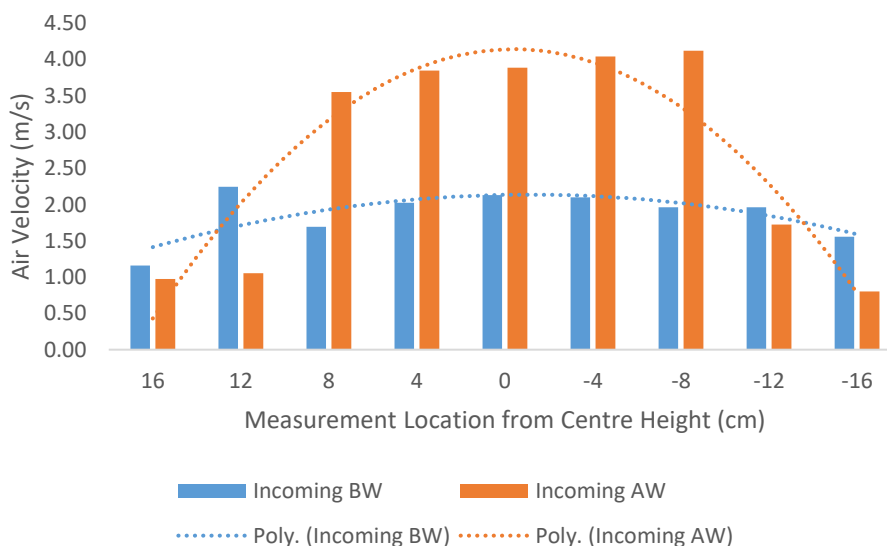


Figure 6-17 – Average air velocity for tests DH-20-1 to DH-20-4 measured before and after the rotary wheel in the incoming airstream

The air velocity after the rotary wheel shows the same profile present in the two measurements of the 32-blade configuration; high velocity either side of the mid-height measurement. Though the same pattern is present, to a lesser degree, the difference

between the mid-height value and the surrounding values is lower compared to the 32-blade configuration. The values show a dominance toward the lower measurement locations, suggesting that the lower mounted axial fan operated at a higher flow rate. The values after the rotary wheel are higher than the 32-blade configuration, reinforcing the proposed theory that the increased volume between radial blades increases the velocities.

The measurements for the average air velocity in the outgoing air channel of the 20-blade configuration are shown in Figure 6-18, along with the trendlines for the flow profile before and after the rotary wheel. The trendline for the values before the rotary wheel show a negative parabolic shape, the opposite of what is expected from the developed flow in a channel. This is due to the high values measured closest to the walls of the channel. When these values are disregarded, the flow profile is as expected. The two high values measured closest to the walls are similar to those in previous test cases. As examples have been characterised in each of the previous analysis cases, this suggests that the cause is experiment error, as described previously.

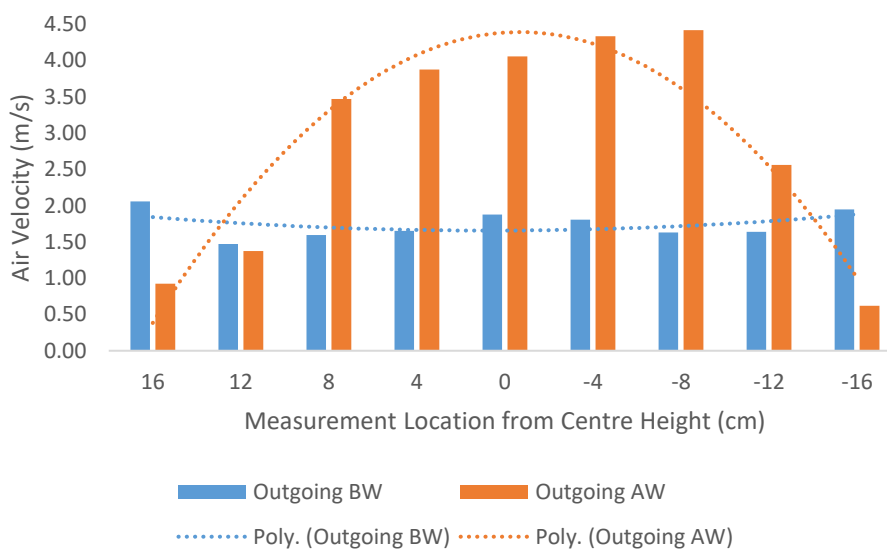


Figure 6-18 – Average air velocity for tests DH-20-1 to DH-20-4 measured before and after the rotary wheel in the outgoing airstream

The air velocity measurements taken after the rotary wheel are higher than the corresponding values in the 32-blade configuration. This reinforces the observation that the fewer radial blades present in the rotary wheel, the higher the resultant air velocities measured 100mm after. This observation has been noted in each analysis case for air velocities of the rotary wheel. The general trend for the flow profile follows the expected fully developed profile of flow in a channel.

However, the two velocities below the channel mid-height measurement location are at higher values than the mid-height value. Though the two measurements above the mid-height do not follow the pattern from the previous cases, the velocities measured are higher than expected. The dominance of the lower mounted axial fan also appears to be evident in the outgoing airstream based on the measurements. This may be affected by the mounting of the rotary wheel on the central shaft of the casing. Given that the fans were mounted in the same way for each test and no previous analysis showed a dominance of the lower velocities, another explanation may be possible. An offset of the rotary wheel on the rotary shaft could direct the flow to the lower part of the channel, resulting in the higher air velocities at the lower measurement locations.

The analysis of the air velocity measurements from the experimental tests of the two dehumidification rotary wheel configurations shows that the air accelerates through the wheel and the velocity is maintained afterwards in the channel. The presence of the radial blades does not impede the flow of air through the wheel. The 3mm thick radial blades used in the dehumidification arrangement result in decreased velocity of the air compared to the heat recovery arrangements with 1mm thick radial blades.

The results from the analysis of the air velocity for the dehumidification rotary wheel show a reduction in the maximum air velocity in the 32 and 20-blade configurations compared to the same configurations in the heat recovery arrangement, reductions of 0.237 and 0.271m/s respectively. This represents a 4.6% and 5.1% reduction in air velocity from the heat recovery arrangement compared to the dehumidification arrangement. This is due to the increased pressure drop across the wheel shown in the following CFD models. The experiments showed that despite the higher pressure drop value, the air velocities remained significantly higher than after the wheel compared to before, increasing the potential of the wheel to deliver adequate supply rates. The increase in blade thickness slows the air velocity within and after the rotary but not to a substantial degree, this could result in the increase of blade thickness for the heat recovery arrangement, sacrificing air velocity for increased heat transfer from one airstream to the other.

The increased thickness of the radial blades appears to have the effect of increasing the velocity around the mid-height of the channel. Ordinarily the maximum velocity of flow in a channel would be expected to be at the centre, this was not the case in a number of instances for the dehumidification radial blade arrangement. The thickness of the radial blades and

short distance from the rotary wheel face to the measurement location are likely to be the cause of this pattern in the dehumidification arrangements.

6.3.3 Air Pressure

Air velocity is tied to gauge air pressure. Reducing the gauge air pressure drop across the rotary wheel was a key goal for the radial blade design. A low-pressure drop would ensure that ventilation supply rates would be maintained above adequate guidelines levels when the rotary wheel was integrated with a passive ventilation system.

Figure 6-19 shows the contours of gauge air pressure for the 32-blade configuration of the dehumidification rotary wheel in the incoming and outgoing airstreams for test DH-32-4. The contours of air pressure show similarity with the contours of air velocity for the equivalent test, shown in Figure 6-13.

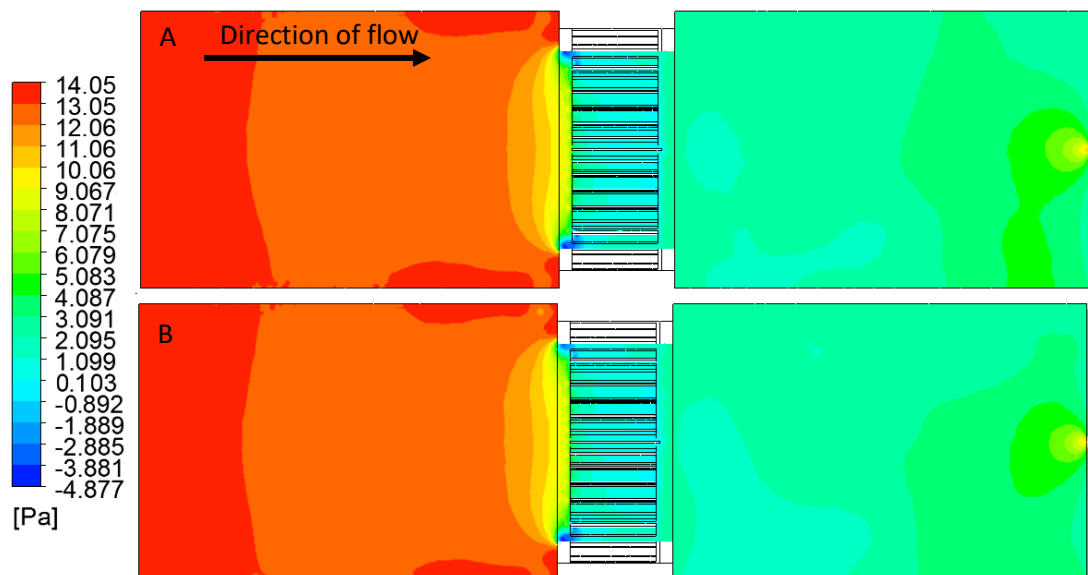


Figure 6-19 – Contours of gauge pressure for the 32 radial blade configuration A) Test DH-32-4 incoming air, B) Test DH-32-4 outgoing air

High-pressure zones are located in the channel before the rotary wheel, in the same zones where the fully developed but slower moving flow is present. In the area directly prior to the rotary wheel, the air pressure reduces. This corresponds to the area prior to the rotary wheel where air velocity increases, shown in the flow visualisation. The air pressure continues to decrease as the flow moves through the rotary wheel and out the opposite side of the channel. The velocity of the flow increases in these areas. A small increase in air pressure exists as the air exits the rotary wheel, reflecting the deceleration of the flow as it exits the narrow wheel volume to the larger volume of the channel.

Table 6-7 shows the measurements for gauge air pressure 100mm before and after the 32-blade rotary wheel configuration in the incoming and outgoing airstreams. The measurements show the effect of different inlet air temperatures of the outgoing airstream. Little noticeable effect on the gauge air pressure can be determined from the measurements for variable outgoing air inlet temperature despite obvious differences in inlet air temperature between the incoming and outgoing airstreams. This observation was also made in the heat recovery rotary wheel measurements.

Table 6-7 – Gauge pressure measurements before and after the rotary wheel in the incoming and outgoing airstreams for the 32 radial blade configuration

	Incoming			Outgoing		
	Before Wheel (Pa)	After Wheel (Pa)	Pressure Drop (Pa)	Before Wheel (Pa)	After Wheel (Pa)	Pressure Drop (Pa)
DH-32-4	12.57	2.38	10.19	12.54	2.25	10.29
DH-32-3	12.51	2.08	10.43	12.53	2.19	10.34
DH-32-2	12.55	2.26	10.29	12.56	2.33	10.23
DH-32-1	12.52	2.20	10.32	12.53	2.16	10.37

The average value for pressure drop across the 32-blade dehumidification configuration is 10.31Pa; this is greater than the 32-blade configuration for the heat recovery rotary wheel by 0.28Pa. Though this is not a large difference in average pressure drop, it clearly shows the impact of radial blade thickness and geometry on the gauge air pressure within the channel and pressure drop across the rotary wheel. Though the targeted pressure drop was 2Pa, the calculated pressure drop of 10.31Pa is significantly lower than previously achieved by rotary dehumidification wheels. Further development may result in increased pressure drop reduction.

The contours of gauge air pressure in the incoming and outgoing channels for the 20-blade configuration of the dehumidification rotary wheel for test DH-20-4 are shown in Figure 6-20. The contours indicate a similar trend to the patterns for the 32-blade configuration, though the values for gauge pressure are lower for the 20-blade configuration.

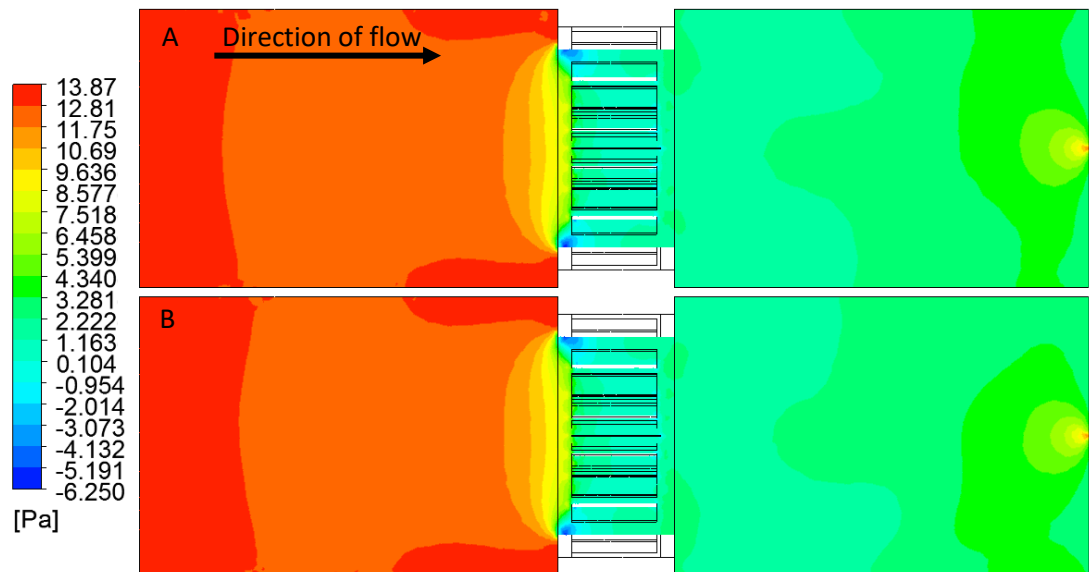


Figure 6-20 – Contours of static pressure for the 20 radial blade configuration A) Test DH-20-4 incoming air, B) Test DH-20-4 outgoing air

High-pressure zones are observed in the channel prior to the rotary wheel, where the flow is fully developed as it moves down the ductwork. As the flow nears the rotary wheel, pressure decreases in an area similarly sized to the 32-blade configuration. The gauge air pressure value in this area is also lower, indicating the increased velocity of the 20-blade configuration. As the flow contracts through the rotary wheel volume, the air pressure further decreases along the length of the rotary wheel before a minor increase as the volume expands to back into the channel. This reflects the slowing of the air velocity as it exits the rotary wheel.

The measurements for gauge air pressure from the CFD simulation are shown in Table 6-8. Measurements have been made in both the incoming and outgoing airstream, 100mm before and after the surface of the rotary wheel. From these measurements, the pressure drop across the wheel in each case has been calculated. As with the 32-blade configuration, little effect of different inlet air temperatures of the outgoing airstream is noticeable. This supports the trend seen in the analysis of the previous cases.

Table 6-8 – Gauge pressure measurements before and after the rotary wheel in the incoming and outgoing airstreams for the 20 radial blade configuration

	Incoming			Outgoing		
	Before Wheel (Pa)	After Wheel (Pa)	Pressure Drop (Pa)	Before Wheel (Pa)	After Wheel (Pa)	Pressure Drop (Pa)
DH-20-4	12.26	2.15	10.11	12.27	2.14	10.13
DH-20-3	12.26	2.18	10.08	12.28	2.12	10.16
DH-20-2	12.28	2.12	10.16	12.28	2.20	10.08
DH-20-1	12.28	2.22	10.06	12.30	2.37	9.93

The average pressure drop across the 20-blade configuration is 10.08Pa. This is 0.23Pa lower than the 32-blade configuration and is only marginally higher than the average pressure drop across the 20-blade configuration of the heat recovery rotary wheel; a pressure drop of 10.02Pa. Given that the difference in average pressure drop between the two heat recovery configurations was 0.01Pa, barely noticeable, the higher change in the dehumidification configurations is noteworthy. The cause of this may be due to the effect of the smaller volume between radial blades of the dehumidification arrangement compared to the heat recovery arrangement.

This difference in average pressure drop between the 20-blade dehumidification and heat recovery arrangements is not high enough alone to determine an effect of the thicker dehumidification radial blades compared to the heat recovery radial blades. However, the average gauge pressure values before and after the wheel in the 20-blade dehumidification configuration are 12.27Pa and 2.18Pa compared to 12.01Pa and 1.99Pa for the 20-blade heat recovery configuration. This displays the increase in pressure caused by the thicker dehumidification radial blades.

Though an increase in gauge air pressure before and after the dehumidification rotary wheel is observed in both the 32 and 20-blade configurations when compared to the heat recovery rotary wheel arrangement, along with increased pressure drop across the device, the increases are not by significant values. The small increases indicate that the thickness of the radial blades affect the gauge air pressure, but are not a major influence. Equally, the number of radial blades in a configuration is not a driver in large changes to the pressure values. The last variable that was maintained for all testing was the rotation speed of the rotary wheel. This was kept at 6rpm for all testing. Given the similarity between all pressure drop values, it is likely that this is the key factor for pressure drop. Previous knowledge would dictate that the higher the rotation velocity of the rotary wheel, the higher pressure drop. With this understanding, further testing for the rotation velocity of the heat recovery and dehumidification rotary wheels would provide more detailed gauge air pressure measurements.

Though the gauge air pressure drop across the rotary wheel was higher for the dehumidification rotary wheel, causing lower air velocities than the heat recovery configuration, the supply rate through the ductwork was calculated as 140.48 litres per second. As specified by the guidelines in Building Bulletin 101 for air supply rates, the flow

rate would adequately supply ventilation air for 17 people [9]. This shows significant potential of the system to deliver the necessary supply air.

6.3.4 Air Temperature

The temperature of air is directly related to the relative humidity of the air. Air at high temperature is able to hold more water vapour compared to air at a lower temperature giving the same relative humidity value. When air is dried through the removal of water vapour content, via the adsorption to the porous surface of silica gel for example, the air temperature increases. When air becomes more humid, through the desorption process and the water content in the air increases, the air temperature lowers. This is because the air no longer requires the same amount of moisture to be saturated as air at a higher temperature.

Given the relationship between air temperature and relative humidity, it was decided that measurements for air temperature before and after the dehumidification rotary wheels should be taken. As the long-term aim of the development of the radial blade rotary wheel design is to integrate the device into a passive ventilation system to supply air to occupied buildings, the temperature of air exiting the rotary wheel and entering a building is a significant concern.

Contours for air temperature generated from the CFD solutions for the 32-blade configuration of the dehumidification rotary wheel are shown in Figure 6-21. The contours show the incoming and outgoing air channels for test DH-32-4, enabling the distribution of temperature around the ductwork to be visualised. Temperature change in the CFD models for the dehumidification configuration were set by applying energy source terms to the incoming air channel tests and energy sink terms to the outgoing air channel tests.

The change in air temperature of the incoming airstream is clear from the contours, as the air flows through the rotary wheel, the air temperature increases by 10°C. The air in the outgoing airstream decreases as it flows through the rotary wheel, by approximately 5°C. The contours are useful to show the areas within the channel that are affected by the temperature change.

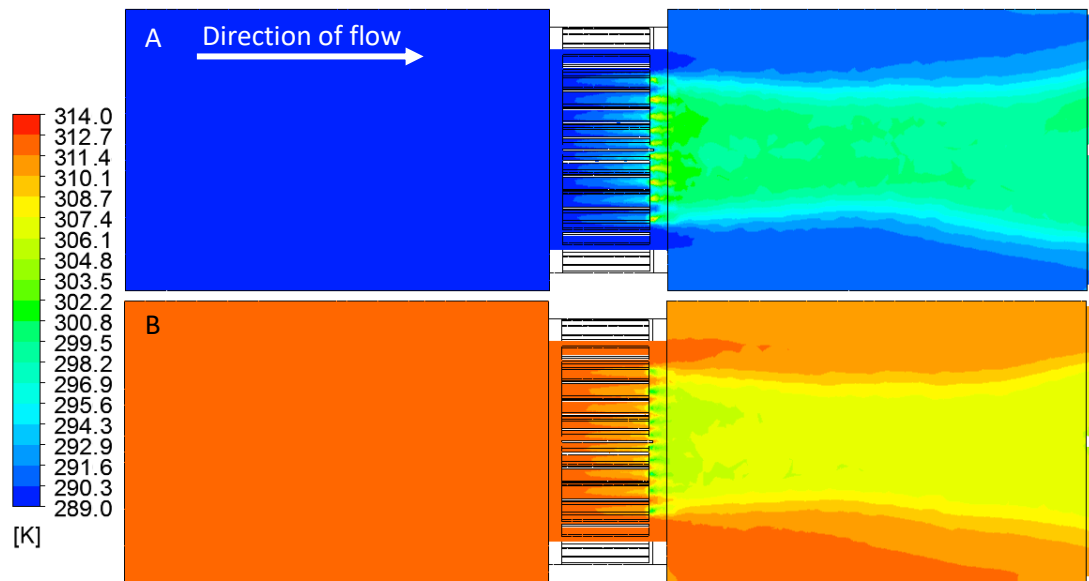


Figure 6-21 – Contours of air temperature for the 32 radial blade configuration A) Test DH-32-4 incoming air, B) Test DH-32-4 outgoing air

The contours show a similar pattern for both the incoming and outgoing air channels, highlighting the areas in which air temperature is altered. Uniform temperature from the inlets and the channel section prior to the rotary wheel can be seen in both cases. As the air exits the rotary wheel, a defined column of air subject to temperature change can be seen. The shape of the affected air is similar to the shape of the contour seen in the flow visualisation after the rotary wheel. The affected air is concentrated at the centre of the channel, this aligns with location of the fluid volumes used to represent the silica gel where adsorption and desorption of the water molecules occurs.

Experimental measurements for the temperature of the air before and after the dehumidification rotary wheel were made in each airstream, at a single location 100mm from each face of the wheel at the channel mid-height. The value for air temperature was collected every 5 seconds for 1 hour, resulting in 720 readings. The average air temperature was calculated to give the average performance of the dehumidification rotary wheel.

The temperature change for the incoming and outgoing airstreams for the 32-blade configuration is shown in Figure 6-22. The inlet air temperature of the outgoing airstream in test DH-32-1 was 25°C and was increased by 5°C in each subsequent test to 40°C in test DH-32-4. The negative values for the incoming airstream indicate that the air temperature has increased; the air temperature before the wheel is lower than the air temperature after the wheel. The positive values for the outgoing airstream indicate that the air temperature has decreased; the air temperature before the wheel is higher than the air temperature after the

wheel. As the temperature change of the air is directly related to the relative humidity change due to the adsorption or desorption of water molecules, the temperature change gives an approximate value of the relative humidity change.

The values for temperature change in both airstreams show a linear relationship with the outgoing airstream inlet temperature increase. As the inlet temperature increases, the temperature change increases. This is the expected result given the relationship between desorption and the regeneration air temperature, which in the experiment is the same as the outgoing channel inlet temperature. The higher the regeneration temperature, the greater the desorption rate of the silica gel, the more water molecules that are desorbed from the silica gel pores. Because of this, the silica gel particles are less saturated and the greater the adsorption of water molecules in the incoming airstream channel. This has the effect of lowering the temperature in the outgoing airstream and raising the temperature in the incoming airstream. This will be covered in more detail in the relative humidity analysis section that follows.

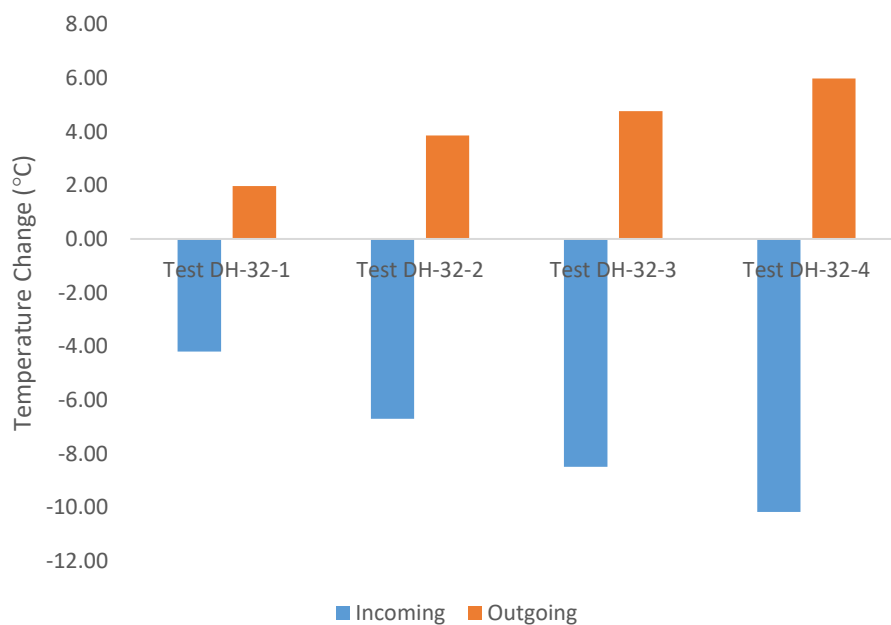


Figure 6-22 – Air temperature change measurements for the 32-blade dehumidification rotary wheel in the incoming and outgoing airstreams

The values for temperature change appear proportional between the incoming and outgoing airstreams. Table 6-9 shows the average value for air temperature and temperature change for the incoming and outgoing airstreams for tests DH-32-1 to DH-32-4. The values for temperature change increase as the outgoing inlet air temperature increases between 1.68-2.52°C for the incoming airstream and 0.91-1.89°C for the outgoing airstream, with the

greatest increase in temperature change occurring between test DH-32-1 and DH-32-2. This suggests that below an inlet temperature of 30°C, the system is less efficient given that the temperature change is reduced.

Table 6-9 – Air temperature measurements for the incoming and outgoing airstreams for the 32-blade dehumidification rotary wheel

	Incoming			Outgoing		
	Inlet Air Temperature (°C)	After Wheel (°C)	Temperature Change (°C)	Inlet Air Temperature (°C)	After Wheel (°C)	Temperature Change (°C)
DH-32-1	17.08	21.27	-4.19	24.83	22.86	1.97
DH-32-2	17.35	24.05	-6.71	30.83	26.97	3.86
DH-32-3	16.63	25.13	-8.50	34.52	29.75	4.77
DH-32-4	17.00	27.18	-10.18	38.84	32.86	5.98

The values for incoming temperature change are approximately twice the value of the corresponding outgoing temperature change. Calculating outgoing temperature change as a percentage of the incoming temperature change gives a range of 47-59%. This suggests that the relative humidity change due to adsorption is greater than the relative humidity change due to desorption.

The values for the energy source and energy sink terms that were applied to the volumes in the CFD models representing the silica gel are shown in Table 6-10, along with the error percentage of the air temperature after the wheel when compared to the values measured in the experiments. The energy source and sink terms increased or decreased the temperature of the air depending on the value assigned. The source and sink terms are adjusted based on the percentage error from the experimental measurements to give the exact values from the CFD simulations. This enhances the future accuracy of the CFD simulations for use in predicting the performance of alternative radial blade configurations and arrangements.

Table 6-10 – Percentage error for CFD model compared to experiment results for air temperature after the wheel. Heat source and heat sink values for incoming and outgoing airstreams and adjusted values for error

	Incoming				Outgoing			
	% Error	Energy Source (w/m ³ s)	Adjusted for %Error	Adjusted Source (w/m ³ s)	% Error	Energy Sink (w/m ³ s)	Adjusted for %Error	Adjusted Sink (w/m ³ s)
DH-32-1	-1.54	900000	-13832	886168	2.74	-500000	-13691	-486309
DH-32-2	0.42	1300000	5495	1305495	0.92	-800000	-7350	-792650
DH-32-3	-1.68	1750000	-29425	1720575	1.25	-1000000	-12470	-987530
DH-32-4	0.13	2000000	2504	2002504	-0.98	-1100000	10740	-1110740

Figure 6-23 shows the distribution of air temperature for test DH-20-3 in the incoming and outgoing air channels for the 20-blade dehumidification rotary wheel configuration. The contours display a similar pattern to that seen in the 32-blade configuration.

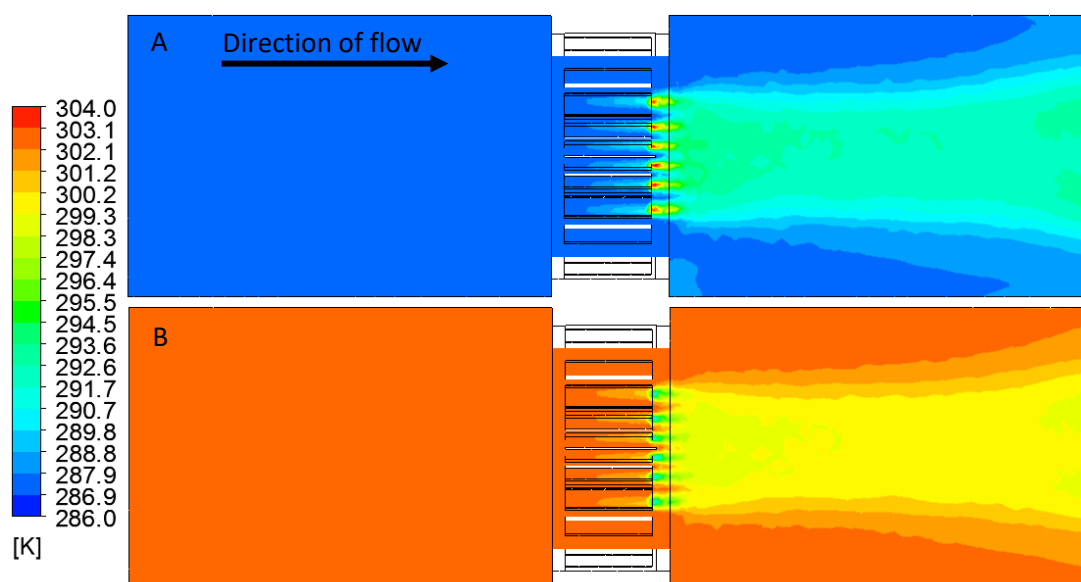


Figure 6-23 – Contours of air temperature for the 20 radial blade configuration A) Test DH-20-3 incoming air, B) Test DH-20-3 outgoing air

The increase and decrease in air temperature, in the incoming and outgoing airstreams respectively, can clearly be seen after the rotary wheel, affecting a channel of air around the centre of the ductwork. The height of the affected areas of air after the wheel is smaller than that in the 32-blade configuration. This is expected as the fewer radial blades reduce the amount of silica gel in the wheel; this in turn reduces the effect of adsorption, lowering the temperature change of the air and volume of air that is in contact with the silica gel.

The measured values for temperature change for the 20-blade configuration of the dehumidification rotary wheel can be seen in Figure 6-24. The temperature change for the

incoming and outgoing airstreams are displayed. The setup for the experiments was the same for the 32-blade configuration; the initial outgoing air inlet temperature was set to 25°C for test DH-20-1 and increased by 5°C in each subsequent test to a maximum of 40°C in test DH-20-4.

The trend for the two datasets shows the same pattern as the 32-blade configuration. As the outgoing inlet air temperature increased from 25°C to 40°C, the temperature change in each airstream increased in a linear manner. The exception for this trend is the measurement in test DH-20-4 in the incoming airstream. The value for temperature change is significantly lower than the other values. The large difference between the measured value and expected value, between 8-10°C given previous experience, infer that an error has been introduced into the experiments and the results. As the air temperature change is a product of the relative humidity change, the cause and explanation for this will be related to the relative humidity change and covered in the section 6.3.5. Low relative humidity change would result in a similar temperature change value to this. The temperature change in the outgoing airstream for the corresponding test follows the linear trend of the remaining results, this suggests that the error is caused by the adsorption of the rotary wheel.

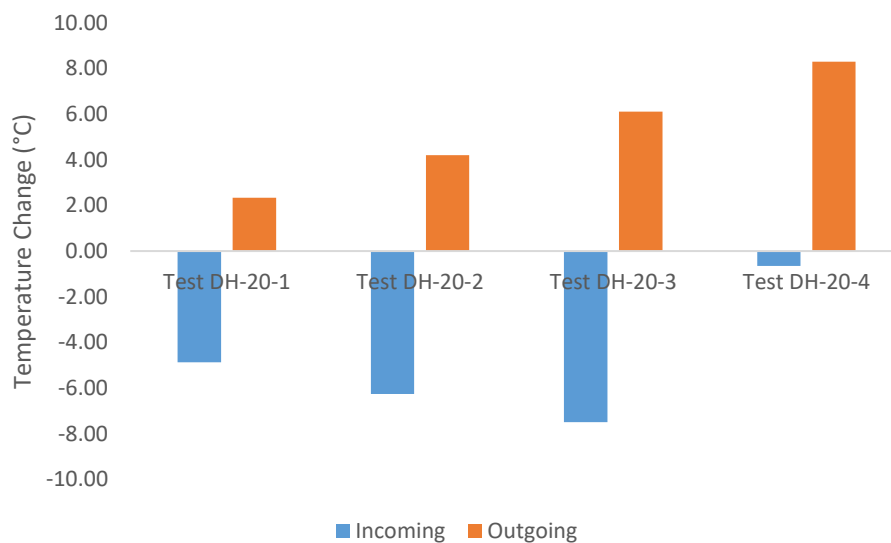


Figure 6-24 – Air temperature change measurements for the 20-blade dehumidification rotary wheel in the incoming and outgoing airstreams

Discounting the error for the test DH-20-4 incoming temperature change, the remaining values for temperature change increase in a linear manner. The difference in temperature change in the incoming airstream between test DH-20-3 and DH-20-2 is 1.22°C and between test DH-20-2 and DH-20-1 is 1.39°C. The difference in temperature change for the outgoing airstream ranges from 1.86-2.19°C. This shows that the outgoing airstream is affected more

by the varying outgoing air inlet temperature. The values for air temperature and temperature change in the 20-blade configuration tests are shown in Table 6-11.

Table 6-11 – Air temperature measurements for the incoming and outgoing airstreams for the 20-blade dehumidification rotary wheel

	Incoming			Outgoing		
	Inlet Air Temperature (°C)	After Wheel (°C)	Temperature Change (°C)	Inlet Air Temperature (°C)	After Wheel (°C)	Temperature Change (°C)
DH-20-1	13.57	18.45	-4.88	25.02	22.68	2.34
DH-20-2	14.21	20.48	-6.27	29.74	25.54	4.20
DH-20-3	16.85	24.34	-7.49	35.43	29.32	6.11
DH-20-4	17.11	17.76	-0.65	39.45	31.15	8.30

The difference between the temperature change values of the incoming and outgoing airstreams is lower for the 20-blade configuration compared to the 32-blade configuration where the difference was approximately double. Calculating the outgoing temperature change as a percentage of the incoming temperature change gives values of 48%, 67% and 82% for test DH-20-1, -2 and -3 respectively. This differs from the 32-blade configuration significantly. The decreasing value of outgoing temperature change as a percentage of incoming temperature change implies that as the inlet temperature decreases, the ability of the silica gel particles to desorb the water molecules reduces but the adsorption process is less effected, as noted by the temperature changes.

The measurements for air temperature before and after the two different radial blade configurations of the dehumidification rotary wheel in the incoming and outgoing air channels provide a reasonable degree of analysis for the performance. The measurements before and after the wheel show that temperature changes occurs in each channel. Increases in temperature in the incoming airstream where adsorption decreases the relative humidity and decrease in air temperature in the outgoing airstream where desorption increases the relative humidity. The simplest observation from the experimental results is that as the inlet temperature of the outgoing airstream increases from 25°C to 40°C, the temperature changes increase. This highlights the connected relationship between relative humidity, temperature change and regeneration temperature; as the regeneration temperature increases the relative humidity change increases and so the temperature change increases.

Table 6-12 shows the percentage error between the values generated by the CFD solutions for air temperature after the rotary wheel in both airstreams and the experiment values for

air temperature measured as the same locations. The energy source and energy sink terms are adjusted for percentage error to give an exact value for use in future CFD simulations.

Table 6-12 – Percentage error for CFD model compared to experiment results for air temperature after the wheel. Heat source and heat sink values for incoming and outgoing airstreams and adjusted values for error

	Incoming				Outgoing			
	% Error	Energy Source (w/m ³ s)	Adjusted for %Error	Adjusted Source (w/m ³ s)	% Error	Energy Sink (w/m ³ s)	Adjusted for %Error	Adjusted Sink (w/m ³ s)
DH-20-1	-0.76	1400000	-10708	1389292	5.34	-1000000	-53441	-946559
DH-20-2	-0.79	1800000	-14272	1785728	-0.33	-1150000	3772	-1153772
DH-20-3	2.43	1950000	47300	1997300	-1.87	-1550000	28919	-1578919
DH-20-4	-0.74	250000	-1844	248156.3	0.87	-2375000	-20775	-2354225

As the air temperature is linked to the relative humidity value, analysis of only the air temperature provides on a limited view on the performance of the dehumidification rotary wheel. The measurements of air temperature after the rotary wheel compared to before show that the temperature change is linked to the temperature of the outgoing airstream inlet. However, this is an effect of the adsorption and desorption process of the silica gel and the impact these processes have on the air temperature. As the inlet air temperatures were provided from the experiment setups, the values calculated in the CFD simulations after the rotary wheel are accurately calculated using the energy source and energy sink terms. This provides a good benchmark for future design and development of the radial blade rotary wheel.

6.3.5 Relative Humidity

As previously mentioned, relative humidity is directly related to the air temperature. As the dehumidification rotary wheel was designed to alter the amount of water vapour in an airstream, changes to air temperature were a consequence of changes to relative humidity. The CFD simulations handled the increase and decrease of the relative humidity in the incoming and outgoing airstreams by dictating mass and species source and sink terms applied to the fluid volumes in the rotary wheel geometry. Matching values was required for the mass and species terms applied to the fluid volumes, this is necessary for calculation stability and continuity due to the method in which the CFD code calculates species transport.

Figure 6-25 shows the contours for relative humidity of the 32-blade configuration in the incoming and outgoing airstreams for test DH-32-4. The contours visualise the distribution of relative humidity around the channel as a function of the air temperature and moisture content. The decrease in relative humidity in the incoming airstream can clearly be seen as the relative humidity falls from 100% to 30% as it exits the rotary wheel. The outgoing airstream increases in relative humidity from 10-15% to 20% as it exits the rotary wheel. The two contours represent the effects of adsorption and desorption in the incoming and outgoing airstreams respectively.

The height and area of the air flow that is affected by the adsorption and desorption of the water vapour by the source and sink terms are similar to the area of air flow in which the temperature change was observed. This is understandable given the connected nature of relative humidity and air temperature, as one changes the other changes. The height of the affected area in the outgoing airstream is shorter than in the affected area in the incoming airstream. This may be due to the lower values for the mass and species source terms compared to the sink terms in the incoming airstream. As the values are lower, less air is affected.

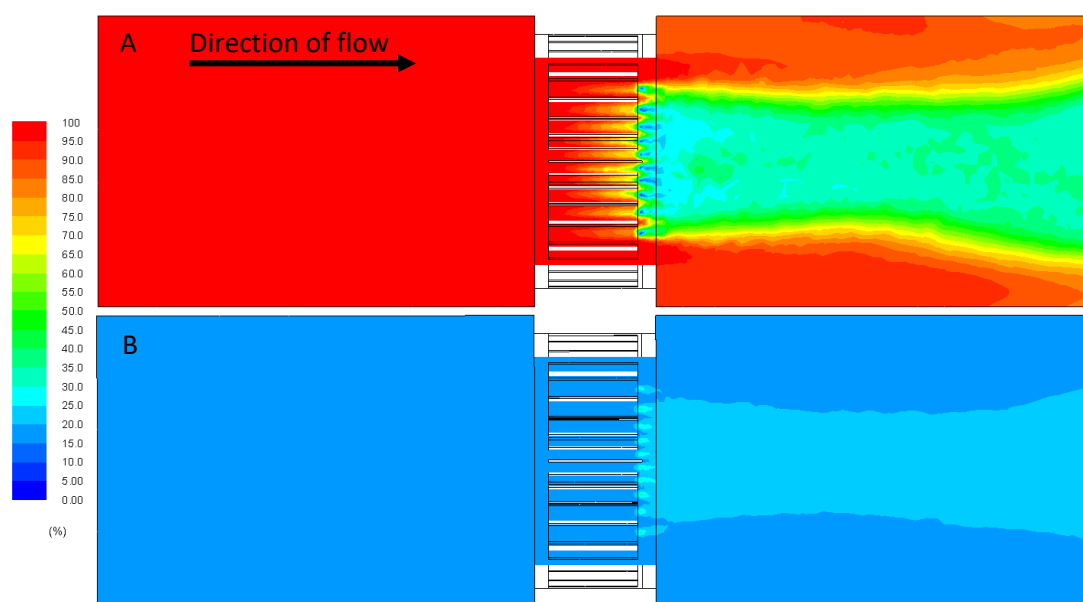


Figure 6-25 – Contours of relative humidity for the 32 radial blade configuration A) Test DH-32-4 incoming air, B) Test DH-32-4 outgoing air

The measurements for relative humidity were made at the same time as the measurements for air temperature due to the equipment used in the experiments; this further highlights the connected nature of air temperature and relative humidity. The average value for relative humidity was calculated from the 720 measurements in the incoming and outgoing airstreams.

One of the goals of the project was to develop a dehumidification rotary wheel capable of constant moisture management of an airstream with a lower regeneration temperature than typically used in commercial dehumidification rotary wheels. This was the reasoning behind the selection of temperatures for the outgoing airstream inlet temperatures. The lower the regeneration temperature, the greater energy saving possible. The range of 25 to 40°C represented possible outgoing air temperatures from an occupied space that could be achieved through convention heating systems and internal gains with minimal additional input to raise the air temperature.

The measurements for relative humidity change in the incoming and outgoing air channels as the outgoing air inlet temperature increased from 25°C to 40°C in 5°C increments are shown in Figure 6-26. The positive values for relative humidity change in the incoming airstream indicate a reduction in relative humidity, the negative values for relative humidity change in the outgoing airstream indicate an increase in relative humidity.

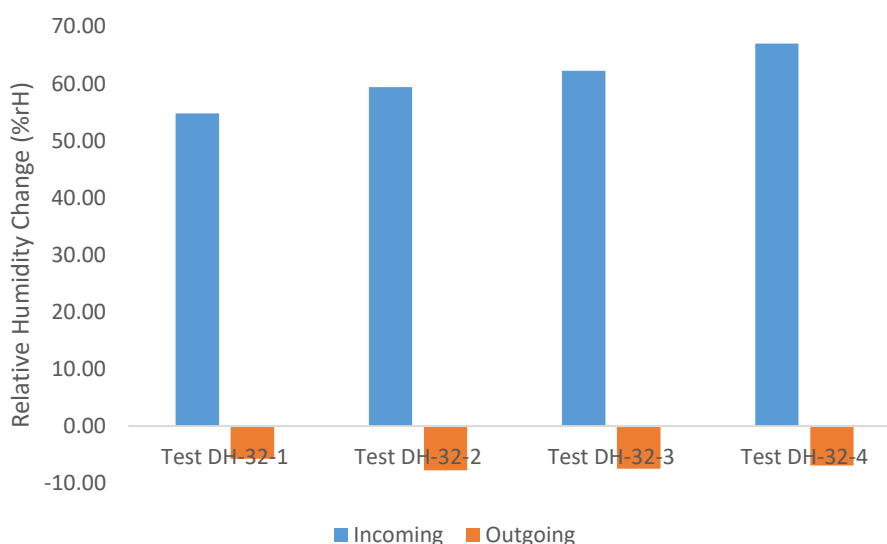


Figure 6-26 – Relative humidity change measurements for the 32-blade dehumidification rotary wheel in the incoming and outgoing airstreams

The values for relative humidity change in the incoming airstream are substantially larger than the values in the outgoing airstream. This shows that at the tested outgoing air inlet temperatures, the silica gel layers either side of the acrylic blades are more effective at adsorbing water molecules to the pore surface than desorbing water molecules; though this may not be true at higher outgoing air inlet temperatures. The trend for the incoming air relative humidity change increases linearly as the outgoing air inlet temperature rises. This is the expected scenario as the higher regeneration temperature results in more water molecules desorbed from the surface of the silica gel pores. As more water molecules are

desorbed from the pore surfaces of the silica gel, the particles become less saturated. The lower saturation encourages high adsorption rates, reducing the overall relative humidity change seen in the tests. However, the same trend is not seen in the outgoing air relative humidity change. The values appear to stay consistent or increase as the inlet temperature changes.

Table 6-13 shows the detailed measurements for relative humidity before and after the rotary wheel and the resultant values for relative humidity change. The values show a decrease in relative humidity change in the outgoing airstream as the inlet temperature increases from 30°C to 35°C in test DH-32-2 to DH-32-3 and again to 40°C in test DH-32-4. This is an unexpected result. Conventional analysis of regeneration temperatures for desorption of silica gel would dictate that as regeneration temperatures increase, the desorption rate would also increase. This would result in the relative humidity change increasing.

Table 6-13 – Relative humidity measurements for the incoming and outgoing airstreams for the 32-blade dehumidification rotary wheel

	Incoming			Outgoing		
	Inlet Relative Humidity (%rH)	After Wheel (%rH)	Relative Humidity Change (%rH)	Inlet Relative Humidity (%rH)	After Wheel (%rH)	Relative Humidity Change (%rH)
DH-32-1	95.83	41.06	54.77	29.36	35.11	-5.75
DH-32-2	98.49	39.11	59.38	23.13	30.86	-7.74
DH-32-3	99.07	36.82	62.25	18.53	26.03	-7.49
DH-32-4	99.63	32.62	67.01	15.24	22.17	-6.93

A possible explanation for this would be the values for relative humidity at the inlet of the incoming airstream. Not all of the inlet conditions of the incoming airstream could be accurately managed. Though the relative humidity was increased significantly above the local levels of the laboratory conditions, the air temperature was dependent on the environment. This causes variation in the relative humidity levels at the inlet of the incoming air channel. The value for relative humidity decreases for each subsequent test, which may influence the unusual relative humidity changes of the outgoing airstream.

The difference between the relative humidity change values in the incoming airstream varies as the inlet temperature changes over the range of tests. From test DH-32-4 to DH-32-3, the change is 4.76%, to 2.87% to 4.61% from tests DH-32-3 to DH-32-2 and DH-32-2 to DH-32-1 respectively. As the difference in relative humidity from test DH-32-3 to DH-32-2 is lower than the other differences, this result appears to be an error. The relative humidity change

in the outgoing airstream for test DH-32-2 is the largest increase in relative humidity measured, despite the inlet temperature of 30°C, 10°C lower than the maximum. This may have resulted in the lower than expected relative humidity change for the corresponding incoming relative humidity change.

Table 6-14 shows the percentage error between the measurements taken from the solutions generated by the CFD models and the experiment measurements. The values for the mass and species sink and source terms for the incoming and outgoing air channels are shown, along with the adjusted values based on the percentage error. The adjusted values give exact measurements of relative humidity from CFD simulations when compared to the experimental measurements.

Table 6-14 – Percentage error for CFD model compared to experiment results for relative humidity after the wheel. Mass source and mass sink values for incoming and outgoing airstreams and adjusted values for error

	Incoming				Outgoing			
	% Error	Mass /Species Sink (kg/m ³ s)	Adjusted for %Error	Adjusted Mass /Species Sink (kg/m ³ s)	% Error	Mass /Species Source (kg/m ³ s)	Adjusted for %Error	Adjusted Mass /Species Source (kg/m ³ s)
DH-32-1	-0.69	-0.96	0.0066	-0.9666	-0.69	0.030	-0.0002	0.0302
DH-32-2	0.31	-0.95	-0.0029	-0.9471	1.24	0.045	0.0006	0.0444
DH-32-3	1.76	-0.83	-0.0146	-0.8154	-1.56	0.080	-0.0012	0.0812
DH-32-4	6.71	-1.00	-0.0671	-0.9329	1.58	0.054	0.0009	0.0531

Figure 6-27 shows the CFD contours for relative humidity in the 20-blade configuration of the dehumidification rotary wheel. The contours for the incoming and outgoing airstreams in test DH-20-3 can be seen. The contours for the incoming airstream show a large decrease in relative humidity before the rotary wheel to after, where relative humidity falls from 80% to 40%. The outgoing airstream relative humidity increases from 15-20% to 25-30%. This is a larger increase than seen in the 32-blade configuration. The height of the area of air that is affected by the relative humidity change in each air channel is similar to that seen in the 32-blade configuration. Greater variation of relative humidity value can be seen at the edges of the affected area in the outgoing airstream. This suggests that the smaller volume of silica gel has less effect at the top and bottom of the rotary wheel.

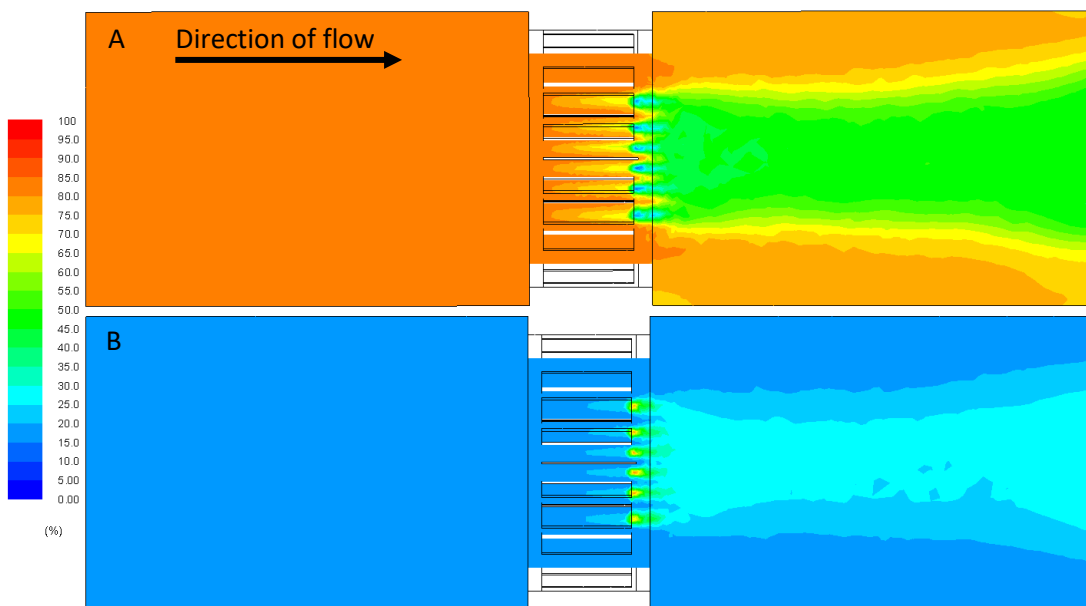


Figure 6-27 – Contours of relative humidity for the 20 radial blade configuration A) Test DH-20-3 incoming air, B) Test DH-20-3 outgoing air

Figure 6-28 shows the values for relative humidity change taken from the experimental tests for the 20-blade configuration of the dehumidification rotary wheel. The values for relative humidity change for the incoming and outgoing air channels is shown for each test as the outgoing air inlet temperature increases from 25°C to 40°C.

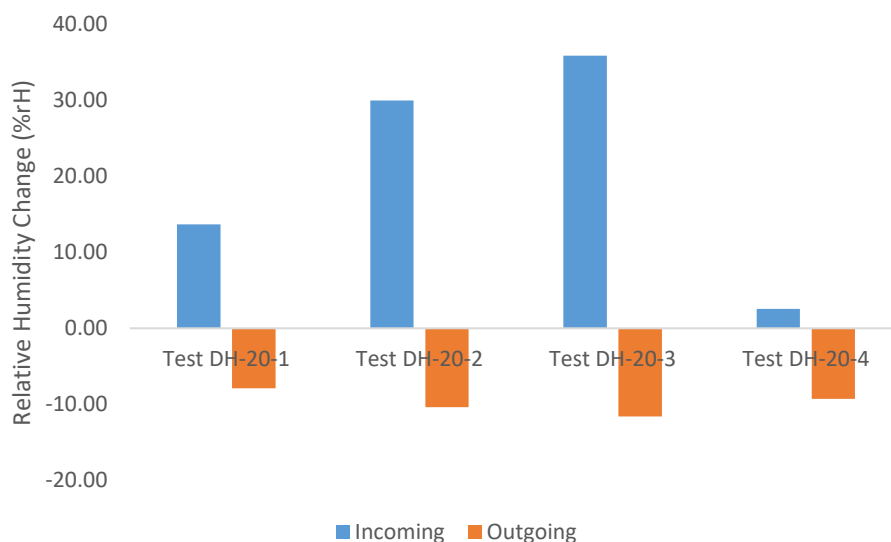


Figure 6-28 – Relative humidity change measurements for the 20-blade dehumidification rotary wheel in the incoming and outgoing airstreams

Overlooking the value for incoming relative humidity change for test DH-20-4, the overall trends for the incoming and outgoing airstreams are similar to those seen in the 32-blade configuration. The relative humidity change in the incoming airstream increases as the inlet

air temperature rises. The change in the outgoing airstream do not follow this trend, increasing or staying consistent as the inlet air temperature increases, as seen in the 32-blade configuration. The difference in relative humidity change between tests is more substantial for the incoming air 20-blade configuration, showing uneven differences between relative humidity changes.

The obvious aspect of the results is the low value for relative humidity change in the incoming airstream for test DH-20-4, which is notably lower than the other values. This also corresponds to the value for temperature change in the same test that was significantly lower than the remaining tests. This value is clearly an error caused by experimental or measurement inaccuracies. Given the large deviation from the trend of the other measurements, this suggests that the cause is experimental error.

The inlet values for relative humidity, shown in Table 6-15 along with the differences between inlet and after wheel measurements, provide some explanation to the relative humidity changes of the incoming airstream. The inlet relative humidity for test DH-20-4 is significantly lower than in the other tests. As fewer water molecules are present in the air, the adsorption rate lowers, resulting in the low relative humidity change value. The cause of the low inlet relative humidity affects each of the tests, with the inlet relative humidity average value of 85.65% compared to 98.26% for the 32-blade configuration.

The fewer radial plates in the configuration may be the cause of the low relative humidity measurements. As previously shown in the CFD analysis of the dehumidification rotary wheel, the air pressure before the rotary wheel is lower for the 20-blade configuration due to the increased volume between blades through which air can flow. The lower pressure prevents or reduces the backflow of air, avoiding the build-up of water molecules in the air before the rotary wheel. Given the experiment setup and design, this is the most logical source of the low inlet relative humidity values.

Table 6-15 – Relative humidity measurements for the incoming and outgoing airstreams for the 20-blade dehumidification rotary wheel

	Incoming			Outgoing		
	Inlet Relative Humidity (%rH)	After Wheel (%rH)	Relative Humidity Change (%rH)	Inlet Relative Humidity (%rH)	After Wheel (%rH)	Relative Humidity Change (%rH)
DH-20-1	88.04	74.38	13.66	28.69	36.58	-7.90
DH-20-2	87.47	57.51	29.96	23.33	33.70	-10.36
DH-20-3	81.44	45.61	35.82	17.00	28.61	-11.61
DH-20-4	63.49	60.94	2.55	12.52	21.80	-9.27

It is likely that the relative humidity change for test DH-20-4 in the outgoing airstream is effected by the low inlet relative humidity of the incoming air channel. As less moisture is adsorbed onto the surface of the silica gel pores, less water molecules are available for desorption, lowering the desorption rate. This accounts for the low relative humidity change value calculated.

All of the values for relative humidity change in the incoming airstream are lower than the values for the corresponding inlet air temperature test for the 32-blade configuration, whereas all the values in the outgoing airstream are higher than the same 32-blade test. The lower values in the incoming airstream are expected, the fewer radial blades in the configuration would be less able to adsorb the same volume of moisture, limiting the change. Furthermore, the low initial inlet relative humidity reduces the total moisture content in the air. The results for the outgoing air suggest that the regeneration air temperature is not the only factor in determining the desorption of water molecules from the silica gel pores.

The increased desorption of moisture from the silica gel in the outgoing airstream is potentially due to the larger volume of air between the radial blades in the 20-blade configuration. The inlet relative humidity in the outgoing airstream is significantly lower than the incoming airstream. As the water molecules are adsorbed to the pore surface of the silica gel particles, the particles become saturated. The low relative humidity in the outgoing channel means the air is less saturated; likely significantly less saturated than the silica gel particles. This difference in saturation levels between the air and silica gel particles results in a pressure difference within the gel pores. The high volume of low moisture content air between the radial blades and the pressure difference may be the significant factors for desorption, even at low regeneration temperatures of 30°C and 25°C. This was the aim of the radial blade rotary wheel for dehumidification. Further testing would be required for the same range of outgoing airstream inlet temperatures but with higher relative humidity content.

Table 6-16 shows the percentage error of the CFD relative humidity measurements after the rotary wheel when compared to the experimental results for the 20-blade dehumidification configuration. The initial input values for mass and species source/sink terms used in the CFD simulations are shown, along with the adjusted values based on the percentage error.

Table 6-16 – Percentage error for CFD model compared to experiment results for relative humidity after the wheel. Mass source and mass sink values for incoming and outgoing airstreams and adjusted values for error

	Incoming				Outgoing			
	% Error	Mass /Species Sink (kg/m ³ s)	Adjusted for %Error	Adjusted Mass /Species Sink (kg/m ³ s)	% Error	Mass /Species Source (kg/m ³ s)	Adjusted for %Error	Adjusted Mass /Species Source (kg/m ³ s)
DH-20-1	0.02	-1E-07	-2.4E-11	-1E-07	3.43	0.005	0.0002	0.0048
DH-20-2	1.96	-0.0875	-0.0017	-0.085789	4.82	0.15	0.0072	0.1428
DH-20-3	8.98	-0.6	-0.0539	-0.546144	0.07	0.38	0.0003	0.3797
DH-20-4	1.71	-0.0002	-3.4E-06	-0.000197	7.36	0.00185	0.0001	0.0017

The results of the CFD simulations relating to the relative humidity in the ductwork channels are directly related to the air temperature measurements, with each condition affecting the value of the other. Analysis of one property without adequate analysis of the other does not provide a full view of the changes to the air as it flows through the channel, affected by the adsorption or desorption process depending on the conditions. The adsorption and desorption processes are modelled in the channel by using source and sink terms for energy, mass and species to alter air temperature and relative humidity respectively.

As the two properties of air closely linked, errors in one dataset will be apparent in the other. This is obvious in the results generated in the incoming airstream in test DH-20-4. As the inputs values for the boundary conditions were dictated by the experimental measurements, the aim of the CFD simulations was to develop models that could be used for future development and testing of the radial blade rotary wheel design. Therefore, values that appear erroneous from the CFD models are a result of experimental errors, not the solutions generated in the CFD analysis.

The accuracy of the CFD models in comparison to the experimental models is the key attribute to be assessed. This ensures that future designs are accurate and developed from established models. The average percentage error for the air temperature measurements was 1.21% and 1.64% for the 32 and 20-blade configurations respectively; the average percentage error for the relative humidity was 1.82% and 3.54%. These values are low enough to satisfy the accuracy of the simulations; furthermore, the CFD models follow the trends of the experimental results.

By calculating the percentage error of the CFD measurements for air temperature and relative humidity, the energy, mass and species source and sink terms used for the solution

of the CFD models are adjusted to provide values for the exact experiment measurements. Using these values for future work will accelerate the design process as CFD simulation can be used in place of extensive time-consuming experiments.

6.4 Summary

Results from the Computational Fluid Dynamics models and experimental testing of the radial blade rotary wheel have been presented in this chapter. The heat recovery and dehumidification arrangements of the radial blades have been presented, along with two separate radial blade configurations for each of these arrangements.

The discussion of these results involved analysis of the air velocities, air temperature, gauge air pressure and relative humidity before and after the rotary wheel, to determine how the radial blade design affected the flow characteristics. The results have been presented through graphical, tabular and chart formats.

Chapter 7

7 Conclusions and Future Work

7.1 Heat Recovery Rotary Wheel Analysis

Following the experimental testing and simulations of CFD models, it is necessary to characterise the radial blade design of the heat recovery rotary wheel in terms of performance. As previously shown, the CFD simulations have been validated by the experiment tests, confirming the accuracy of the solutions. The two configurations of the copper blades provide data that can be used to assess how air velocity is affected by the design, the pressure drop across the device and the heat transfer capabilities of the radial blades. These characteristics inform how successful the integration of the design into a passive ventilation system would be.

A key driving factor for the development of the radial blade heat recovery rotary wheel was to minimise the pressure drop across the device. Existing heat recovery devices cannot be easily integrated with passive ventilation systems without requiring additional components to enhance the air flow through the system due to the high pressure drop across such devices. The spacing and size of the radial blades reduced the skin friction between the air moving through the wheel and the wheel matrix and maximised the opening through which the air could flow.

Both these design features enabled the pressure drop of the device to be reduced to 10.03Pa and 10.02Pa for the 32 and 20-blade configurations. Though the aim was to reduce pressure drop to 2Pa across the device, the results from the CFD simulations show a large reduction from the common values for pressure drop across a rotary wheel, approximately 150Pa. Given the similarity of the pressure drop across each configuration, it can be argued that a different factor affects the pressure drop more significantly. The rotation speed of the wheel was maintained for each configuration, which indicates that this may be an important influence on the pressure drop. Further development and experimentation could decrease the pressure drop down to the goal of 2Pa.

Though the pressure drop did not reach the expected value of 2Pa, analysis of the gauge pressure and air velocity before and after the wheel suggested that the heat recovery wheel did not reduce the air supply rate. The calculated supply rate of 141.12 litres per second through the wheel was suitable to provide ventilation to 17 people.

The objective to integrate a heat recovery device into a passive ventilation system relies on the heat recovery device effectively transferring heat from one airstream to another. The evacuating air from a building, termed as the outgoing air here, acted as a heat source for the incoming air. Then conduction of heat from the outgoing airstream and transfer to the incoming airstream through the rotation of radial blades was tested experimentally by increasing the temperature of the outgoing airstream.

The results from the experiments and CFD testing show that the transfer of heat from the outgoing airstream to the incoming airstream is possible with the radial blade configuration of the rotary wheel. The maximum increase in temperature of the incoming airstream was 0.68°C for the 32-blade configuration when the temperature of the outgoing airstream was 40°C. This is higher than the outgoing air temperature of a standard occupied room and would require additional energy input to increase outgoing air temperature, offsetting any savings of increased incoming air temperature. Furthermore, the low increase of incoming air temperature is unlikely to reduce the energy demands of heating system by a noteworthy degree.

However, the decrease in temperature of the outgoing airstream is much larger than the increase in temperature of the incoming airstream. This indicates that heat conducted by the copper material of the radial blades is stored and not released. This suggests that the radial blade concept is inefficient in terms of heat transfer. By considering the increase of air temperature in the incoming airstream as a percentage of the outgoing airstream temperature change, the efficiency of the system can be calculated. At low outgoing airstream inlet temperatures, the efficiency is as high as 69%. This reduces significantly above inlet temperatures of 30°C to average 22%.

Given the potential for the radial blade rotary wheel not to impede the flow of air through the system, the development of the radial blade design should focus on increasing the efficiency of heat transfer across the device. The high conductivity of the copper material used in the blades is effective at storing heat in the wheel matrix, effective radiation and convection of the heat to the incoming airstream is required. Lowering the incoming airstream inlet temperature is the first condition to change for experimental testing. The current similarity of the inlet air temperatures is unlikely to result in significant air temperature changes. Lowering the incoming air inlet temperature to values more commonly seen in cold winter climates would increase the difference between inlet air temperatures and likely result in greater efficiency.

7.2 Dehumidification Rotary Wheel Analysis

The purpose of the radial blade dehumidification rotary wheel was to assess if the air velocity after the wheel was sufficiently high to provide the required supply rates for occupied buildings, along with low regeneration temperatures for desorption that would lead to significant energy savings whilst maintaining moisture control. The results from the CFD solutions and measurements taken from the experimental tests have been used to evaluate the performance of the radial blade dehumidification rotary wheel based on these criteria.

It was determined that the increased thickness of the radial blades to support the silica gel would affect the pressure drop across the rotary wheel, a higher pressure drop would result in low air velocities not suitable for passive ventilation integration due to the inability to supply the required ventilation rates. The CFD analysis of the 32 and 20-blade configurations showed that the pressure drop across the rotary wheel, calculated by measuring the gauge air pressure either side of the wheel in both airstreams, was higher than the goal pressure drop of 2Pa. The average pressure drop calculated across the rotary wheel was 10.31Pa for the 32-blade configuration and 10.08Pa for the 20-blade configuration. Both of these values are greater than the pressure drop measured for the heat recovery arrangement, as expected due to the thicker radial blades.

The difference between the values for the heat recovery arrangement and dehumidification arrangement, as well as the number of blades in the configuration, is minor. This suggests that the thickness and number of blades is less of a significant factor for pressure drop. The rotation speed for all tests was carried out at 6rpm. This is potentially the major factor affecting pressure drop. Given that the values across all arrangements and configurations were similar, a lower rotation velocity may result in a lower pressure drop.

The air velocities measured resulted in a supply rate of 140.86 litres per second, nominally lower than the supply rate of the heat recovery arrangement. This flow rate would adequately supply ventilation air for 17 people. However, as previously mentioned the axial fans used to drive the flow in the experiments are unlikely to be representative of the flow conditions in a wind tower system.

The secondary objective of the radial blade design for the dehumidification arrangement was to reduce the temperature required for desorption of water molecules from the silica gel particles, whilst maintaining the moisture control abilities. Conventional dehumidification rotary wheels require temperatures up to 120°C for the desorption of water molecules, expending large amounts of energy in the process. Reduction of this energy demand would

improve the low energy credentials of the system, increasing the attractiveness to consumers.

The alternative arrangement of the silica gel in the rotary wheel provided a large volume to surface area ratio. This is important as the porous properties of the silica gel enable water molecules to adhere to the internal pore surfaces, increasing the adsorptive ability. The range of regeneration temperatures for desorption, referred to as the outgoing air inlet temperature, were reflective of internal temperatures of occupied spaces with minimal additional heating.

High levels of relative humidity reduction were achieved with both configurations of radial blades. As expected, the 32-blade configuration lowered relative humidity by a greater value for all outgoing air inlet temperatures. As this configuration had a greater volume of silica gel, the adsorption rate is higher. As the inlet temperature fell, the adsorption and desorption rates also fell. As less water content was removed from the silica gel by the outgoing airstream, the silica gel remained more saturated, resulting in less moisture reduction of the airstream, this was the expected result. The testing suggested that lower regeneration temperatures were effective at desorbing water molecules from the pore surfaces of the silica gel, allowing moisture control of the incoming airstream to continue.

However, the measurements for relative humidity taken from the experiments testing the 20-blade configuration of the dehumidification rotary wheel presented an alternative consideration of the effect of the radial blade design. Though the moisture content of the incoming airstream was not reduced by a similar amount compared to the 32-blade configuration at each of the inlet air temperatures tested, expected given the lower volume of silica gel due to the lower number of blades, the outgoing airstream relative humidity change was greater for each inlet air temperature tested.

The higher rate of desorption for the 20-blade configuration is significant. A dominant alternative factor for the desorption rate of silica gel to the regeneration temperature provides scope for increased energy savings. If high volumes of dry air are capable of achieving the same rate of desorption as high regeneration temperatures, the potential for development of the radial blade design increases. Maximising the volume able to pass through the rotary wheel will increase the desorption rate, potentially increasing the adsorption and longevity of the system as complete saturation is avoided, but also increasing the supply rate of air as greater volume of air can be circulated.

Though the potential for the radial blade dehumidification design for integration into a passive ventilation is high, a number of deficiencies currently exist that require addressing. The ratio of adsorption to desorption is very high, up to 10:1. This presents a limit to the operational time of the rotary wheel. As more water molecules are adsorbed to the pore surface than are removed for each rotation, after a sufficient time the silica gel particles will become fully saturated, preventing further adsorption. When this occurs, the moisture content of the airstream will no longer be reduced. Increasing the desorption to reach an adsorption:desorption ratio as close to 1:1 is desirable or a method to divert air away from the adsorption section of the rotary wheel to allow extended desorption time.

7.3 Key Findings

The research and development of an alternative rotary wheel design carried out in the duration of this project has led to advancements in heat recovery and dehumidification technology, as well as integration with passive ventilation technology. The key findings taken from the research are presented as a comparison with the research objectives set in Chapter 1 Section 1.1.

1. A thorough literature review of existing research was completed encompassing mechanical HVAC, passive ventilation systems, wind towers and wind tower development, heat recovery and desiccant recovery devices. The literature search showed that mechanical HVAC systems are highly energy intensive and are the dominant form of ventilation system in buildings. Wind towers have developed into a viable method for passive ventilation, that have low energy requirements. No current heat recovery or desiccant recovery systems can be adequately integrated into passive ventilation systems. Of the recovery systems reviewed, recovery wheels presented the most suitable option for development and adaption into passive ventilation systems due to the high recovery efficiency and low pressure drop. The literature review, formatted suitably and titled "A Review of Heat Recovery Technology for Passive Ventilation Applications" was assessed and validated by peer-review. This led to the review being published in a leading international journal.
2. A prototype rotary recovery wheel was developed using CAD software and rapid prototyping 3D printing. Developing the internal structure of rotary recovery wheels to encompass greater opening size and reduced skin friction, an arrangement of

radial blades was configured through which recovery, heat or humidity, would occur. Blades extended radially outward, measured in arrangements 10-15° from each other. The prototype was manufactured using 3D printing techniques to improve manufacturing speed and accuracy. The novelty of the design concept of opening the internal structure of the wheel using radial blades was proved through the filing of a patent. The patent, GB1506768.9, secured the unique design of the radial blades for further development.

3. CFD simulations using the CAD data for the design of the radial blade rotary wheels were developed for analysis. The simulations were validated using measurements taken from experimental setups for testing of the same arrangements and configurations. The trends presented from each of the datasets showed high correlation, which was found to provide adequate analysis. Average error percentages of the CFD against the experiments were calculated for each of the configurations. The average percentage error for air velocity for the heat recovery arrangement was 25.28% and 23.9% for the dehumidification arrangement. The accuracy of the CFD simulations allowed confidence in the solutions for the investigations of changes to the air flow, particularly pressure drop.
4. By varying the internal structure of the rotary recovery wheel, properties of the structure were able to be determined. The number of radial blades extending from the centre shaft were altered from 20 blades to 32 blades, correlating to a change of 15° between each blade to 10° between each blade. The purpose of altering the number of blades was to understand the effect of the geometry on the pressure drop, and the volume of material on the heat recovery and dehumidification of the copper radial blades and the silica gel blades respectively.

The copper radial blades were able to transfer heat from the airstream at higher temperature to the airstream at lower temperature. The maximum increase in air temperature was 0.68°C. However, the reduction in air temperature for the same test was 2.40°C showing that a high amount of heat is stored within the blade, improving the transfer mechanism from the blade to air would increase the heat transfer.

Depending on the number of silica gel blades in the configuration, the dehumidification rotary wheel was able to control the moisture of a humid airstream by lowering the relative humidity by up to 67.01% for the 32-blade configuration and 35.82% for the 20-blade configuration. Ongoing adsorption of water molecules to

the pore surface of the silica gel particles was possible at low regeneration temperatures, between 25-40°C.

5. The targeted pressure drop across the device was 2Pa, a significant reduction from conventional rotary wheels where pressure drop can be as high as 150Pa. The large openings between radial blades would reduce recirculation at the wheel entrance and reduce skin friction within the structure between the air and blade materials. The CFD simulations showed that the average pressure drop across the device, dependent on the arrangement and configuration was 10.31-10.02Pa. This is higher than the target pressure drop, but a substantial decrease from the conventional rotary wheel pressure drop.

Though the pressure drop across the device arrangements was higher than the target pressure drop, evaluation of the supply rates possible were carried out as analysis showed that the contraction of volume through the sections between radial blades caused acceleration of the air velocity. By assessing the velocity of the air after the device, the ventilation supply air was calculated. Though the pressure drop across the device was 10.31-10.02Pa, the calculated air supply rates were 140.86 litres per second, enough to adequately ventilate a room occupied by 17 individuals. Further scaling and improvement of the design could increase this value.

6. The aim of the project was to develop a recovery device capable of integration into a passive ventilation system that would provide adequate ventilation supply rates due to low pressure drop across the device. Furthermore, the design of the device was aimed to reduce energy demands from a building through two methods. Firstly, using copper blades to increase the air temperature of incoming air through heat recovery to reduce the heating demand. Secondly, control moisture of an incoming airstream by reducing the moisture content in the air, whilst desorbing water molecules from the silica gel particles at a lower regeneration temperature than previously achieved. The successful integration of the radial blades design into a passive ventilation is based on the performance and potential of these characteristics.

Though the pressure drop across the device was calculated to be higher than anticipated, the air velocity measurements suggested that the ventilation supply rates achievable would be high enough to satisfy guideline ventilation levels. Providing ventilation supply air through passive ventilation systems reduces the demand on mechanical systems and the associated energy costs of such systems.

Heat transfer from a high air temperature airstream to a low air temperature airstream was possible, with increases in air temperature seen for outlet air temperatures as low as 25°C. Though low increases in air temperature were measured, increasing the efficiency of transferring the stored heat in the blades will raise temperature increase. Recirculating exhaust heat from buildings will reduce energy demand on heating systems, lowering costs.

The regeneration of the silica gel particles in the dehumidification arrangement was capable at temperatures between 25-40°C, significantly lower than current temperatures. The reduction of relative humidity in the incoming airstream was as high as 67.1% for these regeneration temperatures. Lowering the regeneration temperature whilst maintaining relative humidity control considerably reduces the energy demand for the system process, lowering costs.

The potential for integration of the recovery device for integration into a passive ventilation system was dependent on the ability to not impede air flow such that sufficient ventilation supply rates were possible, along with the ability to condition the air as required. The measurements from the CFD analysis and experimental testing confirm that this is possible. Further development of the radial blade recovery wheel would improve these characteristics.

The overall aim of this project was to develop a recovery device capable of integration with a passive ventilation system. The device should exhibit a low-pressure drop on the air, allowing suitable ventilation rates, as determined by guidelines, to be delivered to an occupied space. This was achieved by using a radial blade arrangement within the structure of the wheel, incurring a pressure drop of 10Pa. Testing showed that supply air could be provided for 17 people using this arrangement. In addition to this, the radial blade arrangement was shown to have further properties useful for integration with passive systems. Heat was transferred from the exhaust airstream to the inlet airstream using copper radial blades, raising the temperature by a maximum of 0.68°C. When acrylic radial blades were coated in silica gel, the relative humidity of a saturated airstream was reduced from 100% to 33%. This was achieved at a regeneration temperature of 40°C; this is lower than the typical temperature required of 120°C necessary to dry the silica gel, allowing adsorption to continue.

7.4 Recommendations for Future Work

Further work for development of the design is recommended in the following areas to enhance the properties of the recovery device:

- Initial analysis and experimentation of the radial blade design for rotary recovery wheels showed successful testing for heat recovery and dehumidification, along with allowable ventilation supply rates. The design shows significant potential for development. Performance optimisation of various aspects of the design is encouraged. The effect of the number of blades in a configuration was partially explored; further analysis of different blade configurations would provide definite results. Furthermore, the straight shape of the blades was maintained for each of the tests, changing the shape and design of the radial blades may yield improved performance.

All test arrangements and configurations were observed with the same rotation velocity. This suggested that the consistent pressure drop value across the rotary wheel was a function of rotation velocity and not wheel geometry. Testing at a range of rotation velocities would confirm this.

Greater control of the inlet conditions would increase the range over which the performance of the rotary wheels could be tested. Inlet conditions of the incoming airstream were, predominately, dictated by the conditions in the laboratory. Increasing the difference between the inlet air temperatures, particularly for the heat recovery testing, would replicate conditions more similar to those of a colder UK and northern European climate. Greater inlet temperature differences would likely yield greater heat transfer across the device.

- The measured values of the experimental analysis provided a target for the results generated by the CFD analysis. The boundary and cell zone conditions were altered to lower the error between the CFD measurements and experimental measurements. Further development of the CFD models would develop a formula capable of deriving the boundary and cell zone conditions based on the known properties of the rotary wheel and inlet conditions.
- Analysis suggested that the desorption of the water molecules from the silica gel particles was a function of the respective saturation levels of the air and silica,

and not the regeneration temperature as previously thought. Further investigation of this may result in lower regeneration temperatures, resulting in increased energy savings.

- The prototype that was constructed for analysis was a reduced scale due to limitations of the equipment available. Given the standard dimensions of a wind tower are 1000x1000mm in plan, testing of a radial blade rotary wheel built to this size would be advisable. Testing of parameters such as pressure drop and air supply rate would be reflective of the true dimensions of the wind tower and rotary wheel.
- Integrating the design with a full-scale wind tower would be beneficial. Common commercial wind towers are four-sided with a central shaft divided into four individual quadrants. The air in each of the quadrants may have different properties. Therefore, analysing the interaction between the four separate airstreams and the rotary wheel and the effect of the wheel on the airstream properties would be beneficial. Far-field testing of this configuration of full-scale four-sided wind tower and rotary recovery wheel would provide long term data for the performance of the system.

List of References

- [1] International Energy Agency, Key World Energy Statistics 2015, (2015) 82. doi:10.1787/9789264039537-en.
- [2] Parliament of the United Kingdom, Climate Change Act 2008, 2008. doi:10.1136/bmj.39469.569815.47.
- [3] P. Huovila, M. Alla-Juusela, L. Melchert, S. Pouffary, Buildings and climate change: Status, challenges and opportunities, 2007. doi:ISBN: 987-92-807-3064-7 DTI/1240/PA.
- [4] M. Orme, Estimates of the energy impact of ventilation and associated financial expenditures, Energy Build. 33 (2001) 199–205. doi:10.1016/S0378-7788(00)00082-7.
- [5] Committee on Climate Change, Fourth Carbon Budget Review – technical report – sectoral analysis of the cost-effective path to the 2050 target, (2012) 58–79. www.theccc.org.uk (accessed June 1, 2016).
- [6] U.S. Energy Information Administration, U.S. Energy-Related Carbon Dioxide Emissions 2014, Washington DC, 2015.
- [7] D.J. Clements-Croome, H.B. Awbi, Z. Bakó-Biró, N. Kochhar, M. Williams, Ventilation rates in schools, Build. Environ. 43 (2008) 362–367. doi:16/j.buildenv.2006.03.018.
- [8] N. Khan, Y. Su, S.B. Riffat, A review on wind driven ventilation techniques, Energy Build. 40 (2008) 1586–1604. doi:10.1016/j.enbuild.2008.02.015.
- [9] Education Funding Agency, Building Bulletin 101 Ventilation of School Buildings, Dep. Education. (2006) 1–62. doi:011-2711642.
- [10] L. Pérez-Lombard, J. Ortiz, C. Pout, A review on buildings energy consumption information, Energy Build. 40 (2008) 394–398. doi:10.1016/j.enbuild.2007.03.007.
- [11] A. Dadoo, L. Gustavsson, R. Sathre, Primary energy implications of ventilation heat recovery in residential buildings, Energy Build. 43 (2011) 1566–1572. doi:10.1016/j.enbuild.2011.02.019.
- [12] K. Zhong, Y. Kang, Applicability of air-to-air heat recovery ventilators in China, Appl. Therm. Eng. 29 (2009) 830–840. doi:10.1016/j.applthermaleng.2008.04.003.

- [13] P.F. Linden, The Fluid Mechanics of Natural Ventilation, *Annu. Rev. Fluid Mech.* 31 (1999) 201–238. doi:10.1146/annurev.fluid.31.1.201.
- [14] B.R. Hughes, J.K. Calautit, S.A. Ghani, The development of commercial wind towers for natural ventilation: A review, *Appl. Energy*. 92 (2012) 606–627. doi:10.1016/j.apenergy.2011.11.066.
- [15] A.W. Woods, S. Fitzgerald, S. Livermore, A comparison of winter pre-heating requirements for natural displacement and natural mixing ventilation, *Energy Build.* 41 (2009) 1306–1312. doi:10.1016/j.enbuild.2009.07.030.
- [16] O. Saadatian, L.C. Haw, K. Sopian, M.Y. Sulaiman, Review of windcatcher technologies, *Renew. Sustain. Energy Rev.* 16 (2012) 1477–1495. doi:10.1016/j.rser.2011.11.037.
- [17] B.R. Hughes, C.M. Mak, A study of wind and buoyancy driven flows through commercial wind towers, *Energy Build.* 43 (2011) 1784–1791. doi:10.1016/j.enbuild.2011.03.022.
- [18] B.M. Jones, R. Kirby, The performance of natural ventilation windcatchers in schools - A comparison between prediction and measurement, *Int. J. Vent.* 9 (2010) 273–286.
- [19] H. Montazeri, Experimental and numerical study on natural ventilation performance of various multi-opening wind catchers, *Build. Environ.* 46 (2011) 370–378. doi:10.1016/j.buildenv.2010.07.031.
- [20] Y. Jiang, Q. Chen, Study of natural ventilation in buildings by large eddy simulation, *J. Wind Eng. Ind. Aerodyn.* 89 (2001) 1155–1178.
- [21] J.K. Calautit, B.R. Hughes, Measurement and prediction of the indoor airflow in a room ventilated with a commercial wind tower, *Energy Build.* 84 (2014) 367–377. doi:10.1016/j.enbuild.2014.08.015.
- [22] Department for Energy and Climate Change, Average wind speed and deviations from the long term mean, (2016).
- [23] M. Kolokotroni, B.C. Webb, S.D. Hayes, Summer cooling with night ventilation for office buildings in moderate climates, *Energy Build.* 27 (1998) 231–237. doi:10.1016/S0378-7788(97)00048-0.
- [24] D. Mumovic, J. Palmer, M. Davies, M. Orme, I. Ridley, T. Oreszczyn, et al., Winter

- indoor air quality, thermal comfort and acoustic performance of newly built secondary schools in England, *Build. Environ.* 44 (2009) 1466–1477. doi:10.1016/j.buildenv.2008.06.014.
- [25] A. Rackes, A.P. Melo, R. Lamberts, Naturally comfortable and sustainable: Informed design guidance and performance labeling for passive commercial buildings in hot climates, *Appl. Energy*. 174 (2016) 256–274. doi:10.1016/j.apenergy.2016.04.081.
- [26] B.R. Hughes, S.A.A. Abdul Ghani, A numerical investigation into the effect of windvent dampers on operating conditions, *Build. Environ.* 44 (2009) 237–248. doi:10.1016/j.buildenv.2008.02.012.
- [27] L. Shao, S.B. Riffat, G. Gan, Heat recovery with low pressure loss for natural ventilation, *Energy Build.* 28 (1998) 179–184. doi:10.1016/S0378-7788(98)00016-4.
- [28] N. Eyre, P. Baruah, Uncertainties in future energy demand in UK residential heating, *Energy Policy*. 87 (2015) 641–653. doi:10.1016/j.enpol.2014.12.030.
- [29] K. Voss, S. Herkel, J. Pfafferott, G. Löhnert, A. Wagner, Energy efficient office buildings with passive cooling - Results and experiences from a research and demonstration programme, *Sol. Energy*. 81 (2007) 424–434. doi:10.1016/j.solener.2006.04.008.
- [30] B.R. Hughes, H.N. Chaudhry, J.K. Calautit, Passive energy recovery from natural ventilation air streams, *Appl. Energy*. 113 (2014) 127–140. doi:10.1016/j.apenergy.2013.07.019.
- [31] P. Mazzei, F. Minichiello, D. Palma, HVAC dehumidification systems for thermal comfort: a critical review, *Appl. Therm. Eng.* 25 (2005) 677–707. doi:10.1016/j.applthermaleng.2004.07.014.
- [32] S.B. Riffat, M.C. Gillott, Performance of a novel mechanical ventilation heat recovery heat pump system, *Appl. Therm. Eng.* 22 (2002) 839–845.
- [33] B. Givoni, Indoor temperature reduction by passive cooling systems, *Sol. Energy*. 85 (2011) 1692–1726. doi:10.1016/j.solener.2009.10.003.
- [34] C. Giaconia, A. Orioli, A. Di Gangi, Air quality and relative humidity in commercial aircrafts: An experimental investigation on short-haul domestic flights, *Build. Environ.* 67 (2013) 69–81. doi:10.1016/j.buildenv.2013.05.006.
- [35] CIBSE, CIBSE Guide A: Environmental Design, 2015. doi:10.1016/0360-

1323(94)00059-2.

- [36] Y. Tashiro, M. Kubo, Y. Katsumi, T. Meguro, K. Komeya, Assessment of adsorption-desorption characteristics of adsorbents for adsorptive desiccant cooling system, *J. Mater. Sci.* 39 (2004) 1315–1319. doi:10.1023/B:JMSC.0000013937.11959.6a.
- [37] L.Z. Zhang, D.S. Zhu, X.H. Deng, B. Hua, Thermodynamic modeling of a novel air dehumidification system, *Energy Build.* 37 (2005) 279–286. doi:10.1016/j.enbuild.2004.06.019.
- [38] S. Yamaguchi, K. Saito, Numerical and experimental performance analysis of rotary desiccant wheels, *Int. J. Heat Mass Transf.* 60 (2013) 51–60. doi:10.1016/j.ijheatmasstransfer.2012.12.036.
- [39] J. Min, M. Su, Performance analysis of a membrane-based energy recovery ventilator: Effects of membrane spacing and thickness on the ventilator performance, *Appl. Therm. Eng.* 30 (2010) 991–997. doi:10.1016/j.applthermaleng.2010.01.010.
- [40] M. Intini, S. De Antonellis, C.M. Joppolo, The effect of inlet velocity and unbalanced flows on optimal working conditions of silica gel desiccant wheels, *Energy Procedia.* 48 (2014) 858–864. doi:10.1016/j.egypro.2014.02.099.
- [41] B. Crook, N.C. Burton, Indoor moulds, Sick Building Syndrome and building related illness, *Fungal Biol. Rev.* 24 (2010) 106–113. doi:10.1016/j.fbr.2010.05.001.
- [42] S. Ahmed Abdul-Wahab, S.C.F. En, A. Elkamel, L. Ahmadi, K. Yetilmezsoy, A review of standards and guidelines set by international bodies for the parameters of indoor air quality, *Atmos. Pollut. Res.* 6 (2015) 751–767. doi:10.5094/APR.2015.084.
- [43] N.E. Klepeis, W.C. Nelson, W.R. Ott, J.P. Robinson, a M. Tsang, P. Switzer, et al., The National Human Activity Pattern Survey (NHAPS): a resource for assessing exposure to environmental pollutants., *J. Expo. Anal. Environ. Epidemiol.* 11 (2001) 231–252. doi:10.1038/sj.jea.7500165.
- [44] P. Macnaughton, J. Spengler, J. Vallarino, S. Santanam, U. Satish, J. Allen, Environmental perceptions and health before and after relocation to a green building, *Build. Environ.* 104 (2016) 138–144. doi:10.1016/j.buildenv.2016.05.011.
- [45] O. Seppänen, W.J. Fisk, Association of ventilation system type with SBS symptoms in office workers, *Indoor Air.* 12 (2002) 98–112. doi:10.1034/j.1600-0668.2002.01111.x.

- [46] M. Fordham, Natural ventilation, in: *Renew. Energy*, 2000: pp. 17–37. doi:10.1016/S0960-1481(99)00012-9.
- [47] F. Soflaei, M. Shokouhian, S.M.M. Shemirani, Investigation of Iranian traditional courtyard as passive cooling strategy (a field study on BS climate), *Int. J. Sustain. Built Environ.* 5 (2016) 99–113. doi:10.1016/j.ijbsbe.2015.12.001.
- [48] B. Chenari, J. Dias Carrilho, M. Gameiro Da Silva, Towards sustainable, energy-efficient and healthy ventilation strategies in buildings: A review, *Renew. Sustain. Energy Rev.* 59 (2016) 1426–1447. doi:10.1016/j.rser.2016.01.074.
- [49] C.-R. Chu, B.-F. Chiang, Wind-driven cross ventilation with internal obstacles, *Energy Build.* 67 (2013) 201–209. doi:10.1016/j.enbuild.2013.07.086.
- [50] C.R. Chu, B.F. Chiang, Wind-driven cross ventilation in long buildings, *Build. Environ.* 80 (2014) 150–158. doi:10.1016/j.buildenv.2014.05.017.
- [51] W.D. Baines, J.S. Turner, Turbulent buoyant convection from a source in a confined two-layered region, *J. Fluid Mech.* 37 (1969) 51–80. doi:10.1017/S0022112084002007.
- [52] P.F. Linden, G.F. Lane-Serff, D.A. Smeed, Emptying filling boxes: the fluid mechanics of natural ventilation, *J. Fluid Mech.* 212 (1990) 309–335. doi:10.1017/S0022112090001987.
- [53] Y. Li, A. Delsante, Natural ventilation induced by combined wind and thermal forces, *Build. Environ.* 36 (2001) 59–71. doi:10.1016/S0360-1323(99)00070-0.
- [54] Z. (John) Zhai, M. El Mankibi, A. Zoubir, Review of Natural Ventilation Models, *Energy Procedia.* 78 (2015) 2700–2705. doi:10.1016/j.egypro.2015.11.355.
- [55] Q. Chen, Ventilation performance prediction for buildings: A method overview and recent applications, *Build. Environ.* 44 (2009) 848–858. doi:10.1016/j.buildenv.2008.05.025.
- [56] B.E. Launder, D.B. Spalding, The numerical computation of turbulent flows, *Comput. Methods Appl. Mech. Eng.* 3 (1974) 269–289. doi:10.1016/0045-7825(74)90029-2.
- [57] V. Yakhot, S.A. Orszag, Renormalization group analysis of turbulence. I. Basic theory, *J. Sci. Comput.* 1 (1986) 3–51. doi:10.1007/BF01061452.
- [58] Z.J. Zhai, Z. Zhang, W. Zhang, Q.Y. Chen, Evaluation of various turbulence models in

- predicting airflow and turbulence in enclosed environments by CFD: part 1 - Summary of prevalent turbulence models, *Hvac&R Res.* 13 (2007) 853–870. doi:10.1080/10789669.2007.10391459.
- [59] S. Hussain, P.H. Oosthuizen, Validation of numerical modeling of conditions in an atrium space with a hybrid ventilation system, *Build. Environ.* 52 (2012) 152–161. doi:10.1016/j.buildenv.2011.12.016.
- [60] P.C. Liu, H.T. Lin, J.H. Chou, Evaluation of buoyancy-driven ventilation in atrium buildings using computational fluid dynamics and reduced-scale air model, *Build. Environ.* 44 (2009) 1970–1979. doi:10.1016/j.buildenv.2009.01.013.
- [61] M. Cook, Y. Ji, G. Hunt, CFD modelling of buoyancy-driven natural ventilation opposed by wind, 9th Int. IBPSA Conf. (2005) 207–214.
- [62] Z. Zhai, Q. Chen, P. Haves, J.H. Klems, On approaches to couple energy simulation and computational fluid dynamics programs, *Build. Environ.* 37 (2002) 857–864. doi:10.1016/S0360-1323(02)00054-9.
- [63] Z.J. Zhai, Q.Y. Chen, Sensitivity analysis and application guides for integrated building energy and CFD simulation, *Energy Build.* 38 (2006) 1060–1068. doi:10.1016/j.enbuild.2005.12.003.
- [64] Z. Zhai, Q. Chen, Solution characters of iterative coupling between energy simulation and CFD programs, *Energy Build.* 35 (2003) 493–505. doi:10.1016/S0378-7788(02)00156-1.
- [65] Z.J. Zhai, Q.Y. Chen, Performance of coupled building energy and CFD simulations, *Energy Build.* 37 (2005) 333–344. doi:10.1016/j.enbuild.2004.07.001.
- [66] H. Safarzadeh, M.N. Bahadori, Passive cooling effects of courtyards, *Build. Environ.* 40 (2005) 89–104. doi:10.1016/j.buildenv.2004.04.014.
- [67] H.A. Abdulkareem, Thermal Comfort through the Microclimates of the Courtyard. A Critical Review of the Middle-eastern Courtyard House as a Climatic Response, *Procedia - Soc. Behav. Sci.* 216 (2016) 662–674. doi:10.1016/j.sbspro.2015.12.054.
- [68] K. Ward, S. Lauf, B. Kleinschmit, W. Endlicher, Heat waves and urban heat islands in Europe : A review of relevant drivers, *Sci. Total Environ.* 569–570 (2016) 527–539. doi:10.1016/j.scitotenv.2016.06.119.

- [69] M. Taleghani, M. Tenpierik, A. van den Dobbelsteen, D.J. Sailor, Heat in courtyards: A validated and calibrated parametric study of heat mitigation strategies for urban courtyards in the Netherlands, *Sol. Energy*. 103 (2014) 108–124. doi:10.1016/j.solener.2014.01.033.
- [70] S. Hussain, P.H. Oosthuizen, Numerical investigations of buoyancy-driven natural ventilation in a simple atrium building and its effect on the thermal comfort conditions, *Appl. Therm. Eng.* 40 (2012) 358–372. doi:10.1016/j.applthermaleng.2012.02.025.
- [71] J.M. Holford, G.R. Hunt, Fundamental atrium design for natural ventilation, *Build. Environ.* 38 (2003) 409–426. doi:10.1016/S0360-1323(02)00019-7.
- [72] L. Moosavi, N. Mahyuddin, N. Ab Ghafar, M. Azzam Ismail, Thermal performance of atria: An overview of natural ventilation effective designs, *Renew. Sustain. Energy Rev.* 34 (2014) 654–670. doi:10.1016/j.rser.2014.02.035.
- [73] S. Asadi, M. Fakhari, R. Fayaz, A. Mahdavi Parsa, The effect of solar chimney layout on ventilation rate in buildings, *Energy Build.* 123 (2016) 71–78. doi:10.1016/j.enbuild.2016.04.047.
- [74] R. Khanal, C. Lei, Solar chimney-A passive strategy for natural ventilation, *Energy Build.* 43 (2011) 1811–1819. doi:10.1016/j.enbuild.2011.03.035.
- [75] X.Q. Zhai, Z.P. Song, R.Z. Wang, A review for the applications of solar chimneys in buildings, *Renew. Sustain. Energy Rev.* 15 (2011) 3757–3767. doi:10.1016/j.rser.2011.07.013.
- [76] N. Artmann, H. Manz, P. Heiselberg, Climatic potential for passive cooling of buildings by night-time ventilation in Europe, *Appl. Energy*. 84 (2007) 187–201. doi:10.1016/j.apenergy.2006.05.004.
- [77] N. Artmann, H. Manz, P. Heiselberg, Parameter study on performance of building cooling by night-time ventilation, *Renew. Energy*. 33 (2008) 2589–2598. doi:10.1016/j.renene.2008.02.025.
- [78] Z. Hedayat, B. Belmans, M. Hossein Ayatollahi, I. Wouters, F. Descamps, Performance Assessment of Ancient Wind Catchers - an Experimental and Analytical Study, *Energy Procedia*. 78 (2015) 2578–2583. doi:10.1016/j.egypro.2015.11.292.
- [79] M.N. Bahadori, An improved design of wind towers for natural ventilation and passive

- cooling, *Sol. Energy*. 35 (1985) 119–129. doi:10.1016/0038-092X(85)90002-7.
- [80] M.N. Bahadori, M. Mazidi, A.R. Dehghani, Experimental investigation of new designs of wind towers, *Renew. Energy*. 33 (2008) 2273–2281. doi:10.1016/j.renene.2007.12.018.
- [81] Y. Bouchahm, F. Bourbia, A. Belhamri, Performance analysis and improvement of the use of wind tower in hot dry climate, *Renew. Energy*. 36 (2011) 898–906. doi:10.1016/j.renene.2010.08.030.
- [82] M.A. Yaghoubi, A. Sabzevari, A.A. Golneshan, Wind towers: Measurement and performance, *Sol. Energy*. 47 (1991) 97–106. doi:10.1016/0038-092X(91)90040-4.
- [83] B.R. Hughes, S.A. Ghani, A numerical investigation into the feasibility of a passive-assisted natural ventilation stack device, *Int. J. Sustain. Energy*. 30 (2011) 193–211. doi:10.1080/1478646X.2010.503275.
- [84] S. Liu, C.M. Mak, J. Niu, Numerical evaluation of louver configuration and ventilation strategies for the windcatcher system, *Build. Environ*. 46 (2011) 1600–1616. doi:10.1016/j.buildenv.2011.01.025.
- [85] B.R. Hughes, S.A.A.A. Ghani, A numerical investigation into the effect of Windvent louvre external angle on passive stack ventilation performance, *Build. Environ*. 45 (2010) 1025–1036. doi:10.1016/j.buildenv.2009.10.010.
- [86] R. Priyadarsini, K.W. Cheong, N.H. Wong, Enhancement of natural ventilation in high-rise residential buildings using stack system, *Energy Build*. 36 (2004) 61–71. doi:10.1016/S0378-7788(03)00076-8.
- [87] J.K. Calautit, B.R. Hughes, Wind tunnel and CFD study of the natural ventilation performance of a commercial multi-directional wind tower, *Build. Environ*. 80 (2014) 71–83. doi:10.1016/j.buildenv.2014.05.022.
- [88] A.A. Elmualim, Effect of damper and heat source on wind catcher natural ventilation performance, *Energy Build*. 38 (2006) 939–948. doi:10.1016/j.enbuild.2005.11.004.
- [89] P. Moonen, B. Blocken, S. Roels, J. Carmeliet, Numerical modeling of the flow conditions in a closed-circuit low-speed wind tunnel, *J. Wind Eng. Ind. Aerodyn*. 94 (2006) 699–723. doi:10.1016/j.jweia.2006.02.001.
- [90] P. Moonen, B. Blocken, J. Carmeliet, Indicators for the evaluation of wind tunnel test

- section flow quality and application to a numerical closed-circuit wind tunnel, *J. Wind Eng. Ind. Aerodyn.* 95 (2007) 1289–1314. doi:10.1016/j.jweia.2007.02.027.
- [91] C. Walker, G. Tan, L. Glicksman, Reduced-scale building model and numerical investigations to buoyancy-driven natural ventilation, *Energy Build.* 43 (2011) 2404–2413. doi:10.1016/j.enbuild.2011.05.022.
- [92] T. Defraeye, B. Blocken, J. Carmeliet, Convective heat transfer coefficients for exterior building surfaces: Existing correlations and CFD modelling, in: *Energy Convers. Manag.*, 2011: pp. 512–522. doi:10.1016/j.enconman.2010.07.026.
- [93] H. Montazeri, R. Azizian, Experimental study on natural ventilation performance of one-sided wind catcher, *Build. Environ.* 43 (2008) 2193–2202. doi:10.1016/j.buildenv.2008.01.005.
- [94] H. Montazeri, F. Montazeri, R. Azizian, S. Mostafavi, Two-sided wind catcher performance evaluation using experimental, numerical and analytical modeling, *Renew. Energy.* 35 (2010) 1424–1435. doi:10.1016/j.renene.2009.12.003.
- [95] A. Shea, A.P. Robertson, G.J. Levermore, N.M. Rideout, Measurements of performance of a wind-driven ventilation terminal, *Proc. Inst. Civ. Eng. Build.* 163 (2010) 129–136. doi:10.1680/stbu.2010.163.2.129.
- [96] B.M. Jones, R. Kirby, Indoor air quality in U.K. school classrooms ventilated by natural ventilation windcatchers, *Int. J. Vent.* 10 (2012) 323–338. doi:10.5555/2044-4044-10.4.323.
- [97] H.J. Sauer, R.H. Howell, Promise and potential of air-to-air energy recovery systems, *Int. J. Refrig.* 4 (1981) 182–194. doi:10.1016/0140-7007(81)90049-9.
- [98] WBCSD, *Energy Efficiency in Buildings, Switzerland, 2008.* doi:10.1017/CBO9781107415324.004.
- [99] S. Gendebien, S. Bertagnolio, V. Lemort, Investigation on a ventilation heat recovery exchanger: Modeling and experimental validation in dry and partially wet conditions, *Energy Build.* 62 (2013) 176–189. doi:10.1016/j.enbuild.2013.02.025.
- [100] M. Rasouli, C.J. Simonson, R.W. Besant, Applicability and optimum control strategy of energy recovery ventilators in different climatic conditions, *Energy Build.* 42 (2010) 1376–1385. doi:10.1016/j.enbuild.2010.03.006.

- [101] L.Z. Zhang, Y. Jiang, Heat and mass transfer in a membrane-based energy recovery ventilator, *J. Memb. Sci.* 163 (1999) 29–38. doi:10.1016/S0376-7388(99)00150-7.
- [102] A. Mardiana-Idayu, S.B. Riffat, Review on heat recovery technologies for building applications, *Renew. Sustain. Energy Rev.* 16 (2012) 1241–1255. doi:10.1016/j.rser.2011.09.026.
- [103] M. Justo Alonso, P. Liu, H.M. Mathisen, G. Ge, C. Simonson, Review of heat/energy recovery exchangers for use in ZEBs in cold climate countries, *Build. Environ.* 84 (2015) 228–237. doi:10.1016/j.buildenv.2014.11.014.
- [104] P.M. Cuce, S. Riffat, A comprehensive review of heat recovery systems for building applications, *Renew. Sustain. Energy Rev.* 47 (2015) 665–682. doi:10.1016/j.rser.2015.03.087.
- [105] L. Shi, M.Y.L. Chew, A review on sustainable design of renewable energy systems, *Renew. Sustain. Energy Rev.* 16 (2012) 192–207. doi:10.1016/j.rser.2011.07.147.
- [106] H.-Y. Chan, S.B. Riffat, J. Zhu, Review of passive solar heating and cooling technologies, *Renew. Sustain. Energy Rev.* 14 (2010) 781–789. doi:10.1016/j.rser.2009.10.030.
- [107] T. Zou, L. Ma, Y. Xue, RETRACTED ARTICLE: Experimental study on the performance of rotary heat recovery unit, in: *Asia-Pacific Power Energy Eng. Conf. APPEEC, 2010*. doi:10.1109/APPEEC.2010.5449500.
- [108] G. Angrisani, C. Roselli, M. Sasso, Effect of rotational speed on the performances of a desiccant wheel, *Appl. Energy.* 104 (2013) 268–275. doi:10.1016/j.apenergy.2012.10.051.
- [109] C.E.L. Nobrega, N.C.L. Brum, Modeling and simulation of heat and enthalpy recovery wheels, *Energy.* 34 (2009) 2063–2068. doi:10.1016/j.energy.2008.08.016.
- [110] Z. Wu, R.V.N. Melnik, F. Borup, Model-based analysis and simulation of regenerative heat wheel, *Energy Build.* 38 (2006) 502–514. doi:10.1016/j.enbuild.2005.08.009.
- [111] X.J. Zhang, Y.J. Dai, R.Z. Wang, A simulation study of heat and mass transfer in a honeycombed rotary desiccant dehumidifier, *Appl. Therm. Eng.* 23 (2003) 989–1003. doi:10.1016/S1359-4311(03)00047-4.
- [112] K. Hemzal, Rotary heat exchanger efficiency influenced by air tightness, in: *Proc. 17th*

Air-Conditioning Vent. Conf., 2006.

- [113] J. Juodvalkis, E. Blaževi, J. Karbauskait, V. Nenorta, Rotary heat pump, *Mechanika*. 17 (2011) 535–539.
- [114] K. Akbari, R. Oman, Impacts of heat recovery ventilators on energy savings and indoor radon level, *Manag. Environ. Qual. An Int. J.* 24 (2012) 682–694. doi:10.1108/MEQ-06-2012-0050.
- [115] R.K. Calay, W.C. Wang, A hybrid energy efficient building ventilation system, *Appl. Therm. Eng.* 57 (2013) 7–13. doi:10.1016/j.applthermaleng.2013.03.042.
- [116] C. Roulet, F.D. Heidt, F. Foradini, M. Pibiri, Real heat recovery with air handling units, *Energy Build.* 33 (2001) 495–502.
- [117] N.C.L. Brum, Modeling and simulation of heat and enthalpy recovery wheels, *Energy*. 34 (2009) 2063–2068. doi:10.1016/j.energy.2008.08.016.
- [118] T.S. Ge, Y. Li, R.Z. Wang, Y.J. Dai, A review of the mathematical models for predicting rotary desiccant wheel, *12* (2008) 1485–1528. doi:10.1016/j.rser.2007.01.012.
- [119] N. Enteria, H. Yoshino, A. Satake, A. Mochida, R. Takaki, R. Yoshie, et al., Experimental heat and mass transfer of the separated and coupled rotating desiccant wheel and heat wheel, *Exp. Therm. Fluid Sci.* 34 (2010) 603–615. doi:10.1016/j.expthermflusci.2009.12.001.
- [120] Y. Fan, K. Ito, Energy consumption analysis intended for real office space with energy recovery ventilator by integrating BES and CFD approaches, *Build. Environ.* 52 (2012) 57–67. doi:10.1016/j.buildenv.2011.12.008.
- [121] C.X. Jia, Y.J. Dai, J.Y. Wu, R.Z. Wang, Experimental comparison of two honeycombed desiccant wheels fabricated with silica gel and composite desiccant material, *Energy Convers. Manag.* 47 (2006) 2523–2534. doi:10.1016/j.enconman.2005.10.034.
- [122] J.L. Niu, L.Z. Zhang, Membrane-based Enthalpy Exchanger : material considerations and clarification of moisture resistance, *J. Memb. Sci.* 189 (2001) 179–191.
- [123] L.Z. Zhang, J.L. Niu, Performance comparisons of desiccant wheels for air dehumidification and enthalpy recovery, *Appl. Therm. Eng.* 22 (2002) 1347–1367.
- [124] T.S. Ge, Y.J. Dai, R.Z. Wang, Review on solar powered rotary desiccant wheel cooling system, *Renew. Sustain. Energy Rev.* 39 (2014) 476–497.

doi:10.1016/j.rser.2014.07.121.

- [125] M. Fehrm, W. Reiners, M. Ungemach, Exhaust air heat recovery in buildings, in: *Int. J. Refrig.*, 2002: pp. 439–449. doi:10.1016/S0140-7007(01)00035-4.
- [126] T.R. Nielsen, J. Rose, J. Kragh, Dynamic model of counter flow air to air heat exchanger for comfort ventilation with condensation and frost formation, *Appl. Therm. Eng.* 29 (2009) 462–468. doi:10.1016/j.applthermaleng.2008.03.006.
- [127] B.R. Lamb, Plate heat exchangers—a low-cost route to heat recovery, *J. Heat Recover. Syst.* 2 (1982) 247–255. doi:10.1016/0198-7593(82)90018-2.
- [128] M. Nasif, R. Al-waked, G. Morrison, M. Behnia, Membrane heat exchanger in HVAC energy recovery systems , systems energy analysis, *Energy Build.* 42 (2010) 1833–1840. doi:10.1016/j.enbuild.2010.05.020.
- [129] M.M. Abu-Khader, Plate heat exchangers: Recent advances, *Renew. Sustain. Energy Rev.* 16 (2012) 1883–1891. doi:10.1016/j.rser.2012.01.009.
- [130] L. Zhang, Convective mass transport in cross-corrugated membrane exchangers, *J. Memb. Sci.* 260 (2005) 75–83. doi:10.1016/j.memsci.2005.03.029.
- [131] J. Fernández-Seara, R. Diz, F.J. Uhía, A. Dopazo, J.M. Ferro, Experimental analysis of an air-to-air heat recovery unit for balanced ventilation systems in residential buildings, in: *Energy Convers. Manag.*, 2011: pp. 635–640. doi:10.1016/j.enconman.2010.07.040.
- [132] J. Kragh, J. Rose, T.R. Nielsen, S. Svendsen, New counter flow heat exchanger designed for ventilation systems in cold climates, *Energy Build.* 39 (2007) 1151–1158. doi:10.1016/j.enbuild.2006.12.008.
- [133] W. Yaïci, M. Ghorab, E. Entchev, Numerical analysis of heat and energy recovery ventilators performance based on CFD for detailed design, *Appl. Therm. Eng.* 51 (2013) 770–780. doi:10.1016/j.applthermaleng.2012.10.003.
- [134] R. Al-Waked, M.S. Nasif, G. Morrison, M. Behnia, CFD simulation of air to air enthalpy heat exchanger, *Energy Convers. Manag.* 74 (2013) 377–385. doi:10.1016/j.enconman.2013.05.038.
- [135] L. Zhang, Heat and mass transfer in plate-fin enthalpy exchangers with different plate and fin materials, *Int. J. Heat Mass Transf.* 52 (2009) 2704–2713.

doi:10.1016/j.ijheatmasstransfer.2008.12.014.

- [136] L. Zhang, F. Xiao, Simultaneous heat and moisture transfer through a composite supported liquid membrane, *Int. J. Heat Mass Transf.* 51 (2008) 2179–2189. doi:10.1016/j.ijheatmasstransfer.2007.11.006.
- [137] L. Zhang, C. Liang, L. Pei, Heat and moisture transfer in application scale parallel-plates enthalpy exchangers with novel membrane materials, *J. Memb. Sci.* 325 (2008) 672–682. doi:10.1016/j.memsci.2008.08.041.
- [138] S. Lin, J. Broadbent, R. McGlen, Numerical study of heat pipe application in heat recovery systems, *Appl. Therm. Eng.* 25 (2005) 127–133. doi:10.1016/j.applthermaleng.2004.02.012.
- [139] G. Gan, S.B. Riffat, Naturally ventilated buildings with heat recovery: CFD simulation of thermal environment, *Build. Serv. Eng. Res. Technol.* 18 (1997) 67–75. doi:10.1177/014362449701800201.
- [140] D. Liu, F.-Y. Zhao, G.-F. Tang, Active low-grade energy recovery potential for building energy conservation, *Renew. Sustain. Energy Rev.* 14 (2010) 2736–2747. doi:10.1016/j.rser.2010.06.005.
- [141] W. Srimuang, P. Amatachaya, A review of the applications of heat pipe heat exchangers for heat recovery, *Renew. Sustain. Energy Rev.* 16 (2012) 4303–4315. doi:DOI 10.1016/j.rser.2012.03.030.
- [142] J.K. Calautit, B.R. Hughes, H.N. Chaudhry, S.A. Ghani, CFD analysis of a heat transfer device integrated wind tower system for hot and dry climate, *Appl. Energy.* 112 (2013) 576–591. doi:10.1016/j.apenergy.2013.01.021.
- [143] M.A. Abd El-Baky, M.M. Mohamed, Heat pipe heat exchanger for heat recovery in air conditioning, *Appl. Therm. Eng.* 27 (2007) 795–801. doi:10.1016/j.applthermaleng.2006.10.020.
- [144] A. Vali, C.J. Simonson, R.W. Besant, G. Mahmood, Numerical model and effectiveness correlations for a run-around heat recovery system with combined counter and cross flow exchangers, *Int. J. Heat Mass Transf.* 52 (2009) 5827–5840. doi:10.1016/j.ijheatmasstransfer.2009.07.020.
- [145] C.A. Hviid, S. Svendsen, Analytical and experimental analysis of a low-pressure heat exchanger suitable for passive ventilation, *Energy Build.* 43 (2011) 275–284.

doi:10.1016/j.enbuild.2010.08.003.

- [146] H. Davidsson, R. Bernardo, B. Hellström, Theoretical and Experimental Investigation of a Heat Exchanger Suitable for a Hybrid Ventilation System, *Buildings*. 3 (2013) 18–38. doi:10.3390/buildings3010018.
- [147] K. Mahmud, G.I. Mahmood, C.J. Simonson, R.W. Besant, Performance testing of a counter-cross-flow run-around membrane energy exchanger (RAMEE) system for HVAC applications, *Energy Build.* 42 (2010) 1139–1147. doi:10.1016/j.enbuild.2010.02.005.
- [148] J. Wallin, H. Madani, J. Claesson, Run-around coil ventilation heat recovery system : A comparative study between different system configurations, *Appl. Energy*. 90 (2012) 258–265. doi:10.1016/j.apenergy.2011.05.012.
- [149] W.H. Emerson, Designing run-around coil systems, *J. Heat Recover. Syst.* 3 (1983) 305–309.
- [150] J.C.Y. Wang, Practical thermal design of run-around air-to-air heat recovery system, *J. Heat Recover. Syst.* 5 (1985) 493–501. doi:10.1016/0198-7593(85)90216-4.
- [151] R. Baetens, B. Petter, A. Gustavsen, Phase change materials for building applications : A state-of-the-art review, *Energy Build.* 42 (2010) 1361–1368. doi:10.1016/j.enbuild.2010.03.026.
- [152] M.M. Farid, A.M. Khudhair, S. Ali, K. Razack, A review on phase change energy storage : materials and applications, *Energy Convers. Manag.* 45 (2004) 1597–1615. doi:10.1016/j.enconman.2003.09.015.
- [153] R. Parameshwaran, S. Kalaiselvam, S. Harikrishnan, A. Elayaperumal, Sustainable thermal energy storage technologies for buildings : A review, *Renew. Sustain. Energy Rev.* 16 (2012) 2394–2433. doi:10.1016/j.rser.2012.01.058.
- [154] R. Kelly, AMEC, Latent heat storage in building materials, (1997) 1–28.
- [155] P. Kauranen, K. Peippo, P.D. Lund, An organic PCM storage system with adjustable melting temperature, *Sol. Energy*. 46 (1991) 275–278.
- [156] D. Feldman, D. Banu, D.W. Hawes, Development and application of organic phase change mixtures in thermal storage gypsum wallboard, *Sol. Energy Mater. Sol. Cells*. 36 (1995) 147–157.

- [157] D. O'Connor, J.K. Calautit, B.R. Hughes, A study of passive ventilation integrated with heat recovery, *Energy Build.* 82 (2014) 799–811. doi:10.1016/j.enbuild.2014.05.050.
- [158] A. Mardiana, S.B. Riffat, M. Worall, Integrated heat recovery system with wind-catcher for building applications : towards energy-efficient technologies, *Mater. Process. Energy Commun. Curr. Res. Tech. Dev.* (2013) 720–727.
- [159] A. Mardiana, S.B. Riffat, Review on physical and performance parameters of heat recovery systems for building applications, *Renew. Sustain. Energy Rev.* 28 (2013) 174–190. doi:10.1016/j.rser.2013.07.016.
- [160] J.K. Calautit, H.N. Chaudhry, B.R. Hughes, S.A. Ghani, Comparison between evaporative cooling and a heat pipe assisted thermal loop for a commercial wind tower in hot and dry climatic conditions, *Appl. Energy.* 101 (2013) 740–755. doi:10.1016/j.apenergy.2012.07.034.
- [161] S.B. Riffat, G. Gan, Determination of effectiveness of heat-pipe heat recovery for naturally-ventilated buildings, *Appl. Therm. Eng.* 18 (1998) 121–130. doi:10.1016/S1359-4311(97)00033-1.
- [162] G. Gan, S.B. Riffat, A numerical study of solar chimney for natural ventilation of buildings with heat recovery, *Appl. Therm. Eng.* 18 (1998) 1171–1187. doi:10.1016/S1359-4311(97)00117-8.
- [163] A. Flaga-maryanczyk, J. Schnotale, J. Radon, K. Was, Experimental measurements and CFD simulation of a ground source heat exchanger operating at a cold climate for a passive house ventilation system, *Energy Build.* 68 (2014) 562–570. doi:10.1016/j.enbuild.2013.09.008.
- [164] J. Kosny, D. Yarbrough, W. Miller, T. Petrie, P. Childs, A.M. Syed, et al., Thermal Performance of PCM-Enhanced Building Envelope Systems, in: *Proc. ASHRAE/DOE/BTECC Conf. theThermal Perform. Exter. Envel. Whole Build. X, 2007*: pp. 1–8.
- [165] R. Velraj, R. V Seeniraj, B. Hafner, C. Faber, K. Schwarzer, Heat transfer enhancement in a latent heat storage system, *Sol. Energy.* 65 (1999) 171–180.
- [166] U. Stritih, Heat transfer enhancement in latent heat thermal storage system for buildings, *Energy Build.* 35 (2003) 1097–1104. doi:10.1016/j.enbuild.2003.07.001.
- [167] Monodraught, Cool-phase-natural cooling and low energy ventilation, (2014).

<http://www.cool-phase.net/> (accessed July 7, 2016).

- [168] ANSYS, ANSYS Fluent Theory Guide, (2013) 814.
- [169] ANSYS, ANSYS Fluent 15.0 User's Guide, Ansys Inc. (2013) 2692. doi:10.1016/0140-3664(87)90311-2.
- [170] J.K. Calautit, Integration and Application of Passive Cooling Within a Wind Tower, University of Leeds, 2013.
- [171] J.H. Ferziger, M. Peric, Computational Methods for Fluid Dynamics, 2nd Editio, Springer-Verlag, Berlin, 2002. doi:10.1016/S0898-1221(03)90046-0.
- [172] H.K. Versteeg, W. Malalasekera, An Introduction to Computational Fluid Dynamics, 2nd Editio, Pearson Education Limited, Harlow, 2007. <http://www.mie.utoronto.ca/labs/mussl/cfd20.pdf>.
- [173] ANSYS, ANSYS Meshing User's Guide, (2013) 492.
- [174] T.J. Chung, Computational Fluid Dynamic, 2nd Editio, Cambridge University Press, New York, 2010.
- [175] AIAA, Guide for the Verification and Validation of Computational Fluid Dynamics Simulations, AIAA Guid. G-077-1998. (1998).
- [176] Y. A. Cengel, A. J. Ghajar, Heat and Mass Transfer, Fundamentals & Application, Fifth Edition in SI Units, 5th ed., McGraw-Hill, New York, 2015. http://www.osti.gov/energycitations/product.biblio.jsp?osti_id=6008324.
- [177] J.K. Calautit, H.N. Chaudhry, B.R. Hughes, L. Sim, A validated design methodology for a closed-loop subsonic wind tunnel, Jnl. Wind Eng. Ind. Aerodyn. 125 (2014) 180–194. doi:10.1016/j.jweia.2013.12.010.
- [178] Y. Li, P. V Nielsen, CFD and ventilation research., Indoor Air. 21 (2011) 442–53. doi:10.1111/j.1600-0668.2011.00723.x.
- [179] Q. Chen, J. Srebric, A Procedure for Verification, Validation, and Reporting of Indoor Environment CFD Analyses, HVAC&R Res. 8 (2002) 201–216. <http://www.tandfonline.com.proxy.lib.sfu.ca/doi/abs/10.1080/10789669.2002.10391437#.Vn6AcPI97IU>.